BonMobile

The 100% Sustainable Urban Air Mobility Vehicle

AE3200: Design Synthesis

Group 24

Delft University of Technology

TUDelft

This page has intentionally been left blank.

BonMobile

The 100% Sustainable Urban Air Mobility Vehicle

by

Group 24

Student Name	Student Number
Iris van Alkemade	5088291
Harshit Bohra	4681754
Marnix van Breukelen	5099536
Mick Hekkema	5074126
Miruna Iordan	4868293
Miłosz Jezierski	5064066
Maarten Kadijk	4874617
Marco Radaelli	5063973
Luuc Roemer	5083044
Tadé Whenu	4867211

Tutor:	Dr. S. Teixeira De Freitas
Coaches:	Dr. B. Çaglar & Ir. H.F. Mourão Bento
Project Duration:	April, 2022 - June, 2022
Faculty:	Aerospace Engineering, TU Delft

Cover:	`https://wallpaperaccess.com/big-ben-london-england`
Style:	TU Delft Report Style, with modifications by Daan Zwaneveld

TU Delft

Preface

This report is documented by a group of ten aerospace engineering students at Delft University of Technology, working on the final Design Synthesis Exercise of their bachelor. The group is assigned with making a design of a 100% sustainable Urban Air Mobility vehicle. This with the scope of taking away the flight shame that people have because of the poor sustainability image that the flight industry has. Furthermore, this can be a solution to the increasing traffic congestion, caused by the increase in urbanisation. The report assesses this problem and presents a design that tackles this and is the start for a more sustainability future in the growing urban aviation industry.

The group would like to thank all the people involved in this project. For the propulsive design, we would like to thank Dr. Ragni, Dr. Pavel and Dr. Sinnige. A lot of thanks to Dr. Kelder for his help with the battery choice and design and to Dr. Castro for his contribution to the approach of the structural design of the vehicle. Furthermore, the group wants to acknowledge the help by Ir. Poermans for the aerodynamic estimations of the design. In addition, the group would like to thank Mr. Lopez Blas from EASA for his collaboration in terms of certification requirements. The group is very happy with the great availability and contributions of all of these people.

Special thanks go to Mr. Van den Bos and Mr. Atherstone for their outstanding help and availability throughout the entirety of project in terms of the CAD design of the vehicle. Without them, a detailed analysis of the structural performance and the look of the vehicle would not have been possible.

Finally, the group especially wants to thank the supervision team of this project: Dr. S. Teixeira De Freitas, Dr. B. Çaglar and Ir. H.F. Mourão Bento. Their availability and guidance throughout the project has been of immense help in all the technical and organisational fields covered by this project. Without them this project would not have been possible and not exist at all.

Iris van Alkemade
Harshit Bohra
Marnix van Breukelen
Mick Hekkema
Miruna Iordan
Miłosz Jezierski
Maarten Kadijk
Marco Radaelli
Luuc Roemer
Tadé Whenu

Group 24
Delft, June 2022

Executive Overview

The urban mobility system is to modern cities what the blood circulatory system is to every human. Without it, efficient urban transport of people and products would not be possible. Furthermore, the urban mobility development strongly influences the comfort people experience in everyday travels within urbanised areas. Nowadays, when accelerating urbanisation and climate change have become increasing problems globally, the cities are forced to look for new ways of facilitating fast and sustainable transport. A solution to this problem could be the "third dimension", or in other words, the air-space over cities that still remains widely unused. This idea perfectly addresses the problem concerning the increasing congestion on one side [1] however, to meet nowadays expectations, the social and the environmental side of this solution must also be taken into account. This concerns mainly the increase of "flight shame" because of pollution and waste coming from the aviation industry [2]. These aspects lead to the following Mission Need Statement: *"To provide 100% sustainable air mobility transport to meet growing demands of transport in urban environment.* This report aims to present the final design of this Urban Air Mobility vehicle, also by focusing on the details of the subsystems, how each one of them affects the system as a whole and how the process can be made sustainable in the subsystem design already. The result of this report leads to the creation of a new vehicle: *"The BonMobile"*.

Project Logic & Design Process

The report starts off with a general overview of the process of the project. A Gantt chart, together with a Functional Flow Diagram and a Functional Breakdown Structure are presented to show both the organisation of the group, as well as the functions that the vehicle needs to be able to perform respectively. The reader can refer to these diagrams in more detail in chapter 2. Furthermore, a compliance matrix is presented, showing the most important (technical) requirements for the vehicle and their compliance status. Most of the requirements are either complied with, or intended to complied with. The latter means that no direct calculations have been made at this stage of the design, but that it has been thought about and it should mainly be demonstrated during the verification of the requirements at a later stage. There is one requirement that is partially complied with, which is the noise requirement. The requirement stated that the vehicle shall produce less noise than $70\,dB$ at a distance of $100\,ft$. However, at this stage this requirement is not met. However, this noise requirement is met at the cruise altitude, where the vehicle spends most of its time. There are also other requirements that have not been considered, mainly due to the time constraint and the level of detail of this design phase. Thus, the reports also presents a project design and development logic for the continuation of the design. A general overview of this can be found in Figure 1 below.

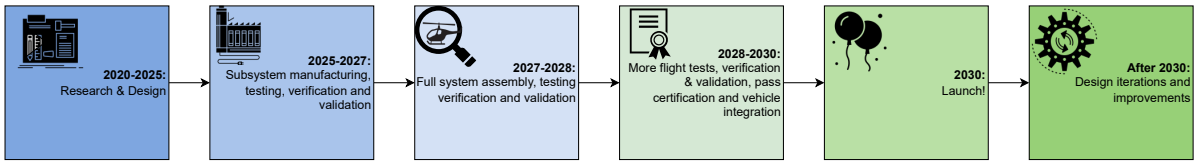

Figure 1: Project Design & Development logic

More detail about the project design and development logic can be found in section 2.2.

Mission & Operations

For the design of the subsystems and especially the required performance of them, the mission of the vehicle has to be specified. A general overview of the mission profile of the vehicle, which contains the most critical mission, namely two times $20\,km$, is presented in Figure 2. This is the most critical flight case as the vehicle goes multiple times through power intensive phases, namely hover and climb. This is important to consider as the battery needs to have enough energy stored to let the vehicle fly to its destination before having to recharge again.

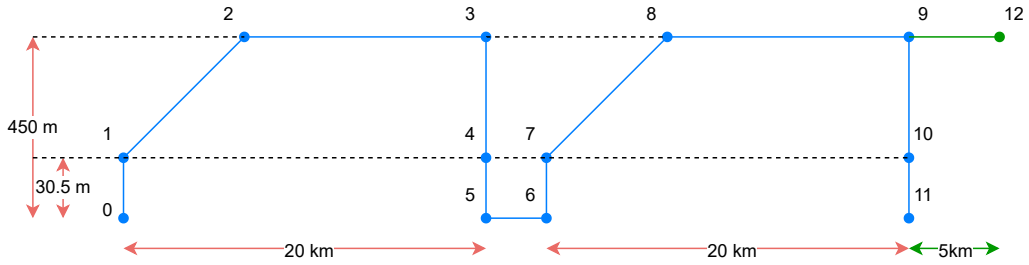

Figure 2: Mission Profile

Having batteries as the source of energy gives the possibility to easily swap the batteries and recharging them without the vehicle having to wait for them to completely recharge. In other words: the batteries can be taken out, charged and serviced separately. Also, for a more detailed overview of the data links and communications within the operations and logistics, the reader can refer to section 3.3.

Market & Infrastructure

In addition to the mission and operations of the vehicle, an analysis has been performed on the market and the infrastructure for the vehicle. As mentioned before, one of the purposes for the design of this vehicle is to solve the problems in urban traffic. In terms of infrastructure, the teams concludes that a lot still needs to be done before the expected launch in 2030. First of all, the vertiports from which the vehicle should take-off and land at still needs to be built. This requires a closer look at the already existing infrastructure of a city and the connection to the electrical power grid. Furthermore, it has been decided to make the vehicle fully autonomous. This comes with higher system development costs and it requires more research into the communication between vehicle and a central command station. To further analyse the possibilities of the vehicle within the market, a case study has been performed for the Greater London area. A comparison has been made between the London taxi service, and the results of this case study is presented in Figure 3. The figure includes 15% error bars to account for uncertainties and for small deviations from the initial flight path angle due to other air traffic.

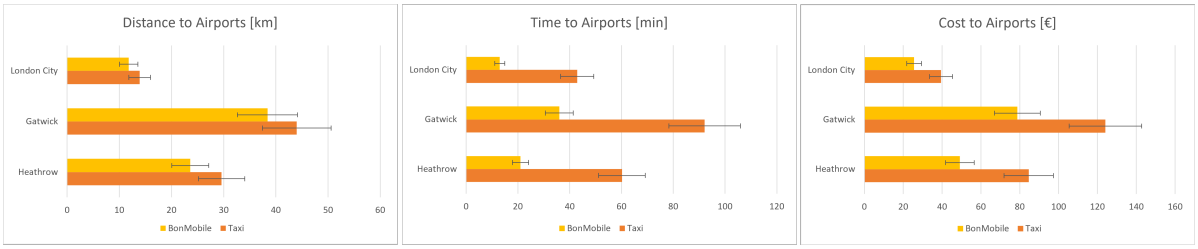

Figure 3: Proposed vehicle design vs ground taxis

This figure shows that compared to ground taxis, the designed vehicle has great potential and can fill the demand for these kind of vehicles and be promising in the near future. On average BonMobile saves 16%, 65% and 38% on distance route, total travel time and costs respectively and the vehicle can be used in at least 10 of the biggest cities in Europe, where also the main airports are located within a range of 40 km from the city centre.

Budget Allocation

In order for the vehicle to be as competitive as analysed in the market and infrastructure analysis, the manufacturing costs per vehicle need to be determined and below the set requirement of €1,500,000. For this, an extensive estimation from one of the Roskam books has been used [3]. The results of this cost estimation are visualised in Figure 4.

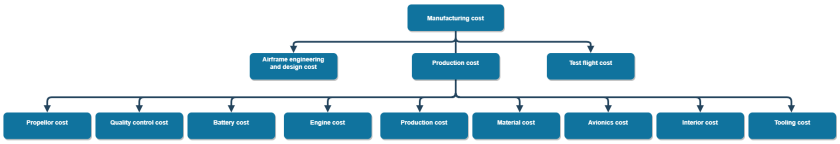

Figure 4: Manufacturing cost breakdown in euro of vehicle

From Figure 4 it becomes evident that most of the costs go into the production of the product itself. This does not include costs such as the tools or the materials. The labour cost per manhour is approximately €46.50, which is similar to large companies such as Airbus [4]. This relatively high labour cost in comparison to other parts of the world has been chosen to also be socially sustainable. The total manufacturing cost per vehicle adds up to €1,369,698. ± €180,000. More detail and discussion on the manufacturing costs can be found in chapter 5.

Aerodynamics

Starting the technical design of the vehicle, it is firstly important to determine some important aerodynamic characteristics of the vehicle, that influence the performance of the vehicle. This is mainly the drag produced by the vehicle. Furthermore, aerodynamic noise is one of the requirements, thus this has to be addressed as well. As no Computational Fluid Dynamics has been used at this stage of the design, the drag of the vehicle has mainly be computed by approximating the structural components by cylinders. The cylindrical shape has been chosen from a structural point of view, as cylindrical shapes are very good in tension and compression. After an aerodynamic drag analysis, it has been found that with the current cylindrical shape of mainly the struts in the upper structure, the vehicle is able to fly and is meeting the requirements as set by the stakeholder. The DSE team proposes for future development to push the aerodynamic design even more, by making the shape of the vehicle even more aerodynamic. By reducing the drag even more, the motors can work at less power to achieve the same amount of thrust needed. Less power also means less energy necessary, thus lowering the weight needed for the battery. This then goes together with a trade-off that has to ensure the structural integrity of the vehicle, and that it keeps complying with the achieved requirements.
As discussed before, the noise requirement at 100 ft has not been complied with at this stage. This is mainly due because of the high minimum angular velocity at which the propellers have to spin. This minimum value is set to first of all provide enough power during certain phases such as hover and secondly to avoid retreating blade stall. The latter happens when the tip velocity of the blades is low compared to the forward velocity of the vehicle. A noise comparison between take-off and cruise conditions at different distances is visualised in Figure 5.

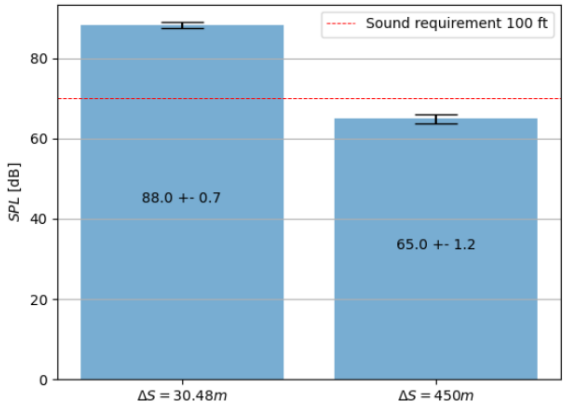

Figure 5: Noise at 100 ft and 450 m in take-off and cruise conditions respectively.

However, to put things into perspective, the noise produced by the vehicle is still far below that of an helicopter, which produces the same amount of noise at a distance five times as large [1]. It is

[1] From: https://aerocorner.com/blog/why-are-helicopters-so-loud/#:~:text=associated%20with%

recommended to spend more resources in the rotor design of the propulsive system to optimise the shape and the performance of the blades, such that the noise produced can be lowered. Furthermore, it is also recommended to re-evaluate the noise requirement at 100 ft as this was not specifically based on any regulations or stakeholder requirements, but on a comparison with cars. However, during the cruise phase, the vehicle produces a noise level equivalent to a normal conversation, which is desirable as the vehicle spends most of its time in cruise.

Propulsive Design

Following the aerodynamic performance of the vehicle, is the design of the propulsive system of the vehicle. It has been found that the maximum thrust and power the vehicle has to provide is during take-off to provide an initial upward acceleration. An analysis using several design inputs such as angular velocity, rotor radius and different motor options resulted in the final engine choice of the Emrax 208. The blades used are made out of carbon fibre and each blade has a weight of 1.34 kg. An overview of the chosen propulsion system can be found in Table 1.

Table 1: Propulsion system parameters

Parameter	Value
Rotor radius (m)	0.8
Total rotor weight (kg)	32.2
Total motors weight (kg)	112.8
Angular velocity range (rpm)	2422-3238
Continuous torque (Nm)	76.1
Peak torque (Nm)	131
Continuous power available (kW)	25.9
Peak power available (kW)	44.5
Figure of merit	0.743

Performance

Before being able to size the energy storage system, the overall performance of the vehicle needs to be analysed, also using the results from the aerodynamic and propulsive performance. The DSE team has looked first of all at what the design speeds would be for an optimal power usage, and after that the climb performance of the vehicle has been analysed. This is important because climb is one of the more power consuming phases, especially because for climb a certain amount of access power is needed. Combining this, together with the mission profile showed before in Figure 2, an estimate for the energy used at different velocities is given. The result of this analysis is presented in Figure 6 below.

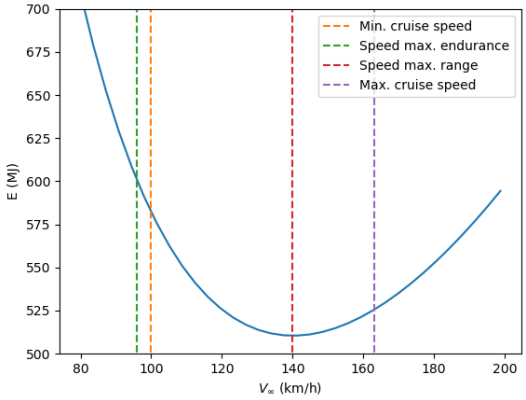

Figure 6: Total energy required for various freestream velocities.

`20helicopters.-,How%20Loud%20Is%20a%20Helicopter%3F,mower%20is%20about%2090%20decibels.`. Visited on 20-06-2022

Figure 6 shows that at the required velocity of $100\,km/h$, for which the vehicle designed, the total energy used during the mission is determined to be approximately $560\,MJ$. This value can be used to size the batteries of the vehicle. The team recommends however to look at higher cruise velocities during future design phases, as in terms of energy used, these seem to be more promising. Nevertheless, the change in cruise velocity would also mean that the other subsystems possibly need to be changed as well, so a close look at the integration of the subsystems should be taken in this case.

Energy Storage

As obtained from the performance calculations, the energy used during the mission is equal to $560\,MJ$. Thus, an adequate energy storage system in forms of batteries needs to be chosen. To choose a battery type that can both provide the required performance and low weight required, as well as good recyclability, a trade-off has been made between several battery types. Mainly because of its high gravimetric and volumetric energy density and good recyclability possibilities, Lithium-Sulfur batteries were chosen for the energy storage of the vehicle. A battery mass and volume of $419.8 \pm 5\%\,kg$ and $0.36 \pm 10\%\,m^3$ are determined. The reader can refer to chapter 7 for more detail on the design of the propulsion system and the energy storage.

Materials

Materials used in the vehicle should be both sustainable and should have excellent material properties. Important when deciding on the materials used in the vehicle is the use of the component. For instance, for the primary structure of the vehicle, performance is considered more important than sustainability. Most components in the interior do not carry a lot of loads. Hence, the performance of the material is less important and the main focus lies on the sustainability of the material. Taking these assumption into account, the materials as shown in Table 2 are found.

Table 2: Parts of the UAM vehicle and the corresponding material used.

Part	**Material used**
Supporting structure	Composite (Carbon fibres & Vitrimer)
Fuselage skin	Composite (Carbon fibres & Vitrimer)
Skid	Composite (Carbon fibres & Vitrimer)
Ribs	Aluminium 2024
Stringers	Aluminium 2024
Interior design	Composite (Flax fibres & Epoxy)
Windows	Polycarbonate
Battery	Lithium Sulphur
Rotor blades	Composite (Carbon fibres & Vitrimer)
Propulsion motors	(Aluminium 6082 & hardened steel & copper with epoxy coating)
Firewall	Steel with aluminium coating
Hubs	Aluminium 2024
Floor	Aluminium 2024

For the composite parts, the properties and the maximal stress failure criterion are computed using Laminate Theory. These composite properties and those for that of the aluminum alloy used can be found in Table 3.

Table 3: Main UAM materials summary table

Material	**Density** $[kg/m^3]$	**Tensile strength** $[MPa]$	**Elastic modulus** $[GPa]$	**References**
Carbon fibres/vitrimer	1494	540	52.7	N//A
Aluminium 2024	2770	469	73.1	Thomas[2]
Flax fibres/epoxy	1320	200	17.7	N/A

Recommended for later design phases is to perform a more in-depth composite failure analysis.

Furthermore, the material properties per layer of the composite could be measured by experiment. Lastly, recommended is to analyse how the vehicle performance is affected by the use of composite parts for the stringers.

Structural Design

The final subsystem that is considered for the design of the vehicle itself, is the structural part of the vehicle. This includes the design for the fuselage, the upper structure and the undercarriage. These parts need to be designed accordingly to the loads each part is subjected to and also for the material that is used for that part. The cross-section of the fuselage is mainly determined by the seating configuration of the passengers. The overall dimensions of the vehicle are not only dependent on the volume needed for things like batteries, luggage and avionics, but also on the maximum allowable stresses and loads that the structure needs to be able to withstand. For the analysis of the loads on these structures, used for the sizing of the components, the DSE group has gone from simple calculations by hand for statically determinant systems, to the use of Finite Element Methods. An overview of the sizing of several components is given in Table 4.

Table 4: Structure summary - dimensions and weight

Subsystem	**Type**	**Dimensions**	**#**	**Total mass**
Cabin	Interior	width: 1190 mm height: 2040 mm		25 kg
	Avionics	-		51.7 kg
Ribs	T-shape	thickness: 3.00 mm width: 47.0 mm height: 50.0 mm length: 26.3 m	4x	21.2 kg
Stringers	L-shape	thickness: 1.50 mm width: 7.00 mm height: 10.0 mm length: 3.57 mm	10x	4.46 kg
Skin		area: 16.8 m^2 thickness: 1.80 mm		45.2 kg
Skid	Leg hollow circular shaft	thickness: 1.80 mm diameter: 100.0 mm	4x	0.806 kg
	Ski rectangular beam	thickness: 30.0 mm width: 100 mm length: 2000 mm	2x	8.96 kg
Top	Struts	centre length: 1344 mm inner triangle: 1900 mm outer triangle: 1900 mm outer: 2664 mm		221 kg

Manufacturing, Assembly & Integration Plan

The plan to produce the vehicle is laid out in the manufacturing, assembly and integration plan. A production plan is a setup where waste is reduced and sustainability is key. To start, the components are manufactured or purchased from vendors. After this phase, the components are assembled into sub-assemblies like the skid, interior components and supporting structure for the engines. Lastly, other interior components, engines, avionics, electric circuits, windows and batteries are purchased from external parties. These systems are subsequently integrated into the airframe of the vehicle. Important to notice is that these components are only purchased after assembly of the airframe of the vehicle. Just in time to be integrated into the vehicle while reducing storage space needed. This process is shown in Figure 7.

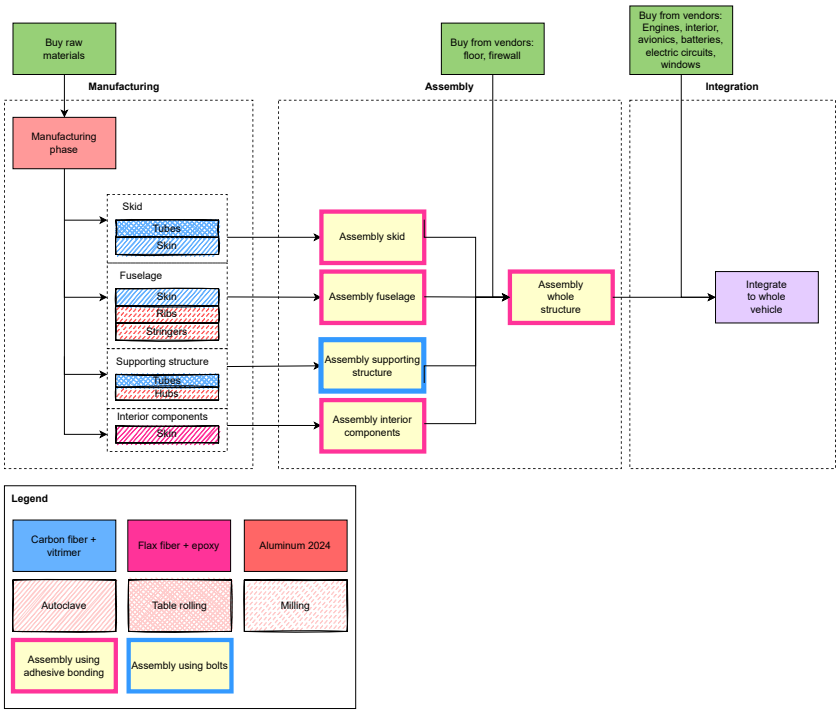

Figure 7: Overview showing the manufacturing, assembly and integration plan

Risks

Next to the organisational and technical side of the design process, it is also of great importance to have a proper risk management and especially a good risk mitigation. There are two major risk themes that this DSE has assessed. First of all, it is decided to have an autonomous piloting system (so no pilot present in the vehicle), which in contrast to the major advantages it has, also introduced a couple of risks that need to be assessed. These concerns have mainly to do with the legislation of the autonomous system and external factors, such as emergency situations or hacks of the control system. On the legislation side, it is possible to work closely with EASA and perform tests for the vehicle separately. For the external factors, an appropriate and more extensive model for the vehicle has to be made to ensure the reduction of the impact of these risks and appropriate software needs to be installed to protect from potential hacks of the system. The second risk theme is the performance of certain chosen materials. This is majorly because the performance of these materials for specific use has not been fully researched yet. To get a greater understanding of these materials and to ensure that the impact and the chance of occurrence of these risks remain low, more resources needs to be put on the research and development of these materials, together with a close collaboration with specialised companies. For more detailed information about the risks and their mitigation, as well as a RAMS analysis, the reader can refer to chapter 13.

Model Validation

The verification and validation of the subsystems can be found in more detail at the end of each chapter about a respective subsystem. In addition to that, it is important to validate the complete model of the vehicle once the subsystems are integrated together. Firstly, the model was compared to another model that estimates the weight of multirotor eVTOLs, based on range and cruise speed. It was found that the vehicle weighs 31% less compared to the model. This difference is accredited to the fact that the vehicle is designed for a different kind of mission profile than used in the model. Secondly, the model of the vehicle is compared to other vehicles. This comparison in terms of range, payload and maximum take-off mass is visualised in Figure 8.

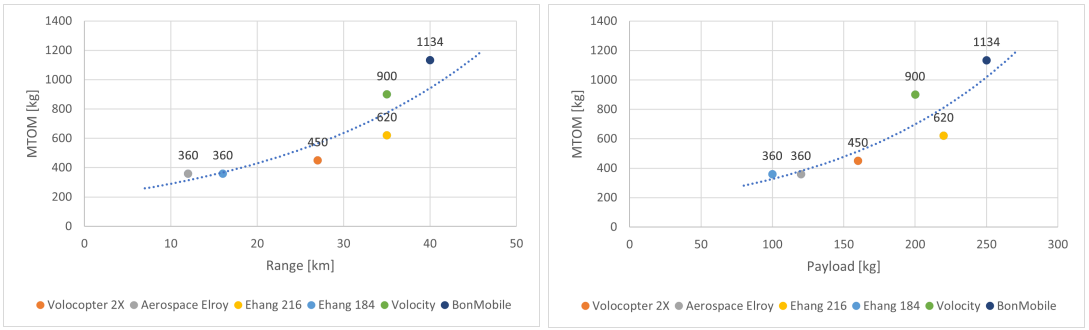

(a) Range against Maximum take-off mass

(b) Payload against Maximum take-off mass

Figure 8: Comparison of mass with other UAM vehicles

The fact that the designed vehicle has a higher mass than other comparable vehicles is because the vehicle is designed for landing and taking off twice, unlike the other vehicles. Thus, the main discrepancy during the validation of the model can be accredited to a different mission profile for which the vehicle is designed.

Sustainability

The sustainability approach taken in developing the UAM is to focus on sustainability in each part of the design process - from the materials chosen to the manufacturing process used. Furthermore, end-of-life and disposal solutions for the UAM materials have also been considered. The biggest percentage of the UAM mass is composed of lithium sulphur, with a value of 32 %, followed closely by carbon fibre/vitrimer composite, with a value of 26 %. For manufacturing processes, most subsystems are purchased from the vendor, hence their production is not considered. For the rest of the subsystems, such as ribs, stringers, hub and others, manufacturing processes include milling, autoclave, table rolling and injection moulding. For the disposal of these materials at the end of life of the vehicle, the conclusion is that all materials used in the UAM are, or will be 100% recyclable by 2030, the launch date. Carbon fibre/vitrimer composite constituting a significant mass of the UAM design will be especially helpful in reaching this goal since it is already a fully recyclable composite. For more detailed information about the sustainability approach and life cycle analysis, the reader can refer to Chapter 15.

Iterations & Conclusions

When integrating all the subsystems together, it is discovered that some parameters and subsystems need to be adjusted in order for the subsystems to work well with each other and comply to the requirements. This change then leads to another, and this goes on for some time. This process is called the iterative process of the design. A classic phenomenon called the 'Snowball effect' arises from this process: if the design of a certain system becomes lighter, and thus a lighter maximum take-off mass (MTOM) is calculated, it influences all the other subsystems. Note that this snowball effect can also work the other way around. The iterative design continues until the design converges to some value for the MTOM. The parameters for the current conceptual design of the vehicle, after four iterations have been performed, are presented in Table 5. In addition to this, a render of the final design has also been made and is presented in Figure 9.

Operating Empty Weight [kg]	**Payload [kg]**	**No. of passengers [-]**	**Range [kg]**	**Flight time [hr]**	**Design speed [km/h]**	**Energy Used [MJ]**	**Turn-around time [hr]**
930	250	2	2x20	TBD	110	445	<1

Table 5: Current BonMobile parameters

Figure 9: Render of the vehicle.

There is still a lot of room for further iterations of the design, including more extensive research on technologies used in the design process. In the end, this will lead to a converged and even more sustainable design for launch in 2030. The team is confident that this report is a start for a more sustainable future where it will be possible to travel more easily and in a new way in urban areas: through the skies.

Contents

Nomenclature

If a nomenclature is required, a simple template can be found below for convenience. Feel free to use, adapt or completely remove.

Abbreviations

Abbreviation	Definition
BoL	Beginning of Life
CFD	Computational Fluid Dynamics
CRP	Coaxial contra-rotating propellers
DoD	Depth-of-Discharge
EASA	European Aviation Safety Agency
EoLC	End of life Capacity
eVTOL	electric Vertical Take-Off and Landing
FBD	Free Body Diagram
FEM	Finite Element Method
FM	Figure of merit
GLARE	Glass Laminated-Reinforced Epoxy
ISA	International Standard Atmosphere
MTOM	Maximum take-off mass
MTOW	Maximum take-off weight
RPM	Revolutions per minute
UAM	Urban Air Mobility
VTOL	Vertical Take-Off and Landing
RAMS	Reliability, Availability, Maintanability and Safety

Symbols

Symbol	Definition	Unit
a	Semi-major axis	$[mm]$
A	Area	$[m^2]$
A_b	Rotor blade area	$[m^2]$
A_{disk}	Rotor disk area	$[m^2]$
b	Width	[m]
B	Number of rotor blades	[-]
c	Chord	[-]
$C_{(a)_m}$	Avionics cost	[€]
C_{aedm}	Engineering cost	[€]
C_{apc_m}	Production cost	[€]
C_{array}	Array capacity	[Ah]
C_{bat}	Battery capacity	[Ah]
C_{bat_m}	Battery cost	[€]
C_{blade}	Blade cost	[€]
C_{cell}	Cell capacity	[Ah]
$C_{(e)_m}$	Engine cost	[€]
C_{fto_m}	Flight test cost	[€]
C_D	Drag coefficient	[-]
C_{D_0}	Zero-lift drag coefficient	[-]

Symbol	Definition	Unit
C_{d_0}	Profile drag coefficient	[-]
C_f	Skin friction coefficient	[-]
C_{int_m}	Interior cost	[€]
$\bar{C_l}$	Blade mean lift coefficient	[-]
C_{man_m}	Labor rate manufacturing	[€/h]
C_{mat_m}	Material cost	[€]
C_{M_x}	Moment around x-axis coefficient	[-]
C_{M_y}	Moment around y-axis coefficient	[-]
C_{P_0}	Profile power coefficient	[-]
C_T	Thrust coefficient	[-]
C_{tool_m}	Tooling cost	[€]
$C_{Q,x}$	X-plane shear coefficient	[-]
$C_{Q,y}$	Y-plane shear coefficient	[-]
C_{qc_m}	Quality control cost	[€]
d	Diameter	[m]
D	Blade diameter	[m]
D	Drag	[N]
D_c	Cruise drag	[N]
E	Young's modulus	[GPa]
E_{tot}	Total energy	[W]
f	Equivalent wetted area (=D/q)	$[m^2]$
F_x	Force in x-axis	$[N]$
F_y	Force in y-axis	$[N]$
F_z	Force in z-axis	$[N]$
h	Height	[m]
I_{xx}	Second moment of area about x-axis	$[m^4]$
I_{yy}	Second moment of area about y-axis	$[m^4]$
K_{prof}	Profile power constant	[-]
K_2	Noise constant (= 0.42689)	$[s^3/m^3]$
l	length	[m]
l/d	Fineness-ratio	[-]
L	Characteristic length	[m]
L	Lift	[N]
m	mass	[kg]
m_{bat}	Battery mass	[kg]
M	Mach number	[-]
M_x	Moment around x-axis	[Nm]
M_y	Moment around y-axis	[Nm]
M_z	Moment around z-axis	[Nm]
$MMOI$	Mass moment of inertia	$[m^4]$
MHR_{aed}	Engineering hours	[h]
n	Rotor revolutions	[Rev/s]
n_{arrays}	Number of arrays	[-]
n_{blades}	Number of blades	[-]
n_{cells}	Number of cells	[-]
N_{rotors}	Number of rotors	[-]
p	Perimeter	[m]
P	Power	[W]
P_a	Actual power	[W]
P_h	Hover power	[W]
P_i	Induced power	[W]
P_{ideal}	Ideal power	[W]
P_o	Profile power	[W]
P_p	Parasitic power	[W]

Symbol	Definition	Unit
P_r	Required power	[W]
P_{req}	Power required	[W]
P_y	Climb power	[W]
q_∞	Dynamic pressure	[Pa]
Q	Torque	[Nm]
Q_r	Rotor torque	[Nm]
Q_{req}	Torque	[Nm]
Q_x	Shear in x-plane	[m]
Q_y	Shear in y-plane	[N]
R	Radius	[m]
R_r	Rotor radius	[m]
Re	Reynolds number	[-]
R_{e_m}	Labor rate	[€/h]
s	Rotor solidity	[-]
SPL	Sound Pressure Level	[dB]
S_{ref}	Reference surface area	$[m^2]$
S_{wet}	Wetted surface area	$[m^2]$
T	Thrust	[N]
T_h	Hover thrust	[N]
T_r	Rotor thrust	[N]
v_h	Inflow velocity for hover	[m/s]
v_i	Induced velocity	[m/s]
V	Velocity	[m/s]
V_{array}	Array voltage	$[V_{DC}]$
V_{bat}	Battery voltage	$[V_{DC}]$
V_c	Climb velocity	[m/s]
V_D	Descent velocity	[m/s]
V_∞	Cruise velocity	[m/s]
V_T	Tip velocity	[m/s]
w	Wake velocity	[m/s]
W	Weight	[N]
...		
α	Angle to flow	[rad]
ΔS	Distance to observer	[m]
κ	Induced power factor	[-]
λ	Inflow ratio	[-]
λ_h	Hover inflow ratio	[-]
μ	Advance ratio	[-]
ρ	Density	[kg/m^3]
σ	Rotor solidity	[-]
σ	Normal stress	[MPa]
σ_{cr}	Critical stress	[MPa]
Ω	Angular velocity	[rad/s]
...		

1 Introduction

In a world where the climate becomes an evermore important factor in people's life, there is also an increase in "flight shame" because of the emissions and the relatively low sustainability of the aviation industry [2]. Simultaneously, there is a growing urban population that is putting even more pressure on the urban infrastructure, causing lots of traffic congestion problems [1]. These problems lead to the following Mission Need Statement, as formulated by the DSE group: *"To provide 100% sustainable air mobility transport to meet growing demands of transport in urban areas".*

This report aims to finalise and present the final design of the 100% sustainable Urban Air Mobility vehicle. This is done by going into detail about the subsystems of the vehicle, how they get integrated together and by presenting the overall performance and sustainability of the vehicle. This report therefore also aims to achieve the Project Objective Statement: *"Design a 100% sustainable Urban Air Mobility (UAM) vehicle with a unit cost of €1.5M by 10 students in 10 weeks".*

The report is structured as follows: chapter 2 addresses the project logic and design and the organisational side of the DSE project. After that, chapter 3 and chapter 4 present the mission of the vehicle and its operations and an extensive market analysis respectively. This also includes a case study to show the demand of the vehicle as an air-taxi service. Following this is the budget allocation, which is described in chapter 5. Then, the report goes deeper into the technical side of the vehicle. First of all, chapter 6 presents an estimate of the aerodynamic properties of the vehicle, such as drag and noise, after which the design of the propulsion system is presented in chapter 7. In addition, some more information about the overall performance and the control of the vehicle is given in chapter 8. Subsequently, based on the vehicle power analysis the energy storage system is designed in chapter 9. After that, chapter 10 and chapter 11 explain the choice of materials and then their implementation with the structural analysis respectively. This analysis leads to the sizing of the vehicle's structural parts. Also, following the choices in materials and structures is a plan for the manufacturing, assembly and integration of all the parts and subsystems, which is described in chapter 12. A proper risk assessment and mitigation, together with a RAMS analysis, needs to be ensured and the result of this is explained in chapter 13. In chapter 14, a comparison is made between other models and vehicles to validate the design presented in this report. As sustainability is a very important factor in this DSE project, it is assessed in a detailed way in chapter 15. At the end of this report, a description of the iterative process of the design and the convergence of the design to a final design proposal is described in chapter 16. Finally, the report closes off with a conclusion and some recommendations for future research and development in chapter 17.

2 Project Logic & Design Process

2.1. Compliance Matrix

At the end of the design of the vehicle, it is necessary to go back to the requirements set at the start of the process and assess which ones are complied with and which are not. This is done by means of a compliance matrix, where the most important (technical) requirements are given, with an indication of their compliance status and an explanation of how this requirement is met (or not). The compliance matrix for this DSE project is given below in Table 2.1.

Table 2.1: Compliance matrix for the set (technical) requirements.

Code	Requirement	Compliance Status	Rationale
UAM-CON-SUS-MAN-1	The waste from the manufacturing shall be assessed for 100% of UAM components	Compliant	Required for Cradle to Cradle certification thus will be performed
UAM-CON-SUS-MAT-1	The materials shall be in compliance with the restricted substances list	Compliant	Materials currently used in the design are not on the restricted substances list
UAM-CON-SUS-MAT-2	The chemical composition of at least 100% of all homogeneous materials within the UAM is defined	Intent to comply	The exact composition of all selected homogeneous materials like Aluminium 2024 or polycarbonate can be obtained once a supplier is selected.
UAM-CON-SUS-MAT-3	A percentage of cycled and/or renewable content shall be incorporated as specified by C2CPII	Intent to comply	Not considered yet [maybe this follows from LCA?]
UAM-TECH-GO-1.1	The minimum payload of the vehicle shall be 250 kg (2 passengers)	Compliant	The UAM vehicle was designed to carry 250 kg payload.
UAM-TECH-ERGO-1	The seat width shall be at least 40.6 cm	Compliant	Minimum seat width was considered in fuselage sizing in section 11.2.
UAM-TECH-ERGO-2	The seat pitch shall be at least 76.2 cm	Compliant	Minimum seat pitch was considered in fuselage sizing in section 11.2.
UAM-TECH-ERGO-3	The headroom space shall be at least 165.1 cm	Compliant	Minimum headroom space was considered in fuselage sizing in section 11.2.
UAM-TECH-ERGO-4	The luggage space volume shall be at least 0.51 m^3	Compliant	Minimum luggage space volume was considered in fuselage sizing in section 11.2
UAM-CON-SFT-EASA-4.1	A safety factor of 1.5 shall be used for a probability of failure higher than 10^{-5}	TBD	The probability of failure is yet to be determined.

UAM-CON-SFT-EASA-4.2	A safety factor of 1.5 shall be used for a probability of failure times the time flown in failure higher than 10^{-5}	TBD	The probability of failure is yet to be determined.
UAM-CON-SFT-EASA-1.5	The configuration of the vehicle from the crew shall be changed only after V_{toss}	Compliant	The configuration of the vehicle cannot be changed during flight.
UAM-CON-SFT-EASA-6.3	Electrical energy storage systems shall be isolated from the energy system	Compliant	Taken into account in the model design, see section 11.2
UAM-CON-SFT-EASA-7.3	An emergency latch shall be present in the vehicle	Intent to comply	Design detail has not considered yet
UAM-CON-SFT-EASA-7.4	Direct visual of the latching mechanism by crew members shall be possible to determine whether all exits are locked	Intent to comply	Design detail has not considered yet
UAM-CON-SFT-2	The vehicle shall show stability for the complete centre of gravity range	Intent to comply	Stability analysis was not priority of the project and is planned after finding exact masses of components
UAM-CON-CST-1	The unit cost of the vehicle shall be below €1.500.000	Compliant	Total cost is €1.369.698. See chapter 5 for a cost breakdown.
UAM-CON-ENV-3	The noise level of the vehicle shall be below 70 dB at a distance of 100 ft	Partial Compliant	The value for noise at 100 ft is around 88 dB. However, the value for noise at cruise is below 70 dB (see section 6.7).
UAM-TECH-FLI-1	The cruise altitude of the vehicle shall be at 450 m	Compliant	Cruise altitude of 450 m was used in designing the mission profile in section 3.1.
UAM-TECH-FLI-2	The cruise speed of the vehicle shall be at least 100 km/h	Compliant	Cruise speed of 100 km/h was used in designing the mission profile in section 3.1.
UAM-TECH-FLI-4	The vehicle shall have a minimum range of 40 km (including 2x20 km) without recharging	Compliant	Minimum range of 40 km (2x20 km) was used in designing the mission profile in section 3.1.
UAM-CON-SFT-EASA-1.2	The vehicle shall have a positive RoC after V_{toss}	Compliant	The vehicle has a positive RoC as it is a VTOL.
UAM-CON-SFT-EASA-6.1	Windshields and windows shall not shatter	Compliant	Polycarbonate, the material the windows are made out of, does not shatter
UAM-CON-SFT-EASA-7.1	The vehicle exists shall be closed during flight	Intent to comply	Not considered yet
UAM-CON-SFT-EASA-7.2	The vehicle exists shall only be able to be opened after the emergency landing	Intent to comply	Not considered yet
UAM-TECH-TO-1	The vehicle shall perform vertical take-off	Compliant	The structures and propulsion have been designed to carry VTOL loads (see chapter 7 and 11)
UAM-TECH-LA-3	The vehicle shall perform vertical landing	Compliant	The structures and propulsion have been designed to carry VTOL loads (see chapter 7 and 11)
UAM-TECH-MAIN-2	All the modules in the vehicle shall be replaceable	Intent to comply	By using adhesives and bolts
UAM-CON-SFT-EASA-1.3	The vehicle shall have a 4.6 m clearance at/after TDP	Intent to comply	Stability and control yet to be assessed.

UAM-CON-SFT-EASA-1.4	The vehicle shall have a climb rate of 4.5% after 30.5 m	Compliant	The vehicle is a VTOL hence can have any climb rate.
UAM-CON-SFT-EASA-6.2	Materials adjacent to fire zones shall be fire resistant	Compliant	There are firewalls present to protect the passengers and fire protection from firezones. (See: subsection 11.2.6)
UAM-CON-SFT-EASA-5.1	The engine limit loads shall be higher than the loads induced at sudden engine stoppage	Compliant	Engine limit load higher than sudden engine stop.
UAM-CON-SFT-EASA-5.2	The engine limit loads shall be higher than (x+0.25) times the maximum mean torque	Compliant	Engine limit load higher than (x+0.25) times the maximum mean torque.
UAM-CON-SFT-EASA-2.1	The vehicle shall be free from aerolastic instability up to the diving speed	TBD	Aerodynamic design of this detail is beyond the scope of DSE
UAM-CON-SFT-EASA-1.1	The vehicle shall be able to fly with a sidewind of at least 17 kts	TBD	Stability and control yet to be assessed.
UAM-CON-SFT-EASA-1.6	The vehicle shall have a trajectory change without descent of at least 3°/s	TBD	Stability and control yet to be assessed.
UAM-CON-SFT-EASA-2.2	The vehicle shall handle gusts loads of at least 50 ft/s also with failure in systems	TBD	Stability and control yet to be assessed.
UAM-CON-SFT-EASA-3.3	The total reaction time of the pilot shall be assumed 1.5s	Intent to comply	Not applicable
UAM-CON-SUS-EMS-1	There shall be zero GHG emissions during maintenance	Intent to comply	Not applicable
UAM-CON-SUS-EMS-2	The propulsion system shall emitt zero GHG	Compliant	Electric propulsion system is used so zero emission.

Note that not all requirements are complied with yet; this is mainly because it is not possible at this stage of the design to assess if the requirement is complied with or not. Thus, recommendations for the next design phase and future research and development are needed. These recommendations can be found in chapter 17.

2.2. Project Design & Development logic

The DSE is a period of ten weeks with ten students, equal to approximately four thousand working hours. However, actual design projects can take up many years. Within the time scope of the DSE it is hence impossible to converge to a truly sustainable, efficient and realistic design. The steps required to go towards a fully designed vehicle, but also get it certified and integrated into the market are presented in the timeline from Figure 2.1. This has also been put into a Gantt chart form to also show the interdependencies between the several activities. Note that this is an estimate on a higher-level without going into the exact details of the activities. This Gantt chart is presented in Figure 2.2

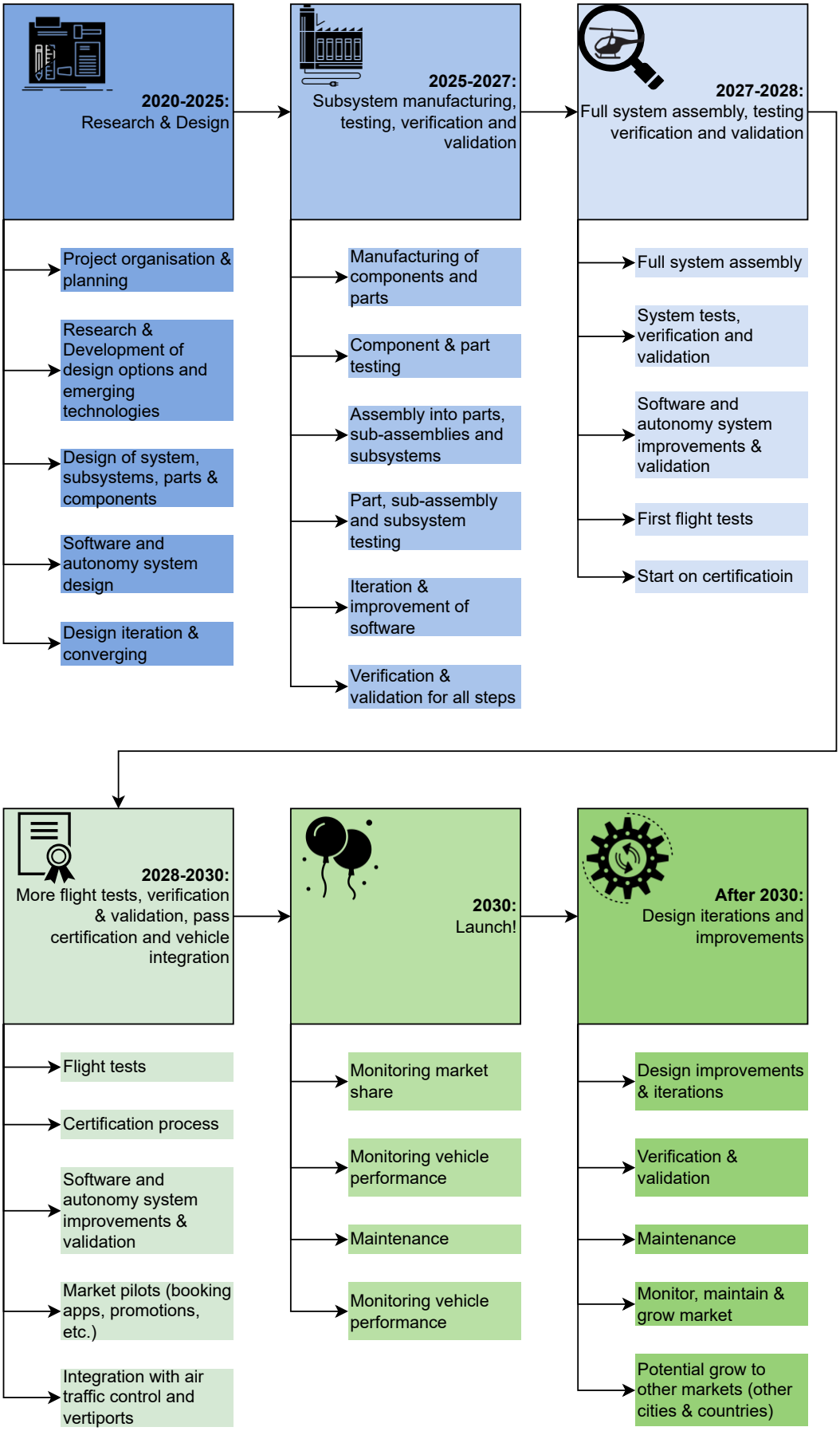

Figure 2.1: Project Design & Development logic

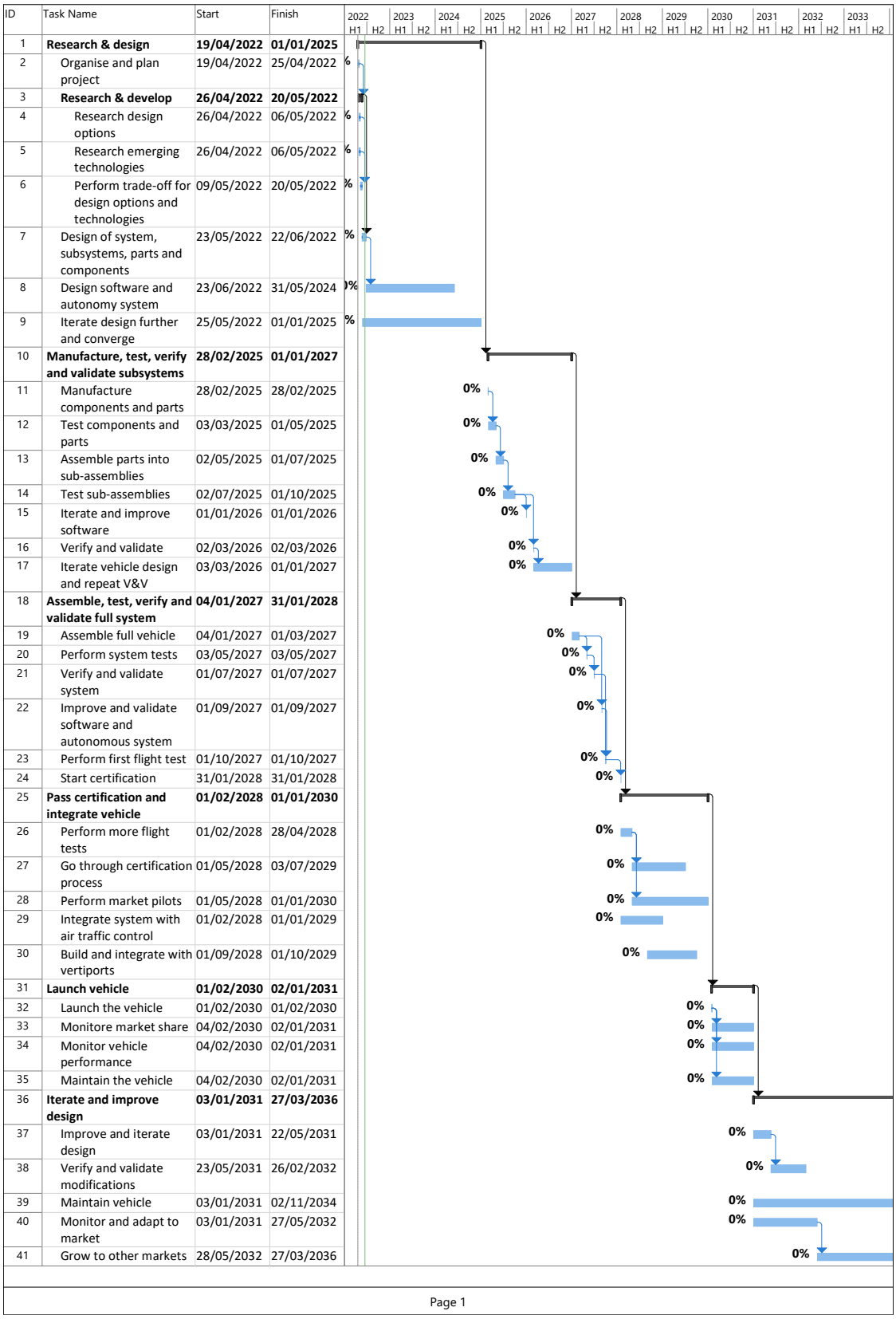

ID	Task Name	Start	Finish
1	**Research & design**	**19/04/2022**	**01/01/2025**
2	Organise and plan project	19/04/2022	25/04/2022
3	**Research & develop**	**26/04/2022**	**20/05/2022**
4	Research design options	26/04/2022	06/05/2022
5	Research emerging technologies	26/04/2022	06/05/2022
6	Perform trade-off for design options and technologies	09/05/2022	20/05/2022
7	Design of system, subsystems, parts and components	23/05/2022	22/06/2022
8	Design software and autonomy system	23/06/2022	31/05/2024
9	Iterate design further and converge	25/05/2022	01/01/2025
10	**Manufacture, test, verify and validate subsystems**	**28/02/2025**	**01/01/2027**
11	Manufacture components and parts	28/02/2025	28/02/2025
12	Test components and parts	03/03/2025	01/05/2025
13	Assemble parts into sub-assemblies	02/05/2025	01/07/2025
14	Test sub-assemblies	02/07/2025	01/10/2025
15	Iterate and improve software	01/01/2026	01/01/2026
16	Verify and validate	02/03/2026	02/03/2026
17	Iterate vehicle design and repeat V&V	03/03/2026	01/01/2027
18	**Assemble, test, verify and validate full system**	**04/01/2027**	**31/01/2028**
19	Assemble full vehicle	04/01/2027	01/03/2027
20	Perform system tests	03/05/2027	03/05/2027
21	Verify and validate system	01/07/2027	01/07/2027
22	Improve and validate software and autonomous system	01/09/2027	01/09/2027
23	Perform first flight test	01/10/2027	01/10/2027
24	Start certification	31/01/2028	31/01/2028
25	**Pass certification and integrate vehicle**	**01/02/2028**	**01/01/2030**
26	Perform more flight tests	01/02/2028	28/04/2028
27	Go through certification process	01/05/2028	03/07/2029
28	Perform market pilots	01/05/2028	01/01/2030
29	Integrate system with air traffic control	01/02/2028	01/01/2029
30	Build and integrate with vertiports	01/09/2028	01/10/2029
31	**Launch vehicle**	**01/02/2030**	**02/01/2031**
32	Launch the vehicle	01/02/2030	01/02/2030
33	Monitore market share	04/02/2030	02/01/2031
34	Monitor vehicle performance	04/02/2030	02/01/2031
35	Maintain the vehicle	04/02/2030	02/01/2031
36	**Iterate and improve design**	**03/01/2031**	**27/03/2036**
37	Improve and iterate design	03/01/2031	22/05/2031
38	Verify and validate modifications	23/05/2031	26/02/2032
39	Maintain vehicle	03/01/2031	02/11/2034
40	Monitor and adapt to market	03/01/2031	27/05/2032
41	Grow to other markets	28/05/2032	27/03/2036

Figure 2.2: Project Gantt chart of (post) DSE activities

3 Mission & Operations

The BonMobile is a vehicle being integrated into a relatively new market. Therefore it is critical to preliminary define the operations performed for the vehicle's mission and to define the required logistics and infrastructure. The global operations and logistics concept is shown in Figure 3.1.

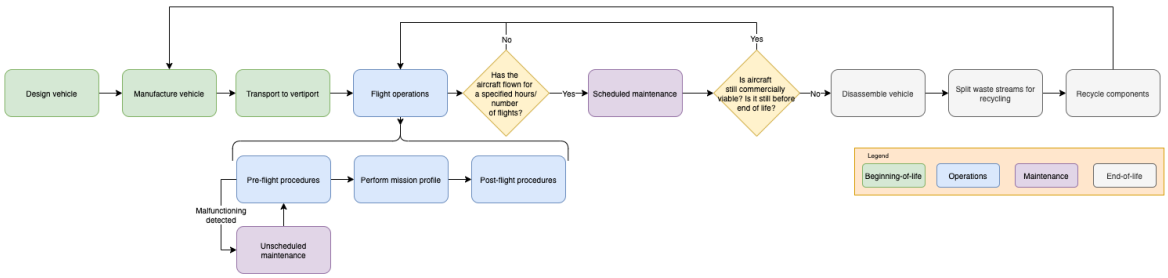

Figure 3.1: Operations and logistics concept

Figure 3.2 shows more details of the flight procedure. It highlights one important aspect: the interactions with the user. The middle block of perform mission profile will be worked out in section 3.1 and the middle block of post-flight procedures will be explained in section 3.2. Furthermore, section 3.3 will present a more detailed data and communications concept that will be adopted within the operations.

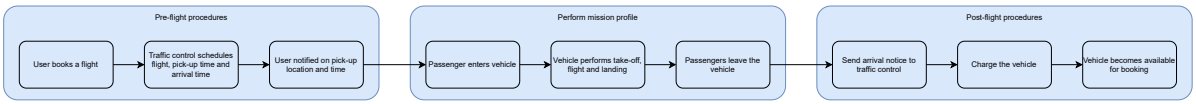

Figure 3.2: Details of the flight procedure

3.1. Mission Profile

The mission profile was designed in the Midterm Report [5] and this report presents an updated version. It is based on a study by NASA on UAM missions [6], EASA requirements [7] and the user requirements presented in section 2.1. The mission profile is presented in Figure 3.3. The time, altitude and distance of each segment is specified in Table 3.1. Note that segment 9-12 corresponds to a five kilometer reserve range for safety purposes.

It is aimed to have a nominal VTOL speed (segments 0,1; 6,7; 3,4; 9,10) of $3\,m/s$. A low vertical speed allows for significant decreases in required power, as will be touched upon in section 8.3. For the diagonal climb and descent a vertical velocity of $6\,m/s$ is assumed, again to significantly lower the power required, but also to limit the climb speed. This vertical velocity leads to a climb time of t_{climb} of $70\,s$ to get to a flight altitude of $450\,m$. Furthermore, a cruise speed of $27.8\,m/s$ turned out to be optimal for the BonMobile, again explained in section 8.3. This velocity leads to cruise time of t_{cruise} equal to $719\,s$ to cover a distance of $20\,km$.

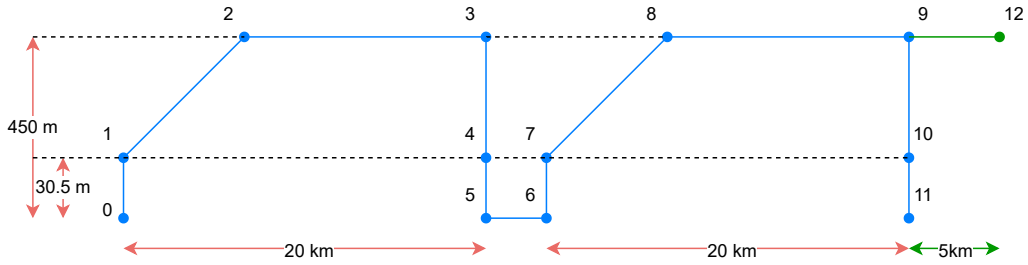

Figure 3.3: Mission Profile

Table 3.1: Mission profile

Segment	Procedure	Time [s]	Initial Altitude [m]	Final altitude [m]	Distance [km]
0,1 | 6,7	Vertical take-off + hover	60	0	30.5	0 | 20
1,2 | 7,8	Climb	70	30.5	450	-
2,3 | 8,9	Cruise	719	450	450	20 | 40
3,4 | 9,10	Descent	60	450	30.5	20 | 40
4,5 | 11,12	Hover + Landing	60	30.5	0	20 | 40
5,6	Prepare for take-off	600	0	0	20

3.2. Charging logistics

As explained in more detail in chapter 9, the battery charge time is $4h$. Having a single UAM with one battery will result in a linear charging cycle as can be seen in Figure 3.4a. The figure shows the state of the battery for five consecutive hours. In the first hour the battery is in use, in the second till fourth hour the battery is charging. At the fifth hour, the battery is ready for swapping. In order to make optimal use of the UAM, three batteries would be required. However, having two or more UAMs will allow for charging concepts as depicted by Figure 3.4b. This figure shows that for each hour (columns), there are five batteries in use. One is in the flying vehicle, a second one is ready for swapping and the other three are charging. This integrated charging system can be extended for more UAMs and flight hours. It can be seen that using more UAMs will result in a lower number of batteries used per vehicle, namely five batteries per two vehicles. This can be integrated at vertiports by for example having a charging station capable of charging four or five batteries at a time, and having two UAMs assigned to the charging station.

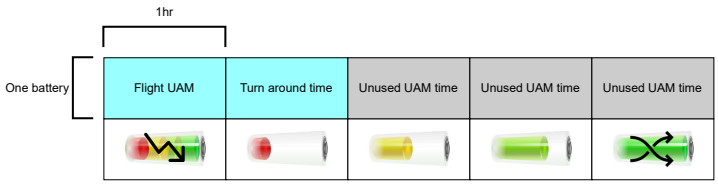

(a) Linear charging with a single UAM

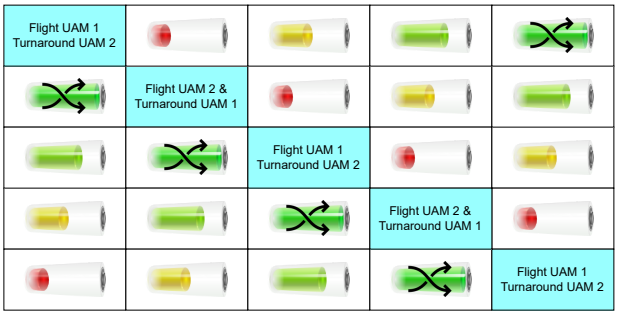

(b) Integrated charging with two UAMs

Figure 3.4: Battery charging concepts

The batteries are made from a set of battery arrays, forty in total. These weigh about 10.5 kg each. The batteries can be taken out, charged, and serviced separately. Multiple options can be explored to realise the swapping of the batteries. Either the batteries can be taken out one-by-one by a single person, but utilising small carts or rails can also be an option. These operations can be performed by a vertiport employee, who can also do the maintenance checks.

3.3. Data & Communications

Within the operations and logistics, frequent data links and communications are made. Figure 3.5 present these links for the current design stage. This is however a simplified representation, since some components have not been designed yet, such as the autonomous system and the control and stability of the vehicle.

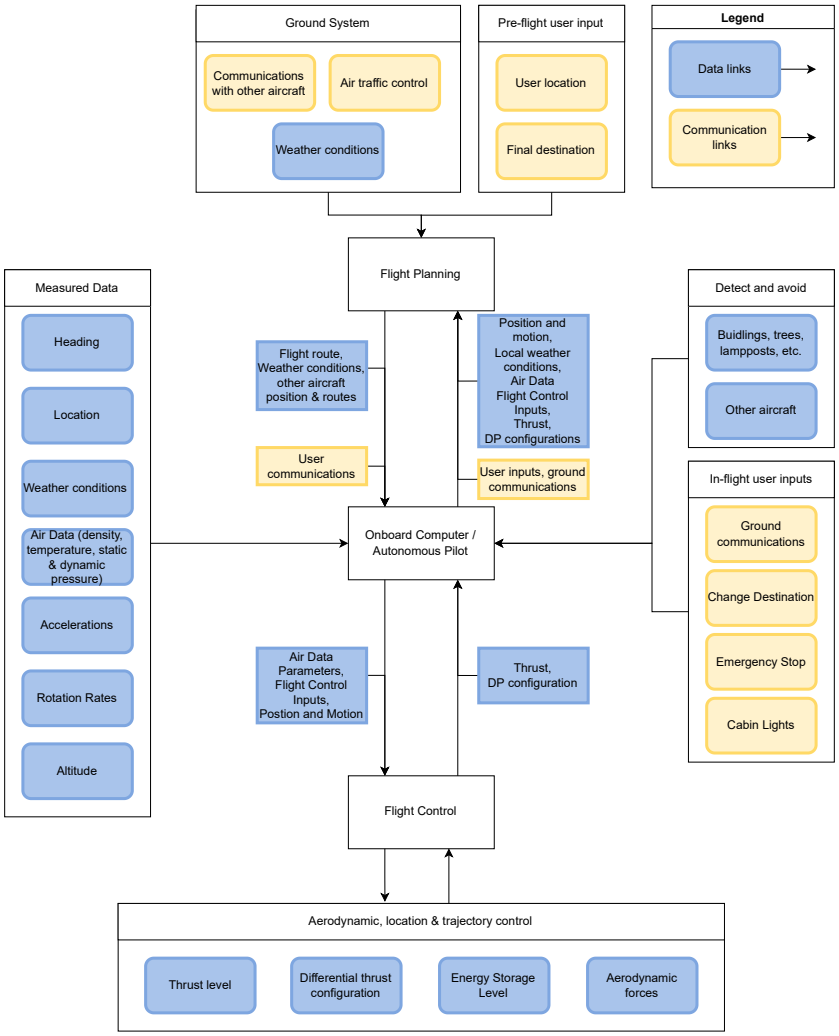

Figure 3.5: Communications and Data handling diagram

3.4. Functional Analysis

To conclude the mission and the operations of the vehicle, an extensive overview of all the functions that the vehicle needs to perform is given in form of a Functional Flow Diagram and a Functional Breakdown Structure. These diagrams are given in Figure 3.6 and Figure 3.7 respectively.

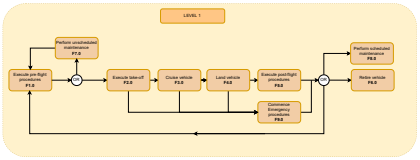

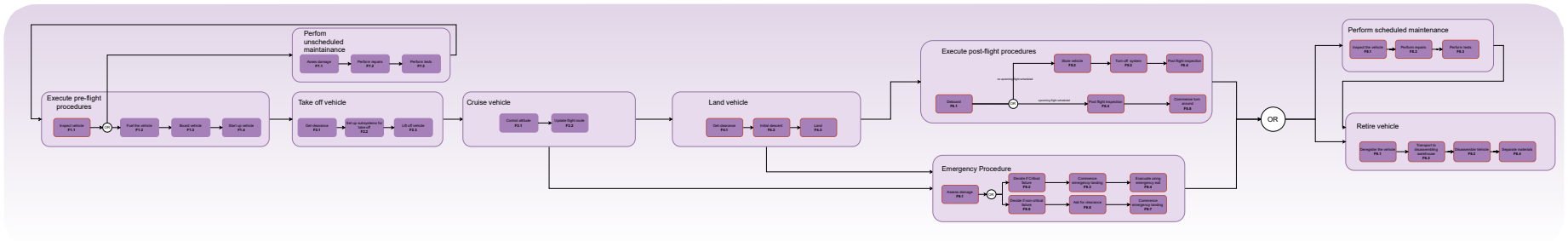

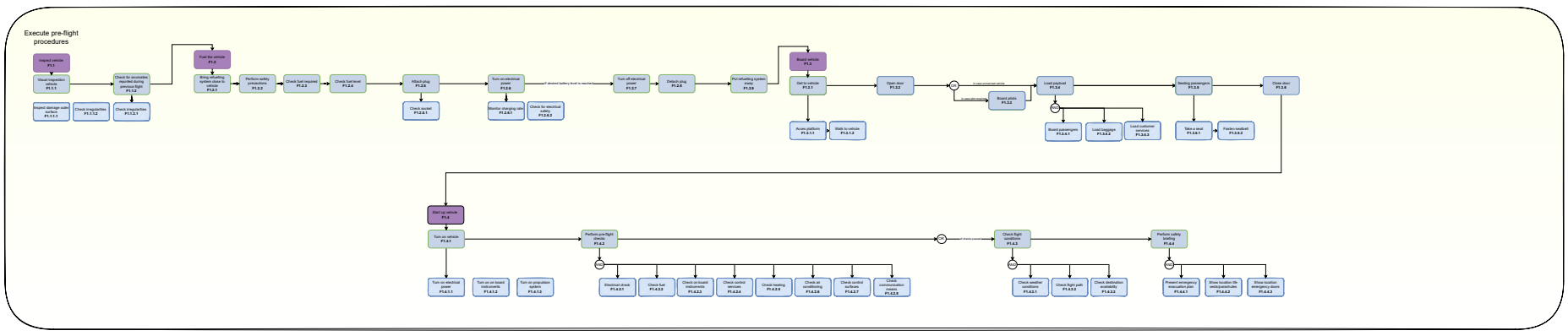

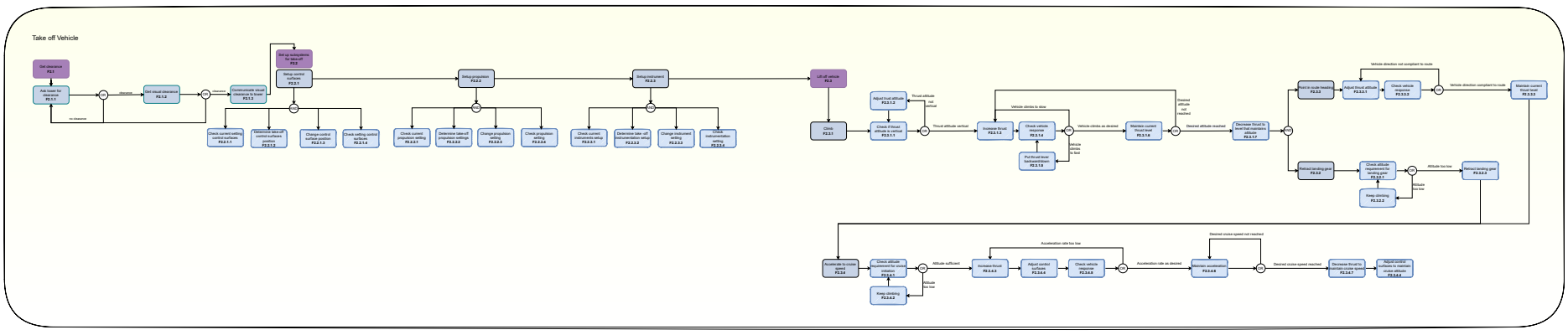

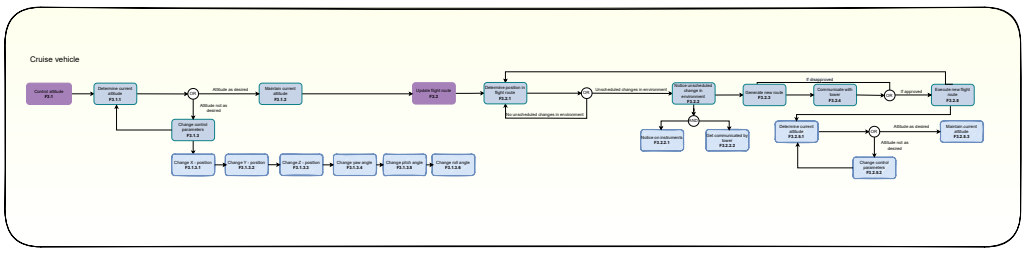

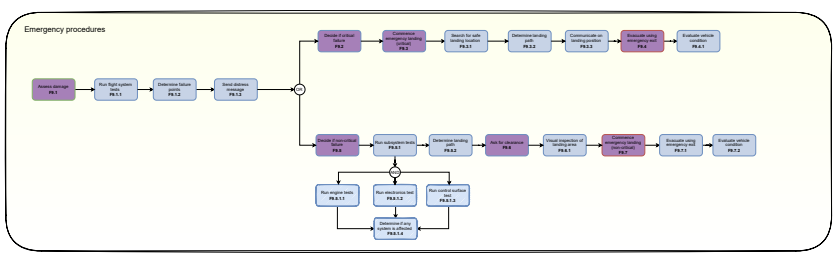

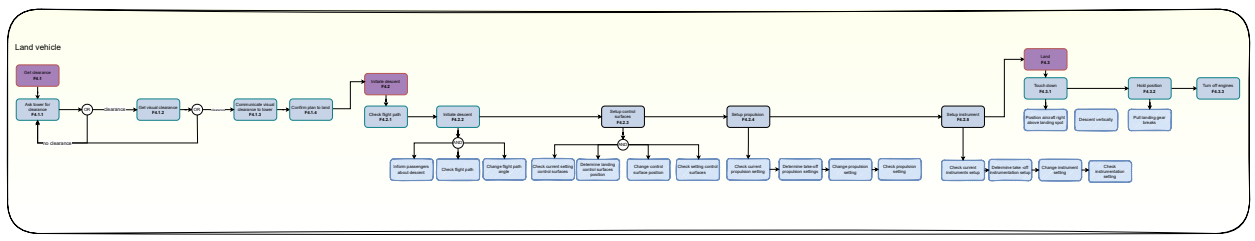

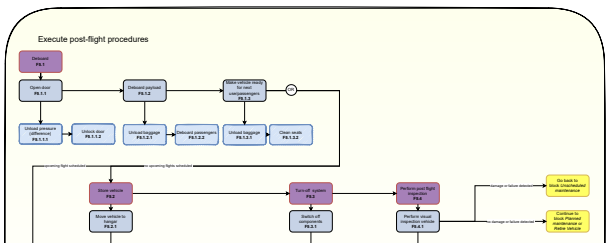

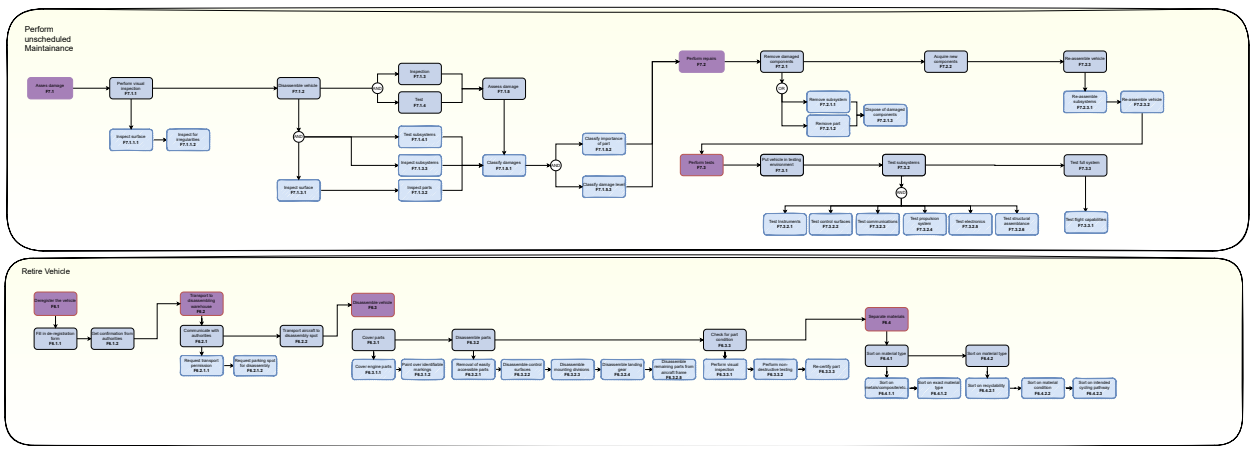

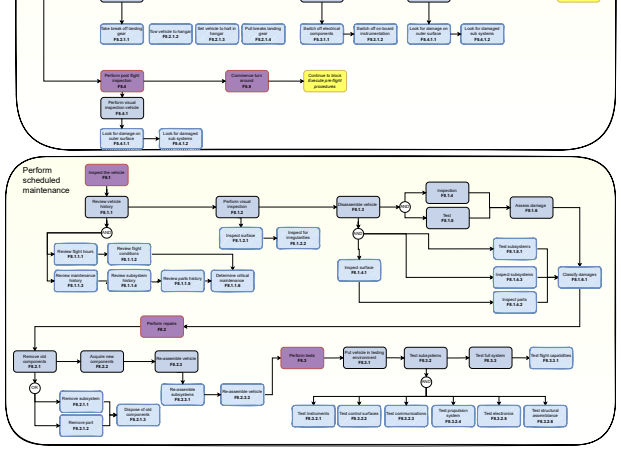

Figure 3.6: Functional Flow Diagram

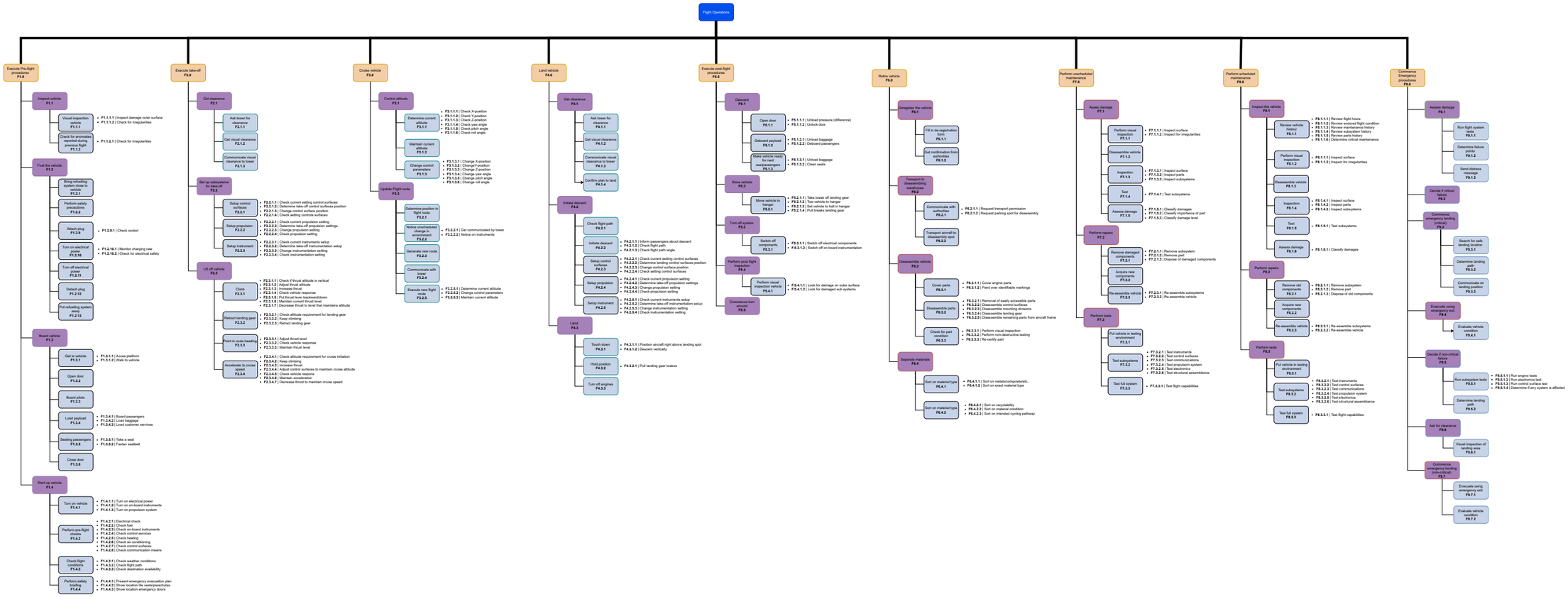

Figure 3.7: Functional Breakdown Structure

4 Market & Infrastructure

This chapter will provide a market analysis of the selected design for the Urban Air Mobility vehicle (UAM); a two-seater eVTOL vehicle made of 100% sustainable materials. In this chapter firstly an introduction and short stakeholder analysis will be performed in section 4.1. The following section 4.2 covers BonMobile's competition within the transport market and among other UAMs. Then the BonMobile's control system will be discussed in section 4.3. How the application of UAMs will be realised in practice is discussed in section 4.4. To finalise the market analysis, a case study is performed on the potential for an air-taxi UAM service in London in section 4.5.

4.1. Stakeholder Analysis

13% of the EU's total CO2 emissions came from cars in 2016 [1] and the need for emission reduction is becoming more pressing. Therefore a new concept for electrical air traffic starts to arise, to be an alternative for cars in the urban environment.

The only urban air transportation mode most people know nowadays is helicopters. Noise, cost, safety and regulations are however the main drivers for these vehicles to not yet have been implemented in urban areas. Enhanced technology, automation and noise reduction provide promise in the implementation of UAM infrastructure in the near future. It is expected that the cost for air taxis will become lower with enhanced automation and commercialisation [2].

The BonMobile will be designed for commercial transport, private use and the domain of entertainment. In order for the BonMobile to be successful in the commercial transport sector, the vehicle must perform better than the current transportation modes. For the BonMobile to compete with the taxi service, the air mobility sector should be more flexible, functional and socially and environmentally responsible.

4.2. Competition

With adequate air traffic management, urban air mobility can be the solution to traffic congestion, transportation problems and the annoyance of rushing cars through cities. Electric aerial vehicles can be the solution to the emerging problem of greenhouse gas emissions and smog in cities influencing the comfort of living. The concept of electric urban air mobility vehicles is on paper the optimal solution to all current problems. As the two problems have been described there are two competitors (upcoming) on the market also addressing and providing solutions to the same problem. Below the competition between UAMs and cars, and UAMs and helicopters are presented.

4.2.1. UAM vs. Cars

The first competitor for UAMs in the transportation market currently is cars. Cars are the most dominant mode of transport and on average in Europe transport less than 2 persons per car in 2021 [3], and they create more than 13% of Europe's CO2 emissions [4]. Since 2009 however, the infrastructure for charging electric cars has started to rise and electric cars became more and more popular. Furthermore electrical vehicles (EV) became more affordable for consumers since the cost of EV batteries halved

[1] From: https://www.europarl.europa.eu/news/en/headlines/society/20190313STO31218/co2-emissions-from-cars-facts-and-figures-infographics. Visited on 31-05-2022

[2] From: `https://www.morganstanley.com/ideas/autonomous-aircraft`. Visited on 01-06-2022

[3] From: `https://ec.europa.eu/eurostat/statistics-explained/index.php?title=Passenger_mobility_statistics`. Visited on 31-05-2022

[4] From: `https://www.europarl.europa.eu/news/en/headlines/society/20190313STO31218/co2-emissions-from-cars-facts-and-figures-infographics`. Visited on 31-05-2022

in 2013 [5]. CO2 emissions can be greatly reduced with this invention, leaving the traffic jams and transportation problems still to be solved. This is one of the reasons autonomous systems are in full development, advanced control systems that can drive themselves using in-vehicle technologies and sensors. (Partially) autonomous cars are already on the roads but challenges in the intelligent transportation field still are still to be tackled. An infrastructure with autonomous vehicles make driving in theory way more efficient and safe. Electric and/or autonomous cars are a disruptive technology in transportation, but they are not alone. The UAM industry can also be disruptive when integrated successfully. If UAMs can integrate in the existing infrastructure, if they are truly accepted by society and if they provide advantages compared to existing transport modes for a price they are willing to pay, this new market can take over the whole current mode of urban travel [8].

A whole new infrastructure must be added for implementation of UAMs, thus UAMs should have significant advantages compared to the existing car infrastructure. In order for the UAM market to win the competition from cars, this new technology should be faster, easier, cheaper and more economically friendly.

4.2.2. UAM vs. Helicopters

Next to cars, helicopters are also seen as competition. Mainly due to their similar characteristics for their VTOL abilities and size. Helicopters are used in and around the urban environment but is mainly limited for integration in commercial transport due to the high noise it produces, and the lack in safety and costs. eVTOLs are expected to perform better in all these three areas.

4.3. Control Level Vehicle

For UAM control three different levels of autonomy are considered; piloted, remotely piloted and fully autonomous. All three will be discussed in subsection 4.3.1 to 4.3.3

4.3.1. Piloted Control

A vehicle controlled by a pilot brings some advantages, the main one being experience. However, by adding a pilot to the vehicle the total weight increases significantly. The extra weight will not be counted as payload and thus the vehicle should provide much extra energy for the additional weight of the pilot. Furthermore will having a pilot increase the operational costs of the vehicle, as for each journey a pilot must be available. For large scale implementation, a research from N. Gunady et al. predicts there to be 50% more pilots necessary than the number of operating UAMs [9]. However, a piloted vehicle does save autopilot development and implementation costs.

4.3.2. Remote Control

Remotely piloted systems work like most drones currently do, where a person controls the vehicle from a distance through a communication link. The equipment will now be distributed between the remotely piloted vehicle, and the remote pilot station. This type of control saves weight and reduces the take-off weight of the vehicle. The pilot and thus operational costs decrease with 75% for remotely piloted control.[10]

4.3.3. Fully Autonomous Control

The last type of control is going fully autonomous. In this case an onboard computer will handle all (input) data and fully control the vehicle. Compared to the two previous control types, this one saves pilot costs during operation. The system development costs are however the highest of all control types. The autonomous system development costs are expected to be ten times higher than for piloted systems. The avionics costs are about two times higher. With the use of this control type the yearly utilisation is expected to double compared to piloted [10]. But, once an autonomous system is developed, it can be implemented into all operational vehicles, saving much operational costs over time compared to (remotely) piloted vehicles.

[5] From: `https://blog.evbox.com/electric-cars-history`. Visited on 31-05-2022

	I.Manual	II. Remotely piloted	III. Fully autonomous
Yearly utilization	900	1500	2000
Pilot cost [%]	100	25	0
Increase in autonomous system development cost [$]	+10M	+240M	+1100M
Avionics cost per aircraft [$]	19075	42775	45250

Figure 4.1: Level of autonomy [10]

4.3.4. Costs

In total costs going to the crew and avionics is 14-15% of the total operating costs per UAM [9], independent of the type of automation.

As mentioned before, a piloted system would require 50% extra pilots required than operating UAMs. The crew cost is estimated to be 110,000 dollars per pilot per year [9].

Artificial intelligence (AI) is currently used more and more in aviation. Overall these systems are able to make faster and more accurate decisions compared to humans, resulting in improved safety. However, there are two challenges still for autonomous operations; certifications and air traffic management. But as aviation regulations advance and the technology around sensors and processors improve, the actual implementation of autonomous control becomes very real in the near future.

Next to improved safety, a fully autonomous system is lighter and has lower operational costs compared to (remotely) pilot systems. The main disadvantage is the high development cost, estimated to go over 1100M dollars, see Figure 4.1 [10]. However, there are several companies working on autonomous systems. For example, Honeywell Aerospace has developed a fly-by-wire flight control system especially developed for eVTOL and UAM platforms. Using existing systems like this reduces costs relative to developmening the system from scratch.

4.3.5. Time frame

Avionic instrumentation costs with processors being the most significant contributors have decreased the past two decades. Since then there has been a significant growth in research for autonomous systems, represented in Figure 4.2 [11]. It follows from the figure that there is high potential in the near future for automation.

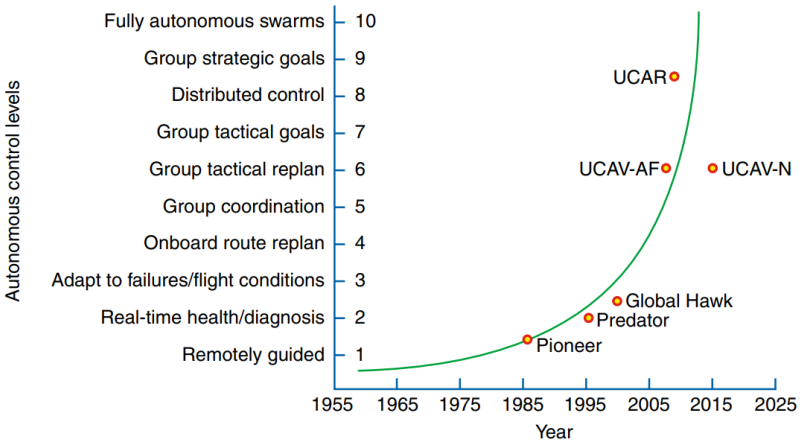

Figure 4.2: Level of autonomy of UAVs [10]

Therefore it is concluded that the BonMobile will be operated autonomously. There is great potential for autonomy in the near future. Such a control system furthermore has the great advantage of weight savings compared to piloted control. Weight minimisation is preferred for costs, but also for energy and materials used. It is therefore critical for sustainability.

4.4. Integration and Infrastructure

Helicopters have been used for UAM purposes in the past. In the 1950's helicopters were used as airway shuttles with prices in the range of 47$ to 86$ (in 2019 dollars). For more than twenty years this service operated successfully until safety concerns rose due to two accidents caused by mechanical failure. This piece of history shows two things, one being that people did use the aerial vehicles to get from A to B, and the other being that in order for it to work again, the product should provide a safer service. The concept for airway shuttles ceased but nowadays on-demand helicopter air traffic is still available, starting at costs from $195 bookable until 30 minutes in advance. Services like this give information on customer preferences around urban air mobility and show the arising challenges for the upcoming eVTOL UAM market. It shows the presence of the demand for these kinds of services.

This section will first discuss the acceptation of new technologies regarding UAM aspects in subsection 4.4.1. Then subsection 4.4.2 will discuss the integration and infrastructure for UAMs and introduce the concept of vertiports. The section concludes with a time estimation of launch of the BonMobile.

4.4.1. Acceptation

In 2018 a case study was performed for which 248 respondents from Munich filled out a survey to explore transportation preferences in urban air mobility environments [12]. The results are given in Figure 4.3 with the resulting numbers going from 1 (strongly disagree) to 5 (strongly agree).

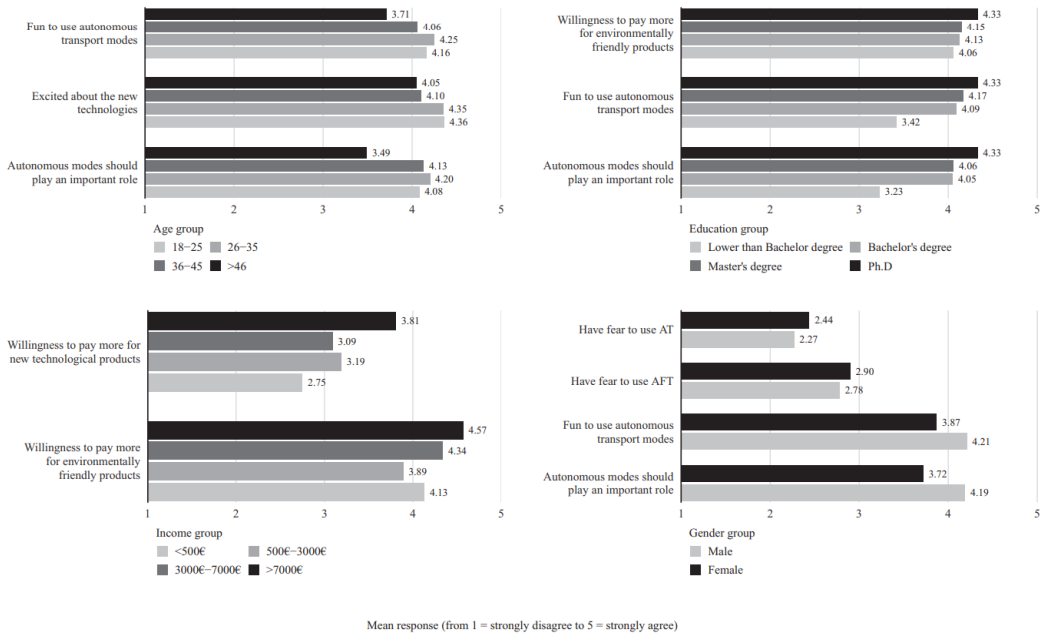

Figure 4.3: Results on attitude studies associated with different groups [12] (AT = autonomous taxi, AFT = autonomous flying taxi)

All topics for the four graphs are ordered on different groups associated with age, education, income and gender. For this paper however, the focus is more on the topics all graphs discuss than what the differences in groups are within the respondents. Still the figure is useful for this research on integration and acceptance of UAMs.
The top left graph in Figure 4.3 discusses the importance of autonomy in transport modes and excitement about new technologies. From the survey follows that all age groups agree on being excited about new technologies, and would thus be open for new initiatives like UAM services. The graphs also show that despite the excitement about new technologies, they are not especially willing to pay more for them. But, if it comes to environmentally friendly products, that willingness to pay more increases significantly. This increment is what BonMobile is; completely sustainable and thus environmentally friendly.

4.4.2. Infrastructure

For successful implementation of UAMs in existing infrastructure certain special facilities are required. Just like cars need a parking spot and space for loading and unloading and to charge, UAMs need just the exact kinds of spaces.

For optimum usage and customer satisfaction and optimal efficiency, preboarding activities (waiting time, security) times should be minimal. If quick services are offered and flight performance is optimised, losing time on (unnecessary) preboarding procedures is a waste. Competition to ground vehicles is lost if UAM is not easily accessible.

Vertiports The BonMobile is able to take-off and land vertically, meaning that the vehicle needs a platform to land on. This can be either on existing helicopter platforms upgraded with charging abilities, locations where there is enough space to land and it is safe, and on vertiports. A vertiport is meant to be a multi-purpose platform. It will be a base hub for the vehicle, the vehicle can take-off and touchdown at this platform. Furthermore the vertiport will provide parking, load and storage facilities, be a waiting terminal for the passengers, and contain other support infrastructure. One may describe it as a small-scale, compact airport in the middle of a city.

UAMs can fly from vertiport to vertiport throughout and between cities and provide all facilities for upcoming flights. Vertiports can contain one or multiple landing platforms, depending on the space available in the city and popularity of the destination. Government guidelines on licensing carriers and maintenance contracts would have to be issued for constructing these new platforms. As a start existing bus terminals could be used for example, already having the space for the vehicles and having waiting terminals and often a small food kiosk facility. Take-off and landing are the actions performed at lowest altitude being closest to inhabitant area so vertiport design should ideally account for noise reduction and safety risk mitigations. The Figure 4.4 shows what vertiports could look like. The network requires long term city planning and certain certifications dependent on both national and international regulations. The stations should furthermore also be connected to the electricity grid with rapid charging abilities for the battery of the UAMs.

Figure 4.4: Vertiplaces [6]

Research has been performed on different designs configurations for vertiports, with platforms with one to multiple landing pads. To give an example, Figure 4.5 shows a vertiport having one landing platform with two staging areas, with 13 estimated arrivals and departures per hour. Such a vertiport is estimated to cost $750,000 and has a surface area of 72 by 99 meters. This is a rough estimation for a vehicle with 15 meter diameter. With use of vertiport design tools (VDT) configurations for specific sizes UAMs and number of landing and staging areas can be designed. A business case was set up by the Center for Air Transportation Systems and Research at George Mason University that takes the costs for vertiport design development, production and maintenance of VDT [13]. According to their model, when selling an expected 21 vertiports within five years, the return of investment for VDT would be

[6] From: `https://medium.com/predict/vertiports-are-the-new-bus-stops-of-the-sky-17bc32c5df80`. Visited on 01-06-2022

more than 400% in five years after installation. Costs for vertiports are not included for BonMobile's production cost estimation, since the infrastructure is not part of the design scope.

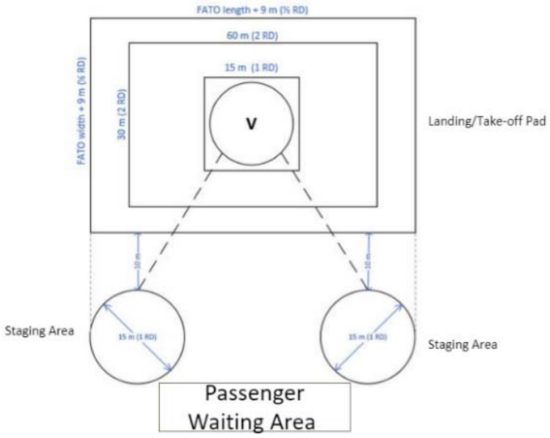

Figure 4.5: Design configuration landing pad with two staging areas [13]

Due to local regulations and space constraints, BonMobile is unlikely to deliver a door-to-door service, but instead from vertiports to vertistops. The platforms have to be registered and must have an approved approach and departure routes. Infrastructure will have to be added to the city for creating available landing spots as there in (crowded) cities, there is a lack of sufficient suitable locations.

4.4.3. Launch term

A market study has been performed by NASA where a regulatory timeline has been set up for air metros and air taxis, see Figure 4.6 [14]. The light blue region represents the likely time frame for such operations. This means that in 5 to 10 years time, the different areas (in dark blue) will most probably be feasible. For now a fully safe and working autonomous control system is not on the market yet and certain certifications for eVTOL have not been completed. The sustainable creation and recycling method for lithium-sulfur batteries (section 9.2) is currently not in place yet, but as it is in full development it is expected to implement these batteries around 2025. This gives autonomous technology, certification and sustainable design eight more years to enhance and refine. This project is planned for the near-future. Therefore, section 2.2 assumes **the year 2030** for integration, realisation and launch of the BonMobile.

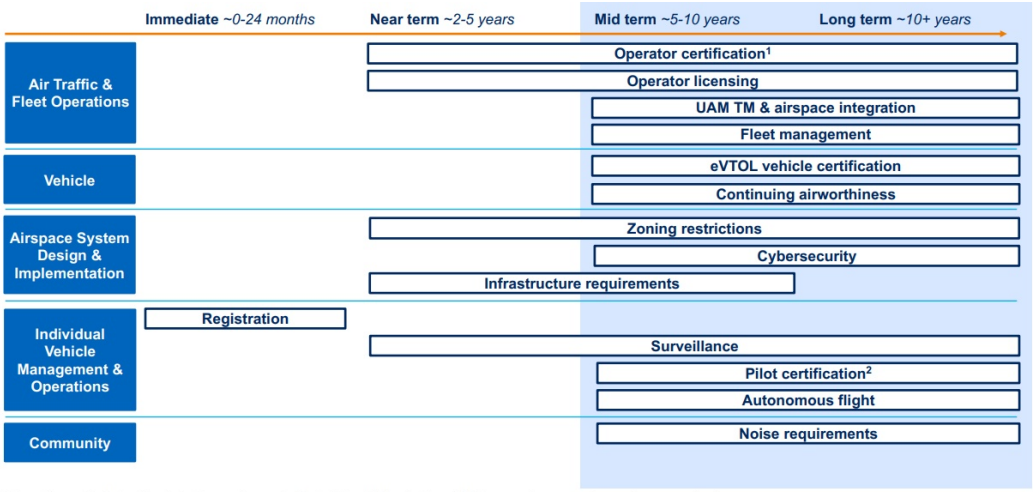

Figure 4.6: Timeline air taxi [14]

4.5. Case Study London

To explore the demand for the BonMobile as an air-taxi service, a case study is performed. For this study London's ground taxi service is observed to investigate the demand and possibilities for partial replacement for ground taxis by UAMs. Three big airports are located just around London's city centre that are all within BonMobile's flying range. Data is available through the UK government data base [15] and an investigation by Greater London Authority [16] on transportation modes of travelers to the airports, making the situation perfect to explore for the integration of BonMobile.

Greater London is the ceremonial county of London, covering the city and the large suburbs of London. The 1,569 square kilometers area (2022) has a population of 9.54 million [7]. London is ranked 55 on the world rank for congestion levels in 2021 with a congestion level of 33%[8]. This means that on average travel time takes 33% longer due to traffic than in free-flow conditions. 14.80 CO2 megatonnes/year were emitted in London in 2021 from which almost 15% was due to increased congestions. The emissions from traffic in London cover 4.49% of the total emissions UK emitted in 2021 [9],[10].

One note to make on this case study: the BonMobile is expected to launch for public in 2030, following from the market analysis in section 4.4. In this study numbers are used from data available from the past few years, bringing an uncertainty in the preciseness of the study. However, realistic estimates will be made to predict the future situation as best as possible.

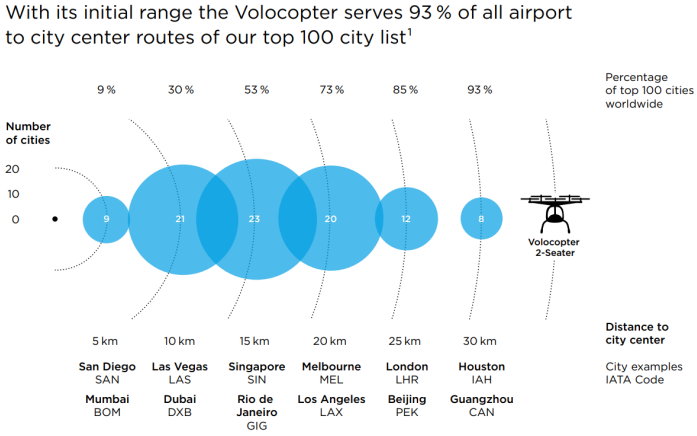

Figure 4.7: Range of 30km is sufficient to serve 93% of all connections between city centre and airports [17]

4.5.1. Range

In this case study the implementation and integration of UAMs in London are investigated. London is a suitable city for this case study with a population of nearly 10 million living in an area with a radius of 30 km, making the city perfect for the BonMobile, having a range of at least 40 km. The case study focuses specifically on the taxi services between the three big airports in London and the city centre. The ground taxi services have been investigated to explore replacing ground travel to airports by UAMs. London is only one out of multiple cities where this air-taxi airport connection by the new UAM technology is possible, see Figure 4.7. The three airports considered are London Heathrow, Gatwick and London City Airport (LCY), all within a $40km$ range around the central of London.

The range for the BonMobile on one battery without charging is two times a distance of 20 km. In one trip 40 km can at least be covered what in London means that all three airports in the city can easily be reached from central London and most places from Greater London. Figure 4.8 presents the map of London with the fastest routes for ground vehicles from the central London to Gatwick Airport, London Heathrow and London City Airport.

[7]From: `https://worldpopulationreview.com/world-cities/london-population`. Visited on 02-06-2022
[8]From: `https://www.tomtom.com/en_gb/traffic-index/london-traffic/`. Visited on 02-06-2022
[9]From: `https://www.tomtom.com/en_gb/traffic-index/london-traffic/`. Visited on 02-06-2022
[10]From: `https://ourworldindata.org/co2/country/united-kingdom`. Visited on 02-06-2022

Figure 4.8: Radius range UAM vs itinerary ground travel

The travel distance from central London to the airports can directly be taken from Figure 4.8. The routes are planned, and the travel times are estimated by Google Maps. Table 4.1 shows the travel details from central London (Waterloo Station) to the three airports. The UAM flight path can theoretically fly in a straight line. Due to other air traffic, unexpected obstacles or vertiports/vertistops not located exactly on the straight flight path however, the UAM might deviate slightly from this straight line.

4.5.2. Estimated Travel Details

The estimated travel costs for Table 4.1 are approximated by a website using a fixed price per kilometer for taxis in UK, including a base fee for each journey [11]. The travel time is also found using the before mentioned resource, and an additional 33% travel time is added to cover the average additional time per trip in central London due to congestions [12].

Table 4.1: Travel details taxis vs UAMs

		Heathrow	**Gatwick**	**London City**
Distance [km]	Taxi	29.6	44	13.9
	UAM	23.6	38.4	11.8
Estimated time [min]	Taxi	57	89	40
	UAM	18	31	11
Approximate costs [Euros [13]]	Taxi	€ 85	€ 124	€ 39
	UAM	-	-	-

The estimated travel time for UAMs for Table 4.1 is calculated based on the flight path distance. For vertical take-off and climb an average time of 2 minutes is taken. When cruise altitude is reached the vehicle accelerates to a velocity of 100 km/h, and decreases again when approaching its destination. For decelerating and landing a time of 2 minutes is taken again. The journey to Heathrow is done in one go while for the journey to Gatwick Airport a stopover is made halfway. The stopover time is

[11] From: `https://www.taxi-calculator.com/taxi-fare-estimation`. Visited on 02-06-2022
[12] From: `https://www.tomtom.com/en_gb/traffic-index/london-traffic/`. Visited on 02-06-2022

included in the total travel time. The approximate costs for ground taxi service are around €2.86 per kilometer. Kilometer cost for air taxi service will be determined later in this case study.

4.5.3. Demand

In 2006 the Greater London Authority has performed a research on the number of passengers flying from airports around London and the modes of transport used to get there [16]. Data from this paper have been used for this case study, this is the most recent research on this specific topic. Still the outcome can be used in this case study. The UK government posted a data sheet on Air traffic at Airports on the modes of transport to the airports with data up to 2019 [15]. A positive trend is seen in the use of taxis to airports over time, and following the same trend the percentages in 2030 of passengers arriving to Heathrow, Gatwick and LCY by taxi will be 40, 19, and 55% respectively (relative to 28, 14 and 40% in 2006).

Table 4.2: Estimation number of UAMs required

	Heathrow	**Gatwick**	**London City**
Terminating passengers per year	44,230,764	29,567,271	2,316,110
Percentage passengers coming from Greater London	51%	39%	78%
Percentage passengers arriving by taxi	28%	14%	40%
Estimated flight duration (incl. clearance time)	21	36	13
Number of flights required per day	125	55	9

A few assumptions are made for the findings in: Two times 2 minutes are added to the total flight time for take-off and landing. A factor of 1.15 is added to the estimated routing distance of the UAM [18], to take avoidance for unexpected obstacles and deviations from initial flight path into account. Flight time is further computed using a cruise speed of 100 km/h. Loading and unloading is expected to take 5 minutes in total for each flight. For a ground taxi trip, 2 minutes are added to each journey, for entering, packing and leaving the vehicle.

In theory, when all passengers from Greater London travelling from central London to the airports, a total of 197 full-time operating UAMs are required. However, this accounts only for the replacement of all ground taxis by UAMs.

Business travellers have an obvious preference to fly from airports quickest reachable, even more than for normal passengers. They prefer to lose as little time for traveling as possible, and unexpected congestions or delays are rather avoided. Therefore this sector would have high demand for a service like BonMobile, and be a suitable target group. The percentage of business travellers traveling from Heathrow, Gatwick and LCY are 40, 16, 64% respectively. Assuming now that only all business travelers will make use of the BonMobile, the same calculations can be performed, giving a more realistic view on the number of travelers truly using UAMs. 65 full-time operating UAMs are now required, see Table 4.3.

Table 4.3: Number of BonMobiles required for business travellers

	Heathrow	**Gatwick**	**London City**
Percentage business travellers	40%	16%	64%
Number of BonMobile flights required per day	50	9	6

4.5.4. Integration

Implementation of vertiports at airports can be rather easy. Existing car parks can easily be transformed to landing platforms. Especially raised parking structures are advantageous, ensuring unobstructed glide path angles to the platform. Moreover raised platforms also provide larger height clearance above road traffic also to minimise distraction to the ground traffic. The area underneath the platform can then also be used for vertiport functionalities like waiting or passenger pickup area. Using existing infrastructure reduces costs.

New challenges will arise for air traffic management around airports with the rise of UAMs. Integration with air traffic control can only succeed with structured route planning and communication with airport and authorities.

Uber Elevate has simulated an infrastructure for potential vertiport locations in London. They set up a model to find a subset of vertiports and vertistops to maximise the total trip coverage. A large-scale integer program is used. 35% of all long-distance trips in London can be covered with the 25 firstly chosen vertiports [18]. There is a high density of journeys between the central business areas and the three considered airports in London. Uber Elevate has put the number of vertiports throughout the city against the trip coverage, see Figure 4.9. The simulation demonstrates the prominent demand for connections between central business districts and the large airports in London.

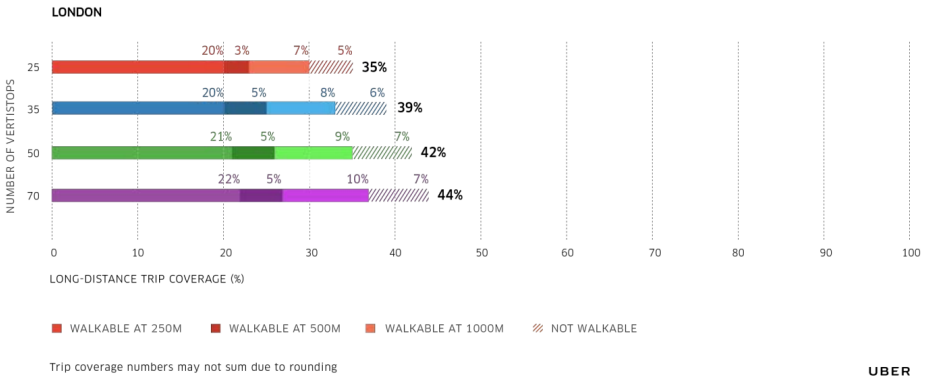

Figure 4.9: Walking distances to destinations per number of vertiports London

From Figure 4.9 follows that the placement of more vertiports in the city increases coverage. For this case study specifically however, placement of 25 vertiports will suffice, covering already great parts of central London to the airports. Construction costs for vertiports are not considered in this study.

4.5.5. Costs

Now that the demand is shown and the target group and placement of vertiports are determined, for the BonMobile to be competitive in the market, the price for the service is essential. From chapter 5 follows that one BonMobile has 1.371 million euro manufacturing costs. 65 full-time operating vehicles are required to transport all business travelers to one of the three airports. Where ground taxi drivers cannot make full days driving, a UAM does not have a pilot on board making the vehicle theoretically able to operate 24/7. However, half times more vehicles are taken for the number of operating BonMobiles required, taking both scheduled and unscheduled maintenance, check-up time and unexpected factors into account. 100 vehicles will thus be necessary for passenger transport in this case study.

The following assumptions are made for the payback period and cost estimations per kilometer for BonMobile.

- 65 full-time operating BonMobiles are required for business travelers transport from central London to the three airports
- All 65 BonMobiles are expected to be used from the day of launch
- Extra vehicles are required to account for (un)scheduled maintenance
- All 100 BonMobiles are expected to be manufactured before launch
- Vertiports are assumed to exist and work fully by the day of launch
- BonMobile operates throughout the whole year
- Starting fee for a BonMobile trip is €2.00

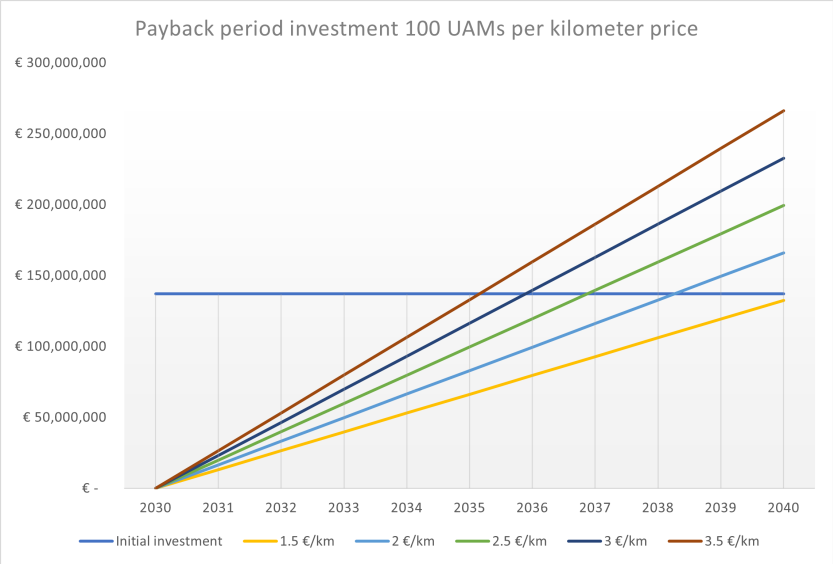

Figure 4.10: Payback period BonMobile in service

Figure 4.10 shows the payback rate and time for BonMobile after investment of 100 vehicles. The higher the kilometer price, the faster the payback time. However, to compete with ground taxis, the kilometer price should not exceed €2.86. For a kilometer price of €2.00, the total payback period is 9 years. When raising the kilometer price with 50 cents, payback period is only 7 years.

4.5.6. Conclusion

To conclude an overview of the advantages in terms of distance, time and cost for BonMobile over ground taxi services are given in Figure 4.11. 15% error bars are taken for the graph as the distances, flight time and costs might all change slightly depending on the available itineraries and air traffic. On average BonMobile saves 16%, 65% and 38% on distance route, total travel time and costs respectively. With a starting fee of €2.00 and kilometer price of €2.00, traveling in a private vehicle from the city centre to one of the three main airports has never been cheaper. And all that for using a 100% sustainable vehicle leaving not any kind of footprint behind.

Furthermore, not only for London would integration of BonMobile be a suitable solution. At least for the 10 biggest cities in Europe, big airports are reachable within a 40 km range, making the service very promising in the near future throughout the whole continent.

As a final remark a discussion point must be addressed, also being a recommendation for further studies. The payback period has for now only been based on the initial investment costs. For a more accurate kilometer price estimation, costs for e.g. operation, maintenance and storage should also be included.

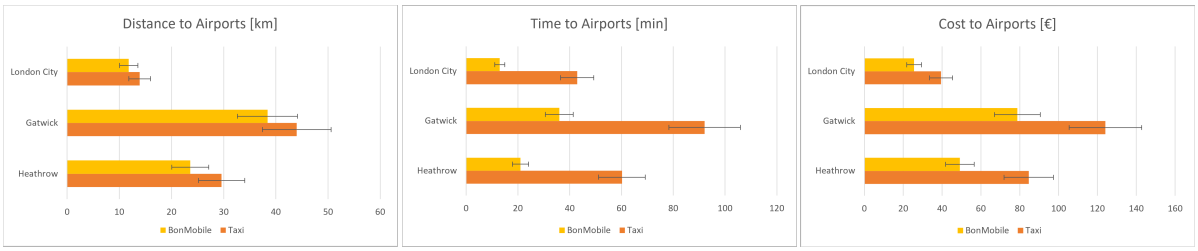

Figure 4.11: BonMobile vs ground taxis

5 Budget Allocation

Important for the market position of the vehicle is to have an understanding of the cost breakdown of the vehicle. In this chapter, the Research & Development cost will be discussed in section 5.1. Furthermore, the manufacturing cost of the vehicle will be computed in section 5.2. The resulting costs will be converted to euros as of June 2022 with an exchange rate of 1.07.

5.1. Research & Development cost

The research and development costs are all activities associated with putting a UAM on the market. It is expected that the cost for doing so is 2.14 billion euros [1]. In this section factors influencing the R& D cost will be discussed.

As seen in the Market Analysis in Chapter 4 the development cost of an autonomous system for the vehicle is estimated to be 1.177 billion euros. Hence, this system alone will take up a significant amount of the total research & development cost. Important to notice for this factor is that it is expected that only for the development of the first vehicle the cost will be this high. In later designs, the same system can be used after making only minor changes to it. Thus, lowering the cost of this system significantly. Furthermore, in the future, if available, this system could be purchased from vendors on the market. As a result, lowering the development cost of the vehicle if the system purchase cost would be lower than 1.177 billion euros.

This same philosophy applies also to other components of the vehicle. Currently, the development of these systems will take a lot of resources because a lot of new technologies are used. As a result, the research to explore how these technologies can be fitted into the design will be extensive. It is expected that if the UAM market is well established, the research needed will decrease. Hence, lowering the research and development cost of the vehicle.

Another important factor influencing the R & D cost of the vehicle is the certification of the vehicle. To bring a UAM on the market the vehicle first has to be certified by authorities. For experimenting with the vehicle, the vehicle can be certified using an experimental certification [2] However, to bring the vehicle on the market, the vehicle shall be type certified. This process is more extensive and therefore will also ask for more resources.

5.2. Manufacturing Cost

The total costs for manufacturing will largely determine the market price of the vehicles. Therefore a manufacturing cost breakdown is performed, a useful tool to make choices for the resources allocated to engineering departments. To understand the market position of the vehicle an estimation of the manufacturing cost is critical. The chapter will start with an explanation of a method for total cost estimation in subsection 5.2.1. subsection 5.2.2 then provides the results of this estimation. The method uses imperial units and US dollars. The results of the final calculation will be converted to euros as of June 2022 with an exchange rate of 1.07.

5.2.1. Manufacturing Cost Method

To determine the manufacturing cost of the vehicle, a method explained by Roskam is used [3]. This method is used to break down the manufacturing cost but is not used in solitude. The method is combined with other cost estimations sources when appropriate.

[1] Retrieved from `https://www.rolandberger.com/en/Insights/Publications/Urban-Air-Mobility-Targeting-autonomous-flight-opera` `html`. Visited on 16/06/2022.

[2] Retrieved from `https://www.faa.gov/aircraft/air_cert/airworthiness_certification/sp_awcert/experiment/`. Visited on: 16/06/2022.

Total manufacturing costs are estimated by Equation 5.1 where the capital C describes the costs, and the subscript the type of costs.

$$C_{MAN} = C_{aed_m} + C_{apc_m} + C_{fto_m} \tag{5.1}$$

C_{aed_m} are all related to airframe engineering and design costs and estimated by Equation 5.2. The costs are related to all engineering activities needed during the manufacturing phase. For example, engineering tasks related to sustaining errors made in manufacturing.

$$C_{aedm} = MHR_{aed} R_{e_m} \tag{5.2}$$

MHR_{aed} is the total number of engineering hours required per vehicle for production. R_{e_m} is the average wage for engineers per hour in the US [3].

C_{apc_m} is the production cost of the vehicle and is determined by Equation 5.3.

$$C_{apc_m} = C_{bat_m} + C_{(e)_m} + C_{(a)_m} + C_{int_m} + C_{man_m} + C_{mat_m} + C_{tool_m} + C_{qc_m} + C_{blade} \tag{5.3}$$

$C_{(e)_m}$ is the cost of the engines is the cost of the engines used for the vehicle. . $C_{(a)_m}$ is the cost for the avionics installed in the vehicle. The interior cost is given by C_{int_m}. C_{blade} is the cost of the blades. The cost of the batteries is computed using Equation 5.4:

$$C_{bat_m} = c_{bat} \cdot E_{used}\,, \tag{5.4}$$

where c_{bat} is the price of the batteries per kWh. It equals $150\,USD\,/kWh$ for the battery package used for the BonMobileEquation 5.4. E_{used} is the total amount of energy stored in the battery in kWh.

The costs for the engines, avionics and interior are obtained from vendors.

The total labour cost for manufacturing C_{man_m} is computed using Equation 5.5:

$$C_{man_m} = 28.984 \cdot W_{ampr}^{0.740} \cdot V_{max}^{0.543} \cdot N_{pro}^{-0.476} \cdot F_{diff} \cdot R_{man_m}\,, \tag{5.5}$$

where W_{ampr} is the empty weight of the vehicle in lbs and V_{max} represents the maximum design speed of the vehicle in m/s. N_{pro} is the total number of vehicles produced, which from the market analysis followed to be 100. F_{diff} is the complexity factor of the vehicle and must be a value between 1 and 2. The closer the number to 2, the higher the complexity. For this design, a value of 1.7 is chosen as BonMobile with respect to conventional aircraft designs, which uses significantly more new techniques. This can be seen in the rather complex and new structure design of the vehicle, also accommodated by the battery pack and the electric engines. At last R_{man_m} describes the man-hour manufacturing wage.

For the material cost of the vehicle Equation 5.6 is used:

$$C_{mat_m} = 0.6 \cdot W_{str} c_{vit+carbon} + 0.4 \cdot W_{str} c_{flax+epoxy}\,. \tag{5.6}$$

W_{str} is the structural mass of the vehicle in pounds, and $c_{vit+carbon}$ is the specific cost for the carbon fibres with the vitrimer resin material per weight and equals $16\,USD/lb$. The specific cost for the material for the secondary structure is given by $c_{flax+epoxy}$ and equals $22.7\,USD/lb$ [3],[4] [19]. Notice that 75% of the structure mass is the load-carrying structure of the vehicle. The interior structure carries the other 25% of the total mass. As found in section 11.6.

The quality control cost of the planes is computed by Equation 5.7:

$$C_{qc_m} = 0.13 \cdot C_{man_m}\,. \tag{5.7}$$

Tooling costs for manufacturing are covered by

$$C_{tool_m} = 4.0127 \cdot W_{ampr}^{0.764} \cdot V_{max}^{0.899} \cdot N_{pro}^{-0.822} \cdot N_{r_m}^{0.066} \cdot F_{diff} \cdot R_{t_m}\,, \tag{5.8}$$

where N_{r_m} describes the number of vehicles produced per month which for now is assumed to be 3. R_{t_m} is the tooling labor rate per hour of work. The other parameters have already been covered before.

Finally, the costs for the propellers are computed byEquation 5.9.

[3]From: `https://www.junksupply.com/product/bcomp-flax-45-biax-300gms/`. Visited on 09-06-2022

[4]From: `https://www.chemanalyst.com/Pricing-data/epoxy-resin-79`. Visited on 09-06-2022

$$C_{CS_{Prop}} = 210 \sum_{i=1}^{N_{Prop}} \cdot D_{P_f}^2 \cdot (\frac{P_{hp}\eta_{prop}}{D_{P_f}})^{0.12} \cdot CPI \tag{5.9}$$

The individual cost of a propeller is first computed and then added to the total cost of the blades. D_{P_f} is the diameter of the propellers in meters. CPI is the inflation index since 2012 which equals 1.252 for the year 2022. P_{hp} is the power that should be produced by a single-engine in hp and η_{prop} describes the propeller efficiency [5].

C_{fto_m} is the cost associated with the required test flight hours before de to the customer:

$$C_{fto_m} = C_{ops/hr} t_{pft} F_{ftoh} \tag{5.10}$$

By doing so the vehicles are checked on the functionality of their systems. $C_{ops/hr}$ is the vehicle operating cost per hour. t_{pft} is the number of hours flown before delivery of the vehicle, for now, assumed to be 2 hours. F_{ftoh} is a factor accounting for the overhead costs for the flight before delivery, which equals 4 [3].

5.2.2. Manufacturing Cost Results

In this section, the results of the cost estimation are presented. The exact costs of all the subsystems and/or tasks given earlier are shown in Table 5.1. To visualise the differences between these numbers Figure 5.1 is provided.

Table 5.1: Cost breakdown table of BonMobile with used sources

Cost	**Subcost**	**Value [K€]**	**Source**
C_{aedm}	-	0.822	[3] Zippia [5]
C_{apc_m}	C_{bat_m}	23.5	[3]
	$C_{(e)_m}$	36.7	EMRAX [6]
	$C_{(a)_m}$	42.3	[10]
	C_{int_m}	74.8	ThePoints [7]
	C_{man_m}	800	[3] [4]
	C_{mat_m}	21.8	BComp [8] Chemanalyst [9] [19]
	C_{tool_m}	131	[3] [4]
	C_{qc_m}	104	[3]
	C_{blade}	126	[20]
C_{fto_m}	-	0.102	[3]
Total cost		**± € 1,369**	

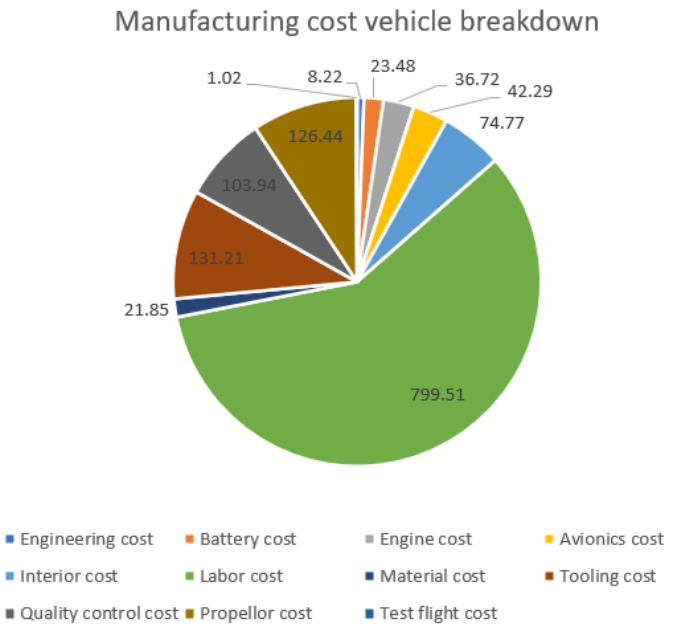

Figure 5.1: Manufacturing cost breakdown in euro of vehicle

Furthermore, the cost breakdown structure for the manufacturing cost is shown inFigure 5.2, with the total manufacturing cost of ± € 1,369,698.

The values shown in Table 5.1 are all estimations and therefore there values can vary. Especially because of certain assumptions made. Therefore in the verification and discussion of Method and Results these effects are discussed. In addition, an margin of error is provided for the manufacturing cost.

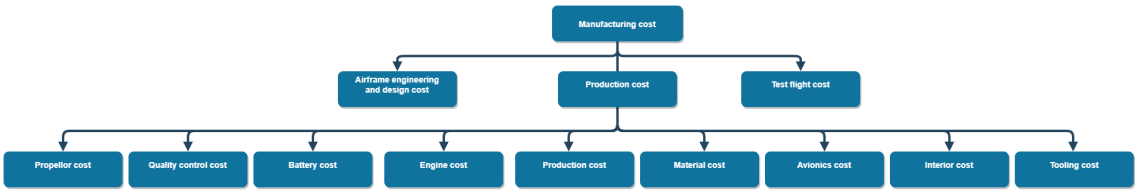

Figure 5.2: Manufacturing cost breakdown structure

5.2.3. Verification and Discussion of Method and Results

The total costs are found using the equations given in subsection 5.2.1 and input values retrieved from the sources given in subsection 5.2.2. Verification is performed by comparing the performed computations by hand calculations. By doing so found was that the model and hand calculations gave the same results.

Noticeable is the relatively high labour cost compared to other cost sources due to multiple reasons. First of all, the number of vehicles produced is relatively little, therefore making the labour cost per vehicle high. If more vehicles are produced, workers get more experienced and can become better and work more efficiently. As a result of improvement along the learning curve, less time will be required for the production of one vehicle. Hence also the labour cost will decrease. This effect is confirmed by looking at the manufacturing cost for 1000 vehicles and 50 vehicles produced per month. A decrease of 52 % in total cost is observed. The labour cost decreases from 58 % share of the total cost, to 40 % share of the cost.

Furthermore, the labour cost is heavily influenced by the cost per work hour. The computation uses a wage of € 46.5 per hour [4]. However, this labour cost heavily depends on the company or country considered, this labour rate being approximately that of large aerospace companies like Airbus. Nevertheless, due to sustainability reasons, manufacturing is decided to happen in Europe. Producing the vehicle in other parts of the world to lower production costs has not been considered due to aspects concerning social sustainability. For economic sustainability it is also considered advantageous to produce

the vehicles locally, letting the industry not only create the vehicles but also enjoy the UAM service. Furthermore, most raw materials and subsystems obtained from vendors will come from the US or Europe. Therefore, making it more sustainable to have production facilities close to the manufacturers to lower emissions due to transportation.

Another important aspect of the manufacturing cost is the influence of F_{diff}, describing the complexity of the vehicle. As the chosen value is based on engineering judgment while having large effects on the total costs, it is wise to perform a sensitivity analysis or introduce an error. Therefore a F_{diff} of 1.5 is chosen as a minimum, and 2.0 as a maximum value, comparing costs for conventional aircraft to that of most complex UAMs. With this range for F_{diff}, found is that the total cost will be between 1.248 and 1.553 million euros.

5.3. Operating cost

The operational cost is of great importance for the customer of the vehicle. Therefore important is to give an estimation of this cost. Table 5.2 shows the breakdown of the operational cost for the vehicle. Prices are given in euros per kilometre flown. Notice that for the sake of sustainability the price to charge the battery is determined by the average cost of green energy in the US.

Table 5.2: Operational cost breakdown [1] [2]

Cost	**Value [cent €]**
Maintenance	19
Skyport support	11
Battery charging	25
Aircraft infrastructure	9
Other	12
Total	76

[1] Retrieved from `https://www.futureflight.aero/news-article/2021-11-15/counting-cost-urban-air-mobility-flights`. Visited on 20/06/2022.

[2] Retrieved from: `https://www.inspirecleanenergy.com/blog/clean-energy-101/cost-of-renewable-energy`. Visited on 20/06/2022.

6 Aerodynamics

One of the important forces to consider during flight is the drag that the vehicle produces. This is because the amount of thrust, and therefore the amount of power that the propulsion needs to provide, increases with increasing drag. Furthermore, aerodynamic noise becomes an ever more important factor to consider with growing urban population. Thus, this chapter aims to assess the aerodynamic properties of the vehicle. Section 6.1, section 6.2 and section 6.3 provide a method to approximate the drag produced by the fuselage, the upper structure and the skid of the fuselage respectively. Section 6.4 and section 6.5 provide the results of the drag estimations in forward and vertical flight respectively. Then, section 6.6 assesses retreating blade stall, which is a possible limiting design factor that needs to be considered to fly safely. After that, section 6.7 gives an estimate of the noise produced by the vehicle, after which section 6.8 provides the means by which the methods in this chapter are verified and validated. Lastly, section 6.9 gives recommendations for further research and development in the next stages of the design for the aerodynamic design of the vehicle.

6.1. Fuselage Drag

The first part considered is the fuselage. The fuselage is the largest part of the vehicle in terms of surface area of a single component. Thus, it is important to look closely at the parameters that affect the fuselage drag in order to optimise the fuselage design as much as possible. The fuselage is assumed to be a streamlined shape and in terms of drag, it is approximated as such as well. The shape of the fuselage is shown below in Figure 6.1.

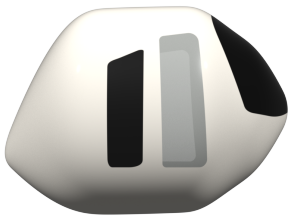

Figure 6.1: Side view of the fuselage of the vehicle.

The shape with which the fuselage in Figure 6.1 is approximated, follows the method proposed by Hoerner [21]. This method makes use of a so-called fineness-ratio, which for an object with a circular cross-section is simply the length divided by the diameter of the cross-section, $\frac{l}{d}$. However, the cross-sectional shape of the vehicle is not circular, but rather elliptical (see subsection 11.2.1 for more detail). Thus, an alternative definition for the fineness-ratio needs is determined in order to take into account both the width and the height of the proposed cross-sectional shape. Hoerner gives the following definition for the fineness-ratio of an oval cross-section [21]:

$$\frac{l}{d} = 2 \cdot \frac{l}{b+h} \tag{6.1}$$

where l, b and h are the length, width and height of the fuselage respectively. Using this ratio, the drag coefficient for the fuselage can be estimated by Equation 6.2 [21]:

$$C_{D_{wet}} = \left(1 + 1.5 \cdot \left(\frac{d}{l}\right)^{\frac{3}{2}} + 7 \cdot \left(\frac{d}{l}\right)^{3}\right) \cdot C_f \tag{6.2}$$

where $\frac{d}{l}$ is the reciprocal of the fineness-ratio and C_f is the skin-friction drag coefficient. The skin friction coefficient is dependent on the Reynolds number as can be seen in Equation 6.3 [22].

$$C_f = \frac{1.328}{\sqrt{Re}} \tag{6.3}$$

The drag estimation given in Equation 6.2 consists of two major drag contributions: drag due to friction, represented by $1.5 \cdot \left(\frac{d}{l}\right)^{\frac{3}{2}}$, and drag due to a pressure gradient over the fuselage, represented by $7 \cdot \left(\frac{d}{l}\right)^{3}$. In order to calculate the total drag of the fuselage with the obtained value of the drag coefficient, the following equation is used:

$$D = C_D \frac{1}{2} \rho V^2 S_{ref} \tag{6.4}$$

where C_D is the drag coefficient, the $\frac{1}{2}\rho V^2$ term is the dynamic pressure of the flow the vehicle is flying in and S_{ref} is the reference area corresponding to the drag coefficient estimation method. The latter is important because taking the wrong reference area would result in an incorrect estimation of the drag of the vehicle. The corresponding area used for the estimation given by Equation 6.2 is the wetted area of the fuselage. The wetted surface area of the fuselage is approximately [21]:

$$S_{wet} = (0.7\,to\,0.8) \cdot l \cdot p$$

where for further calculations, a value of 0.75 is taken as an average between 0.7 and 0.8 and p is the perimeter of the cross-section of the fuselage. Hoerner proposes another method for the estimation of the fuselage drag, which uses the frontal area of the fuselage as a reference area. The drag coefficient with this method is estimated as follows:

$$C_{D_{wet}} = \left(3 \cdot \left(\frac{l}{d}\right) + 4.5 \cdot \left(\frac{d}{l}\right)^{\frac{1}{2}} + 21 \cdot \left(\frac{d}{l}\right)^{2}\right) \cdot C_f \tag{6.5}$$

The difference between these two methods is displayed in Figure 6.2 below as a function of the fineness-ratio:

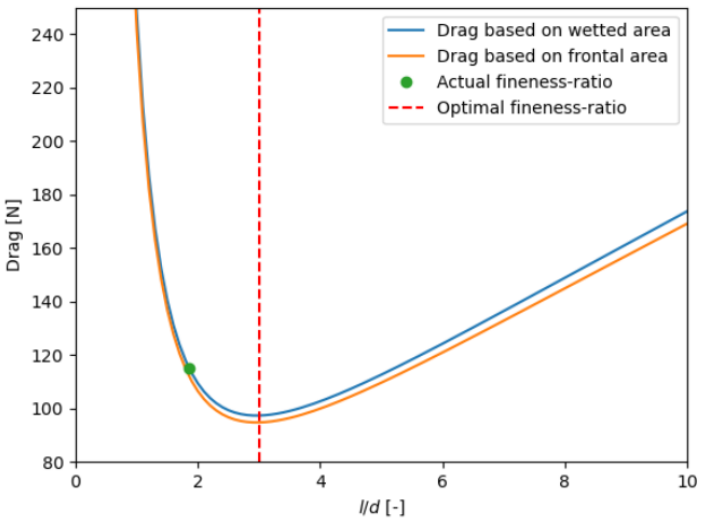

Figure 6.2: Difference in drag estimation methods based on wetted and frontal area by keeping a constant cross-sectional area and varying the fuselage length.

The difference between the estimation methods in percentage remains approximately the same for all fineness-ratios and is around 8.52%. To keep a conservative approach, also considering the effect of

the drag on the minimum power required, the method based on the wetted area is chosen to estimate the drag of the fuselage. With the current vehicle dimensions, the drag of the fuselage is estimated to be around $115\,N$, with a contingency margin of $-30\,N$ and $+40\,N$. These margins take into account a possible variation in dimensions of the fuselage of 10% and a small variation in angle of attack of the fuselage.

6.2. Upper Structure Drag

The next major source of drag is the upper structure supporting the propulsive system of the vehicle. In terms of drag, this component is rather complex as it consists of many tubes connecting the various engines and the hubs of the engines themselves. Furthermore, the flow induced by the propellers also causes a disturbance to the free-stream flow. To approach this problem, the drag of the upper structure is approximated as the sum of individual cylindrical tubes. As the connecting struts have the shape of a cylinder, this is considered a valid approximation. This approach has it limitations however; when air flows over the first strut, it creates a turbulent wake, which then arrives at the next strut. Thus, the flow over the next strut is not ideal anymore. In addition, as mentioned before, there is also an induced flow from the propellers, accelerating the flow over some parts of the upper structure, thus increasing the drag. The induced flow velocity is approximately $6.24\,m/s$, as explained in more detail in section 7.4. This is approximately 20% of the free-stream velocity. To take into account the fact that the wake disturbances and the flow acceleration over some parts are not considered, the free-stream velocity is taken to be 20% higher; instead of $27.78\,m/s$, it is taken as $33.33\,m/s$ for the drag calculations in cruise condition.

The decision to approximate the upper structure by multiple cylindrical shapes caused another problem to arise: the orientation of the cylinder with respect to the flow. There are three orientations possible: the cross-section is perpendicular to the flow, parallel to the flow, or at an angle. These three cases will be explained in more detail below.

Cylinder Parallel to Flow

The first case to consider is when the cross-sectional area of the cylindrical shape is pointing in the direction of the flow. This means that the air flows parallel to the cylinder. A visualisation of this, together with an estimate for the drag coefficient of a cylinder in this situation, can be seen in Figure 6.3 below:

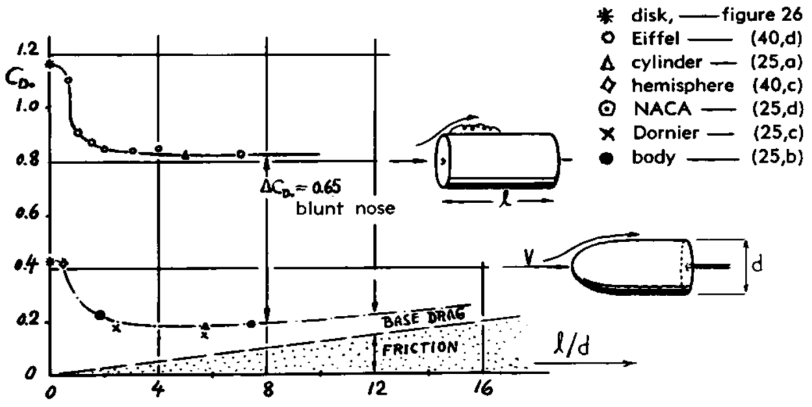

Figure 6.3: Drag coefficient of cylindrical bodies in axial flow, with blunt shape (in the upper part) and with rounded or streamlined head forms (lower part) -as a function of the fineness ratio l/d [21].

Note that for this analysis, the upper curve is chosen as this shape is used for the upper structure, rather than a rounded form at the start of the cylinder. Furthermore, the upper curve only represents the pressure drag of the cylinder; at a low fineness-ratio, $\frac{l}{d}$, the cylinder starts looking similar to a disk, resulting in a more extreme flow separation. This causes a bigger pressure difference between the front and back of the more disk-looking shape, thus a higher pressure drag. However, when the fineness-ratio becomes higher, the drag coefficient does not change anymore, because after a certain value for $\frac{l}{d}$, the pressure difference created by the wake of the cylinder does not change anymore, thus the pressure

drag remains the same. Therefore, the drag coefficient for fineness-ratios above 2 is assumed to remain constant at a value of 0.81. The reference surface area that Hoerner uses for this is the frontal area, for which ,in the case of a cylinder, the area of a circle can be used. However, from the fact that with an increase in fineness-ratio the drag does not increase anymore, it becomes apparent that no increase in skin-friction is taken into account with an increase in (relative) length of the cylinder. Therefore, in addition to the pressure drag, the skin friction drag of a flat plate with an equivalent wetted area is considered. Using Equation 6.3, the equation for the skin friction of a flat plate is given by Equation 6.6 [22].

$$D_f = C_f \cdot q_\infty \cdot S_{wet} = \frac{1.328}{\sqrt{Re}} \cdot \frac{1}{2}\rho V^2 \cdot L\pi d \tag{6.6}$$

where Re is the Reynolds number of the flow over the cylinder, q_∞ is the dynamics pressure of the flow, consisting of the air density and free-stream velocity, and S_{wet} is the wetted area of the cylinder. The latter is taken as the surface area of the cylinder without the top and bottom cross-sectional parts. Furthermore, the Reynolds number of the flow is given by the following equation [22]:

$$Re = \frac{\rho V L}{\mu} \tag{6.7}$$

where ρ and V are the free-stream air density and velocity respectively, L is the characteristic length of the object the air is flowing past; in the case of a parallel cylinder, it is the entire length of the cylinder. In addition, μ is the dynamics viscosity of air, which at a temperature of $20\,°C$ is given to be $1.825 \cdot 10^{-5}\ \frac{kg}{m \cdot s}$. Combining the drag components, the total drag for a cylinder placed in parallel to the flow, can be given by:

$$D = D_p + D_f = 0.81 \cdot \frac{1}{2}\rho V^2 \cdot \pi \left(\frac{d}{2}\right)^2 + \frac{1.328}{\sqrt{Re}} \cdot \frac{1}{2}\rho V^2 \cdot L\pi d \tag{6.8}$$

Rewriting Equation 6.8 in a more compact way results in Equation 6.9:

$$D = \frac{1}{2}\rho V^2 \pi \cdot \left(0.81 \left(\frac{d}{2}\right)^2 + \frac{1.328}{\sqrt{\frac{\rho V}{\mu}}}\sqrt{L}d\right) \tag{6.9}$$

Equation 6.9 shows that the pressure term mainly depends on the diameter of the cylinder, while the skin friction term also depends on the length.

Cylinder Perpendicular to Flow

The second case mentioned before considers a cylinder that is placed perpendicular to the flow. The situation is also visualised in Figure 6.4.

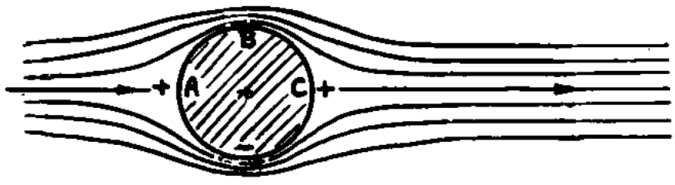

Figure 6.4: Flow pattern of circular cylinder in non-viscous flow; no drag [21].

Figure 6.4 considers a non-viscous flow, which results in no drag because of the presence of the cylinder. This is called d'Alembert's paradox [23]. However, this is not the case, because the presence of the cylinder does actually result in drag, which could even be very significant. Similar to the parallel cylinder case, there have been attempts to estimate and predict the drag of a cylinder. Figure 6.5 is the result of one of these studies, which analyses the effect of the Reynold's number on the drag coefficient.

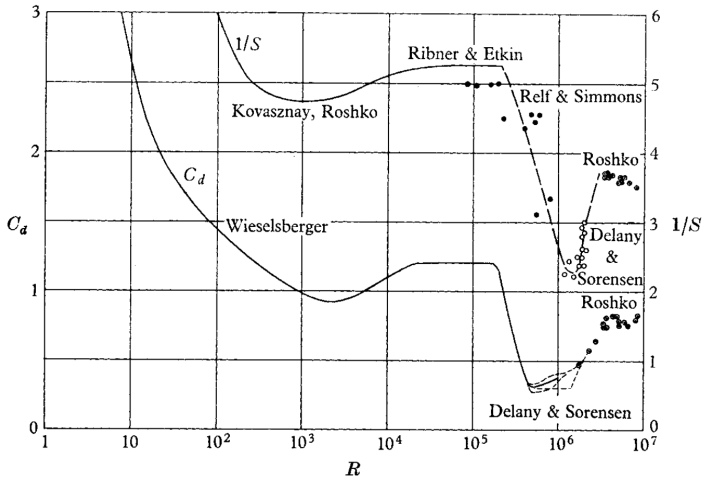

Figure 6.5: Drag coefficient and reciprocal of Strouhal number [24].

As can be seen from Figure 6.5, the drag coefficient of a cylinder perpendicular to the flow is very sensitive to the Reynolds number. Therefore, the determination of the Reynold's number is very important to estimate the drag and then also explain the flow conditions. For this case, the characteristic length taken for the Reynold's number is the diameter of the cylinder and the reference surface area taken for the use of Equation 6.4 is the frontal area of the cylinder. This frontal area is equal to $L \cdot d$. Figure 6.5 also shows a curve representing the reciprocal of the Strouhal number; this however is not relevant for this DSE project, so only the lower curve is taken into consideration for the calculations. When the correct drag coefficient is determined, based on the Reynold's number, and the correct frontal area is found, it is then possible to calculate the drag of the cylinder with Equation 6.4. The main drag source that comes from the perpendicular cylinder is pressure drag.

Cylinder at an Angle to Flow

The last case considered is when the cylinder is at an angle α, so neither parallel nor perpendicular to the flow. To approach this problem, the flow is decomposed into two components: a component parallel and one perpendicular to the cylinder. This way the problem can be approached as a combination of the two mentioned above. The situation is visualised in Figure 6.6 below.

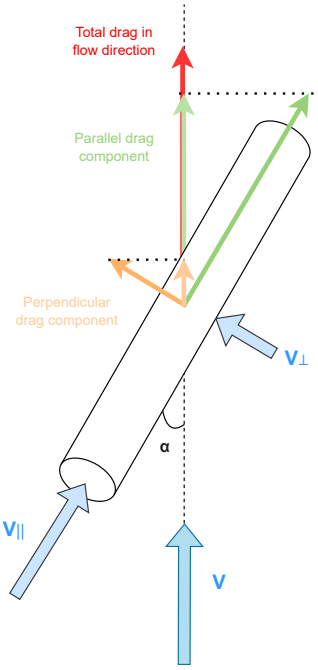

Figure 6.6: Decomposition of the drag forces for a cylinder at an angle to the flow.

What follows is that the flow velocity parallel to the cylinder, $V_{\parallel}$, is equal to $V \cdot cos(\alpha)$ and the flow velocity perpendicular to the cylinder, $V_{\perp}$, is equal to $V \cdot sin(\alpha)$. This results in a drag force again parallel and perpendicular to the cylinder. However, this is not the drag desired for the total drag estimation. This desired drag is rather the summation of the components that are in the direction of the free-stream flow. Just adding the two components parallel and perpendicular to the cylinder would result in a too high of a drag value. Thus, the total drag for a cylinder at an angle α to the flow can be written as:

$$D = sin(\alpha) \cdot D_{\parallel} + cos(\alpha) \cdot D_{\perp} \tag{6.10}$$

Note again that also the drag components parallel and perpendicular to the cylinder, $D_{\parallel}$ and $D_{\perp}$ respectively, depend on the angle the flow is at.

Hub Drag

The upper structure does not only consists of the cylindrical struts supporting the propulsion system; the propellers themselves are namely connected by a so-called hub to the supporting upper structure. This hub also has a cylindrical shape and, thus, can be approximated by using the methods described above. As the hub-cylinder is oriented upwards, the drag of the hub can be approximated by using the method of a cylinder perpendicular to the flow, as the air flows around the cylinder similarly to what is visualised in Figure 6.4.

6.3. Skid Drag

The third component of the vehicle considered for the drag estimation is the skid. Similar to the upper structure, the skid is made out of several cylindrical struts, which makes it possible to use the same approach as described in the previous section, section 6.2. The vertical struts are approximated as cylinders perpendicular to the flow, while the longer horizontal ones, on which the vehicle supports when landed, are approximated as cylinders parallel to the flow.

6.4. Drag Results for Forward Flight

The previous sections explained the methods used to estimate the drag of the complete vehicle. This section aims to provide the results of these estimation methods, with an explanation of the results. The

results of the drag estimations are given in Figure 6.7, where it is also visible how much each component contributes to the total drag.

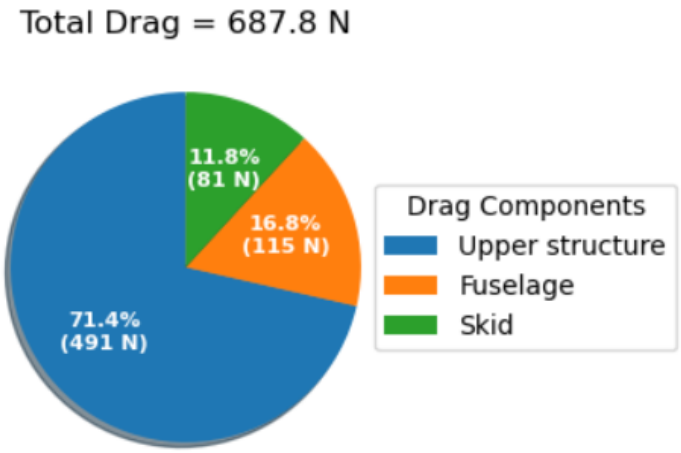

Figure 6.7: Drag contribution per vehicle component.

From Figure 6.7 it becomes evident that the biggest contribution to the drag comes from the upper structure. This is curious at first sight as the fuselage is bigger in terms of occupied volume and surface area. To analyse further where the drag comes from, the drag from the upper structure is also decomposed into several components, based on the estimation methods described in section 6.2. The drag decomposition for the upper structure can be seen in Figure 6.8.

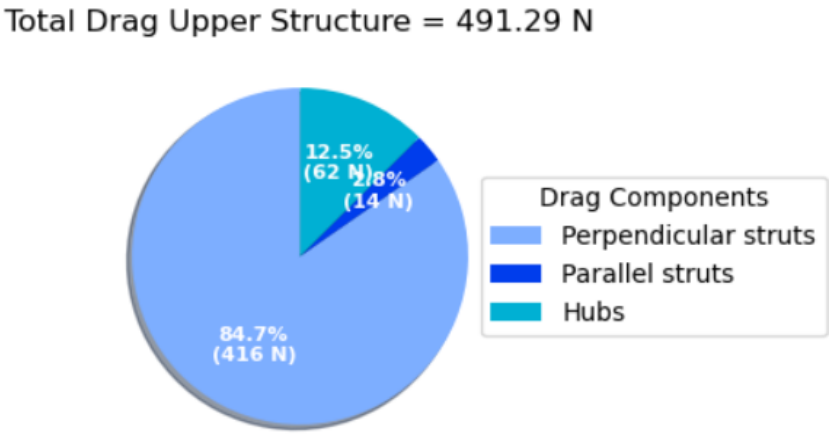

Figure 6.8: Drag contribution of upper structure components (cruise).

Figure 6.8 shows that the biggest contribution to the drag comes from the perpendicular drag components of the struts and then from the hubs. The first of these also includes the perpendicular drag components from the struts placed at angle. Note that the drag of the hubs is also calculated using the ”perpendicular cylinder” method. To understand where all this drag comes from, a closer look at the method is needed. A cylinder placed perpendicularly in the flow mostly has pressure drag. As can be seen from Figure 6.5, the drag coefficient is very dependent on the Reynold’s number. A simplified model representing the curve in Figure 6.5 has been made and can be seen in Figure 6.9 below. This figure also includes the drag coefficients of the perpendicular struts and hubs and where they are on this curve with respect to each other. In addition, a change in velocity is included to show the effect of the velocity on these components.

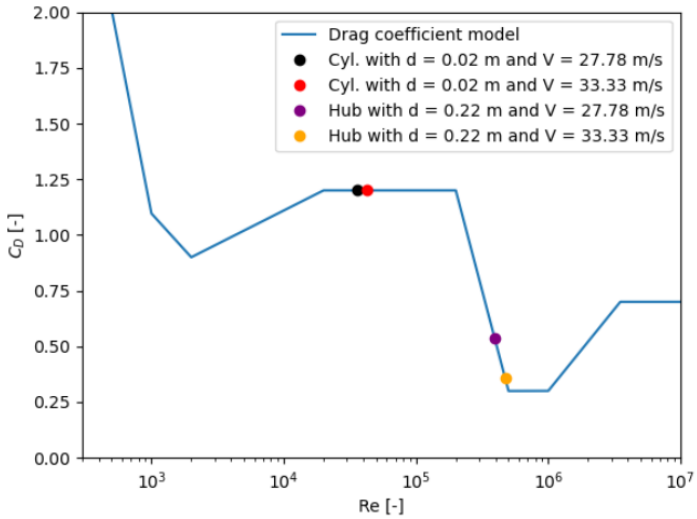

Figure 6.9: Drag coefficient against Reynolds number including several cases in the upper structure of the vehicle (cruise).

From Figure 6.9 it can be observed that the drag coefficient for a perpendicular cylinder, with the diameter dimensions used for the upper structure, is quite high ($C_D = 1.2$). The explanation for this is that the wake behind cylinders with a Reynold's number in the range of 10^4 and 10^5 becomes very turbulent and has vortex streets. This can be seen in Figure 6.10. This turbulent wake is the cause of a high pressure drag.

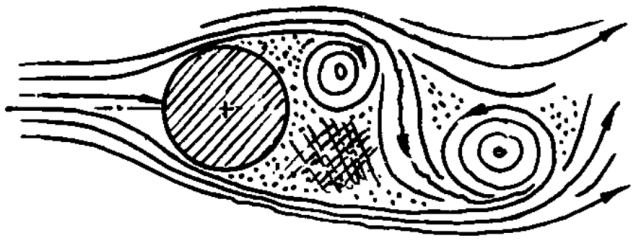

Figure 6.10: Cylinder between Re = 10^4 and 10^5; vortex street with $C_{D_0} = 1.2$ [21].

The other extreme case is when the Reynold's number is between $5 \cdot 10^5$ and 10^6. This case is visualised in Figure 6.11 below.

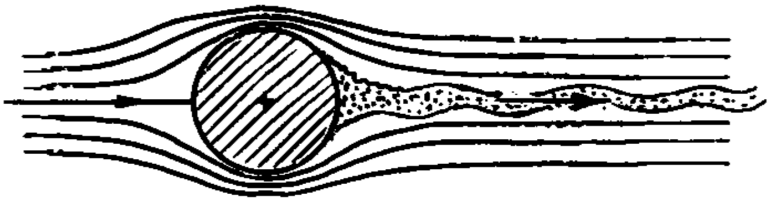

Figure 6.11: Cylinder above critical Reynolds number with $C_{D_0} = 0.3$ [21].

The flow in Figure 6.11 is also turbulent, but already at the start of the cylinder. Thus, the flow has a lot of turbulent kinetic energy, which makes it possible for the flow to remain attached longer to the cylinder. Therefore, the wake behind the cylinder is smaller, which results in lower pressure drag. In the case of the hubs, their higher diameter compared to the struts makes it possible to be closer to the case visualised in Figure 6.11, and thus having a lower drag coefficient than the struts (also see Figure 6.9). What makes the contribution of the perpendicular struts even higher than the hubs is the large diameter of some of the struts; especially the inner struts are very large in order to withstand the

loads induced by the propellers on the structure, which makes these struts more inefficient in terms of drag. In section 6.9 more recommendations are given to optimise the aerodynamic performance of the structure in terms of drag.

6.5. Drag Results Vertical Flight

The drag during vertical flight is also needed for the determination of the total energy used during operations, as this affects the amount of power needed during the vertical flight phase. Note however, that when the vehicle descends, the drag is actually used as an advantage, as less power is needed to keep the rate of descent constant. However, the drag during vertical climb becomes more important as the power increases because of the drag. The drag calculated during vertical flight is similar to the drag calculated during the forward flight phase, with the only difference that the fuselage is approximated not as a streamlined body anymore, but rather as a cylinder as well, similar to the rest of the structure. The method of a cylinder perpendicular to the flow will be used to approximate the drag of the fuselage during vertical flight. For the climb velocity used in the estimation, a velocity of $6\,m/s$ is used. This value is determined by looking at the amount of excess power the vehicle has in this phase (see section 7.4 for more detail). Furthermore, it also already takes into account an additional factor because of the induced velocity due to the rotors (similar to the forward flight situation). The reference length used for the calculations is the height of the vehicle, while the width is used to determine the frontal area with respect to the flow coming from either below or above. Also, for the upper structure and the skid the same methods as described in section 6.2 can be used. The difference is the orientation of some of the components. The results of the vertical drag estimation is given in Figure 6.12

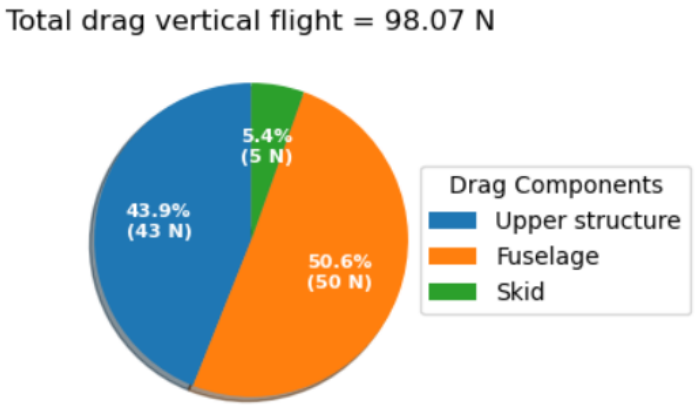

Figure 6.12: Drag contribution per vehicle component (vertical flight).

In comparison to Figure 6.7, the contributions of the the fuselage is much larger. The larger contribution of the fuselage is mainly due to the less aerodynamic shape the fuselage has vertically. Furthermore, note that the upper structure does not have as much of a contribution as during forward flight. This is due to the hubs not creating that much pressure drag anymore, because in vertical flight they are parallel to the flow, and not perpendicular as in forward flight. Furthermore, the Reynolds number of the upper structure in vertical flight is apparently more beneficial in terms of drag than the fuselage.

6.6. Retreating Blade Stall

So far, only the drag of the vehicle has been considered. In terms of lift, the vehicle creates its lift with the propellers on top of the upper structure. There is one important phenomenon, however, that has to be considered: retreating blade stall. If not dealt properly with this phenomenon, this could prevent the vehicle from flying or even lead to critical failure during flight. This phenomenon is caused by the fact that in forward flight (so especially in the cruise phase) the advancing blade moves faster than the retreating blade. The flow velocity on the retreating side is then actually less than it would be during hover. In combination with a (relatively) high angle of attack, this could lead to blade stall and a loss in lift. The prevention of blade stall is also important to prevent more sources of noise, as is mentioned in the next section, section 6.7. This phenomenon is depicted in Figure 6.13.

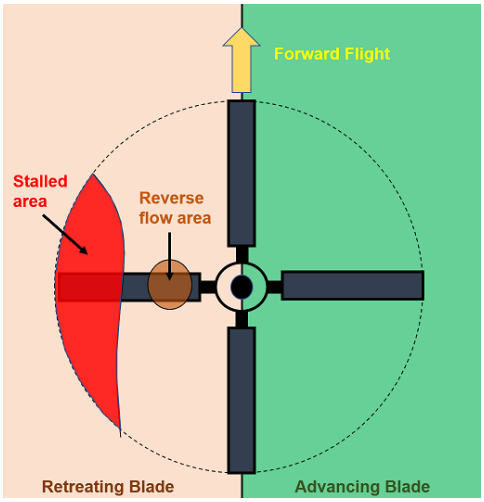

Figure 6.13: Retreating blade stall in forward flight condition [1].

Similar to a wing, blades have a lift coefficient, which is called the blade mean lift coefficient, given by the symbol $\bar{C}_l$. Normally, values for $\bar{C}_l$ around 1.5-1.6 can be achieved before the blade stall [25]. However, to keep also enough control during other phases, such as hover, a constraint has to be put on this lift coefficient. Thus, an upper limit for this lift coefficient of 1.0 is given for the design of the vehicle. The blade mean lift coefficient can be written as

$$\bar{C}_l = 6 \cdot \frac{C_T}{s} = 6 \cdot \frac{T}{\rho A_{disk}(\Omega R)^2} \frac{A_{disk}}{A_b} = \frac{6T}{\rho A_b (\Omega R)^2} \tag{6.11}$$

where T is the thrust generated by one engine, Ω the angular velocity, R the radius of the blades and ρ the air density. The rotor solidity, s, is defined as the ratio between the rotor blade area, A_b, and the rotor disk area, A_{disk} [26]:

$$s = \frac{A_b}{A_{disk}} = \frac{BcR}{\pi R^2} = \frac{Bc}{\pi R} \tag{6.12}$$

An important parameter that needs to be decided upon when choosing the engine used for the vehicle is the angular velocity of the blades. Thus, Equation 6.11 can be rewritten as

$$\Omega = \sqrt{\frac{6T}{\rho A_b C_l R^2}} \tag{6.13}$$

Equation 6.13 gives a lower limit for what the angular velocity of the blades shall be for a given blade radius, in order to prevent blade stall.

6.7. Noise

Not only is drag an important factor aerodynamically, but also the noise produced by the propellers. Thus, this section aims to address the determination of the noise the vehicle produces at 100 ft, which is equal to 30.48 m as stated in the requirements, and at a distance of 450 m, which is equal to the cruise altitude. To determine the type of noise that needs to be calculated to give an estimate for the noise produced by the vehicle, the model of Brown and Harris is followed. They consider three types of noise, namely blade slap, rotational noise and vortex noise [25]. The first of these three, blade slap, can occur in three occasions: with shockwave formation, blade stall and/or blade-vortex interaction. For this design, the tip velocity of the blades is chosen as such that shockwaves do not occur. The retreating blade stall also does not occur and is dealt with in more detail in section 6.6. In addition, "blade-vortex interaction occurs when the strong tip vortices shed from the main rotor pass in close to the following blades during descending or maneuvering flight" [27]. Thus, this can be avoided with specific landing and take-off procedures [25]. When considering rotational noise, Brown and Harris conclude

[1] From: `https://mediawiki.ivao.aero/index.php?title=Retreating_Blade_Stall`. Visited on 02-06-2022

that, compared to vortex noise, the frequency at which this rotational noise occurs is (relatively) low (around $10^2\,Hz$). As the human ear is less sensitive to these low(er) noise, rotational noise is not considered either. This conclusion is supported by Brown and Harris with the use of an A-weighting scheme, which predicts the response of the human ear to a range of frequencies [25]. Thus, vortex noise is the only source of noise that is considered to predict the noise of the vehicle. Brown and Harris give the following equation for the noise, given as Sound Pressure Level (SPL) [25]:

$$SPL = 20\,log_{10}\left[K_2 \frac{V_T}{\rho(\Delta S)}\sqrt{\frac{N_{rotors}T}{s}\left(\frac{T}{A_{disk}}\right)}\right] \tag{6.14}$$

where K_2 is a constant equal to $0.4259\,s^3/m^3$, V_T the rotor tip velocity and ΔS the distance to the observer. When computing the noise at a distance of $100\,ft$, as stated in the requirement, and at cruise altitude, an approximation of the noise produced by the vehicle can be made. These results can be found in Figure 6.14.

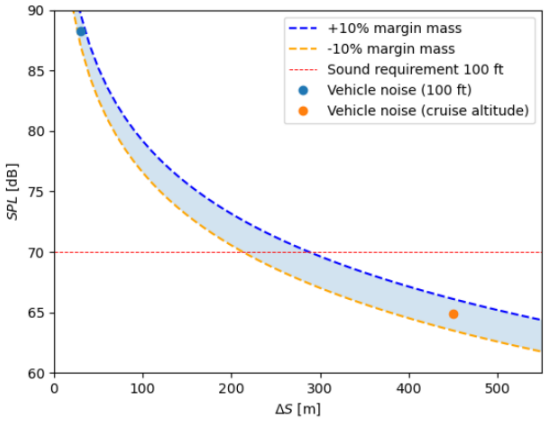

(a) Noise as a function of distance to the observer with a 10% lower and upper mass margin evaluated at take-off conditions.

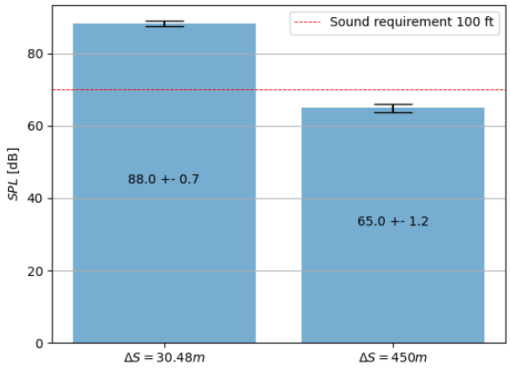

(b) Noise at $100\,ft$ and $450\,m$ in take-off and cruise conditions respectively, including adjusted thrust and tip velocities for each condition.

Figure 6.14: Noise of the vehicle with mass contingencies.

Figure 6.14a on the left shows how the noise decreases with the distance to the observer. A 10% upper and lower margin are also taken to take into account some margins in case the mass, and thus the thrust, of the vehicle changes in future iterations. It can be seen that for a distance of $100\,ft$, the vehicle produces more noise than stated in the requirement. This means that for the iterations presented in this report, the vehicle does not comply yet with the noise requirement stated for a distance of $100\,ft$. However, this requirement for a distance of $100\,ft$ was not taken either from regulations nor from the stakeholders, but rather as a reference to try and stay within. If a distance equal to the cruise altitude is taken, it can be seen that the requirement is well met. This is deemed sufficient for this design phase as the vehicle spends most of its time at a distance larger than the specified $100\,ft$. Further recommendations to lower the noise produced by the vehicle are presented in section 6.9. Figure 6.14b shows the same results as Figure 6.14a, but with a more clear margin indicated that takes into account several contingencies for future iterations; this is mostly a variable mass of +- 10%.

6.8. Aerodynamics Verification & Validation

This section aims to justify, verify and validate the choices made and models chosen for the aerodynamic analysis of the vehicle. This is done by comparing obtained values with other vehicles and performing sensitivity analyses.

In terms of verification, several steps are taken to make sure the model calculates the different components of the drag correctly. To make sure that the formulas are implemented correctly, unit tests are carried out by comparing the obtained values to values obtained by calculations by hand or by the use of online verified (graphical) calculators, such as Desmos. Moreover, one of parts of the model that was verified and then corrected after the verification process, was the calculation of the drag of a parallel cylinder. By varying the length of the cylinder and keeping the diameter constant, it was noticed that

the drag would not change, which in reality is not the case. Thus, as described in section 6.2, the skin friction of a flat plate with the wetted surface area as the cylinder is added to the (pressure) drag obtained from Figure 6.3. The difference in drag between the incorrect and the (verified) correct model is visible in Figure 6.15.

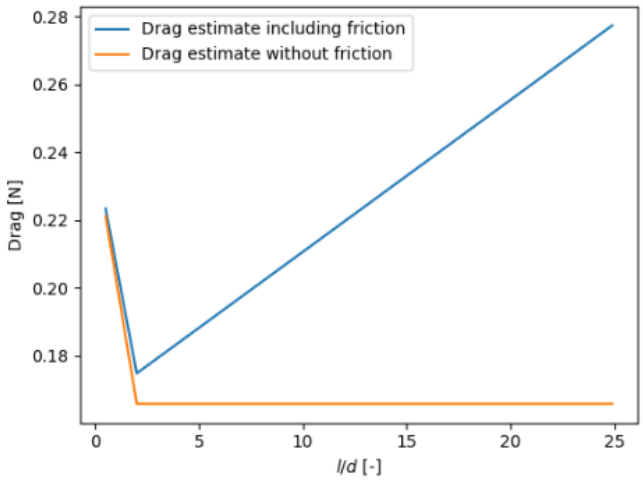

Figure 6.15: Model including and excluding the skin friction with a variation in length and a cylinder diameter of 0.02 m.

Figure 6.15 shows the importance of the verification and the change made in the model, especially for higher fineness-ratios, as the difference in estimated drag is significant. In addition, in section 6.2, a certain value was chosen to take into account the induced velocity due to the rotors. To verify this chosen value, a sensitivity analysis is performed to show the effect, first of all, of the free-stream velocity on the total drag and then also the effect of the choice on the induced velocity factor. This sensitivity analysis is shown below in Figure 6.16.

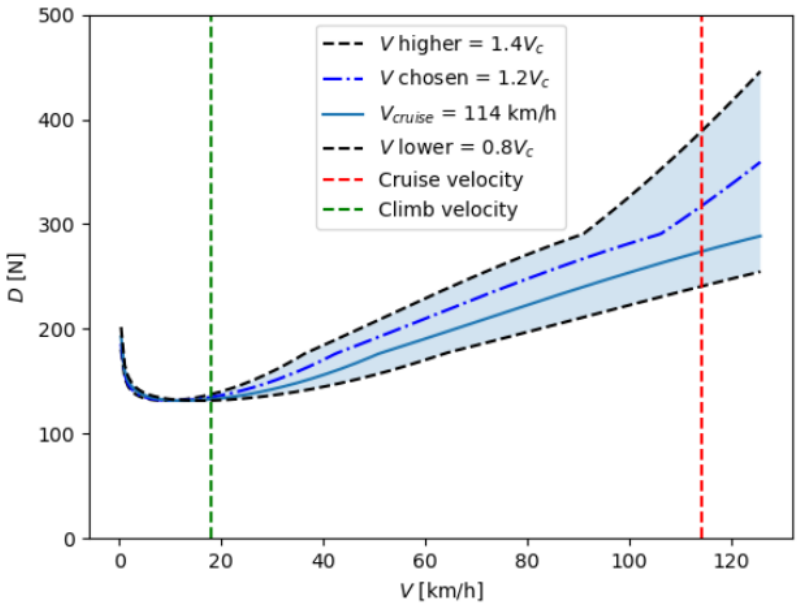

Figure 6.16: Effect of choosing a factor to include the rotor induced velocity on the total drag.

From Figure 6.16 it can be concluded that at velocities higher than the cruise velocity of 100 km/h, an induced velocity factor of 1.4 would result in a very high increase in drag, if this factor would remain constant. In reality, the effect of the induced velocity becomes less with increasing velocity, thus a factor of 1.4 does not seem to be feasible. Furthermore, this factor was not valid in the first place, as

the induced velocity is not as high as 40% of the free-stream velocity. Furthermore, for the velocities the vehicle has to fly at, the differences between the free-stream velocity and the velocity including the induced one do not seem to diverge from each other, which makes this chosen value acceptable for this range of velocities. Note, however, that the model for drag in general seems to provide incorrect values for lower velocities. This is because a low velocity also results in a lower Reynolds number. As the vehicle is mainly approximated with (perpendicular) cylinders, from Figure 6.5 it can be seen that the drag coefficient increases to very high values. This is the reason why for low velocities, the curve in Figure 6.16 goes up. Thus, for a combination of velocity and characteristic length where the Reynolds number drops below 10^{-1}, the model is not reliable. However, for the design of the vehicle, the Reynold's number does not drop to these low values.

In terms of validation, a closer look is taken to the total drag of the vehicle; this value is compared to statistical data of other rotorcraft. The statistical relation between the take-off mass of the vehicle and the equivalent wetted area, $f(= D/q)$, can be seen in Figure 6.17 [28]. In this figure, the actual value for the mass and equivalent wetted area is shown.

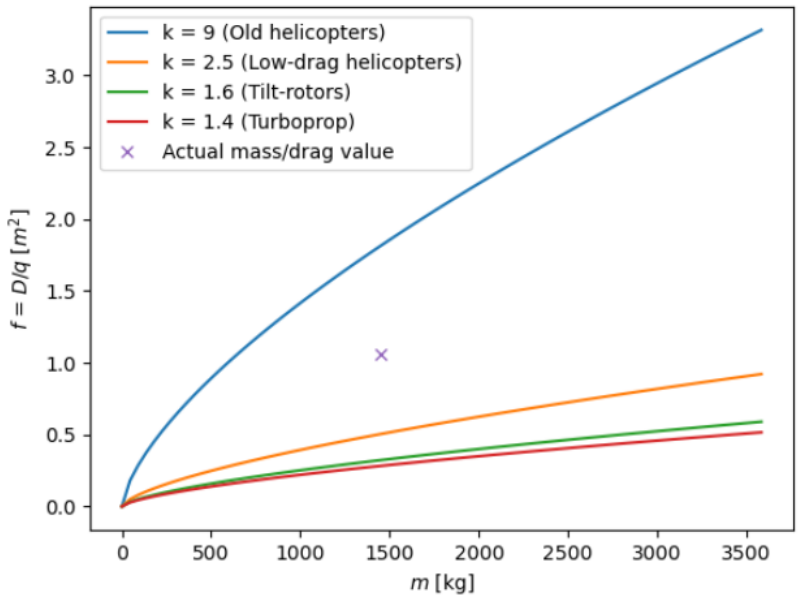

Figure 6.17: Statistical relationship between drag and mass of different rotorcraft.

Figure 6.17 shows that the current estimate for the vehicle drag is between current low-drag helicopters and old helicopters. The used model even over-estimates the drag when comparing it to these low-drag helicopters, which means a more conservative approach is taken for the estimation. When comparing the vehicle to old helicopters, the estimations seems to be low. However, the helicopters used for this estimation are mainly from the 50s and 60s, hence it is valid to assume that with the current technologies and resources it is possible to make more detailed estimations. Therefore, the comparison to current low-drag helicopters is more logical and thus, based on historical statistical data, the model is deemed to be valid, because of the conservative approach. Furthermore, as there are no UAMs currently on the market, helicopter-like rotorcraft are the closest vehicles to compare the designed vehicle with. Furthermore, to further support the validation of the model, a closer look is taken to the contribution of the hubs. Typically, the hub(s) of a rotorcraft contribute for 20% to 50% to the total drag [28]. By looking at Figure 6.7 and Figure 6.8, it is possible to compute a total hub contribution of approximately 10%. Where the UAM vehicle differs from the common drag decomposition of a helicopter, is the fact that it has a big upper structure, which a helicopter does not have. Therefore, the contribution of the hubs is in comparison lower than for a conventional helicopter, which validates the results obtained.

The noise model used by Brown and Harris is already verified and validated, so it can accurately be used to predict the noise of a rotorcraft that has not any blade slap [25]. A comparison to similar

UAMs is not possible as these still need to come on the market and thus detailed performance data is not shared yet at this point in time. If a comparison is made with helicopters, it can be observed that the noise generated by helicopters is much higher compared to the designed vehicle: approximately $87\,dB$ at $500\,ft$, while this same amount of noise is achieved by the BonMobile at $100\,ft$ [1]. However, it is more difficult to make an exact comparison between the two to validate the noise produced by the vehicle, as these two vehicles are structured differently and have another approach in terms of the design of the propulsion system.

6.9. Recommendations

There are several recommendations for further improvement of the aerodynamic design of the vehicle. Starting with the drag, it can be concluded that especially the drag of the upper structure is very high. This is because a cylinder is aerodynamically speaking a bad shape which, especially in a particular Reynolds number range, has very high pressure drag. Thus, what is recommended is to shape the bars out of which the upper structure is made of in a more aerodynamic shape, such that the drag could decrease. Furthermore, this could also result in a higher lift force. Both of these effects would reduce the power required by the engines, thus the total amount of energy used during the flight. This could then result in a smaller and lighter battery. However, what needs to be taken into account is that when the shape is made aerodynamic in forward flight, this can have negative consequences for the drag in vertical direction. Therefore, it is recommended to perform an adequate trade-off between several shapes.
Another recommendations in terms of drag is to make use of Computational Fluid Dynamics (CFD), which could first of all validate the model presented in this report. Moreover, the use of CFD would provide a more accurate and adequate estimate of the drag produced by the vehicle, thus reducing the uncertainties in terms of drag estimations; the model described in this report approximates most of the shapes as cylinders as does not take into account the interactions between all the elements. It also does not consider into much detail which exact parts of the vehicle are affected by the induced flow of the rotors. This is now rather taken into account by multiplying the free-stream flow by a factor.

In section 6.7 it is concluded that the noise requirement at a distance of $100\,ft$ is not met. First of all, it is recommended to revise this requirement as this is not a requirement set by either airworthiness regulations, nor by the client. This value has rather been set by the DSE group at $70dB$ at a distance of $100\,ft$ as this is the noise produced by a passing car and a distance that is frequently used for noise measurements. This however does not take away that there are improvements to be made when optimising the vehicle for noise. From Equation 6.14 it can be seen that there are several factors that affect the noise. By further lowering the mass of the vehicle, it would be possible to reduce the thrust provided by each of the propellers. Moreover, the radius of the propeller could be varied. By lowering the radius, the disk loading becomes higher, but the effect the radius has on lowering the tip speed is bigger, thus the noise reduces with $\propto \sqrt{R}$. The same goes for the angular velocity: by lowering the angular velocity, the tip speed and thus the noise reduces. Note, however, that the tip speed has a minimum value to avoid retreating blade stall (see Equation 6.13). Similar to these parameters, there are other blade parameters that could be changed to optimise the noise of the vehicle. Therefore, a more in depth blade design is recommended to investigate further upon the possibilities to reduce noise, while maintaining enough performance.

[1] From: https://aerocorner.com/blog/why-are-helicopters-so-loud/#:~:text=associated%20with%20helicopters.-,How%20Loud%20Is%20a%20Helicopter%3F,mower%20is%20about%2090%20decibels.. Visited on 20-06-2022

7 Propulsion System Design

This chapter will discuss the design of the propulsion system which is divided into two components: electric motors and rotors. Firstly possible design choices will be discussed in section 7.1, followed by a selection of a range of electric motors in section 7.2. In section 7.3, possible constraints on the propulsion design will be given. Then power and thrust requirements are computed in section 7.4 through which an electric motor is selected and the rotors are sized. Lastly, blade design is performed in section 7.6.

7.1. Design Choices

In this section, possible design choices are considered for the propulsion system. First, coaxial contra-rotating propellers are discussed and considered. Secondly, variable pitch and fixed pitch blades are discussed.

7.1.1. Coaxial Contra-rotating Propellers

Something that has to be considered for the propulsion system is coaxial contra-rotating propellers(CRP). In this configuration, two propellers rotate in opposite directions on the same axis, what can possibly increase the efficiency [29]. However, Figure 7.1 shows the advantage in the specific case of rotors. Here it is shown that the increase in efficiency for CRP is small. CRP also introduce an increase in noise level of up to 30 decibels[30]. With noise as trade-off criteria and urban areas as operational environment CRP are unfeasible for the propulsion system. l

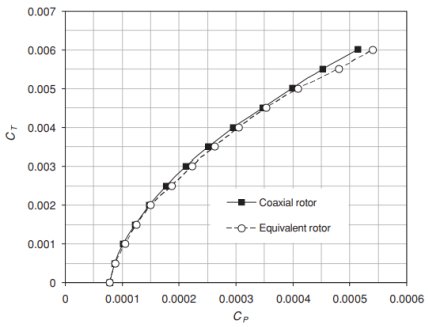

Figure 7.1: Power vs thrust for conventional and coaxial rotor [30]

7.1.2. Variable Pitch Blades vs. Variable RPM Blades

Most conventional helicopters have a constant Revolutions Per Minute (RPM) rotor as RPM is hard to control for most combustion engines. To alter the lift produced by the rotor, the blade pitch is changed and thus the angle of attack of the blades is increased. These blades are called variable pitch blades. Another kind of blade is fixed blades. These blades are positioned at a constant angle of attack and the lift of the rotor is changed by changing the RPM. These kinds of blades become more inefficient at broader ranges as the airfoil of the blades is not operating at the optimum L/D ratio, which generally determines efficiency.

For electric propulsion, fixed-pitch blades are often used as it reduces complexity and weight[31]. Additionally, for variable pitch electric motor-powered propellers both the RPM and the blade pitch need to be actively controlled instead of only the RPM for fixed pitch[32]. This increases system complexity and weight. Therefore, as complexity and weight are driving factors for sustainability; variable RPM rotors with fixed pitch blades are chosen.

7.2. Approach

For the propeller design Dr. M. B. Pavel, Dr.ir. T. Sinnige and Dr. Ragni of TU Delft were consulted. They have recommended to make a preliminary estimation of the power requirements per rotor. Accordingly, an electric motor has to be chosen complying with the power requirement of the estimation. Then, through analysis, the rotor design is optimised.

7.2.1. JavaProp

For the analysis of the rotor and the rotor blades JavaProp is used[33]. This program uses both momentum theory and blade element theory [34]. The inputs for this program are thrust, rotor diameter, number of blades, axial velocity, angular velocity and airfoil type. Axial velocity is the incoming velocity component tangential to the rotor.

7.2.2. Selecting an Electric Motor

For the propulsion system a lightweight electric motor that meets the power requirements needs to be found as recommended by Dr.ir. T. Sinnige. It was found that for cruise the power requirement is approximately $20\,kW$ [5].A factor should be taken for thrust because of manoeuvring. So a margin of 1.5 is chosen on the maximum required thrust. This margin makes the minimum required power for cruise $28\,kW$. Power provided by electric motors is dependent on the angular velocity.As iterations are expected during the project, multiple electric motors are selected to find the best option. . The selected motors are specifically designed to be lightweight and are all from the same manufacturer but vary in size and weight. Additionally, they vary in power and torque. The motors are shown in Figure 7.2 and their specifications are presented in Figure 7.3.

The electric motor's efficiency varies with RPM and torque, additionally, the RPM also affects power required by the rotors. An analysis will point out the optimum combination of electric motor, RPM and rotor area. The relation of power, angular velocity and torque is shown below[35].

$$P = \omega \cdot Q$$

Figure 7.2: the Emrax 188, 208 and 228

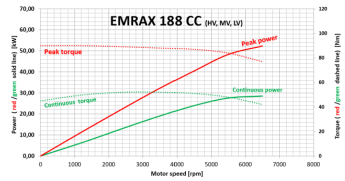

(a) Performance graph of the Emrax 188

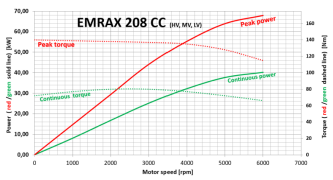

(b) Performance graph of the Emrax 208

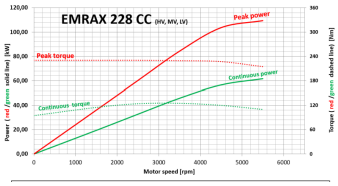

(c) Performance graph of the Emrax 228

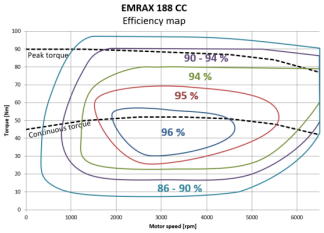

(d) Efficiency map of the Emrax 188

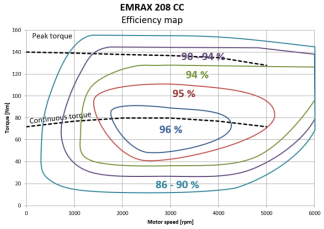

(e) Efficiency map of the Emrax 208

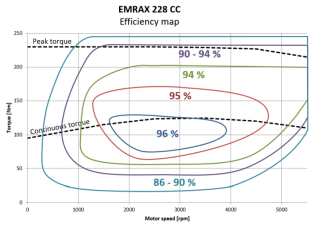

(f) Efficiency map of the Emrax 228

Figure 7.3: Electric motor specifications

7.2.3. Analysis-Number of Blades

The effect of increasing the number of blades on both the power required and the thrust is presented in this subsection. Adding blades increases the production cost and could increase the weight of the vehicle. The gain in required power and torque should therefore be analysed. The analysis is performed in JavaProp where thrust and axial velocity is kept constant while changing the number of blades. In Figure 7.4 the effect of an increase in the number of blades is presented. The best option for the number of blades for both the required torque and the required power is 3 blades. However, the decrease in required power is merely 1.7%, recognizing that adding a blade increases the weight and also increases the production costs and materials used. It is decided that a rotor with 2 blades is the best option.

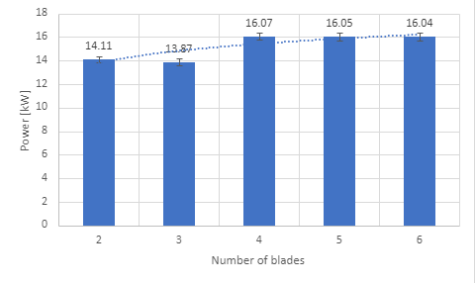

(a) Required power against number of blades for constant thrust

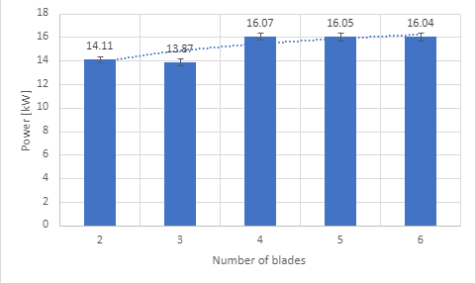

(b) Required torque against number of blades for constant thrust

Figure 7.4: Sensitivity analysis of number of blades change on required power and torque

7.2.4. Analysis: Rotor Area

An important factor of efficiency for rotorcraft is hover efficiency. This hover efficiency is correlated with disc loading. The lower the disc loading, the higher the hover efficiency as seen in Figure 7.5. Therefore increasing the rotor area as much as possible while staying within constraints is desired. As the number of rotors is fixed, decreasing the disc loading results in increasing the rotor area and thus also increasing the rotor diameter. The required torque and additionally tip speed increase. The torque is limited by the performance of the electric motors, and the tip speed is limited by the sound level. When the tip speeds get too high, the sound level can in turn also get too high. Compactness is also a constraint on increasing the disc area. The vehicle needs to land in urban areas where platform surface areas can be limited. By increasing the disc area too much, the vehicle can become too large. As the RPM and the rotor diameter determine the constraints, they should be analysed to stay within the boundaries.

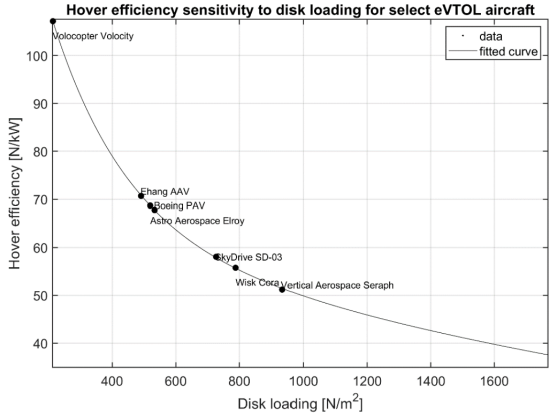

Figure 7.5: Hover efficiency and disc loading [36]

7.2.5. Analysis: Angular velocity

The vehicle needs to provide differential thrust through variable angular velocity, therefore being an important parameter to analyse. Also, the angular velocity is an important factor in electric motor

efficiency. Rotors designed for lower angular velocity require higher torque and wider propellers but could require less power. This analysis is performed in this subsection through JavaProp by changing the angular velocity while keeping thrust, rotor diameter and axial velocity constant.

Figure 7.6 shows the correlation between the angular velocity, power and torque. Increasing the angular velocity shows higher required power but a lower required torque. A lower angular velocity is more beneficial in terms of power but requires higher torque. The available torque and power depend on the electric motor as seen in Figure 7.3. The maximum continuous torque is almost constant for the entire RPM range of the electric motor but the maximum continuous power of the electric motor is dependent on the RPM. The available power of the electric motor increases linearly with the RPM. This fact should be taken into account when designing the propeller.

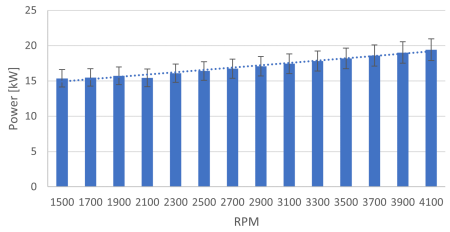

(a) Required power against RPM for constant thrust

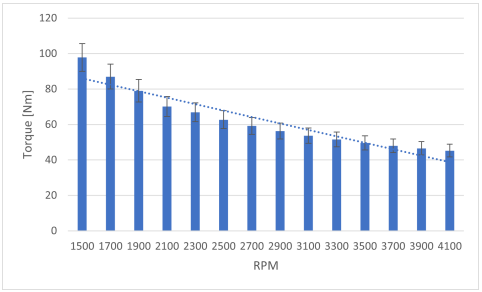

(b) Required torque against RPM for constant thrust

Figure 7.6: Sensitivity analysis of RPM change on required power and torque

7.3. Constraints

This section will consider possible constrains on the propulsion design. Firstly, constrains introduced by tip speeds are elaborated. Secondly, constrains by available torque and power are discussed.

7.3.1. Tip Speed

As seen in subsection 7.2.4, increasing the rotor area is beneficial for hover efficiency. However, by increasing the rotor area, the tip increases speed as well. The tip speed has to remain transonic $M < 0.8$ as otherwise noise levels become too large and compressibility effects have to be taken into account. As seen in Figure 7.7 the tip speed only exceeds the speed of sound at high diameters and high RPM. The actual decibel levels for the rotors need to be computed to check if noise requirements are met.

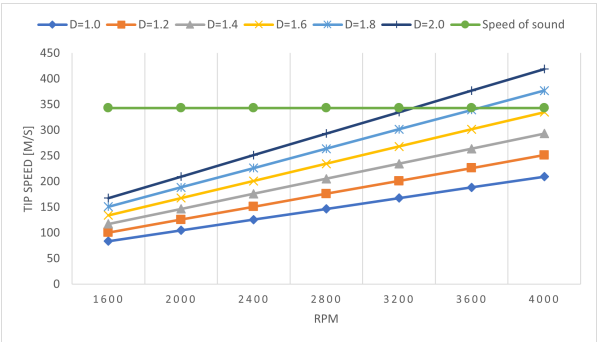

Figure 7.7: Tip speed of rotors for different area and RPM

Furthermore, a minimum tip speed is also defined to avoid retreating blade stall, see Figure 6.13. Therefore when sizing the rotors it should always be confirmed that the design tip speeds fall inside the allowable range.

7.3.2. Maximum Continuous Power and Torque

It can be seen in Figure 7.3 that all electric motors operate at almost constant torque and at linearly increasing power. The torque and power requirements of the propeller have to stay within the limits of the electric motor. These constraints are included in the multidisciplinary optimisation of the following chapter.

The required torque is computed via the following equation:

$$Q_{req} = \frac{60 \cdot P_{req}}{2\pi \cdot RPM} \tag{7.1}$$

7.4. Power required

In general, the total power the vehicle has to deliver can be divided into four components: [37]

$$P = \kappa P_i + P_p + P_o + Py \tag{7.2}$$

P_i is the induced power or the power to overcome the lift, P_p is the parasitic power or the power to overcome the drag. P_y and P_o are the powers needed for climb and overcoming profile drag respectively. The following sections assume inviscid flow and will explain the determination of the first three components to the right of Equation 7.2 for the different flight phases. Viscous forces are taken into account using the induced power factor κ. κ, which is often taken as 1.15 [37], encompasses non-ideal physical effects such as: nonuniform inflow, tip losses and wake swirl. In the following subsections, the power and thrust requirements will be written in terms of rotor radius R and angular velocity rpm, which will later be determined when sizing the propulsive system.

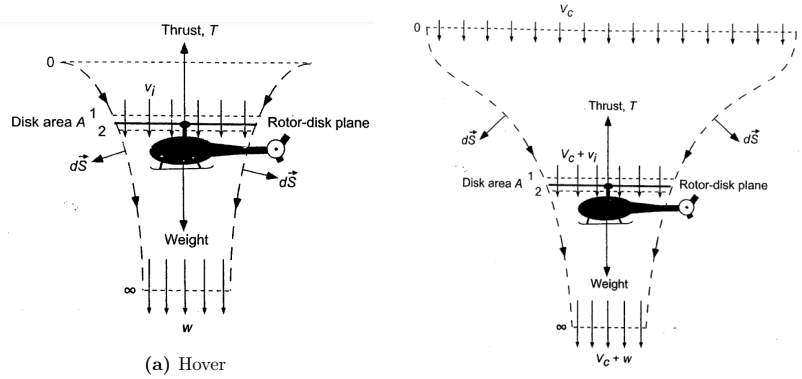

(a) Hover

(b) Axial climb

Figure 7.8: Flow model for momentum theory analysis

Induced and propulsive power

For a first-order derivation of the thrust and induced power of the vehicle momentum theory can be used. The theory makes the assumption that the flow is one-dimensional, quasi-steady, incompressible and inviscid. Under those assumptions, a control volume can be defined around the vehicle for the multiple flight phases as can be seen in Figure 7.8 and Figure 7.9. By then applying the conservation of mass, momentum and energy predictions can be made for the vehicle's performance. The induced power is defined for three distinct flight scenarios: hover, axial climb and descent and cruise.

Hover: The model used for hover is shown in Figure 7.8a. The thrust and power are respectively the force and energy needed to accelerate the flow from the induced velocity v_i to the wake velocity w.. Through momentum analysis, it can be shown that under the assumptions taken they equal:

$$T_h \equiv W = 2\rho A v_i^2 \tag{7.3}$$

$$P_h = T v_i = 2\rho A v_i^3 \tag{7.4}$$

where ρ is the density and A is the rotor area. What is also apparent from Figure 7.8a is that the inflow velocity for hover v_h equals the induced velocity. By rewriting equation Equation 7.3, v_h can

thus be found (Equation 7.5). Here the total area is found by multiplying the single rotor area πR^2 with the number of rotors n_r The inflow velocity can be non-dimensionalised by dividing by the tip speed $V_t = \Omega * R$, which is the radial velocity of the propeller times its radius. For hover this is shown in Equation 7.6.

$$v_h \equiv v_i = \sqrt{\left(\frac{W}{n_r \pi R^2}\right)\frac{1}{2\rho}} \tag{7.5}$$

$$\lambda h = \frac{v_h}{\Omega R} \tag{7.6}$$

Finally the non-dimensional thrust coefficient is defined as seen in Equation 7.7 and can be related to the inflow ratio by Equation 7.8.

$$C_T = \frac{T}{\rho A \Omega^2 R^2} \tag{7.7}$$

$$\lambda_h \equiv \lambda_i = \sqrt{\frac{C_T}{2}} \tag{7.8}$$

Axial climb and descent: For climbing flight the model in Figure 7.8b is used. Due to the extra climb velocity V_c the inflow velocity of the rotor does not equal the induced velocity anymore. The thrust needed for climbing flight is given in Equation 7.9, here the induced velocity for climb can be related to the hover induced velocity by Equation 7.10.

$$T = 2\rho A(V_c + v_i)v_i \tag{7.9}$$

$$\frac{v_i}{v_h} = -\left(\frac{V_c}{2v_h}\right)\sqrt{\left(\frac{V_c}{V_h}\right)^2 + 1} \tag{7.10}$$

$$\frac{P}{P_h} = \frac{V_c + V_i}{V_i} = \frac{V_c}{V_h} + \sqrt{\left(\frac{V_c}{V_h}\right)^2 - 1} \tag{7.11}$$

A similar approach is used for hover, however the model diverges for $\frac{V_d}{v_h} < 2$ therefore a model is used based on statistical data [37].

$$\frac{v_i}{v_h} = 0.974 - 1.125\frac{V_D}{v_h} - 1.372\left(\frac{V_D}{v_h}\right)^2 - 1.718\left(\frac{V_D}{v_h}\right)^3 - 0.655\left(\frac{V_D}{v_h}\right)^4 \tag{7.12}$$

$$\frac{P}{P_h} = 0.974 - 0.125\frac{V_D}{v_h} - 1.372\left(\frac{V_D}{v_h}\right)^2 - 1.718\left(\frac{V_D}{v_h}\right)^3 - 0.655\left(\frac{V_D}{v_h}\right)^4 \tag{7.13}$$

Forward flight: For forward flight the flow model as depicted in Figure 7.9 is used.

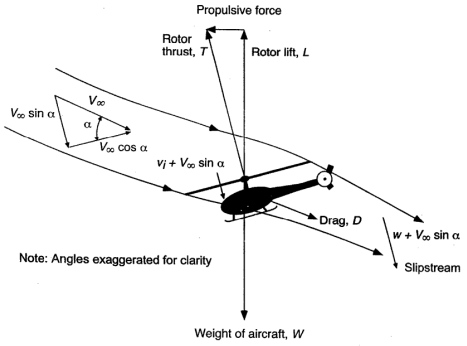

Figure 7.9: Flow model for momentum theory analysis of forward flight

From this model it follows that the thrust is given as:

$$T = 2\rho A v_i \sqrt{V_\infty^2 + 2V_\infty v_i \sin\alpha + v_i^2} \tag{7.14}$$

Here the induced velocity is harder to find directly, but can be found with the inflow ratio. The inflow ratio for cruise is defined in Equation 7.15

$$\lambda = \frac{V_\infty \sin\alpha}{\Omega R} + \frac{v_i}{\Omega R} = \mu \tan\alpha + \lambda_i \tag{7.15}$$

Here μ is the advance ratio (see Equation 7.17), furthermore the inflow ratio can be found by Equation 7.16.

$$\lambda = \mu \tan\alpha + \frac{C_T}{2\sqrt{\mu^2 + \lambda^2}} \tag{7.16}$$

$$\mu = \frac{V_\infty cos\alpha}{\Omega R} \tag{7.17}$$

As the inflow ratio is present at both sides of the equation it needs to be find iteratively. This iterative process is describes by Equation 7.19. In the following calculations the iteration will stop if $\epsilon < 0.0005$.

$$\lambda_{n+1} = \mu \tan\alpha + \frac{C_T}{2\sqrt{\mu^2 + \lambda_n^2}} \tag{7.18}$$

$$\epsilon = \left\| \frac{\lambda_{n+1} - \lambda_n}{\lambda_{n+1}} \right\| \tag{7.19}$$

Finally, for forward flight the power is defined by Equation 7.20, the ratio with hover power is then given by Equation 7.21. Thus the power required for forward flight depends solely on the inflow ratio compared to hover. In Equation 7.16 the first term after the equal sign dictates the power to propel the vehicle forward, while the latter term influences the power to generate the lift. In hover, the second term is dominant, which reduces when increasing the forward velocity from hover reaching a minimum afterwards the first term becomes dominant and the ratio increases again.

$$P = T(V_\infty sin\alpha + v_i) \tag{7.20}$$

$$\frac{P}{P_h} = \frac{\lambda}{\lambda_h} \tag{7.21}$$

To solve the equations for forward flight listed above a knowledge of the rotor angle of attack of the vehicle is required. This angle of attack is found by solving for static equilibrium (see Figure 7.9). For straight and level flight α is given as:

$$tan\alpha = \frac{D}{W} \tag{7.22}$$

The drag for cruise is known from chapter 6. However, the drag has to be known for a given free stream velocity V_∞ not only for cruise speed. . As the reference area of the vehicle S_{ref} is not known C_{d_0} can not be found for the vehicle. Therefore, an equivalent wetted area f is used which is defined by Equation 7.23[37]. The drag can then easily be calculated for a given free stream velocity V_∞ [37] with Equation 7.24.

$$f = C_{D_0} S_{ref} = \frac{D_c}{\frac{1}{2} * \rho V^2} \tag{7.23}$$

$$D = f \frac{1}{2} \rho V^2 \tag{7.24}$$

Parasitic power
With the drag known the parasitic power needed for a given flight velocity is easily found:

$$P_p = D V_\infty \tag{7.25}$$

Profile power
Lastly the power to overcome the profile drag of the rotor blades needs to be accounted for, given by Equation 7.26[37]. The power coefficient for hover is influenced by the profile drag coefficient of the blade C_{d_0} and the rotor solidity σ, which is the area of the blades divided by the rotor area. For forward flight, the profile power changes with the square of the advance ratio μ multiplied with constant K. This model assumes a value of $K = 4.65$, which is an average often used in literature [37]. It must be noted that this equation is only valid for advance ratios $\mu < 0.5$, as for higher advance ratios radial and reverse flow plus compressibility effects will play a role. For the flight speeds considered however, the advance ratio does not come close to this value and thus Equation 7.26 remains valid.

$$P_o = C_{P_0}\pi\rho\Omega^3 R^5 = \left(\frac{\sigma C_{d_0}}{8}(1 + K_{prof}\mu^2\right)\pi\rho\Omega^3 R^5 \tag{7.26}$$

7.5. Propulsion System Sizing

With the model described in section 7.4 the required power for a given flight condition can be found for variable rotor angular velocity Ω and radius R_r. Furthermore, the motor power available for the three electric motors described in subsection 7.2.2 is also known for a given Ω. The inputs to the model are summarised in Table 7.1. The values for the induced power factor κ, profile drag coefficient C_{d_0}, solidity σ and profile power constant K_{prof} were taken based on average values often used in literature [37].

Table 7.1: Input parameters power estimation

Parameter	**Symbol**	**Value**
Maximum take-off weight (kg)	MTOW	1159
Drag at cruise (N)	D_c	688
Number of rotors	N_r	12
Induced power factor	κ	1.15
Profile drag coefficient	C_{d_0}	0.0085
Solidity	σ	0.1
Profile power constant	K_{prof}	4.65

The rotors are designed such that they pass three flight scenarios: hover, cruise and maximum thrust. For each of these scenarios, the available power of the motor needs to equal the required power for a given rotor radius and angular velocity. For the hover and cruise scenarios, the available power is based on the continuous torque the motors can deliver (see subsection 7.2.2). For maximum thrust, the power required is held up against the engine power available at maximum torque. As has been explained in subsection 7.3.1 there are constraints set for the minimum and maximum tip speed of the rotors. A minimum tip speed is defined to avoid blade stall, while the maximum prevents the blades from going transonic ($M > 0.8$). Tip speed is defined as $V_t = R_r\Omega$, Table 7.2 gives the range of allowed rotor angular velocity for several rotor radii considered.

Table 7.2: Allowable rotor angular velocity ω for various rotor radii R_r

R_r	Min. Ω (rpm)	Max. Ω (rpm)
0.7	2959	3701
0.8	2422	3238
0.9	2029	2878
1.0	1733	2590
1.1	1502	2355

Finally, for the sizing, the combination of motor and rotor radius was chosen that minimises Ω, while passing the power requirements of all flight scenarios. Ω is minimised as this results in less power required and reduces tip speed which is beneficial for noise, see section 6.7. Furthermore, regarding engines, the lightest motor is chosen that passes all aforementioned requirements. Figure 7.10 - Figure 7.12 present

the design point selection (left) and the power breakdown for the flight scenario flying at the design point Ω.

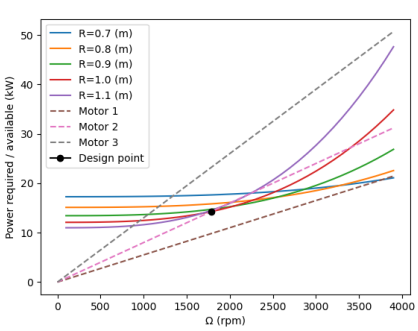

(a) Design point

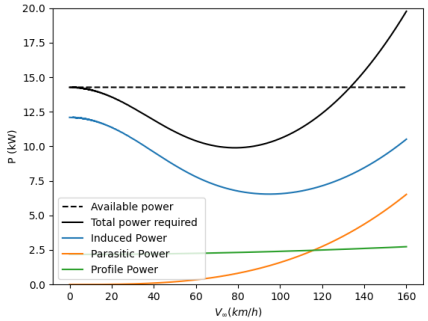

(b) Breakdown required power when flying at design point settings

Figure 7.10: Hover scenario

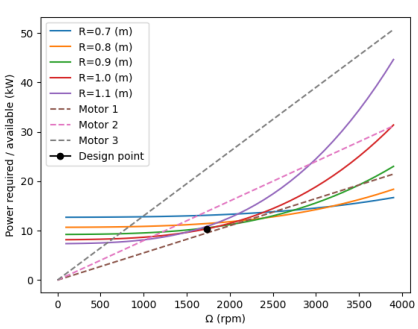

(a) Design point

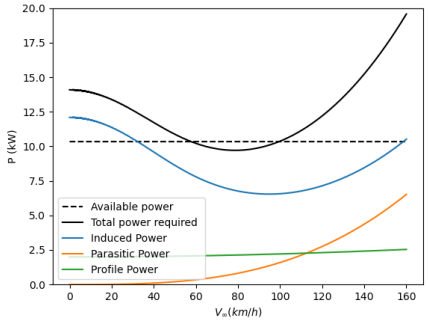

(b) Breakdown required power when flying at design point settings

Figure 7.11: Cruise scenario

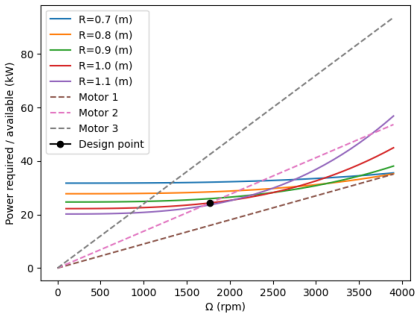

(a) Design point

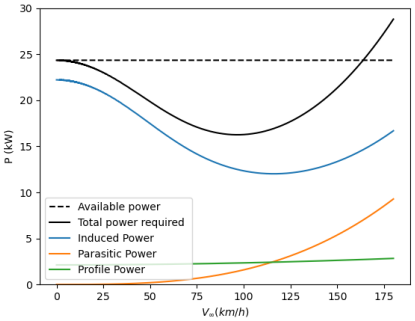

(b) Breakdown required power when flying at design point settings

Figure 7.12: Maximum thrust scenario

From figures Figure 7.10 - Figure 7.12 it was decided that the final engine chosen is the Emrax 208 in combination with a rotor radius $R_r = 1.0m$. Table 7.3 summarises the engine settings for the three design scenarios considered. Table 8.1 gives the propulsion performance when flying with maximum angular velocity with continuous and peak torque.

Table 7.3: Propulsion system parameters for hover, max. thrust and cruise

Scenario	$T_r(N)$	$P_r = P_a(kW)$	$R_r(m)$	$\Omega(rpm)$	$Q_r(Nm)$
hover	946	14.3	1.0	1 784	75.6
max. thrust	1 421	24.3	1.0	1 770	131
cruise	946	10.3	1.0	1 733	56.8

To give an estimate of the efficiency of the rotor, an efficiency factor called the figure of merit (FM) can be used. The figure of merit determines the efficiency of a rotor in hover and is defined as the ideal power required to hover divided by the actual power required to hover and is therefore always smaller than 1 . The figure of merit together with all propulsion system parameters are presented in Table 7.4.

$$FM = \frac{P_{ideal}}{P_{actual}} = \frac{P_i}{\kappa P_i + P_o} \tag{7.27}$$

Table 7.4: Propulsion system parameters

Parameter	**Value**
Rotor radius (m)	1.0
Rotor area (m^2)	3.14
Thrust coefficient (-)	0.0073
Angular velocity range (rpm)	1733-2590
Continuous torque (Nm)	75.6
Peak torque (Nm)	131
Continuous power available (kW)	20.7
Peak power available (kW)	35.6
Disk loading (N/m^2)	301
Figure of merit (-)	0.713

7.6. Blade Design

Now that the rotor diameter, number of blades and the required thrust is known, a blade design can be made. For the blade design an airfoil is assumed and a simple geometry. With this, the volume and the mass moment of inertia (MMOI) are calculated. With the highest load conditions, the highest shear and normal stresses are computed. With these stresses, a material is chosen and the weight per blade is found.

The chosen airfoil is a Clark Y airfoil with a L/D of 29.2. For both the area computation and the calculation of the MMOI a rectangle is assumed. The dimensions of the rectangle are depicted in Figure 7.13a. For the area, the difference with the actual area is expected to be negligible. For the MMOI calculation, the MMOI around y is expected to be overestimated. However, a factor of 1.5 in the stresses is included as a margin, this will account for this overestimation. Also, the MMOI around x is expected to be underestimated. The stresses created by the bending moment around x however are small and the MMOI around x is big. So these are not expected to be critical in material selection.

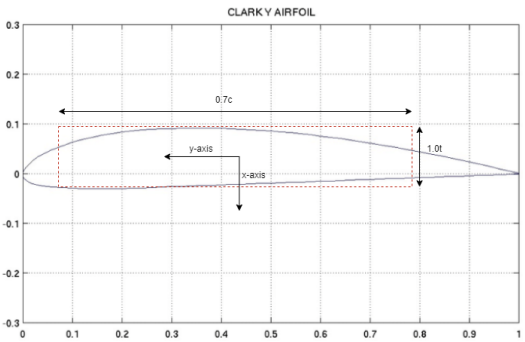

(a) Clark Y airfoil

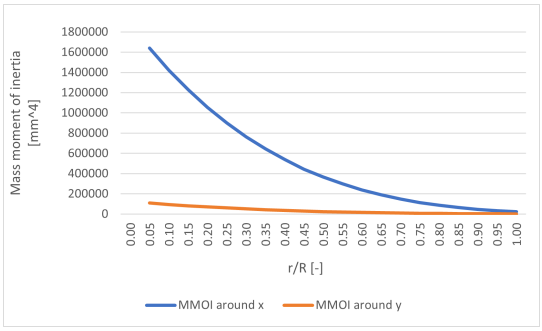

(b) MMOI around x-axis and y-axis

Figure 7.13: Blade area and MMOI

The MMOI of the airfoil across the radius of the blade is presented in Figure 7.13b. With JavaProp the highest load conditions are analysed. The highest provided thrust per engine is $1500\,N$ with an angular velocity of approximately 3400 RPM. JavaProp computes the moment coefficient and the shear coefficients. The bending moment and shear are then calculated with the following equations below. Then, the highest normal and highest shear stresses are computed along the blade. The coefficients, shear, bending moment and stresses are presented in Figure 7.14

$$Q_{(x,y)} = C_{Q,(x,y)} \cdot \rho \cdot n^2 \cdot D^4 \qquad (7.28)$$

$$M_{(x,y)} = C_{M,(x,y)} \cdot \rho \cdot n^2 \cdot D^5 \qquad (7.29)$$

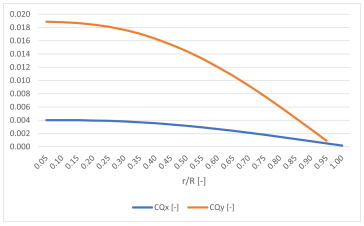

(a) Shear coefficients along blade

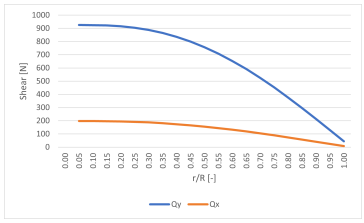

(b) Shear along blade

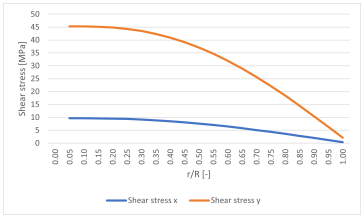

(c) Shear stresses along blade

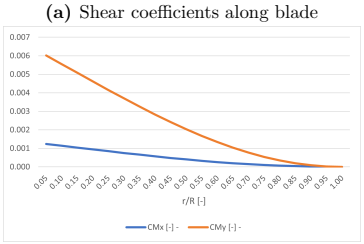

(d) Bending moment coefficients along blade

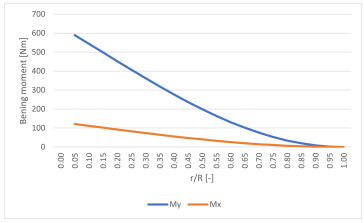

(e) Bending moment along blade

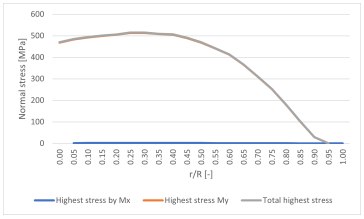

(f) Normal stresses along blade

Figure 7.14: Forces along blade during highest thrust loading

The highest shear stress with a factor of 1.5 is $45\,MPa$ and the highest normal stress with a factor of 1.5 is $515\,MPa$. Carbon fibre with vitrimer can withstand both these loads. As Carbon fibre with vitrimer is lightweight and sustainable as stated in section 10.1, Carbon fibre with vitrimer is chosen as the designated material for the blades. The weight of the blades is calculated through computing the volume of the blades. This volume is estimated by summing up the volume of all blade elements. The blade is divided into 20 blade elements and the volume is then calculated by multiplying the length of the blade element with the area in the middle of the blade element. The density of Carbon fibre with vitrimer is $1494\,[kg/m^3]$ what makes the weight of single blade $1.68\,[k]g$. The total weight of all rotors is then $40.2\,[kg]$.

7.7. Sensitivity Analysis on Motor Sizing

A sensitivity analysis is performed on some of the more critical input parameters used for the motor sizing (Table 7.1). For these parameters, it was checked if the propulsion system was able to pass the power requirement for hover, as it was found that hover was critical for propulsion sizing. The available motor power was based on the maximum power available for continuous torque (Table 7.4).

Table 7.5: Input parameters sensitivity analysis

Parameter	Symbol	Value
Maximum take-off weight (kg)	MTOW	**869-1449**
Drag at cruise (N)	D_c	**344 - 1032**
Number of rotors	N_r	12
Air density	ρ	**1.173-1.225**
Induced power factor	κ	**1.0 - 1.3**
Profile drag coefficient	C_{d_0}	0.0085
Solidity	σ	0.1
Profile power constant	K_{prof}	4.65
Rotor radius	R_r	1.0
Rotor angular velocity	Ω	2590
Continuous power available (kW)	P_a	20.7
Engine	-	Emrax208

The first input to be analysed is the drag at cruise, which was determined by an aerodynamic analysis performed in chapter 6. A sensitivity analysis was done on drag as for the estimation there is quite a large uncertainty, which could not be mitigated by testing in a wind tunnel. It is furthermore interesting to analyse the power reduction from optimising the vehicle for drag. A range of $\pm 50\%$ was taken, the result is presented in Figure 7.15a. As can be seen in the figure, the drag only begins to have a noticeable effect for $V_\infty > 60\,(km/h)$. The available power is still enough to pass the hover power requirement as at $V_\infty = 0$ drag plays no role. For higher free stream velocities the effect of the drag on the vehicle's performance is noticeable, however.

The second parameter to analyse is the air density. Using the international standard atmosphere (ISA) it was found that at cruise altitude $h = 450\,m$ the air density is $\rho = 1.173\,\frac{kg}{m^3}$. The result of the analysis is shown in Figure 7.15b. Again the power available is enough for hovered flight. As the density increases by a relatively small amount, the power required does not change significantly as well. As the effect is so small, from now on all calculations assume sea-level conditions.

The third parameter that is checked is the induced power factor κ, which takes into account all non-ideal physical phenomena increasing the induced power required to meet the various flight phase requirements. The sensitivity analysis encompasses a range from $\kappa = 1$ meaning ideal efficiency to $\kappa = 1.3$ or bad rotor efficiency. As can be seen in Figure 7.15c, the choice of κ has a significant effect on the overall power required but has the most influence at hover $V_\infty = 0$. For the most ideal scenario $\kappa = 1$, the required power at hover reduces to $P_r = 17.1\,kW$, this is not enough of a decrease to change engines. For the worst-case scenario $\kappa = 1.3$ a switch of the engine is not needed as well. The rotor radius has to be reduced to R_r, however, decreasing the efficiency of the propulsion system.

Finally, an analysis is done on a change in the maximum take-off mass (MTOM) of the vehicle. As the vehicle's mass is expected to change during iterations, it is important to analyse the effect of a change in vehicle mass. As expected, it can be concluded from Figure 7.15d that the weight has a significant effect on the required power. The contribution of the weight on the required power reduces, however, with increasing free stream velocity V_∞ as the dominating power component becomes the parasitic power. When looking at the effect on the design of the propulsion system the 'snowball' effect of weight reduction/increase is immediately noticeable. A weight reduction of 25% leads to power required that has decreased enough to choose the lighter Emrax 188 engine (motor 1), using rotors with a smaller radius $R_r = 0.9m$. A 25% increase in weight would require a switch to the heavier Emrax 228 and would require larger rotors $R_r = 1.0m$ resulting in a significantly increased vehicle weight.

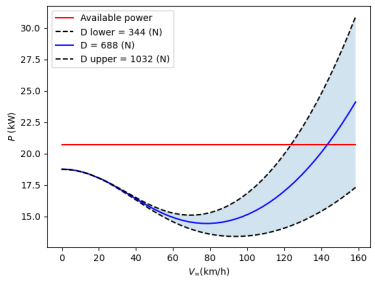

(a) Power required versus free stream velocity for varying vehicle drag.

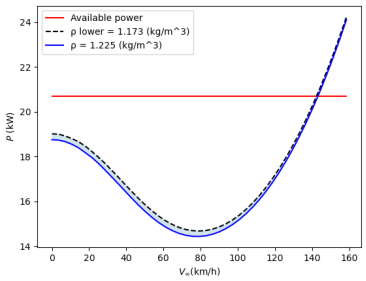

(b) Power required versus free stream velocity for varying air density.

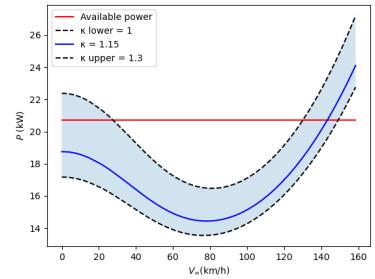

(c) Power required versus free stream velocity for varying induced power factor.

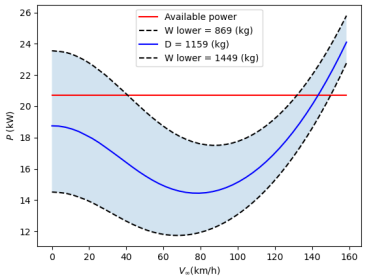

(d) Power required versus free stream velocity for varying vehicle weight.

Figure 7.15: Sensitivity analysis on model for required power

The changes in design point resulting from the aforementioned parameter changes is summarised in the table below.

Change	Motor (-)	Rotor Radius (m)
D_c -50%	2	0.8
D_c + 50%	2	0.8
ρ -	2	0.8
κ - 0.15	2	1.0
κ + 0.15	2	0.9
W - 25%	1	0.9
W + 25%	3	1.0

7.8. Propulsion Verification & Validation

The model to calculate the power required is verified in multiple ways. Each different module making up the final model is unit tested by comparing the outputs of the modules by calculations done by hand. It was furthermore checked that different models give equal outputs for equal flight cases. The outputs of the models for forward flight and axial climb and descent should for example give the hover power required when having as inputs $V_\infty = 0$ and $V_c = 0$ respectively. Finally visual inspection was used to check if the model give reasonable plots as output to variations in input. An example of such visual inspection is the sensitivity analysis performed in section 7.7.

In Table 7.4 the final design parameters of the rotor are shown. The rotors have a disk loading during hover of 301 $[N/m^2]$ and a figure of merit of 0.713. These parameters can be used to validate the results. The hover efficiency is the amount of thrust over power during hover [N/kW]. The hover efficiency of the BonMobile is 66 $[N/kW]$. Figure 7.16 shows the hover efficiency against the disk loading of multiple propellers. Note the different units. The hover efficiency of the BonMobile is 6.744 $[g/W]$ and the disk loading is 30.68 $[kg/m^2]$. These numbers almost exactly coincide with the data on propeller data. Therefore, the rotor design is assumed valid.

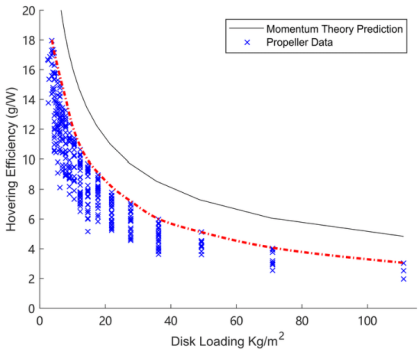

Figure 7.16: Hover efficiency and disk loading of propellers[38]

For the blade design 2 possible solutions were presented to validate the values presented in Figure 7.14[33]. The first is that the following 2 conditions need to hold. Firstly that the thrust coefficient divided by the amount of blades equals the shear coefficient at the root. Secondly, that the center of thrust lies within 60%-70% of the root.

$$Q_y = \frac{C_T}{n_{blades}} \tag{7.30}$$

$$\left(\frac{r}{R}\right)_{Centerofthrust} = 2 \cdot \frac{C_{M_{y-root}}}{C_{Q_{y-root}}} \tag{7.31}$$

Both conditions hold so the calculations on the blade design are assumed valid.

7.9. Recommendations

In this section further steps to detail the design are recommended. Subjects that have to be studied further or estimations that have to be performed more profound.

7.9.1. Sustainable Electric Motors

For the propulsion design the Emrax motors presented in Figure 7.2 are used. These motors are chosen without sustainability in mind. As sustainability is an important requirement the sustainability of these electric motors needs to be explored further. Materials often used in electric motors are rare-earth metals like copper and iron. There are electric motors that do not use rare-earth metals [1]. For a 100 % sustainable UAM-vehicle these electric motors have to be explored in more detail. Another option that can be explored are Carbon Electric motors. These motors also do not use rare-earth materials and could have a higher power-to-weight ratio than conventional electric motors.[39]. Another possibility is further looking into the recycleability of conventional electric motors.

7.9.2. Blade Design

For the blade design a more profound design is recommended. The MMOI of the blade is currently estimated with a rectangle and can be estimated more accurately, the same is true for the area calculation of the airfoil. Additionally, for the design an arbitrary taper and airfoil is selected for the design. To design a more efficient rotor blade a more thorough method should be used. Blade element theory is a method that could improve the design. This method was shortly considered for this project but was set aside due to the time scope of this DSE. A deeper investigation into material selection for the blade is also recommended.

[1] https://www.electrichybridvehicletechnology.com/news/motor-technology/uk-company-creates-worlds-most-sustainable-electric-vehicle-motors.html

8 Performance

After having analysed the aerodynamic performance of the vehicle in chapter 6, and sized the propulsion system and battery in chapter 7 the flight performance of BonMobile can be analysed. This chapter presents a detailed examination of the performance of the vehicle by determining the design speeds for optimal power usage in section 8.1 and BonMobile's climb performance in section 8.2. The chapter then concludes with an updated energy estimation in section 8.3.

8.1. Design Speeds

To begin the performance analysis of the vehicle, first, the power required in terms of free stream velocity V_∞ is examined again. The total power can be broken down into four components, as shown in Equation 8.1. We distinguish the power to provide the thrust of the vehicle (the *induced power* P_i), the power to overcome the drag (*parasitic power* P_p), the power to overcome the rotor blade's profile drag (*profile power* P_o) and finally the power to climb (P_y).

$$P = P_i + P_p + P_y + P_o \tag{8.1}$$

The power estimations in this section and section 8.2 assume a power available P_a equal to the electric motors available power at hover settings and maximum continuous torque. The corresponding parameters for the propulsion system are given in Table 8.1. It must be noted that during real life operations, the angular velocity will be adjusted for the free stream velocity V_∞ so that $P_a = P_r$ and the vehicle flies most efficiently. For sake of comparison, however, the angular velocity is held constant resulting in a constant available power.

Table 8.1: Propulsion system parameters design speed analysis

Parameter	**Value**
Rotor radius (m)	1.0
Angular velocity (rpm)	1784
Continuous torque (Nm)	75.6
Continuous power available (kW)	14.27

The main contributor at low V_∞ is P_i, while at higher V_∞, P_p becomes dominant. The decrease of the induced power when increasing V_∞ has as effect that the minimum total power required is reached. The speed at which this minimum power is obtained is furthermore the speed for maximum endurance. The endurance for a given amount of energy E is easily calculated by Equation 8.2. To maximise the endurance of the vehicle, therefore, straightforwardly P should be minimised. The minimum power required and its corresponding V_∞ is indicated by the vertical blue line in Figure 8.1.

$$t = \frac{E}{P} \tag{8.2}$$

$$d = tV_\infty = E\left(\frac{V_\infty}{P}\right) \tag{8.3}$$

The speed and power for the maximum range are then also easily obtained by Equation 8.3. From the equation it can be seen that the speed is obtained when the ratio $\left(\frac{P}{V_\infty}\right)$ is minimum. Graphically, this can be visualised with a line through the origin tangent to the total power required. In Figure 8.1

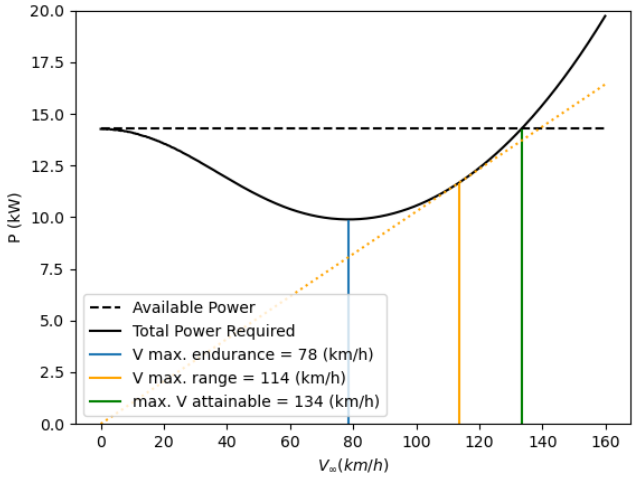

Figure 8.1: Determination of design speeds

this is the orange dotted line, with the vertical orange line showing the speed and power for maximum range.

The last design speed that can be obtained from Figure 8.1, is the maximum cruise speed obtainable. This speed is found at the point where the total available power equals the total power required $P_a = P_r$. At higher speeds than V_{max}, the power available will be less than the power required, making the vehicle unable to fly.

8.2. Climb Performance

Climb performance is primarily based on the amount of excess power available. Thus for analysing climb performance, the vehicle is analysed at maximum motor speed (or angular velocity Ω) at maximum continuous torque so as maximise the excess power. The motor settings are summarised in Table 8.2 and corresponding powers are shown in Figure 8.2.

Table 8.2: Propulsion system parameters climb performance analysis

Parameter	Value
Rotor radius (m)	1.0
Angular velocity (rpm)	2590
Continuous torque (Nm)	75.6
Continuous power available (kW)	20.7

In Figure 8.2 the excess power can be seen as the red area between the horizontal available power P_a line and the total power required P_r curve. Assuming that for the rates of climb considered, the components making up the power required for level flight (Equation 8.1) remain constant. The climb velocity can then be found by dividing the excess power by the thrust (see Equation 8.4). Here D_y is the drag in the vertical direction, similar to the approach for forward flight the drag for a given climb velocity V_c is calculated with an equivalent wetted area f.

$$V_c = \frac{P_a - P_{level}}{T} = \frac{P_a - P_{level}}{W + D_y} = \frac{P_a - P_{level}}{W + \frac{1}{2}\rho f_y V_c^2} \tag{8.4}$$

As V_c is present in both sides of Equation 8.4 an iterative process is used to solve for V_c. Here $V_{c_0} = \frac{P_a - P_{level}}{W}$ and $\epsilon < 0.0005$.

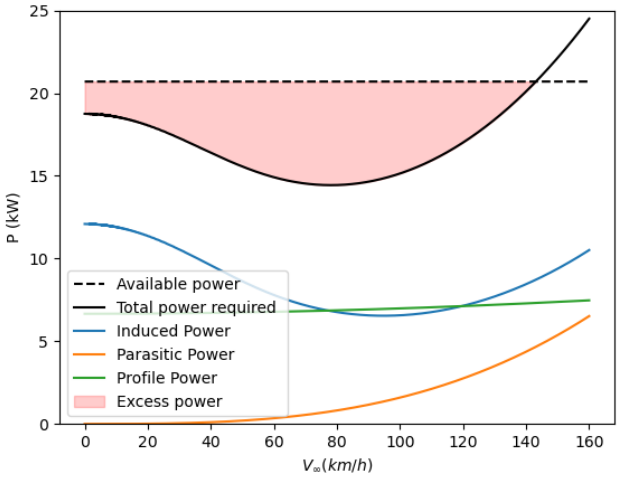

Figure 8.2: Power against flight speed when flying at maximum angular velocity

$$V_{c_{n+1}} = \frac{P_a - P_{level}}{W + \frac{1}{2}\rho f_y V_{c_n}^2} \tag{8.5}$$

$$\epsilon = \left\| \frac{V_{c_{n+1}} - V_{c_n}}{V_{c_{n+1}}} \right\| \tag{8.6}$$

To visualise the effect of the vertical drag, the climb performance is plotted with the inclusion of drag and for the assumption that drag is zero in Figure 8.3. As can be seen from the figure including the drag leads to an insignificant decrease in climb velocity ($< 1\%$). Henceforth, in the following calculations the vertical drag is neglected and the maximum climb speed can simply be found by Equation 8.7.

$$V_c = \frac{P_a - P_{level}}{W} \tag{8.7}$$

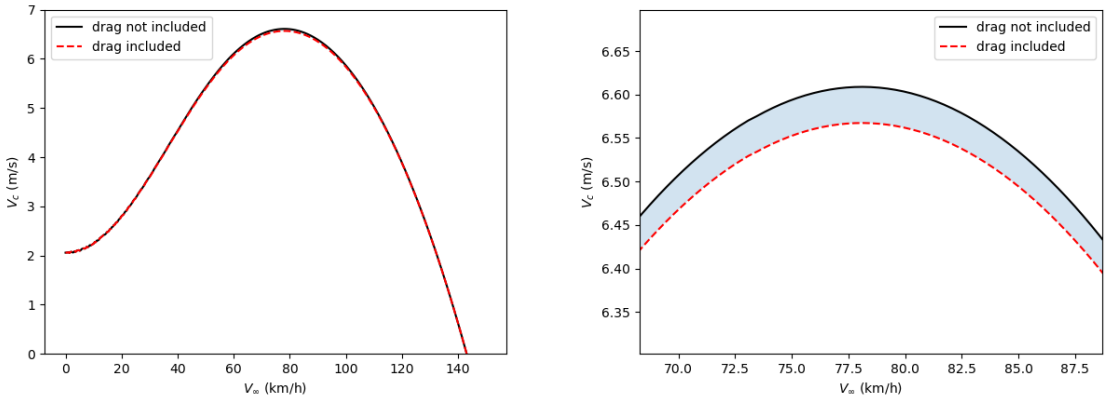

Figure 8.3: Maximum rate of climb as function of airspeed drag included versus not-included, right figure shows a zoomed-in view.

The climb performance of the vehicle is presented in Figure 8.4. The climb performance is furthermore analysed for changes in payload and power available. As the payload taken for a certain flight is extremely variable, it is important to analyse the effect on the vehicle's climb performance. Figure 8.4a presents this from maximum payload at maximum take-off weight (MTOW) to no payload at operating empty weight (OEW). Figure 8.4b. The climb performance is furthermore analysed for an increase in power available up to the absolute peak power the engine can deliver. This is interesting for cases where

the continuous power is not enough to fulfill the climb requirements and short periods of extra power are needed. An example of such a situation is climb at hover at maximum payload.

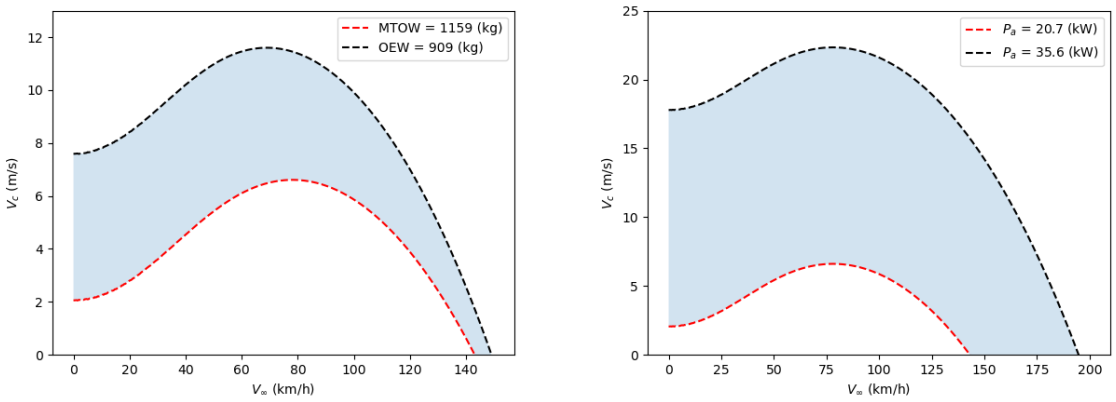

(a) Varying payload

(b) Varying maximum available power

Figure 8.4: Maximum rate of climb as function of airspeed

While the climb performance estimated by Equation 8.4 is a good estimation for small V_c, it can become inaccurate for larger climb velocities. Furthermore, an accurate estimation for axial descent is also needed for the final energy estimation. The power for axial climb and descent could be estimated by momentum theory section 7.4 and the results for various climb and descent rates are given in Figure 8.5.

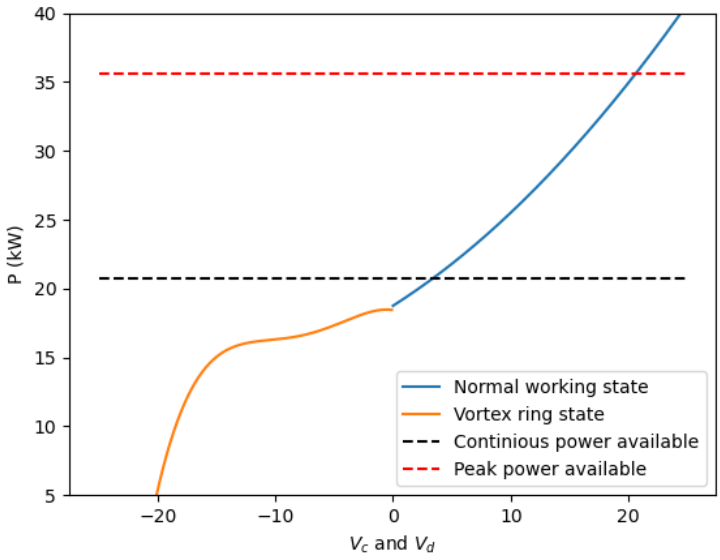

Figure 8.5: Power required for different axial climb and descent rates

8.3. Energy

Now that the design speeds are determined and the climb performance is analysed a new estimation for the total required energy for a flight mission can be made. The energy estimation is based on the mission profile presented in section 3.1. For each flight segment, the power is estimated based on the free stream and climb velocities. The total energy is then found by multiplying this power with the time it takes to complete the segment. The initial estimation is done per engine after which the total energy required E_{tot} is easily found by multiplying by the number of rotors. For this estimation

accelerations are not taken into account, furthermore, the time it takes to accelerate to a given free stream or climb velocity is also not taken into account. To accommodate this a rather conservative safety factor of $sf = 1.3$ is included. It is furthermore important to note that the extra energy required is independent of climb speed V_c. Since the vertical drag is neglected, the extra total energy required to climb is determined by the potential energy to overcome (see Equation 8.8). Therefore for forward flight, the total energy does not depend on climb speed. For axial flight and descent, however, extra hover time is added for lower climb/descent velocities, increasing the total energy. For forward climb the rate of climb is therefore determined from Equation 8.4. For axial climb and descent, the value for V_c is taken from the mission profile section 3.1.

$$\Delta E = t_c \Delta P = \frac{h}{V_c} V_c W = hW \tag{8.8}$$

As was known from Figure 7.13 a cruise speed of $V_\infty = 100\,m/s$ is not the most efficient speed to fly at. Rather the vehicle should fly at the speed for maximum range to minimise the energy usage for a mission. Figure 8.6 presents the total energy required for different cruise speeds.

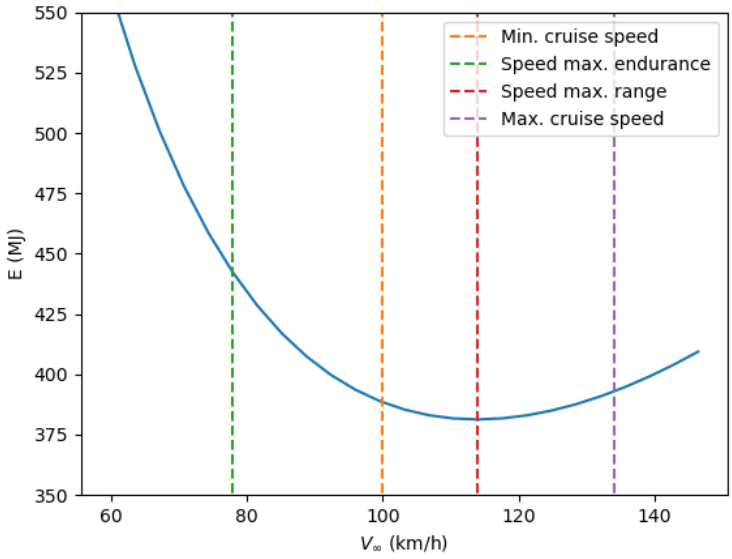

Figure 8.6: Total energy required for various freestream velocities

8.4. Performance Verification

Most of the performance analysis follows from the power estimations performed in section 7.4. The model performing the power estimations was verified as described in section 7.8. Sensitivity analyses were performed on the model for climb performance (Figure 8.3, Equation 8.4) which were checked to show reasonable results.

8.5. Recommendations on Performance

Figure 8.6 shows the opportunities in saving the energy used for a mission when flying at specified design velocities. For sustainable flight preventing the usage of energy is always preferred over solving the effect of energy by buying green energy. Looking from a flight performance perspective it would therefore quickly seem logical to set a new cruise speed at the speed for maximum range. Raising the cruise speed would effect all other subsystem however. Thus a recommendation is made to carefully analyse the effect of increasing the cruise speed for all subsystems to determine the opportunities in lowering the energy used.

9 Powertrain & Battery Sizing

In the Midterm Report of the design process, it was decided to go with a battery system to power the vehicle [5]. This section will perform the powertrain and battery design required for the vehicle. Section 9.1 presents the power budget for the vehicle, and section 9.2 will provide a choice for the battery type. Section 9.3 and 9.4 contain the battery sizing and configuration. The configuration of the electrical system is presented in section 9.5. Finally, a sensitivity analysis, verification and validation will be done in and section 9.6 and 9.7.

9.1. Power Budget

For proper battery sizing and configuration, a power budget is used to determine the maximum required power from the batteries. The power budget is based on a paper by Pranoto [40].

Table 9.1: Power Budget

Subsystem or part	**Peak Power [W]**
Internal and external lights	117
Avionics/Autopilot	252
On-board computer	205
Battery temperature control	370
Air-conditioning	3000
Vehicle temperature control & de-icing	1000
Contingency power	400
Propulsion subsystem	**Peak Power [kW]**
Engines (12 total)	68 (per engine)

From the power budget, it can be seen that the total peak power excluding the propulsion system is $5344\,W$. This is less than 1% of the total peak power of $821\,kW$. With the contingency power, the low percentage of total peak power and the agreement with the Electrical Power System lectures from A. Cervone [41], it can be assumed the power values from Table 9.1 are deemed valid for this design stage.

9.2. Battery Type

To determine the battery size and mass, a specific battery type must be chosen. The battery types from which will be chosen are presented in Table 9.3. Lead acid is added to this table not as a viable option, but as a reference for recycling. As they are well recyclable [42]. Furthermore, Tesla Model 3's Lithium Iron Phosphate battery [1] is also added as an option, because these are used for preliminary cost estimation in the Midterm Report [5]. Furthermore, Lithium-Sulfur, Metal-Air and Lithium-Air batteries are added due to their promising high gravimetric energy densities [43].

"The metal-air batteries are the batteries of the future."[44]. These types of batteries are still in their Research & Development stage, but show very high energy densities, good recyclability and make use of abundant and eco-friendly materials [42], [44], [43], [45]. These batteries are evaluated for the design, but will most likely not pose a possibility yet due to their Technology Readiness level (TRL).

[1] From: `https://www.cnbc.com/2021/10/20/tesla-switching-to-lfp-batteries-in-all-standard-range-cars.html`. Visited on 02-06-2022

A trade-off is performed for all the battery types. Sustainability and gravimetric energy density are weighed highest, as sustainability is the driver requirement and gravimetric energy density has a big influence on total vehicle weight. The technology readiness level has a weight of one since the technology does not need to be at the end of the development stage yet. If the technology is ready by 2025, it is deemed viable. The TRL is measured using the nine levels defined by the European Union [2]. Level one corresponds to the properties definition stage, where technologies are just discovered. Level nine corresponds to the product being on the market. Volumetric energy density and life cycles are weighed by two. The volume is critical for the vehicle size but less critical than the mass. Life cycles can be influenced by the Depth of Discharge (DoD, this will be further explained in section 9.3) and are therefore also deemed important, but not critical. The weights can be found in Table 9.2.

Table 9.2: Battery type criteria and their corresponding weights

Gravimetric Energy Density	Volumetric Energy Density	Life Cycles	Sustainability	TRL
3	2	2	3	1

Table 9.3: Trade-off matrix battery types

Type	Gravimetric Energy Density [Wh/kg]	Volumetric Energy Density [Wh/L]	Life Cycles at 100% DOD [-]	Sustainability	TRL
Lead-Acid	50 [46]	50[2]	200[2]	99.5% recyclabillity, designed for recycling [42]	9
Li-Ion	100-256 [3]	350 [2]	2000	Large opportunities in recycling, but trend is not in right direction yet. (EV's end-of-life, design philosophy) [42]	9
Li-Iron-Phosphate	140 [47]	350 [2]	2000 [2] [47]	Similar to Li-ion	9
Li-S	350-700[3] [43]	700 with possible development towards 1700 [48] [49]	500 [4]	New technology. Sulfur can be recycled and is not harmful to environment. However, little recycling infrastructure is in place [42]	5 [42]
Li-Air	500, with development towards 5200 [43], [44], [48]	700, with development towards 1700 to be competitive with gasoline [50] [51]	TBD	New technology with very promising recyclability. However, no recycling infrastructure in place. [42]	3 [42]
Metal-Air	1000+ [48]	development towards 1700 to be competitive with gasoline [51], [52]	TBD	New technology with very promising recyclability. However, no recycling infrastructure in place. [42], [44]	2 [44], [42]

From the trade-off matrix, the following total scores are determined. Below a color legend can be found showing the scores for each color. The total scores can be found in Table 9.4. Four sensitivity analyses are performed by setting all weights to 0 except for one criterion. This is done for the criteria Gravimetric, Volumetric Energy Density, Life Cycles and Sustainability. The integral take-away from the sensitivity analysis is that Lithium-Sulfur has the best realisable performance in energy density, whilst not compromising sustainability for it. This can be clearly seen from Figure 9.1. The lighter

[2]From: `https://euraxess.ec.europa.eu/career-development/researchers/manual-scientific-entrepreneurship/major-steps/trl`. Visited on: 20-06-2022

[2]From: `https://www.epectec.com/batteries/cell-comparison.html`. Visited on 07-06-2022

[3]From: `https://spectrum.ieee.org/with-ultralight-lithiumsulfur-batteries-electric-airplanes-could-finally-take-off`. Visited on 02-06-2022

[4]From: `https://oxisenergy.com/`. Visited on 02-06-2022

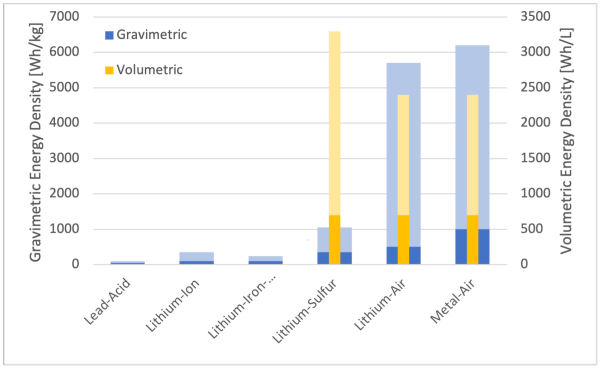

Figure 9.1: Energy Densities battery types

shaded areas in the graph show the expected development of the batteries. From this, it was determined that Li-S will be the battery type used in the vehicle.

Color codes	[red]	[orange]	[yellow]	[light green]	[dark green]
Score	1-Unacceptable	2-Bad	3-Medium	4-Good	5-Excellent

Table 9.4: Battery type trade-off scores

Lead-Acid	Li-Ion	Li-Iron-Phosphate	Li-Sulfur	Li-Air	Metal-Air
31	36	36	42	35	40

9.3. Battery Volume & Mass

The mass and volume of the battery are required for iteration of mass estimations and structural design. If energy density values of current batteries would be used, the batteries would most likely be oversized due to the fast development of new battery technologies. Note that the values in Table 9.3 already take into account packaging and integration weights [43], [44], [51]. Both equations are factored by the $DoD \cdot EoLC$. Oxis Energy, a company researching and developing Lithium-Sulfur batteries, claims their batteries can safely be discharged to 100% without compromising their performance [3]. Using a contingency of 5% the DoD from Table 9.5 was found. Furthermore, the End of Life Capacity (EoLC) is used to factor in the degradation of the battery throughout the operational life. This essentially means the battery capacity will be 70% the capacity of the brand-new battery (Table 9.5). The value was based on a paper by Yan [53]. In their paper, they showed that the capacity of Lithium-Sulfur batteries using a special electrolyte stayed almost constant after initial battery wear in the first 20 cycles. Although the 70% might be optimistic currently, it is expected that Lithium-Sulfur batteries will have this performance on a larger commercial scale by 2025 [53].

Table 9.5: Battery characteristics

Characteristic	Value
EoLC	70%
DoD	95%
Energy required throughout operational life	377 MJ
E_g	600 Wh/kg
E_v	700 Wh/kg

[3] From: `https://oxisenergy.com/`. Visited on 02-06-2022

$$m_{bat} = \frac{E_{tot}}{E_g} \cdot \frac{1}{DoD \cdot EoLC} \quad (9.1) \qquad V_{bat} = \frac{E_{tot}}{E_v} \cdot \frac{1}{DoD \cdot EoLC} \quad (9.2)$$

These equations are from A. Cervone's lecture series on Electrical Power Systems [41]. E_g and E_v are the gravimetric and volumetric energy densities, respectively. V_{bat} and m_{bat} are the battery volume and mass respectively. A battery mass and volume of $262 \pm 5\%\, kg$ and $0.225 \pm 10\%\, m^3$ are determined. The discrepancies are discussed in section 9.6

9.4. Battery Configuration & Charging

The battery will be configured according to multiple factors: nominal required voltage, maximum cell current, safety (redundancy) and maximum required power. To determine the configuration, the datasheet of a current Lithium-Sulfur cell from Oxis Energy is used [4] *NB.: It is assumed that the values from this datasheet will not change if energy densities become higher in 2025, but rather the cells become lighter. This is not realistic, but will be sufficient to determine a preliminary battery configuration since battery voltage and peak discharge will most likely not change significantly.*

Table 9.6: Cell characteristics

Characteristic	Value
Nominal voltage	$2.1 V_{DC}$
Capacity	$14.7 Ah$
Maximum charge rate	$4h$
Maximum discharge rate	$2C$
Maximum continuous discharge rate	$1C$

$$V_{bat} = V_{array} = n_{cells} \cdot V_{cell} \quad (9.3) \qquad C_{bat} = n_{arrays} \cdot C_{array} = n_{arrays} \cdot C_{cell} \quad (9.4)$$

The Emrax 208 electromotors require a voltage potential of $430\, V_{DC}$. The peak power that should be delivered is equal to $821\, kW$ and the required capacitance calculated with Equation 9.5 is equal to $366\, Ah$. Using the above equations, the potential and the capacitance, the battery configuration is found. This is presented in Table 9.7 and Figure 9.2.

Table 9.7: Battery configuration

Cells per array	205
Number of battery arrays	25

$$C_{bat} = \frac{E_{req}}{V_{DC}} \cdot \frac{1}{DoD \cdot EoLC} \quad (9.5)$$

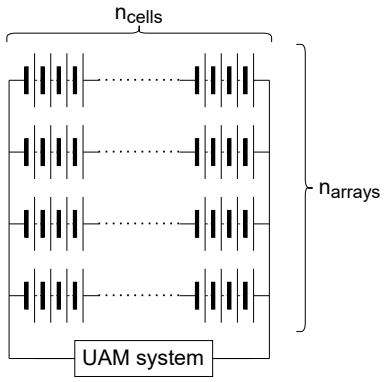

Figure 9.2: Graphical representation of the battery system

The battery charge time specified by Table 9.6 is 4 hours. By increasing the power of the charger, the cells will not be charged faster, but multiple cells can be charged at the same time. Thus, the charging time will not decrease below four hours. In order to meet the turn-around requirement *TECH-POSF-1*, swappable batteries can be implemented. This means that a set of batteries will be charging whilst the UAM is in flight. Then during the pre-flight procedure of the next flight, the batteries will be

[4] From: `https://45uevg34gwlltnbsf2plyua1-wpengine.netdna-ssl.com/wp-content/uploads/2019/07/OXIS-Li-S-Ultra-Light-Cell-spec-sheet-v4.2.pdf`. Visited on 07-06-2022.

swapped such that the UAM is fully charged again. A more detailed description of this can be found in section 3.2.

9.5. Electrical Block Diagram, Hardware & Software

The electrical block diagram can be found in Figure 9.3. It shows variable resistors as a means of controlling the electrical motors. Furthermore, it should be noted that the battery arrays are shown as one single battery source. The diagram is a rather simplified representation of an electrical system within a UAM. Section 9.8 will elaborate on the design steps still required for this system. Two other nominal segments of a technical report, the hardware and software diagram and data handling diagram, have not been explicitly added to this report. A preliminary data handling diagram has however been integrated into the communications diagram in Figure 3.5, section 3.3. Flight control, stability and autonomy are still to be assessed in the coming design stages. Since these systems create a major set of above-mentioned diagrams' components, the diagrams have for now been considered superfluous for this report.

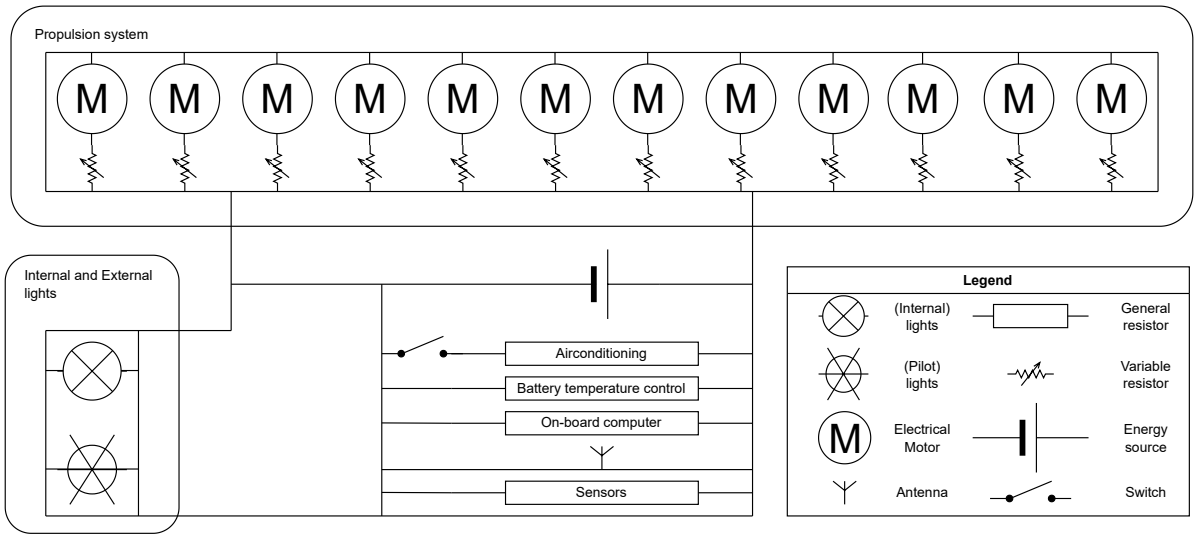

Figure 9.3: Electrical Block Diagram

9.6. Battery Verification & Validation

Microsoft Excel is used for the calculations, hence only system verification is required for the battery calculations. These are performed by doing the equations from section 9.3 and section 9.4 by hand. Some minor issues were found and have been resolved. However, since the battery has not yet been fully developed, the model can currently not be validated. To validate the model, the battery should be constructed and thoroughly tested. This can be done first by making a small-scale battery and eventually scaling it up to a full-size system, while performing tests along the way. A similar process is performed by Oxis Energy currently, validating the current design of their Lithium-Sulfur batteries [5] It should be noted that section 9.7 will give a preliminary validation with the use of Figure 9.1. This will however be regarded as a sensitivity analysis, due to the large margins in exact values currently available.

9.7. Sensitivity Analysis of Battery Calculations

In other to confirm the validity of the results, sensitivity analyses were performed on the inputs of the battery sizing. The results of this sensitivity analysis can be found in Figure 9.4. It can be seen that the mass and volume vary with $1/x$ to gravimetric and volumetric energy density respectively. This behaviour is as expected. Furthermore, it can be seen from the figures that gravimetric and volumetric leave the volume and mass constant respectively, as expected. The last notice is that the mass and

[5] From: `https://oxisenergy.com/support/`. Visitend on 20-06-2022.

volume become respectively lower and higher for DoD and EoLC. This is again as expected because higher DoD means lower capacity required. Higher battery wear in turn means a higher capacity required at beginning of life (BoL).

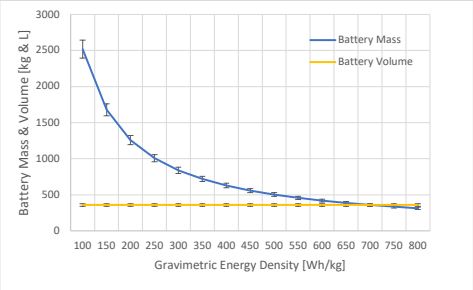

(a) Mass and volume against gravimetric energy density

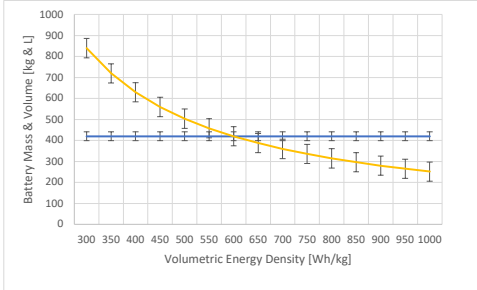

(b) Mass and volume against volumetric energy density

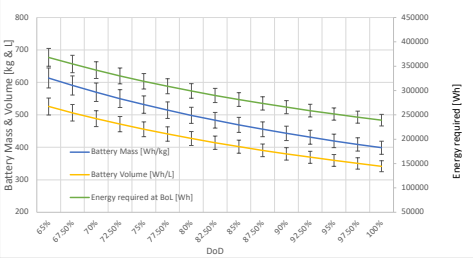

(c) Mass, volume and Energy required at BoL against DoD

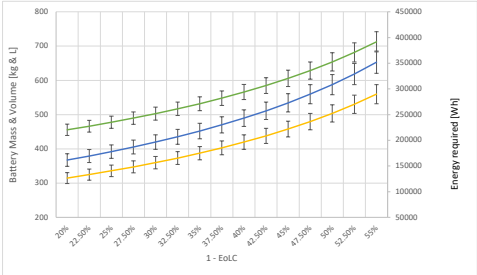

(d) Mass, volume and Energy required at BoL against EoLC

Figure 9.4: Sensitivity analysis for gravimetric and volumetric energy density, DoD and EoLC.
Added axis labels

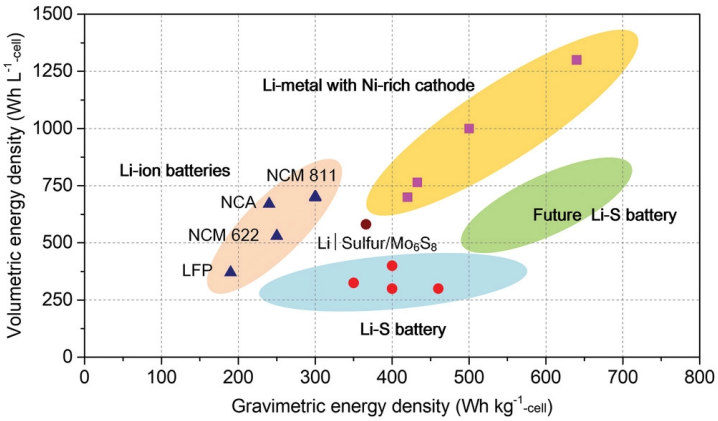

Figure 9.5: Future Li-S energy densities [54]

The battery mass and volume are calculated with progressive values for 2025. Although it is expected that these values shall be reached by 2025, there is a large uncertainty integrated within these values. For this reason, an error margin of 5% will be added to the estimated mass. The margin was based on the fact that Oxis Energy has already produced battery cells with an energy density of 500 Wh/kg in 2019[6]. This is less than 17% away from the desired energy density. Considering that from this energy

[6]From: `https://45uevg34gwlltnbsf2plyua1-wpengine.netdna-ssl.com/wp-content/uploads/2019/07/OXIS-Li-S-Ultra-Light-Cell-spec-sheet-v4.2.pdf`. Visited on 07-06-2022.

density and the estimated energy densities from Liu [54], graphically represented in Figure 9.5, there are six years until 2025, the 5% margin is assumed conservative enough for the mass estimation.

The battery volume error is taken at 10% for the same reasoning, except that volumetric energy density of $700\,Wh/L$ is more optimistic than the gravimetric energy density, as can be seen from Figure 9.5. The reason why a less conservative value is taken for the volumetric energy density is that volume is a less pressing constraint for the UAM than weight. A higher battery volume would require a larger fuselage and therefore increased weight, but lower gravimetric energy density will not only cause a higher battery mass but also more structural weight to carry these loads.

9.8. Recommendations on Battery and Electrical System

The battery type that has been chosen is Lithium-Sulfur. There is still development required to apply these batteries in the vehicle, but meeting the development goals by 2025 is considered realistic, when looking at progress made by companies such as ZenLabs [7]. Therefore it is not only a realistic choice but also a sustainable one. It will allow for less mass and therefore less energy required for the mission, but also less energy required for the production of the vehicle, all lowering the stress on the environment significantly.

However, a new type of battery was also discussed: metal-air. These batteries are in an early Research & Design stage but promise to have even better recyclability and performance than Lithium-Sulfur. This would result in an even better recyclable and lighter UAM. Thus, if the vehicle needs battery replacements or is being produced in 2030-2050, these battery types should definitely be considered as a design option.

Two more recommendations shall be made on the electrical system. The electrical system requires a lot more detail, which is beyond the time scope of the DSE. It is suggested that in the future the system will be worked out into a safe and redundant system. This can be done by having components in place that allow for battery disconnection in case of failure, protect the batteries against high power loads and regulate the battery temperature according to their best performance.

The final recommendation concerns the wiring of the electrical systems. The wiring has not yet been designed but can have a major effect on sustainability and mass of the vehicle. A contingency is added to the mass budget of the frame of $50\,kg$ for the electrical wiring, taking into account also the hub and bolting of the system. Therefore it is recommended to research how to minimise the use of wiring, but also research the type of wiring used. Often copper is used within the wires [55], which is 100% recyclable

[7] From: `https://www.zenlabsinc.com/aerial-vehicles`. Visited on 20-06-2022

10 Materials

To design a fully sustainable UAM, material choice is of great importance. Materials should both provide great performance to make the vehicle energy efficient but also should be sustainable. Consequently, this section will lay out to process to choose the materials for the vehicle.

First in section 10.1 an overview of promising materials for the vehicle will be given. After that in section 10.2 a trade off between the materials will be performed to choose materials for primary structure and interior application in the vehicle. section 10.3 gives the applied materials in various parts of the vehicle. The layout of the fabric for the composites will be explained in section 10.4. The composite properties are given in section 10.5. The failure of the composites is discussed in section 10.6. The material properties for most important materials used in the vehicle are summarized in section 10.7. Validation and verification will follow in section 10.8. Finally, the chapter will end with recommendations.

10.1. Material Options

In this section promising materials for the UAM will be presented. In this section a short description of each material is provided, further information is provided in the Midterm Review [5]. In subsection 10.1.1 metals that could be used for various applications in the UAM are presented. After this, in subsection 10.1.2 the composites which could be used in the vehicle are presented.

10.1.1. Metals

Metals are still the most applied materials in the aerospace industry of which aluminium it the most commonly used. Aluminium is widely used due to its high performance and ease to work with. However, recyclability of aluminium may be difficult. Especially in the aerospace industry as aluminium often is mixed with other materials to alter the material properties. Therefore, it is rather difficult to use recycled aluminium in the vehicle when specific material characteristics are asked [56].

Other promising material are titanium alloys. Titanium alloys have a high strength combined with a rather low density. Furthermore, the titanium used can almost be completely recycled. Therefore, this metal could be promising for the vehicle [57] [58]. The material properties for the two most common used aluminium and titanium alloys are shown in Table 10.1 The most commonly used aluminium alloy in the aerospace industry is Aluminium 2024 [1]. Most frequently used titanium alloy in aerospace structures is Ti-6AI-4V [2]

10.1.2. Composites

Composites are a relatively new materials compared to metals. In most aerospace applications composites are used due to their high strength compared to their weight. An analysis of two kinds of composite families is presented. First fibre metal laminates are considered. After that an analysis of fibre reinforced polymers is considered.

A widely used fibre metal laminate is GLARE. GLARE is a strong material and low in weight when compared to metals. GLARE consists of thin sheets of metal, often aluminium, separated by glass fiber: "prepreg". [3]

[1] From: `https://www.thyssenkrupp-materials.co.uk/aerospace-grade-aluminum`. Visited on 03-06-2022

[2] From: `https://fs-precision.com/articles/2017/12/aerospace-titanium-what-makes-it-special/`. Visited on 03-06-2022

[3] From: `https://materialdistrict.com/material/glare/`. Visited on 03-06-2022

Table 10.1: Metal and fibre metal laminates Summary Table

Material	Density $[g/cm^3]$	Tensile strength $[MPa]$	Elastic modulus $[GPa]$	References
GLARE	0.83–1.00	484 - 880	52 - 72	EMBRY [4]
Aluminium 2024	2.77	469	73.1	Thomas[5]
Ti-6Al-4V	4.43	1170	114	Kyocera [6]

For fibre reinforced polymers the material selection will be divided in the selection of resins and fibers. First the fibers will be discussed. In fibre reinforced polymer materials either synthetic or natural fibres can be used. Most common synthetic fibres are carbon fibres. The material is characterized by its high tensile strength. However, as the material is synthetic this is not the most sustainable option. Therefore, in this design also natural fibres are considered. Most promising natural fibre are flax fibres. These fibres have the highest tensile strength and elastic modulus of the natural fibres. Most important material characteristics of these fibres are shown in Table 10.2.

Table 10.2: Fibres Summary Table

Fibre	Diameter $[\mu m]$	Density $[g/cm^3]$	Tensile strength $[MPa]$	Elastic modulus $[GPa]$	References
Carbon fibres	7-11	1.74-2.19	1730-7060	155-860	[59]
Flax fibres	12–600	1.4–1.5	343–2000	27.6–103	[60]

Resins are used as matrix for the reinforcement of fibers. Resins again can be divided in natural and synthetic types. Most commonly used resin is that of epoxy. Epoxy is already often used in combination with carbon fibres. The problem with epoxy is the relative difficult recycle processes and the synthetic materials used as raw material. As a result, epoxy is not the most sustainable option. Other promising resins are vitrimers. Vitrimers are often made of synthetic materials but have the advantage that they can be easily recycled [61]. Two natural resins are considered; Poly Lactic Acid (PLA) is a resin made of natural materials which is biodegradable. The disadvantage of PLA is it relatively low glass-transition temperature between 50 and 80 $^\circ C$ [62]. Therefore not making it applicable for every part of the vehicle. The second natural resin considered is PHA which again has a low glass-transition temperature, even lower than PLA. Therefore also making it only applicable for selected parts of the design.

Table 10.3: Resin Summary Table

Resin	Density $[g/cm^3]$	Tensile strength $[MPa]$	Elastic modulus $[GPa]$	References
Epoxy	1.11–1.14	36-71	2.35-3.08	[63]
Vitrimer	1.05	117.7	3.6	[64]
PLA	1.21–1.25	48–60	3.45–3.83	[63]
PHA	1.25	22.4 - 28.7	2.00 - 3.76	NCBI[7]&MDPI[8]

10.2. Material Application

To choose the materials for all components in the vehicle a trade-off is performed. The trade-off is performed for both the primary load carrying structure and the interior structure. With the primary structure all components in the vehicle which carry load are meant. The interior structure are panels used in the inside of the fuselage to cover the frame and electric circuits.

In the trade-off the most promising composites are compared on 3 criteria. The sustainability criterion accounts for the recyclability of the composites. For recyclability it is important to analyse

[4]From: `https://commons.erau.edu/cgi/viewcontent.cgi?article=1021&context=edt`. Visited on 03-06-2022

[5]From: `https://www.thomasnet.com/articles/metals-metal-products/2024-aluminum/`. Visited on 03-06-2022

[6]From: `https://kyocera-sgstool.co.uk/titanium-resources/titanium-information-everything-you-need-to-know/ti-6al-4v-grade-5-titanium-alloy-data-sheet/#:~:text=Properties%20of%20Grade%205%20titanium,density%20of%204.43%20g%2Fcc.`. Visited on 03-06-2022

[7]From: `https://www.ncbi.nlm.nih.gov/pmc/articles/PMC6524128/`. Visited on 03-06-2022

[8]From: `https://www.mdpi.com/2073-4360/10/7/751/htm`. Visited on 03-06-2022

the energy used for the process and the lost value of the material after recycling, known as downcyling. In addition, the sustainability criterion will take into account whether a material is natural or synthetic.

Performance accounts for the material properties of the material. Flying vehicles have to be low in mass while still providing strength to the vehicle. As lower mass means less energy used. Thus, performance is an important criterion for selecting the materials and therefore is considered in the trade-off for primary and interior structure of the vehicle.

Lastly, the availability of the materials is considered. Materials widely available for a fair price will be advantageous compared to materials in the research and development phase. Existing materials already have proven their ability to be used in structures. Furthermore, for weaknesses the design could be altered. Thus, unexpected behaviour of the material is unlikely. In comparison to a new material where use in a complex structure still has to be proven to work. Therefore, availability of materials is a relevant criterion.

The trade off for the material for the primary load carrying structure of the vehicle is shown in Table 10.4. Performance is considered most critical for the primary structure. As the primary structure has to carry high structural loads, performance is critical for these components. For the trade off the interior, sustainability is considered most important criterion. As this structure will carry considerably less loads compared to the primary structure. Therefore, performance will not be of the highest priority which makes it possible for these panels to focus more on sustainability. These considerations are reflected in the assigned weights of the criterion as seen in Table 10.5. In the tables the total scores of the composites are shown. The colour scheme used is the same as used in chapter 7,

Table 10.4: Trade off material for primary structure

Criteria	Weight	Vitrimer + carbon fibres	Vitrimer + flax fibres	PLA + flax fibres	Epoxy + carbon fibres	Epoxy + flax fibres	PHA + flax fibres	Ti-6Al-4V	Aluminium 2024	GLARE
Sustainability	2	3	4	5	3	4	5	4	4	3
Performance	3	5	3	1	4	3	1	3	3	3
Availability	2	4	1	4	5	5	2	4	5	5
	Total score	29	19	21	28	27	17	25	27	25

Table 10.5: Trade off material for interior

Criteria	Weight	Vitrimer + carbon fibres	Vitrimer + flax fibres	PLA + flax fibres	Epoxy + carbon fibres	Epoxy + flax fibres	PHA + flax fibres	Ti-6Al-4V	Aluminium 2024	GLARE
Sustainability	3	3	4	5	3	4	5	4	4	3
Performance	2	5	3	1	4	3	1	3	3	3
Availability	2	4	1	4	5	5	2	4	5	5
	Total score	27	20	25	27	28	21	26	28	25

Regarding sustainability the natural composites, PLA and PHA with flax fibres, are seen most sustainable and therefore score a 5 for this criterion in the trade-off. These material are biodegradable and made from unlimited natural resources. Hence, receiving the highest sustainability score. As the composites using flax fibres with a synthetic resin also are partly biodegradable and the resins can be recycled by using relatively low energy consuming processes these composites are assigned a 4 on sustainability. The same score is given to the titanium and aluminium alloys. Most aluminium used in today's market is retrieved from recycled aluminium [9]. However, for specific aerospace alloys it is difficult to retrieve the exact composition of the material and therefore recycling of aerospace aluminium often is seen as downcycling. Lastly, the fully synthetic composites are all recyclable. However, these materials are mostly made from materials out of fossil resources. Hence, the carbon fibres combined with vitrimer and epoxy resins and GLARE are all given a score of 3 for sustainability.

As seen in Table 10.2 carbon fibres have a considerably higher strength than flax fibres. Furthermore, shown in Table 10.3 is that vitrimer is the highest performance resin. Hence, the carbon fibres combined with vitrimer get the highest score of 5 in the trade-off for performance. As epoxy is less strong than vitrimer this resin combined with carbon fibres get a performance score of 4. The natural fibres are less strong compared to the synthetic carbon fibres and therefore combination with synthetic resins score a 3 for performance. The same yields for all materials using metals. The materials have favourable material properties like thermal behavior and yield behavior however, as a result of relatively high mass score for performance a 3. The fully natural materials have poor thermal behavior. Furthermore, strength is also relatively low. Thus, these fully natural composites score a 1 for performance.

[9] From:`https://www.epa.gov/facts-and-figures-about-materials-waste-and-recycling/aluminum-material-specific-data`. Visited on 07-06-2022

For the availability of the materials, materials already used in existing products and purchasable from various companies score highest. Therefore, epoxy with carbon fibres, epoxy with flax fibres, aluminium 2024 and GLARE score highest. The combination of vitrimer and PLA with carbon fibres is not widely used, as these materials are only for a couple of years on the market. The titanium alloy is rather expensive and therefore is given an availability score of 4. PHA resin with flax fibres is currently not widely used in aerospace products, however, products are potentially easily purchasable. Therefore, this material receives a score on availability of 4. Lastly, vitrimers combined with flax fibres are currently not in use. In addition, vitrimers have only been on the market for a couple of years. Therefore, this composite receives a score of 1 on availability.

Concluding, for the primary structure of the vehicle carbon fibres with a vitrimer resin scores the highest in the trade-off. The primary structure of the vehicle will transfer all the loads. Therefore it will be important to select materials which have high strength while still complying with the sustainability requirements. For the interior structure both epoxy combined with flax fibres and Aluminium 2024 top the trade off for the interior structure.

10.3. UAM Parts and Applied Materials

Every component in the UAM vehicle must be assigned a material. In Table 10.6 a summary of material decisions is provided for the most critical parts of the vehicle.

As shown in the trade-off performed in the previous section the carbon fibre/vitrimer composite performs best when applied to the primary structure. Thus, as presented in Table 10.6 the supporting structure, fuselage skin and the skid use a composite of carbon fibres & vitrimers. This is not the case for the ribs. The chosen cross-section, the curved shape and potential cut-outs in the future rib design may make it difficult to apply the carbon fibre/vitrimer prepregs. Because of this; Aluminium 2024 is chosen for the ribs.

This decision was also the driven by the fact that having different materials for the stringers and ribs can introduce thermal stresses. So, to keep the materials for the fuselage consistent for both the stringer and the ribs Aluminium 2024 is used.

For interior design the flax fibre/epoxy will be used as it does not carry any significant loads compared to structures made of carbon fibre/vitrimer. For the windows polycarbonate was picked which is often used for windows in aircraft. It provides good visibility with sufficient stiffness and it is easy to recycle as it is a thermoplastic. For battery the lithium-sulfur was specified as it turned out to be the best compromise between recyclability and readiness level when compared to other batteries considered in section 9.2.

The rotor blades were also assumed, just as the primary structure, to use carbon fibre/vitrimer composite as this can significantly decrease its mass. Similar rotor blades with carbon fibre/epoxy have already been produced. Next, the motors materials were adopted from a manual of already accessible motors [65].

For the firewall steel with aluminum coating is chosen. This because the material scored the best in terms of density as explained in subsection 11.2.6. Finally, the hub, due to its more complex shape, will be made of Aluminium 2024. The floor should be able to carry loads applied across the floor in multiple places. The floor will therefore have to transfer bending moments, as composites are not well suited for bending moments, the floor is decided to be made of aluminium.

Table 10.6: Parts of the UAM vehicle and the corresponding material used.

Part	Material used
Supporting structure	Composite (Carbon fibres & Vitrimer)
Fuselage skin	Composite (Carbon fibres & Vitrimer)
Skid	Composite (Carbon fibres & Vitrimer)
Ribs	Aluminium 2024
Stringers	Aluminium 2024
Interior design	Composite (Flax fibres & Epoxy)
Windows	Polycarbonate
Battery	Lithium Sulphur
Rotor blades	Composite (Carbon fibres & Vitrimer)
Propulsion motors	(Aluminium 6082 & hardened steel & copper with epoxy coating)
Firewall	Steel with aluminium coating
Hubs	Aluminium 2024
Floor	Aluminium 2024

10.4. Composite Fabric Layout

Choosing a composite for the primary structure requires a specific layout of the fibres within the composite. Unidirectional composites, where fibres are aligned along one single direction, feature great mechanical properties once loaded in the direction of fibres. Unfortunately, their strength in the direction perpendicular to the fibres is very low and corresponds mostly to what the resin itself is able to resist. Thus, it can be dangerous to use this kind of an unidirectional composite in a structure where various loads are acting on the structure.

To improve the material properties of the composites, the composites are made by stacking multiple layers where fibres are oriented differently in each layer. This allows the composite to become more isotropic. Of course, this also has a disadvantage in terms of the manufacturing process. Therefore, a trade-off should be performed which will both satisfy the manufacturing and material performance aspects.

For the composites used in the UAM it is decided to use $0°/90°/45°/-45°$ fibre orientation. It features only 4 different fibre directions while it is already considered to closely represent an isotropic material. It is also one of the most frequently used orientations for composites which strive to imitate isotropy. This kind of fabric pattern may be obtained through various manufacturing processes. A relatively easy processes for this is putting two fibre fabrics with $0°/90°$ fibre orientation on top of each other at an angle of $45°$. This fibre stacking is shown in Figure 10.1. Once the first fabric layer (red lines on the left) are applied, the next layer (green lines) is placed on top but rotated by $45°$. Then, the next applied layer on top is again rotated by $45°$. and this continues until the required composite thickness is obtained.

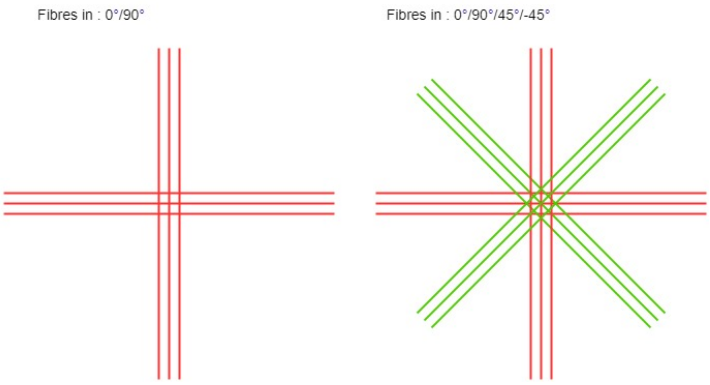

Figure 10.1: Composite fibres layout represented by two fibre fabrics with $0°/90°$ orientation

10.5. Composite Properties

When the composite fibre layout and composite material is defined it is possible to estimate composite mechanical characteristics. This section will focus on finding composite parameters for carbon fibres with vitrimer resin as this material will be used mostly for primary structure. Data for flax fibre/epoxy composite is also provided but it is not treated in such detail.

Before estimating the properties for the whole composite it is necessary to find properties of a single layer used within the composite. As mentioned in section 10.4 due to a more forward manufacturing process, it is assumed for every composite layer to be made out of a fibre fabric with a fibre orientation of $0°/90°$.

Below, all necessary data used in subsequent calculations for carbon fibre, vitrimer, flax fibre and epoxy is provided. For all values a corresponding reference is provided. The carbon fibre properties were taken from an existing supplier of high quality fibres also used in aerospace applications.

Table 10.7: Characteristics of carbon fibres and the vitrimer resin used for lamina calculations

Variable	Variable name	Value	Reference
E_f	Fibres Young's modulus	243 GPa	Hexcel [10]
E_{resin}	Resin Young's modulus	3.6 GPa	[64]
ρ_f	Fibres density	1790 kg/m^3	Hexcel [10]
ρ_{resin}	Resin density	1050 kg/m^3	[64]
$\sigma_{f_{max}}$	Maximum fibre stress	4930 MPa	Hexcel [10]

Table 10.8: Characteristics of flax fibres and the epoxy resin used for lamina calculations

Variable	Variable name	Value	Source
E_f	Fibres Young's modulus	65.3 GPa	Average value from Table 10.2
E_{resin}	Resin Young's modulus	2.715 GPa	Average value from Table 10.3
ρ_f	Fibres density	1450 kg/m^3	Average value from Table 10.2
ρ_{resin}	Resin density	1125 kg/m^3	Average value from Table 10.3
$\sigma_{f_{max}}$	Maximum fibre stress	1171.5 MPa	Average value from Table 10.2

First, the two Young's moduli responsible for material stiffness along the two axes are estimated. For unidirectional composites these moduli are quite different as one corresponds to the stiffness direction along the fibres E_L and one in the transverse direction E_T. This is represented on the left side in Figure 10.2. For the unidirectional composite,E_L is found by the rule of mixture as presented by Equation 10.1 [66].

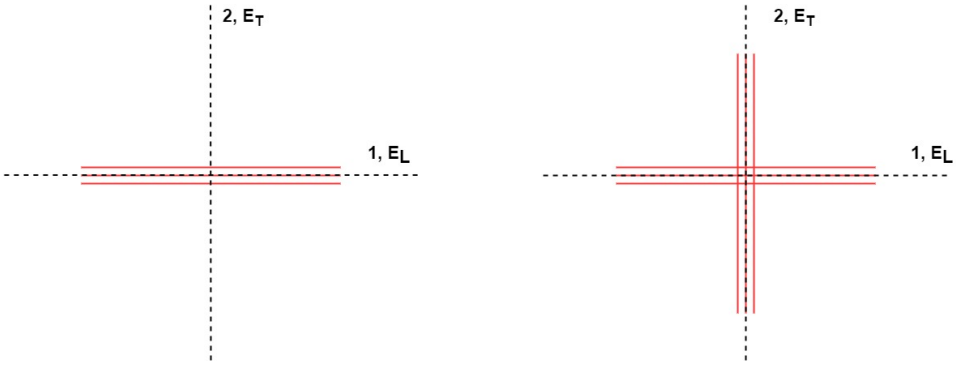

Figure 10.2: Layer's directions with Young's moduli for a composite layer

$$E_L = V_f \cdot E_f + (1 - V_f) \cdot E_{resin} \tag{10.1}$$

[10] From:https://www.hexcel.com/user_area/content_media/raw/AS7_Aerospace_HexTow_DataSheet.pdf.Visited on 13-06-2022

Where V_f corresponds to the fibre volume in the composite and E_f with E_{resin} correspond to the Young's moduli of the fibres and of the resin. However, for 0°/90° layer considered here, only half of fibre volume is directed in one direction. For this reason Equation 10.1 was modified to:

$$E_L = \frac{V_f}{2} \cdot E_f + (1 - V_f) \cdot E_{resin} \tag{10.2}$$

Now by looking again at the right part of Figure 10.2 it can be seen that due to symmetry it can be assumed that:

$$E_L = E_T \tag{10.3}$$

Now, E_f and E_{resin} are quite limited and stay within a specific range for a chosen material. However, the fibre volume V_f can be easily changed by the composite designer. It can be beneficial for composite characteristics like stiffness to have high fibre volume since fibres have superior properties in comparison to the resin. There is however, an upper limit on this volume above which the resin can have difficulties with joining the fibres together. This limit oscillates around 60% and this is also the percentage currently provided by the company providing the carbon fibre with vitrimer prepregs [11]. Thus, a value of 60% for V_f is used in the calculations.

Density is another parameter which must be found to estimate the mass of components made of a composite. Here, just as for Young's modulus, the rule of mixture is applied [66] resulting in:

$$\rho_c = V_f \cdot \rho_f + (1 - V_f) \cdot \rho_{resin} \tag{10.4}$$

With ρ_f as fibre density and ρ_{resin} as density of the resin.

Additionally, there is also Shear modulus G_{LT} and Poisson's ratio v_{LT} and v_{TL} which should be defined for a composite. This data is easily defined in an experimental set-up but for carbon fibre/vitrimer composite calculations these are taken from existing data for carbon fibre/epoxy composites as it is assumed that these characteristics should remain similar. This is believed to be a valid assumption as mechanical characteristics for vitrimers do not change too much compared to epoxy as seen in Table 10.3. Also, just as for Young's moduli, it can be stated because of symmetry that:

$$v_{LT} = v_{TL} \tag{10.5}$$

The final lamina property which is vital in estimating the failure of a composite is the maximal stress in lamina direction 1 and 2 in Figure 10.2. Due to the symmetry in both directions of the fabric, the maximal stresses will be the same. Now the maximal stress is estimated by assuming that the fibres will carry the whole stress in the ply coming from one direction. This means that within each ply's cross-section there is an effective cross-section taking all the stress. This can represented by:

$$\sigma_f \cdot A_{eff} = \sigma_{max} \cdot A \tag{10.6}$$

Where A_{eff} is the effective cross-section area and A the total one. To find σ_{max} it is necessary to assign a value to A_{eff}/A ratio. This should correspond to fibre volume ratio V_f divided by 2 as only half of all fibres in the layer is aligned in direction 1 and 2. Using this methodology and the carbon fibres characteristics from Table 10.7 the maximal strength of carbon fibres/vitrimer lamina is determined to be $1479\,MPa$.

To summarise all the properties found for carbon fibre/vitrimer and flax fibre/epoxy laminas in this section, two representative tables are provided below. Some of these properties are calculated directly and some are retrieved from outside sources specified in the last column. In the table for flax fibre/epoxy some values are left TBD as this composite is not used for any loading scenarios and thus, finding this data is not deemed essential at this level of the design.

[11] From: `https://mallinda.com/wp-content/uploads/2021/10/Mallinda-TDS-T130_10.12.21.pdf`.Visited on 15-06-2022

Table 10.9: Characteristics of a carbon fibres/vitrimer 0°/90° fabric layer

Variable	Variable name	Value	Source
E_L	Lamina Young's modulus, direction 1 Figure 10.2	74.27 GPa	Equation 10.2
E_T	Lamina Young's modulus, direction 2 Figure 10.2	74.27 GPa	Equation 10.3
v_{LT}	Major Poisson ratio	0.1	Performance Composites Limited[12]
v_{TL}	Minor Poisson ratio	0.1	Equation 10.5
G_{LT}	Shear modulus	5 GPa	Performance Composites Limited[12]
V_f	Fibre volume	0.6	Mallinda[13]
ρ_c	Lamina density	1494 kg/m^3	Equation 10.4
τ_{max}	Max shear stress	70 MPa	Performance Composites Limited[12]
σ_{max}	Max stress in fibre direction	1479 MPa	Equation 10.6

Table 10.10: Characteristics of a flax/epoxy 0°/90° fabric layer

Variable	Variable name	Value	Source
E_L	Lamina Young's modulus, direction 1 Figure 10.2	20.68 GPa	Equation 10.2
E_T	Lamina Young's modulus, direction 2 Figure 10.2	20.68 GPa	Equation 10.3
v_{LT}	Major Poisson ratio	TBD	-
v_{TL}	Minor Poisson ratio	TBD	-
G_{LT}	Shear modulus	TBD GPa	-
V_f	Fibre volume	0.6	Assumed same as for carbon fibres
ρ_c	Lamina density	1320 kg/m^3	Equation 10.4
τ_{max}	Max shear stress	TBD MPa	-
σ_{max}	Max stress in fibre direction	350 MPa	Equation 10.6

10.6. Composite Failure

Predicting failure of a composite is a complicated task because of the multi-layer nature of the composite. Usually it is assumed that if one composite layer breaks the whole composite fails. That means that for a specific loading case every single layer must be examined to see if it meets the chosen failure criterion or not.

For the composite design in this report the maximum stress is chosen as criterion. That is, under specific loading, every layer is checked whether the occurring stress exceeds the ultimate stress of the lamina as presented in Figure 10.3. Where circles represent fibres in a fibre fabric. It should be recalled that the lamina coordinate system 123 is different from the xyz-coordinate system used for laminates (the whole composite) as can be seen in Figure 10.4. Where lamina axes 1,2 is rotated to the laminate axes x,y by an angle θ.

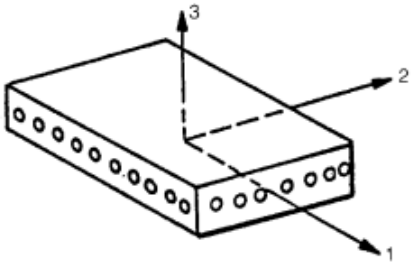

Figure 10.3: Axis system of a lamina [66]

[12]From: `http://www.performance-composites.com/carbonfibre/mechanicalproperties_2.asp`.Visited on 13-06-2022

[13]From: `https://mallinda.com/wp-content/uploads/2021/10/Mallinda-TDS-T130_10.12.21.pdf`.Visited on 13-06-2022

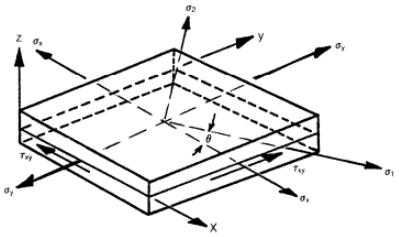

Figure 10.4: Axis system of a laminate with illustrated stresses [66]

Common for all lamina within a composite is the strain that they experience in the xy-plane because they form a body together. To find these strains the Laminate Theory must be applied which can define the stiffness of a composite consisting of many layers at different angles. When this composite stiffness and the acting loads are known, the strains can be found. This is done by Equation 10.7 [67] where strains are related to the loads by a so called ABD matrix. This matrix is the essence of Laminate Theory. It determines the composite stiffness and behaves like a Young's modulus in the Hook's law equation.

$$\begin{bmatrix} N_x \\ N_y \\ N_{xy} \\ M_x \\ M_y \\ M_{xy} \end{bmatrix} = \begin{bmatrix} A_{11} & A_{12} & A_{16} & B_{11} & B_{12} & B_{16} \\ A_{12} & A_{22} & A_{26} & B_{12} & B_{22} & B_{26} \\ A_{16} & A_{26} & A_{66} & B_{16} & B_{26} & B_{66} \\ B_{11} & B_{12} & B_{16} & D_{11} & D_{12} & D_{16} \\ B_{12} & B_{22} & B_{26} & D_{12} & D_{22} & D_{26} \\ B_{16} & B_{26} & B_{66} & D_{16} & D_{26} & D_{66} \end{bmatrix} \begin{bmatrix} \epsilon_x \\ \epsilon_y \\ \gamma_{xy} \\ \kappa_x \\ \kappa_y \\ \kappa_{xy} \end{bmatrix} \tag{10.7}$$

However, this equation can be significantly simplified. If the laminate consists of layers which are stacked in the same order from the center to the top and to the bottom, meaning it is stacked symmetrically, then all B entries in the ABD-matrix are zero. Exemplary symmetry is presented in Figure 10.5.

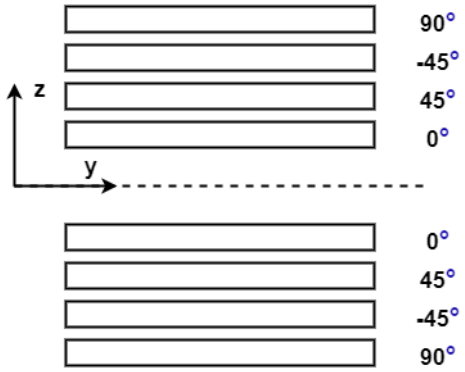

Figure 10.5: Exemplary symmetrically stacked laminas

Moreover, for the whole UAM design the approach for a failure of a flat composite will not consider bending moments directly. This is because the main parts made out of composites will be the fuselage skin and the hollow beams in the skid and in the supporting structure. The skin itself, because of its low thickness, can carry only very low bending moments. For hollow beams the bending moments will be considered but through the stresses they induce. This stress normally varies with the distance from the cross-sectional center but for thin-walled hollow beams it can be assumed to be uniform throughout the thickness. Thus, when analysing a small piece of beam skin, the stresses due to bending can be treated as if it came from an axial force. This approach will simplify equation Equation 10.7 to Equation 10.8 [67] where bending moments and induced curvatures are neglected.

$$\begin{bmatrix} N_x \\ N_y \\ N_{xy} \end{bmatrix} = \begin{bmatrix} A_{11} & A_{12} & A_{16} \\ A_{12} & A_{22} & A_{26} \\ A_{16} & A_{26} & A_{66} \end{bmatrix} \begin{bmatrix} \epsilon_x \\ \epsilon_y \\ \gamma_{xy} \end{bmatrix} \tag{10.8}$$

The entries remaining in th matrix are evaluated using Equation 10.9[67] where z_k and z_{k-1} correspond to the z-coordinates of a lamina as in Figure 10.5. Q_{ij} is a value specific for every layer and depends on the values of E_L, E_T, v_{LT}, v_{TL} and the layer's angle θ [67].

$$A_{ij} = \sum_{k=1}^{n} Q_{ij}(z_k - z_{k-1}) \tag{10.9}$$

So far Equation 10.8 related axial forces and shear acting on the composite. However, from the perspective of structural analysis it may be easier to relate predicted stresses to strains rather than loads. This is done by going from Equation 10.8 to Equation 10.10 and finally to Equation 10.11[66].

$$\begin{bmatrix} N_x \\ N_y \\ N_{xy} \end{bmatrix} = [A] \begin{bmatrix} \epsilon_x \\ \epsilon_y \\ \gamma_{xy} \end{bmatrix} \tag{10.10}$$

$$[A]^{-1} \begin{bmatrix} \bar{\sigma_x} \\ \bar{\sigma_y} \\ \bar{\tau_{xy}} \end{bmatrix} t = \begin{bmatrix} \epsilon_x \\ \epsilon_y \\ \gamma_{xy} \end{bmatrix} \tag{10.11}$$

With Equation 10.11 the relation between stresses and strains in the composites xy-plane is found. In the equation t is the total thickness of the laminate. This thickness can change by adding layers when it is discovered that the composite will fail otherwise. This is also the iterative process of designing a composite for a known loading case. For a single layer the thickness is assumed to be $0.15\,mm$ as this is the nominal ply thickness used by a company offering carbon fibre/vitrimer prepregs. This means that the pattern of two stacked fabric layers repeats itself every $0.3\,mm$. However, to keep the analysis simple regarding the ABD-matrix, the symmetry must be kept when iterating the total composite thickness as explained before. That is why the composite thickness should be changed by steps of $0.6\,mm$ as the composite thickness is always changed by $0.3\,mm$ on the top and on the bottom to keep symmetry and the pattern of the stacked layers.

Equation 10.11 provide composite strains for a concrete total composite thickness but still only in the xy-plane. To find what strains are occurring for every single layer in the 12-axis plane the Equation 10.12[66] is used.

$$\begin{bmatrix} \epsilon_1 \\ \epsilon_2 \\ \gamma_{12} \end{bmatrix} = \begin{bmatrix} \cos^2(\theta) & \sin^2(\theta) & \sin(\theta)\cos(\theta) \\ \sin^2(\theta) & \cos^2(\theta) & -\sin(\theta)\cos(\theta) \\ -2\sin(\theta)\cos(\theta) & 2\sin(\theta)\cos(\theta) & (\cos^2(\theta) - \sin^2(\theta)) \end{bmatrix} \begin{bmatrix} \epsilon_x \\ \epsilon_y \\ \gamma_{xy} \end{bmatrix} \tag{10.12}$$

Finally, after composite strains are transformed to lamina strains Equation 10.13[66] is considered to determine every layer's stresses in its own 12-plane. For a maximum stress criterion of either σ_1,σ_2 or τ_{12} allowable stress, the layer fails and so does the whole composite.

Normally, the Laminate Theory is universal and defines the composite failure for when the loading comes from different directions where the composite stiffness and maximum strength are different. However, when a composite is loaded only in one direction, for example in the x-axis, then it is easy to provide the ultimate strength of such a composite and to compare it with other materials. For carbon fibre/vitrimer parameters used in this section the multi-layer composite reach ultimate strengths of $540\,MPa$ in a single-loaded direction case.

$$\begin{bmatrix} \sigma_1 \\ \sigma_2 \\ \tau_{12} \end{bmatrix} = \begin{bmatrix} \frac{E_L}{1-v_{LT}v_{TL}} & \frac{v_{LT}E_T}{1-v_{LT}v_{TL}} & 0 \\ \frac{v_{LT}E_T}{1-v_{LT}v_{TL}} & \frac{E_T}{1-v_{LT}v_{TL}} & 0 \\ 0 & 0 & G_{LT} \end{bmatrix} \begin{bmatrix} \epsilon_1 \\ \epsilon_2 \\ \gamma_{12} \end{bmatrix} \tag{10.13}$$

10.7. Main Materials Properties

The main materials chosen for the UAM vehicle are Aluminium 2024, carbon fibre/vitrimer composite and flax fibre/epoxy composite. For this reason the main mechanical properties are summarised in the table below. It should be noted that the strength and stiffness for composites are defined for loading in x-direction of the xy-plane as in Figure 10.4. When the loading changes its orientation these properties may change. Also, the values that are not specified (TBD) for flax fibre/epoxy in Table 10.8 are assumed to be the same as for the carbon fibre/vitrimer in Table 10.9.

Table 10.11: Main UAM materials summary table

Material	**Density** $[kg/m^3]$	**Tensile strength** $[MPa]$	**Elastic modulus** $[GPa]$	**References**
Carbon fibres/vitrimer	1494	540	52.7	N//A
Aluminium 2024	2770	469	73.1	Thomas[14]
Flax fibres/epoxy	1320	200	17.7	N/A

10.8. Composite Failure V&V

The resulting entries of the A-matrix are obtained using a software module provided by Dr.ing. S. G. P. Castro from TU Delft. This software is compared to an existing public ABD-matrix calculator for an additional verification. The online calculator [15], provides the same A-matrix entries for a symmetrical composite $0°/45°$ made of carbon fibre fabrics in vitrimer resin.

Moreover, the composite failure is validated through comparison of ultimate strength in a single load case with existing values. When a carbon fibre/vitrimer fabric layer with $0°/90°$ orientation considered in this chapter is loaded in tension at an angle of $45°$ to the x-axis of the composite it failed at $140\,MPa$. This value does not differ too much from $120\,MPa$ for which an average carbon fibre/epoxy layer with fibre volume of 50% should fail [16].

10.9. Materials Recommendation

The first recommendation regarding materials would be to approach composite failure in a more detailed way. In this chapter the considered failure criterion is chosen to be the maximal stress criterion. However, this criterion only takes into account the maximal stress a layer can handle but not the maximal strain for example. A better approach could be to choose for instance the Tsai-Hill failure criterion which takes into account the interaction between stresses and strains [67]. This means this criterion should be able to predict a failure even when the maximal stress or strain criteria do not.

Another recommendation would be to directly measure some of the composite layer characteristics to better estimate the mechanical properties of a multi-layer composite. This is especially important as for example the Shear modulus and Poisson's ratios for carbon fibre/vitrimer layer are assumed to be similar to the ones for the carbon fibre/epoxy layer. In reality it should be quite straightforward to measure these features experimentally. The same applies to specifying the unknown parameters for flax fibre/epoxy composite lamina.

Recommendations regarding material selection would be to analyze in detail how the change of stringer material from Aluminium 2024 to carbon fibre/vitrimer would effect the frame design through possible thermal stresses and similar effects. Applying carbon fibre/vitrimer could potentially safe some mass on the stringers. Similar point can be made for hubs which also could maybe in later stages of the design change its material to a composite solution.

[14]From: `https://www.thomasnet.com/articles/metals-metal-products/2024-aluminum/`. Visited on 03-06-2022
[15]From: `https://abdcomposites.com/`, Visited on 13-06-2022
[16]From: `http://www.performance-composites.com/carbonfibre/mechanicalproperties_2.asp`.Visited on 13-06-2022

11 Structural Design

The major structural components of the vehicle are divided into 3 parts. The structure supports the propellers, the fuselage, and the undercarriage. Section 11.1, provide different load factors in different stages of the vehicle. Through this, a maximum load factor can be used to approximate forces. These forces are then used in Section 11.2, to approximate structural stresses in the fuselage. Section 11.3 refers to the stress sizing for the undercarriage of the vehicle. Section 11.4 analyses the top structure of the vehicle that attaches the propellers to the body of the vehicle. Section 11.7 to the verification and validation conducted for the complete structures analysis and Section 11.8 refers to future recommendations for a more in-depth analysis of the vehicle.

11.1. Load factor

The design cruise speed has been taken from *UAM-SYS-04* Section 2.1 and is equal to $100\,km/h$ or $27.8\,m/s$. As seen from section 8.3, the maximum cruise speed is set at $134\,km/h$. This can be used to categorise the vehicle as a small rotorcraft in the specification provided by EASA to use different certified load requirements.[1]

11.1.1. Manoeuvring Loads

EASA certification specification 27.337(b) requirement state that small rotorcrafts should be designed for limited manoeuvring loads ranging from a positive limit of 2 to a negative limit of -0.5 [2]

11.1.2. Banking Loads

As the vehicle will have no counteracting rotors and no tail, it is not possible to yaw. All turns will thus be performed by banking the vehicle. The extra lift the vehicle produces is limited by the banking angle ϕ (see Equation 11.1), which also defines the load factor via Equation 11.2.

$$Lcos\phi - W = 0 \tag{11.1}$$

$$n = \frac{L}{W} = \frac{1}{cos\phi} \tag{11.2}$$

$$S = Lsin\phi = Wtan\phi \tag{11.3}$$

11.1.3. Safety Factor

For each load, a safety factor of 1.5 is added. This is implemented to meet the requirements UAM-CON-SFT-EASA-4.1 UAM-CON-SFT-EASA-4.2 seen in Section 2.1.

11.2. Fuselage Design

The primary role of the fuselage in the BonMobile is to house the payload and power unit. This section discusses the design of the fuselage in order to fill the requirements. Subsection 11.2.1 discusses the internal layout of the fuselage and cabin. Subsection 11.2.2 discusses the primary load structures of the fuselage: the ribs and stringer, elaborated further in subsection 11.2.3 and subsection 11.2.4 respectively. subsection 11.2.5 designs the skin of the vehicle.

[1] From: https://www.easa.europa.eu/downloads/1943/enl. Visited on 28-05-2022
[2] From: https://www.easa.europa.eu/downloads/1943/enl. Visited on 28-05-2022

11.2.1. Internal Layout

The fuselage should be able to fit a cabin with passengers. Therefore the size of the cabin must be determined to find the fuselage and therefore structure size. This section will determine the cabin size and approximate the furnishing mass for the UAM.

Requirements *UAM-TECH-ERGO-1*, *UAM-TECH-ERGO-2* and *UAM-TECH-ERGO-3* Section 2.1 specify minimal seat dimensions. To also allow for comfortable vehicle entering, seating and leaving, clearances are added to the minimal dimensions. The seat dimensions and clearances can be found in Table 11.1.

Table 11.1: Required passenger cabin dimensions

Type of dimension	Symbol	Length [m]
Seat pitch	s_{pitch}	0.762
Seat width	s_{width}	0.406
Headroom length	$s_{headroom}$	1.143
Clearance at shoulder height (including armrest)	$s_{clear,u}$	0.250
Clearance at floor level	$s_{clear,l}$	0.150
Shoulder height	$h_{shoulder}$	0.950
Headroom space and top clearance	$h_{headroom}$	1.651

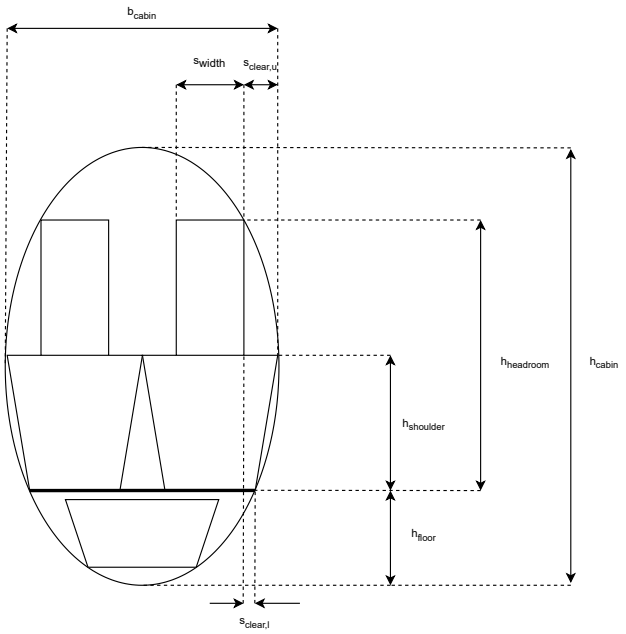

Figure 11.1: Cross-section

These dimensions of the cabin cross-section are graphically represented in Figure 11.1. From this figure, the inner dimensions of the fuselage are determined to be $1.9\,m$ horizontally and $2.55\,m$ vertically. A side view can be found in Figure 11.2 where the longitudinal distance from nose to tail is $3.5\,m$, and the distance from nose to end of luggage space is $2.1\,m$.

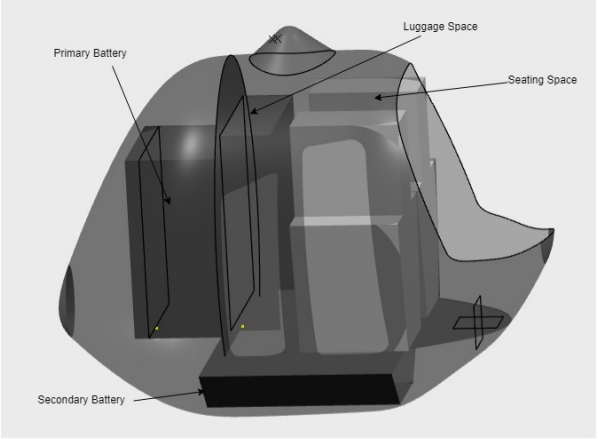

Figure 11.2: Side view

Furnishing & Avionics Mass Estimations
To estimate an initial mass for the cabin furnishing, an estimate is made using Martin Baker aircraft seats[3]. They present aircraft seats with weights ranging from 9.5 to 12.5 kg. These chairs are designed for aircraft loads, which are significantly higher than those of a UAM. Moreover, since sustainability is a main driver and ranges are way shorter than an aircraft, seats will be designed for an, even more, lightweight approach. Therefore the lower limit of 9.5 kg is used as a seat weight estimate for the vehicle. For two seats and a contingency of 6 kg for seat fastening and other user interfaces, a total interior mass of 25 kg is found.

To estimate the mass of the avionics system, a paper by Babetto on the conceptual sizing of autonomous vehicles is conducted [68]. The paper states that avionics weigh approximately 3% of the maximum take-off mass. Using a contingency of 1% on top of the 3% results in a mass estimation for the avionics of 4%. This corresponds to 51.7 kg.

11.2.2. Fuselage Frame Design

From the Sub-section11.2.1, the fuselage width and height can be derived.

There are two major load cases for which the frame of the fuselage needs to be designed. The first load case considered is forward flight. For this load case, the lift force will be acting upon the hub(seen in Figure 11.3) of the fuselage that connects the 12 propellers.

The fuselage needs to be aerodynamic so there are low forces on the skin which would allow for a use of smaller skin thickness for weight reduction. Since the fuselage is not pressurised no major loads are acting on the skin. To distribute the lift and drag force, into small bending moments there are 4 ribs placed which are connected through stringers from the hub. Figure 11.3 shows the design of the frame with ribs and stringers and Figure 11.4 shows how they are placed in the fuselage.

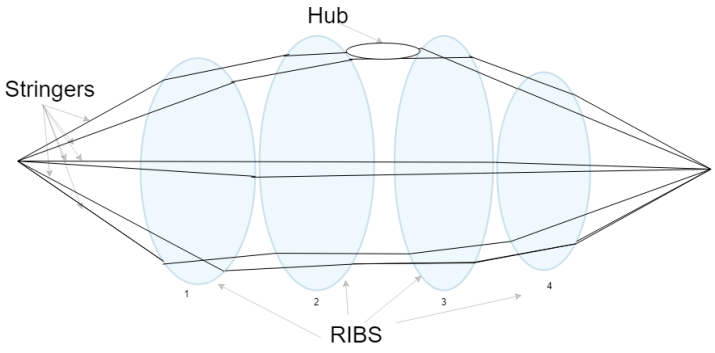

Figure 11.3: The frame of the fuselage

[3]From: `https://martin-baker.com/products/passenger/`. Visited on 24-05-2022.

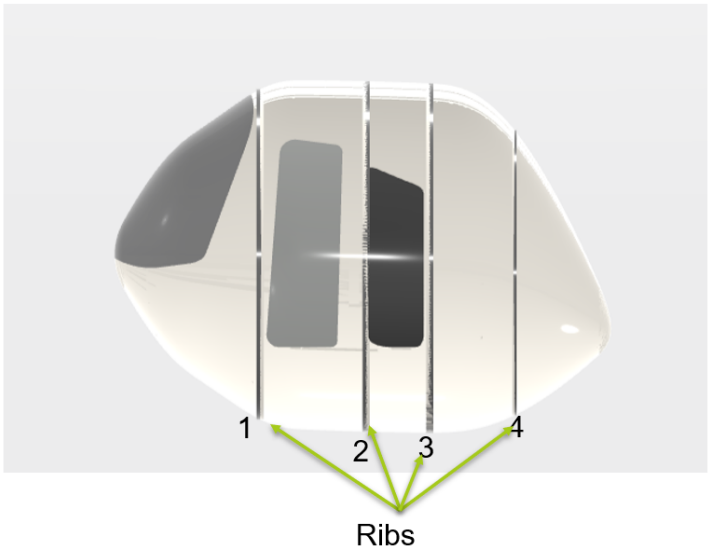

Figure 11.4: Side-View with ribs

The other load Case that needs to be considered is vehicle landing loads. These are considered to be acting directly from the undercarriage to the ribs so that no other structure of the vehicle undergoes high stresses.For the frame, the analysis of these loads is not going to be the critical load case compared to first load case. This load is, however, considered to design the undercarriage in Section 11.3 .

For initial design, a total of 4 ribs and 10 stringers across the vehicle are considered. These are explained further in Sub-section 11.2.3 and Sub-section 11.2.4

11.2.3. Ribs

In the designed UAM vehicle ribs are a crucial part of the fuselage frame which transfers the lift generated by rotors from the supporting structure to the whole fuselage. The vehicle's ribs were modelled as 4 ellipses with dimensions presented in Table 11.2 and depicted in Figure 11.5, l refers to the distance from the first rib. To analyse what loads are transferred through the ribs the structural analysis was performed. The critical region regarding loads for all ribs was deemed to be in the middle of the ellipses, meaning at the level of the semi-minor axis b, see Figure 11.5. This is because when load P is applied at point M, the stresses due to the moment around x-axis induced by force P in the structure should be the highest at point N.

Table 11.2: Dimensions of UAM vehicle's ribs

Ribs	**a** [mm]	**b** [mm]	**l** [mm]
Ribs 1	1041	775	0
Ribs 2	1275	950	615
Ribs 3	1275	950	1065
Ribs 4	1205	900	1815

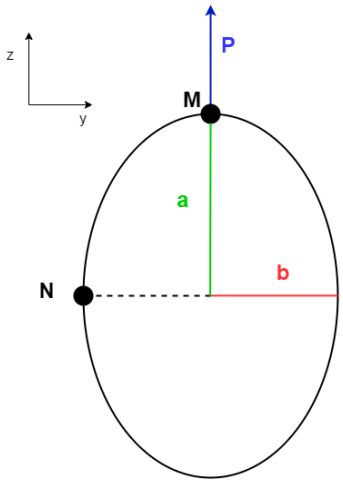

Figure 11.5: The depicted dimensions of rib ellipses with an arbitrary load P and points M,N

However, when for the analysis, all the ellipses are cut at the height of point N on both sides there are 8 fully constrained points. Each has 3 moments and 3 forces to be determined. This makes the problem statically indeterminate. To estimate the reaction forces a free program for solving statically indeterminate problems called *Easyciv* was used. With the help of this program a 3D model of ribs cut in half is visualised in Figure 11.6. The curvature of every ellipse is approximated by 6 beams and an arbitrary load P is applied in the middle between two major ribs. All ribs are also connected using only 1 stringer. This 1 stringer assumption was done for analysis simplification and although it does not reflect exactly the frame design it is believed the stress concentrations and stresses due to bending, in this case, are higher and thus, the ribs should not be under designed.

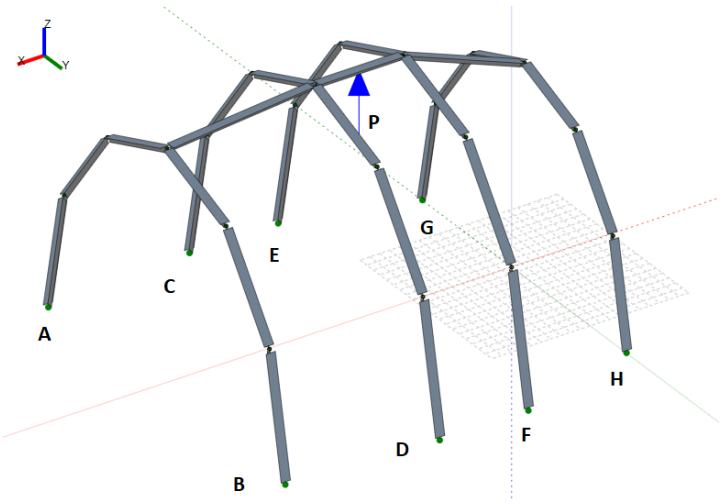

Figure 11.6: The structural analysis of UAM ribs cut in half in easyciv programme [4]

Now to perform the indeterminate analysis of the frame depicted in Figure 11.6 it is necessary to first define the cross-section and the material used. Due to the curved ribs' shape, Aluminium 2024 was picked and the cross-section of the rib was taken to be T-shaped as shown in Figure 11.7. The exact dimensions of the T-shape cross-section are presented in Table 11.3.

[4]From: `https://www.easyciv.com/EasyCivApp.html`. Visited on 15-06-2022.

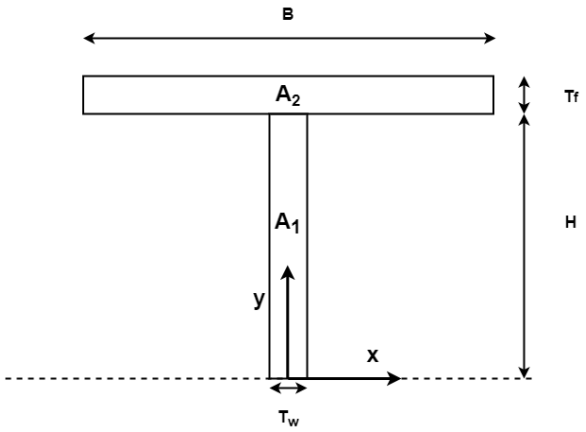

Figure 11.7: Ribs' T-shape cross-section with dimensions

Table 11.3: T-shape ribs' cross-section

Dimension	**Value** [mm]
B	47.0
T_f	3.00
T_w	3.00
H	50.0

These dimensions are the final ones after finalising the iteration process to keep the critical stress below the allowable one in the cross-section for a specific load. In this case for the arbitrary load P a value of $28.2\,kN$ was taken which came from:

$$P = m \cdot n \cdot g \tag{11.4}$$

Where m is the UAM mass from the second design iteration, n is the load factor of 2 and g is the gravity constant.

For the specified load P in every iteration, a set of reaction forces at the constrained points from Figure 11.6 were found by the used software. These were later used to estimate whether the picked dimensions for T-shape cross-sections were enough to prevent failure. A set of such reaction forces is presented in Table 11.4 for load P of $28.2\,kN$ and final dimensions from Table 11.3. Signs of forces and moments refer to the axis system from Figure 11.6.

Table 11.4: Reaction forces for T-shape cross-section from Table 11.3 and P load of $28.2\,kN$

Point	F_x **[N]**	F_y **[N]**	F_z **[N]**	M_x **[Nm]**	M_y **[Nm]**	M_z **[Nm]**
A	31	104	156	-25.2	26.5	-6.3
B	31	-104	156	25.2	26.5	6.3
C	33	-4817	-7263	1235.8	28.2	-6.5
D	33	4817	-7263	-1235.8	28.2	6.5
E	-19	-4709	-7101	1208.2	-14.8	3
F	-19	4709	-7101	-1208.2	-14.8	-3
G	-45	86	129	-17.9	-32.5	7.6
H	-45	-86	129	17.9	-32.5	-7.6

Out of all 6 reaction forces, the design was driven by three forces which highly influence the stress within the cross-section. These were the M_y, M_x bending moments and the F_z tension force which can overlap with resulting stresses and feature high values when compared to other forces and moments as seen in Table 11.4.

From the performed structural analysis it was observed that points C and D will be subjected to the highest loading. This is why the stress analysis was focused on the cross-section at one of these

constrained points, point C. within the cross-section there will be one point where all the stresses will overlap and this will be the critical point to design for. But first, every stress must be found separately.

To do this, for every iteration of the T-shape cross-section the second moments of the area were calculated. This process starts with finding the centroid of the analysed cross-section. For this, the coordinate system as in Figure 11.7 was adapted. Due to symmetry, the x-coordinate of the centroid should be zero and the y-coordinate follows from:

$$y_c = \frac{(H + T_f/2) \cdot A_2 + H/2 \cdot A_1}{A} \tag{11.5}$$

with A as the total area of the cross-section meaning:

$$A = A_1 + A_2 \tag{11.6}$$

with:

$$A_1 = T_w \cdot H \tag{11.7}$$

$$A_2 = T_f \cdot B \tag{11.8}$$

After localising centroid c as in Figure 11.8 the second moments of area needed for estimating stresses from bending can be defined with the help of parallel axis theorem [69] in this new coordinate system y', x' as follows:

$$I_{xx'} = \frac{1}{12} T_w H^3 + A_1 \cdot (H/2 - y_c)^2 + \frac{1}{12} B T_f^3 + A_2 \cdot ((H + T_f/2) - y_c)^2 \tag{11.9}$$

$$I_{yy'} = \frac{1}{12} H T_w^3 + \frac{1}{12} T_f B^3 \tag{11.10}$$

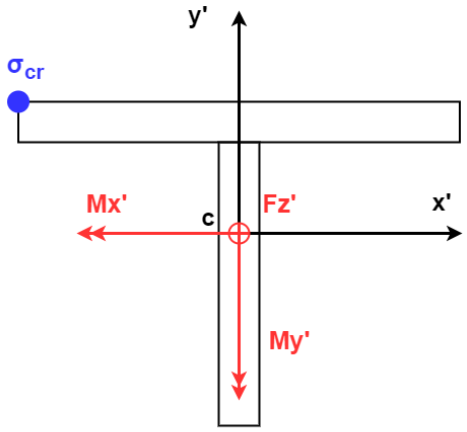

Figure 11.8: Reaction forces at point C acting in the T-shape cross-section of a rib

Now for the further analysis of stresses in the T-shape cross-section using Figure 11.8the coordinate system the reaction forces M_y, M_x and F_z from Table 11.4 must be transformed. This transformation is defined as:

$$M_y' = -M_y \tag{11.11}$$

$$M_x' = -M_x \tag{11.12}$$

$$F_z' = -F_z \tag{11.13}$$

Eventually, the stress due to M_x' and M_y' moment can be calculated. For theses Equation 11.14 and Equation 11.15 are used [69]. As seen in the provided formulas the highest stress should occur the

farthest from the x and y centre possible. This would correspond to one of two corners in the considered cross-section as indicated by σ_{cr} in Figure 11.8.

$$\sigma_{z_{M'_x}} = \frac{M_{x'} \cdot x}{I_{xx'}} \tag{11.14}$$

$$\sigma_{z_{M'_y}} = \frac{M_{y'} \cdot y}{I_{yy'}} \tag{11.15}$$

However, to these bending stresses, the additional tension stress due to F'_z force must be also included. This stress from F'_z is simply found by Equation 11.16. Then the critical stress in the T-shape cross-section can be calculated as in Equation 11.17

$$\sigma_{z_{F_z}} = \frac{F_z}{A} \tag{11.16}$$

$$\sigma_{cr} = \sigma_{z_{M_x}} + \sigma_{z_{M_y}} + \sigma_{z_{F_z}} \tag{11.17}$$

The critical stress obtained from the previous equation should at all times stay below the value of the material maximal strength divided by the safety factor. In case of a safety factor equal to 1.5 and Aluminium 2024 as the material, this critical stress should not exceed 312.7 MPa. The final cross-section dimensions from Table 11.3 this critical stress reach 277.8 MPa.

By knowing the dimensions of the ribs' the total mass of the rib structure can be calculated. For this purpose it is necessary to multiply the material density by the total volume of the ribs as follows:

$$m = \rho \cdot A \cdot L \tag{11.18}$$

Where A is the ribs' cross-section, ρ is density for Aluminium 2024 as defined in Table 10.11 and L is the total ribs length where the length of each rib is estimated by the circumference of an ellipse using:

$$L = \pi \cdot (a + b) \tag{11.19}$$

With a and b as already defined for every ellipse in Table 11.2. These lets arrive at a final value for ribs' total length of 26.3 m which results in a mass of 21.2 kg for all ribs when made of Aluminium 2024.

11.2.4. Stringers

Ribs provide column support for the longitudinal stringers. These stringers then distribute the stresses from different forces and moments acting upon the ribs and skin. From the forces and moments, given in the Table 11.4 analysis of the stringers can be done. Maximum forces and moments can be considered for the analysis.

To start, stringers come in different shapes and sizes as seen in Figure 11.9. Between these options, a rough trade-off must be considered for complexity, stiffness and weight.

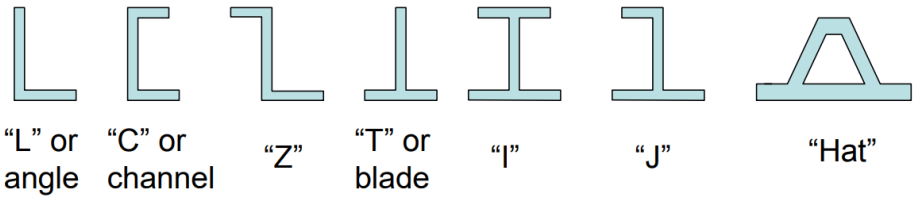

Figure 11.9: Types of stringers

Considering only stiffness it can be expected that the ”Hat” and ”I” shapes are most beneficial, however, the ”Hat” stringer creates closed pockets, which makes it difficult to inspect for corrosion inside the fuselage. Between ”L”, ”I”, ”J”, ”Z”, ”C”, and ”T” shapes ”L” shape can be expected to

be the lightest and least complex and hence, the "L" shaped stringers are used for the stringer. The configuration for this can be seen in Figure 11.10 and.

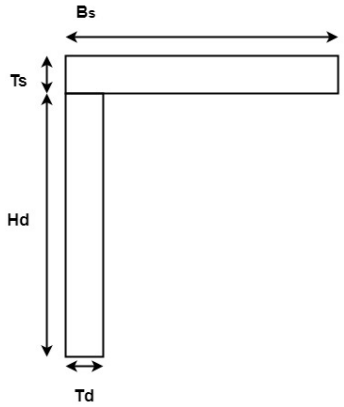

Figure 11.10: L-shaped Stringer

Table 11.5: L-shape Stringer's cross-section

Dimension	**Value** [mm]
B_s	7.00
T_s	1.50
H_d	10.0
T_d	1.50

To approximate the number of stringers, area and placement of these stringers, the cross-section of the fuselage is idealized into booms. The distance between each stringer can be considered equidistant for this design phase. These points can then be calculated using the properties of an eclipse which is the shape of the fuselage. As the major axis, and the semi-minor axis is known. The numbering of stringer and axis is seen in Figure 11.11. Stringer 1 can be placed at the the y-axis at a 0 deg angle from the centre. Using Equation 11.20, coordinates from centre axis of each stringer can be found.

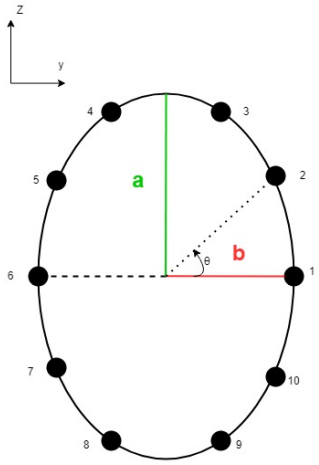

Figure 11.11: Idealised fuselage

$$\begin{aligned} \theta_{st_i} &= \frac{360}{N_S} + \theta_{st_{i-1}} \ |i = 1, 2, N_S \\ z_i &= a \cdot \sin\left(\theta_{st_i}\right) \\ y_i &= b \cdot \cos\left(\theta_{st_i}\right) \end{aligned} \tag{11.20}$$

where N_S refers to the number of stringers, θ_{st_i} refers to the angle of stringer I from the y axis, z_i is the z co-ordinate, a is the radius on the z axis, y_i is the y coordinate, and b is the radius on the y axis.

Based on different load cases, shear, torsion, and moments can be applied to this cross-section in order to calculate the stresses along these stringers. However, the idea is to design for maximum stress based on a material to minimise the weight rather than to check if geometry is feasible or not. The first design parameter that can be treated is the number of stringers. The initial geometry of the stringers used is as seen in Table 11.5. To start-off, it is assumed that all the stringer sizes are the same. Since the cross-section of an eclipse considered, is symmetric on both axis, the centroid and shear centre is at the centre of the eclipse. For the idealised structure, since the ellipse is symmetric on both the axis, a moment of inertia $I_{zy} = 0$. I_{zz} and I_{yy} can be calculated through Equation 11.21the idealised structure. [69].

$$\begin{aligned} I_{zz} &= \sum_{n=1}^{N_s} A_S tr_n \cdot y_n^2 \\ I_{yy} &= \sum_{n=1}^{N_s} A_S tr_n \cdot z_n^2 \end{aligned} \tag{11.21}$$

where $A_S tr_n$ refers to the Area of the stringer.

The first load case considered is a Moment in z and y direction Figure 11.12, moments are defined as positive using the right-hand rule. Using the equation Equation 11.22, the stresses through the moment can be calculated.

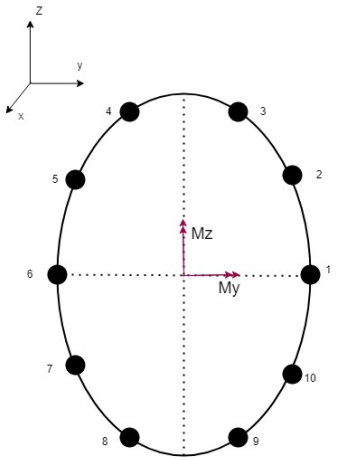

Figure 11.12: Free body diagram under a moment

$$\sigma_x = \left(\frac{M_y}{I_{yy}}\right) z + \left(\frac{M_z}{I_{zz}}\right) y \tag{11.22}$$

M_y and M_z refers to the moment force around the y and z axis, I_{yy} and I_{zz} refers to moment of inertia in y and z axis, z and y refers to distance of the stringers from the centroid of the ellipse.

The results of the stresses produced are shown the Figure 11.13. The stresses produced from the moment loading are low since the vehicle experience low moment. This is because the vehicle is expected to travel at low speeds.

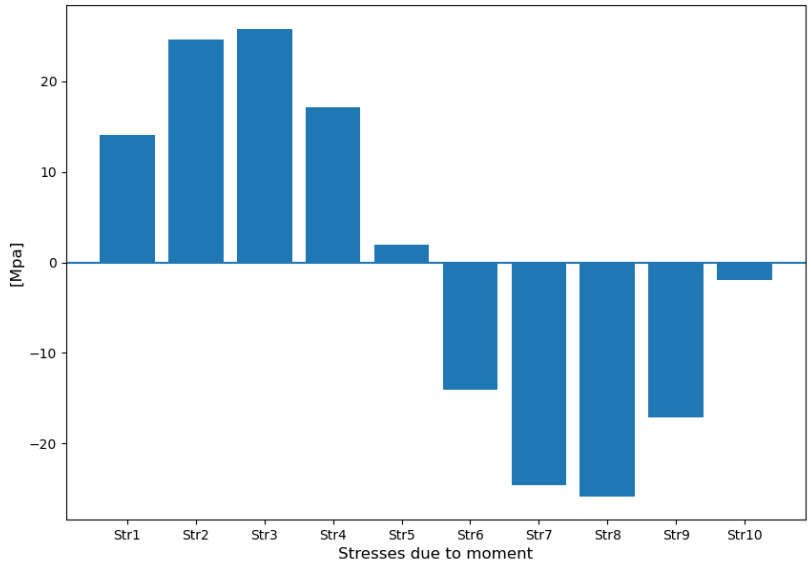

Figure 11.13: Bending moment σ_x for each stringer

The second load case considered is when the cross-section is under shear forces and torsion, Figure 11.14 depicts the free body diagram of the forces and moment considered. To calculate the shear stresses of a closed section, Equation 11.23 is used.

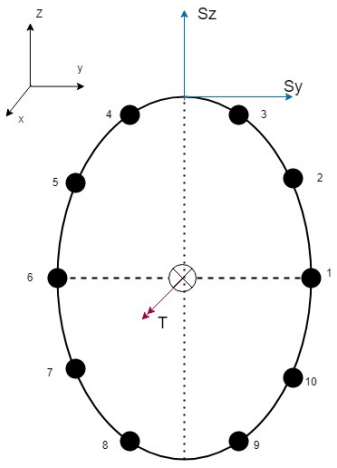

Figure 11.14: Free body diagram under shear and torsion

$$q_{s_n} = q_{b_n} + q_{s_0} \tag{11.23}$$

where q_{s_n} is the complete shear stress due to a certain shear force in section n. q_{s_0} is the shear force translated to torsion to the shear center, where q_{b_n} is the shear force between boom n and $n+1$.

A cut out is made in order to calculate the shear forces for this closed section from start of the ellipse at boom 1 and hence $q_{b_{1-2}} = 0$ and then for each boom Equation 11.24 is used. The torsional moment that is created by the shear stresses at the shear centre is equal to the torsional moment from the shear force and hence an equation for q_{s_0} can be derived Equation 11.25.

$$\begin{aligned} q_{b_n} = +q_{b-1} - \left(\frac{S_z}{I_{yy}}\right)(A_{Str_n} \cdot z_n) \\ - \left(\frac{S_y}{I_{zz}}\right)(A_{str_n} \cdot y_n) \end{aligned} \tag{11.24}$$

$$q_{s_0} = \frac{1}{A}\sum_{n=1}^{N_s} y_n z_n q_{b_n} \tag{11.25}$$

where S_z, S_y is the shear force in Z and y axis, N_s is the number of stringers. A_Str is the area of stringers, z_n & y_n is the distance of the stringers from the centroid.

As it is a closed section, the shear added in the structure due to torsion can be calculated with Equation 11.26.

$$q_t = \frac{T}{2A_m} \tag{11.26}$$

where T is the torsional moment, q_t is the shear from torsion, A_m is the enclosed area of the ellipse.

By summing the results from Equation 11.24, Equation 11.25, and Equation 11.26, for shear forces through every stringer section, the complete shear stress distribution is found. As seen in Figure 11.15, the shear force is highest near the horizontal axis and lowest on the vertical axis.

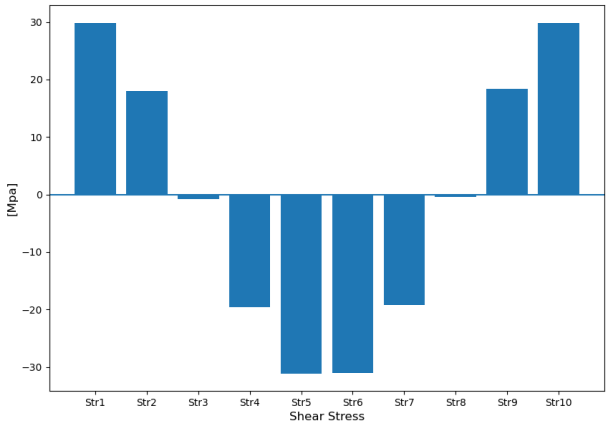

Figure 11.15: Shear stresses throughout strigner sections under Shear force and torsion

This analysis can be done throughout the vehicle, however, the most critical case is going to be at centre of the aircraft whereas shear at front and tip of the vehicle to be nearly zero.

As seen, all the analysis is completed with 10 stringers with the cross sectional values provided. The results from the above analysis and a preliminary estimation of the mass of the stringers is provided Table 11.6. The stringers are expected to run from the nose of the vehicle to the tip, to provide stiffness to the skin overall.

Table 11.6: Detailed Stringer Design

Parameter	Value
Material	Aluminium 2024
Area	25.0 mm^2
Length	3.57 m
Total mass stringer	4.46 kg

To find the optimum number of stringers, the best analysis that can be completed is to design the fuselage with stiffness required for skin. This is not completed for this report, however, it is an analysis that must be completed.

11.2.5. Skin Design

The previous analysis completed in subsection 11.2.3 and subsection 11.2.4 can be extended to find the minimum thickness for the skin of the fuselage that is required to sustain the loads. As mentioned in subsection 11.2.2, due to non pressurised fuselage, there are no pressure forces acting on the skin of the fuselage.

The skin is added to idealisation of the cross-section of the fuselage. The moment of inertia for this can be added to the stringer's moment of inertia by using Steiner's term for the skin as the geometric moment of inertia is a order of magnitude smaller. The moment of inertia then can be calculated by using Equation 11.27 where $d\theta$ can be of the step value 0.01.

$$\begin{aligned} I_{zz} &= \int_0^{2\pi} t_{sk} a^2 \cos^2(\theta) \cdot d\theta + \sum_{n=1}^{N_s} AreaStr_n \cdot y_n^2 \\ I_{yy} &= \int_0^{2\pi} t_{sk} b^2 \sin^2(\theta) \cdot d\theta + \sum_{n=1}^{N_s} AreaStr_n \cdot z_n^2 \end{aligned} \tag{11.27}$$

wheret_{sk} is the thickness of the skin, a is the radius on y axis, b is the radius on z axis, θ is the angle from y axis, the right side of the equation is the same as Equation 11.21.

For moment, Equation 11.22 can be used, from this the maximum bending stresses across the skin is achieved.

The equation for shear flow through skin and boom is given below Equation 11.28, note that the Equation 11.24 was in a numerical solution form, whereas Equation 11.28 is in analytical form, although, it can also be converted into numerical form by removing the integral and summation and calculating shear with a step value to go across the ellipse. To calculate q_{s_0}, Equation 11.25 is used and with Equation 11.23 the complete shear for the section can be calculated.

$$\begin{aligned} q_b = &- \frac{S_y}{I_{yy}} \left(\int_0^{2\pi} t_{sk} acos(\theta) \mathrm{d}\theta + \sum_{n=1}^{N_s} Areastr \cdot y_n \right) \\ &- \frac{S_z}{I_{zz}} \left(\int_0^{2\pi} t_{sk} bsin(\theta) \mathrm{d}\theta + \sum_{n=1}^{N_s} Areastr \cdot z_n \right) \end{aligned} \tag{11.28}$$

Since, both normal stresses and shear stresses are computed, the Von Mises stress can be calculated to see the maximum yield strength required for the skin and stringers combination can be calculated. For the analysis, 1.5mm of skin thickness was considered for initial calculations.

$$Y = \sqrt{\sigma_x^2 + 3\tau_{xy}^2} \tag{11.29}$$

where Y is the Von Mises stress, σ_x is the normal stress, and τ_{xy} is the shear stress across.

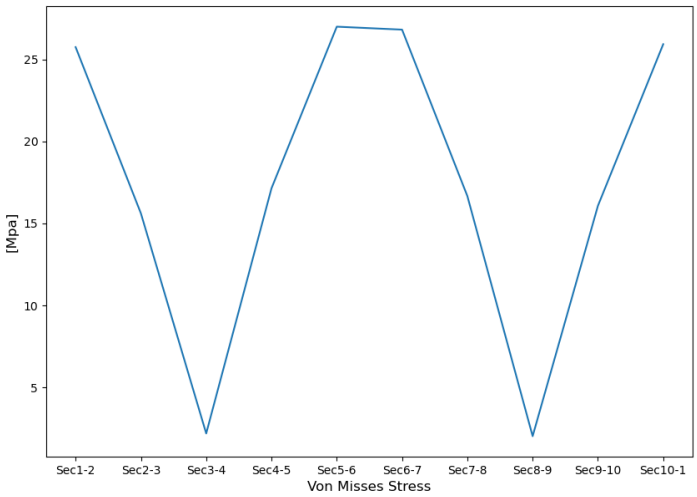

Figure 11.16: Von Misses stress with the skin

As seen from the Figure 11.16 Von Mises stresses that forces expected to impact the skin and stringers are low. However, this analysis does not consider stiffness and buckling, which are more likely to be critical in optimization of skin thickness and number of stringers. The final design material has been chosen to be Carbon-fibre vitrimer because of the low density and high strength properties compared to other sustainable materials available. The thickness is increased to $1.80 m\,m$ as it is required keep the layup symmetric in multiples of $0.600\,mm$ explained further in Section 10.6. Table 11.7 gives detailed properties for the skin.

Table 11.7: Detailed Skin Design

Material	Carbon-fibre vitrimer composite
Area	16.8 m^2
Thickness	1.80 mm
Total mass skin	45.2 kg

11.2.6. Firewall Design

The firewall is the part of the fuselage surrounding the battery, as the battery is the part of the vehicle most likely to catch fire. Since the rest of the interior of the cabin is made out of materials with decreased flammability performance, a firewall is strictly necessary in the design. Its exact location is behind the luggage compartment and below the floor. The material chosen for the firewall is mild steel sheet, coated with aluminium. This choice was made based on the fact that the material needs to be completely fire-resistant, and from all the materials found in list of fire-resistant materials [4], steel has the smallest density, [5] and hence it is the lightest. The thickness needed for the firewall is 0.0180 inches - 0.457 millimeters [6].

The dimensions of the firewall walls are given to be 3.08 m^2 and 2.63 m^2.The total weight of the firewall is then 20.4 kilograms.

[4]From: `https://www.eaa.org/eaa/aircraft-building/BuilderResources/while-youre-building/building-articles/engines-and-firewalls/firewalls`. Visited on 13-06-2022.

[5]From: `https://sciencenotes.org/table-of-density-of-common-materials/`. Visited on 13-06-2022.

[6]From: `https://www.eaa.org/eaa/aircraft-building/BuilderResources/while-youre-building/building-articles/engines-and-firewalls/firewalls`. Visited on 13-06-2022.

11.3. Undercarriage Design

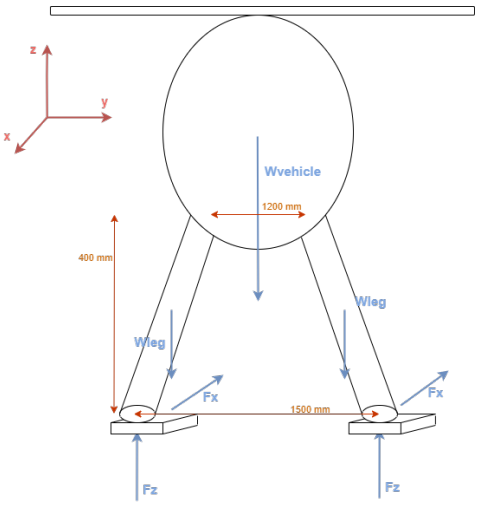

(a) Skid FBD complete vehicle

(b) Example skid design helicopter [1]

In this section the undercarriage structure will be designed. The landing gear design will be a fixed structure, also called a skid landing gear. Skids are simple, light and need very little maintenance, see Figure 11.17b for an example of common a skid design for helicopters. The skid design will be a construction with 4 hollow shafts (the *legs*) and 2 rectangular shaped beams (the *skis*). For a front view and a free body diagram (FBD) of the vehicle, see Figure 11.17a (not drawn to scale). The undercarriage structure experiences the highest loads during landing, so the design is based on the maximum loads occurring in different sections in this phase in operation. The loads and stresses (in the cross-sections) of the two different structures will be discussed in subsection 11.3.1 and 11.3.2 respectively.

11.3.1. Skid Leg Design

Four straight legs will support the vehicle during landing and when standing on the ground. The legs will mostly experience compression loads and thus a circular section is chosen. For minimising the weight, stress calculations are performed on hollow circular shafts.

The height of the legs and the distance between the legs are determined based on the fuselage dimensions and are $400\,mm$ and $1200\,mm$ respectively. The ends of the legs are $1500\,mm$ separated from each other, protruding slightly from the side of the fuselage.

Load and stress calculations require the following inputs:

- Maximum take of weight = $1435\,kg$
- Maximum g force landing = 1.33 g [70] [71]
- Friction coefficient = 0.700
- Safety factor = 1.5

Furthermore a material must be chosen for the skid. The density of the material is required just like the failure stresses in perpendicular and parallel directions to the cross-section. There are several failure modes for materials. A shaft can fail in tension or compression, caused by normal loads and bending. A material can also fail due to shear loads from shear forces and torsion. Figure 11.18 shows the coordinate frame used and the loads and moments acting on the hollow shaft.

The required wall thickness for the hollow shaft is found by fixing a value for the outer radius of the shaft, and then iterating over different thicknesses, and inspecting for which thickness the stresses become too high and the material fails. The top of the shaft connected to the fuselage is a fixed support. The following equations of motion apply (all according to the coordinate frame given):

[1] From: `https://en.wikipedia.org/wiki/Bell_430`. Visited on 20-06-2022

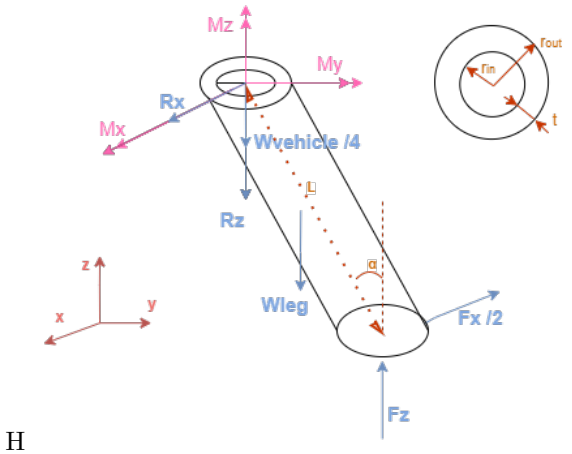

H

Figure 11.18: Skid FBD leg

$$\sum F_x : 0 = R_x - F_x/2 \tag{11.30}$$

$$\sum F_y : 0 = R_y \tag{11.31}$$

$$\sum F_z : 0 = R_z - W_{vehicle}/4 - W_{leg} \tag{11.32}$$

$$\sum M_x : 0 = M_x - W_{leg}(\frac{L}{2}sin\alpha) + F_z(Lsin\alpha) \tag{11.33}$$

$$\sum M_y : 0 = M_y + F_x(Lcos\alpha) \tag{11.34}$$

$$\sum M_z : 0 = M_z + F_x(Lsin\alpha) \tag{11.35}$$

Four kinds of stresses are considered in a cross section; normal, shear, bending and torsion. A member can be in tension or in compression based on the direction of the normal force, while bending stresses create both tension and compression in one plane. The maximum absolute stress for bending occurs at the distance furthest from the centroid, which is r_{out} for a shaft, and taken for the stress calculations. The resultant internal moment in the section due to multiple moments in one plane is given by the vector addition $M = \sqrt{M_x^2 + M_z^2}$. Equation 11.36, 11.37, 11.38 and 11.39 are used for finding the stresses in circular cross section [72].

$$\sigma_{normal} = \frac{P}{A} \tag{11.36}$$

$$\sigma_{bending} = -\frac{My}{I} \tag{11.38}$$

$$\tau_{shear} = \frac{VQ}{It} \tag{11.37}$$

$$\tau_{torsion} = \frac{Tc}{J} \tag{11.39}$$

Equation 11.40 and 11.41 describe the surface area and the moment of inertia of the cross section of a hollow shaft. A circular shaft is assumed, being symmetrical around the x and y axis, thus the moment of inertia is also equal along the two axes. Q describes the first moment of inertia which is the area of the surface multiplied by the distance between centroid and reference axis, and is maximal at the furthest distance from the centre. At last J describes the polar moment of inertia, used for circular sections when torques are present.

$$A = \pi(r_{out}^2 + r_{in}^2) \tag{11.40}$$

$$I = \frac{\pi}{4}(r_{out}^4 + r_{in}^4) \tag{11.41}$$

$$Q = \frac{2}{3}(r_{out}^3 - r_{in}^3) \tag{11.42}$$

$$J = \frac{\pi}{2}(r_{out}^4 - r_{in}^4) \tag{11.43}$$

The thickness required for the four shafts to hold the vehicle can now be found using the knowledge that torsion produces pure shear, and bending produces tensile and compressing stresses. The chosen material has final values for material properties for failure due to total normal and shear forces. For the weight of legs the density of the material is also used. See Table 11.8 for final dimensions for the leg design.

Table 11.8: Details skid leg

Characteristic	Value
Material	Carbon-fiber vitrimer composite
Length	427 mm
Outer radius	50.0 mm
Thickness	4.20 mm
Mass leg	0.806 kg

11.3.2. Skid Ski Design

The design process for the skis follow somewhat the same procedure as the leg design described in subsection 11.3.1. A material is chosen and based on the all loads from the vehicle and legs now an appropriate thickness is chosen. The skis have a rectangular cross section and are slightly curved up at the ends for smoother landings. The width of the skis are the size of the outer diameter of the legs.

The following parameters are updated from subsection 11.3.1 for rectangular subsections. t describes the height of the rectangle.

$$A = w \cdot t \tag{11.44}$$

$$I_y = \frac{w \cdot t}{12} \tag{11.45}$$

$$Q = \bar{y}' \cdot A' = \frac{t}{2} w \frac{t}{4} \tag{11.46}$$

$$\tau_{max} = \frac{3T}{8\frac{t}{2}(\frac{w}{2})^2}[a + 0.6095\frac{t}{w} + 0.8065(\frac{t}{w})^2 - 1.8023(\frac{t}{w})^3 + 0.9100(\frac{t}{w})^4] \tag{11.47}$$

The critical points on the skis occur at the locations where the legs are attached to the skis. The curved edges do not experience any critical loads and are thus not considered in the thickness calculations. The results are presented in Table 11.8.

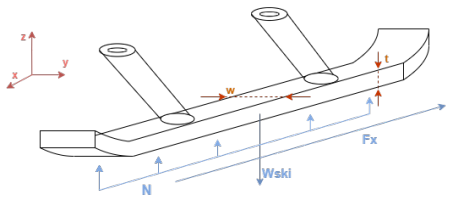

Figure 11.19: Skid FBD ski

Table 11.9: Details skid ski

Material	Carbon-fibre vitrimer composite
Length	2000 mm
Width	100 mm
Thickness	30.0 mm
Mass ski	8.96 kg

11.4. Top Structure Design

The top structure of the vehicle accommodates the twelve rotors that will propel the vehicle. This section will elaborate on the design of the top structure of the vehicle.

11.4.1. Top Structure Lay-out

The lay-out of the top structure accommodates for distributed propulsion of the vehicle, as was decided upon after an extensive trade-off process [5]. Twelve rotors (combination of electric motor and propeller) will be mounted symmetrically over the top structure. The hubs in which the motors are placed are connected by struts. The top structure lay-out concept can be seen in Figure 11.20. This model was made using the 3D modelling program CATIA within the 3DExperience environment.

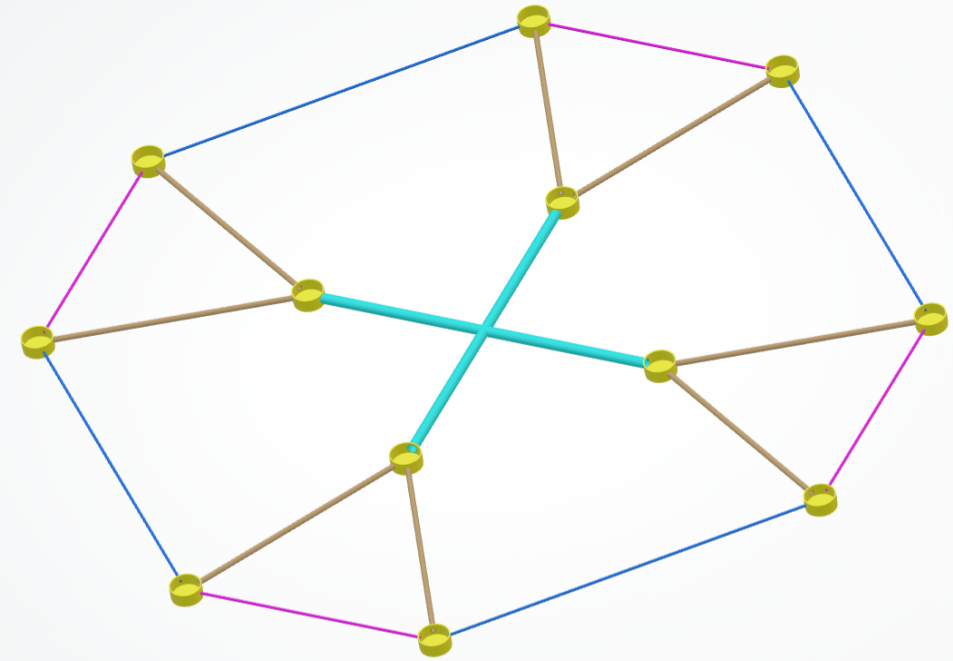

Figure 11.20: Top structure lay-out

The struts connecting the motor hubs were not treated equally. Rather were they split up in four groups, according to the loads that the struts will be put under. This way, the top structure can be structurally optimised and become as light as possible. The four groups are center, inner triangle, outer triangle, and outer struts and can be distinguished by colours light blue, brown, pink, and dark blue in Figure 11.20, respectively.

The lengths of the struts are set as seen in Table 11.10.

Table 11.10: Top structure strut lengths

Struts	**Length [mm]**
Centre	1344
Inner triangle	1900
Outer triangle	1900
Outer	2664

The length of the centre struts was determined by choosing that the top structure would be assembled to the fuselage such that it is fully above the fuselage. This choice was made, because the length of the struts play a major role in the stress and displacement at the root of the centre struts. Therefore, it was aimed to keep this length as short as possible. With the width of the fuselage being 1900 mm, and the centre struts being placed at a 45° angle of the lateral axis of the fuselage, the length of the centre struts was found,as seen in Equation 11.48.

$$centre\,struts\,length = \frac{950}{sin(45°)} \tag{11.48}$$

$$= 1344\,mm \tag{11.49}$$

The inner and outer triangle struts were given the same length of 1900 mm. This length was obtained by taking twice the radius of the propeller, which is 900 mm, as described in chapter 7, and adding a clearance of 100 mm between the blades. The difference between the inner and outer triangle struts is the diameter and thickness of these struts. The inner triangle struts carry more loads and are therefore sized differently compared to the outer triangle struts, as will be described subsection 11.5.2.

The length of the outer struts was not sized for, but adjusted with the length of the centre and triangle struts. The outer and outer triangle struts were sized separately for diameter and thickness.

Important to note is that the lengths of the struts cover the distance from hub centre to the centre of the top structure for the centre struts, and from hub centre to hub centre for the other struts. The strut lengths used in the drag calculations is therefore smaller than the strut lengths stated here.

The diameter of the motor hubs was set to 230 mm, since the chosen electric motor has a diameter of 208 mm, and a hub thickness of 10.0 mm was chosen[7]. The extra millimeter around in the hub will allow for smooth assembly, but will ensure a tight fit.

The length of the hubs was set to 100 mm, and was sized to accommodate connection to the centre struts.

11.4.2. Initial Structural Calculations on the Top Structure

As a first sizing method, it was desired to analytically solve the forces in the top structure. This would help to size cross-sectional areas for stress requirements. However, even a simple analysis, using a rigid structure and twelve point loads turned out to be to difficult to analyse. The structure would be statically indeterminate and needed at least twelve compatibility equations to analytically solve the structure sizing. Therefore, soon after it concluded that a Finite Element Method (FEM) would be more time-efficient. This will be discussed in section 11.5.

11.5. FEM for Top Structure Sizing

As was mentioned in subsection 11.4.2, the top structure poses a statically indeterminate problem. In order to still properly size the structural elements finite element analysis was done on the structure to size the struts for thickness and diameter. This analysis was performed in the appropriate programs within the 3DExperience environment from Dassault Systèmes. These programs are similar to Abaqus by Dassault Systèmes. First, subsection 11.5.1 will describe how the finite element model is set up. Subsequently, subsection 11.5.2 will elaborate on the sizing of the top structure using the finite element model.

11.5.1. Set up of Finite Element Model

Before simulations could be run, the finite element model has to be set up. This process will be described in this subsection.

Combination of Bodies First step in setting up the model is combining all strut and hub bodies into one so called 'partbody'. This way, one mesh is applied to the whole model, which ensures that the applied loads are transferred in the most accurate way between the hubs and struts. Otherwise, all connecting surfaces had to be manually inserted and mesh interactions of the different parts would reduce accuracy of the simulation.

Meshing After combining the bodies, a mesh can be applied to the structure. For this structure, linear tetrahedral mesh elements are chosen, which can be automatically applied to the structure by the program. A mesh size of 10 mm was mostly used for the simulations. The mesh was updated after each change to the geometry of the model, followed by checking the quality of the mesh before running a simulation. Checking the quality is a function within the modelling program and assesses the whole mesh on quality criteria. In the few cases that a mesh size of 10 mm was not sufficient for the mesh to pass all quality criteria, a mesh size of 8 mm was used, which proved sufficient. An absolute sag of 5 mm was used in all simulations. This will be reflected on in subsection 11.8.3.

[7]From: `https://emrax.com/e-motors/emrax-208/#1482059435741-232ed37a-accc`. Visited on 09-06-2022

Load Application Next step is to apply loads to the model. Three types of loads are applied to the model. The first load is the fuselage weight, applied at the centre of the top structure. The second load is the weight of the propeller blade and electric motor, applied as one force at the bottom of the hubs. The third force is the thrust generated by the rotors, applied at the upper side of the hub bottom plates. This thrust is meant to equate to the other two forces. This way, the resultant force, and with that the acceleration of the structure, is kept zero, which gives accurate simulations. This could be compared to the top structure being sized for hover, or non-accelerating flight. The forces applied to the structure can be seen in Figure 11.21, for which it must be noted that the forces are not to scale. The green and yellow shape in the middle of the structure represents the 'inertia relief' function, which is described below.

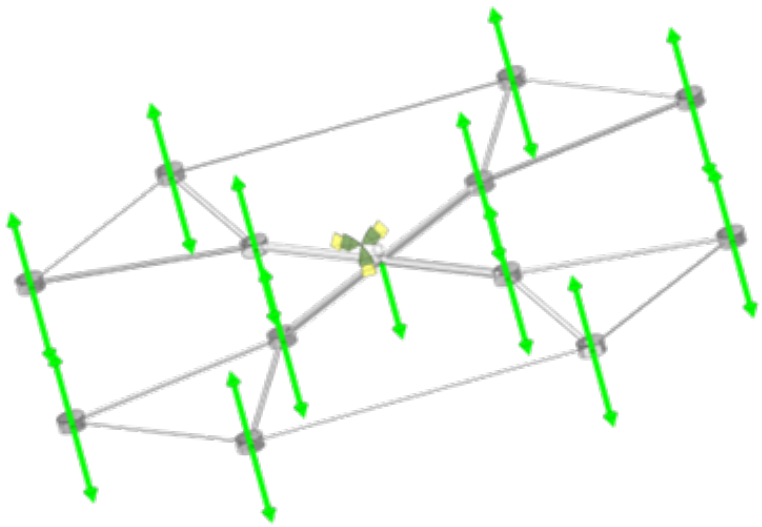

Figure 11.21: Loads applied to model in 3DExperience (arrows not to scale)

The mass of the structure itself is taken into account by using a function called 'inertia relief'. This function applies inertia to bodies that are not constrained, which applies to our vehicle in flight, and with that allows for accurate static analysis of such a body[8]. The material properties for carbon fibre/vitrimer as specified in section 10.7 are applied to the model, from which the density is used to calculate the mass.

11.5.2. Sizing of Top Structure Using FEM Analysis

With the finite element model set up, sizing of the top structure can be done. More specifically, the diameter and thickness of the struts are being determined such that the structure is able to withstand sufficient load, while still keeping in mind the mass of the structure.

Design Stress The strength requirement of the structure is determined by applying a safety factor of 1.5 to the tensile strength of carbon fibre/vitrimer, which was concluded to be $540\,MPa$ in section 10.7. Hence, the stress that the top structure is sized for is $\frac{540}{1.5} = 360\,MPa$. A safety factor is applied to account for assumptions made when estimating the tensile strength of $540\,MPa$ of the new carbon fibre/vitrimer material, as well as accounting for other simplifications made when sizing the top structure (which will be reflected on in subsection 11.8.3).

Initially, arbitrary values of $30\,mm$ and $5\,mm$ were applied to all struts. This resulted in way too high stresses in the centre of the top structure. Therefore, the diameter and thickness of the centre struts were increased until the stress in the centre of the structure was below the design limit.

[8]From: `https://help.3ds.com/2022x/English/DSDoc/SimMecsUserMap/mpm-c-InertiaRelief.htm?contextscope=cloud&id=8698f37989964aad8532dd2e62c734f6` (login required). Visited on: 09-06-2022

Sensitivity Analysis After having over-designed the centre struts, the sensitivity of the stress in the centre structure, as well as the mass and displacement of the structure to changes in diameter and thickness of the struts was determined. This was done in order to structurally optimise the top structure in the most mass effective way. This sensitivity analysis was done by decreasing the diameter and thickness of the centre struts by 10% and determine the percentage change in stress, displacement and mass. The numerical outcome of this sensitivity analysis is presented in Table 11.11.

Table 11.11: Sensitivity analysis of struts

Strut sizing criteria	Stress (MPa)	Displacement (mm)	Top structure mass (kg)
Base situation	307	417	250
10% decrease in diameter	393	539	243
10% decrease in thickness	325	439	246

From Table 11.11 it can be seen that a 10% decrease in diameter results in a $\frac{393-307}{307} \cdot 100\% = 28.0\%$ increase in stress, $\frac{539-417}{417} \cdot 100\% = 29.3\%$ increase in displacement, and $\frac{243-250}{250} \cdot 100\% = 2.84\%$ decrease in mass.

In the case of decreasing the strut thickness with 10%, it can be concluded from Table 11.11 that this results in a a $\frac{325-307}{307} \cdot 100\% = 5.86\%$ increase in stress, $\frac{439-417}{417} \cdot 100\% = 5.28\%$ increase in displacement, and $\frac{246-250}{250} \cdot 100\% = 1.96\%$ decrease in mass.

In other words, much more stress and displacement decrease is obtained when the strut diameter is increased, than when the strut thickness is increased, while these two approaches do not differ so much when looking only at mass decrease. Therefore, the approach chosen for the final optimising is to set the strut thickness to a low value and increase the diameter of the struts as much as possible for the structure to stay within the set stress limit. It has to be noted that increasing the diameter of the struts causes more drag from the top structure. However, bringing the weight of the top structure down was deemed more important than keeping drag to a minimum. Namely, a lighter top structure results in a lower total vehicle weight, which may result in less energy required and with that a lighter battery. A lighter battery means a lower fuselage weight, which means that the top structure can be optimised even more etc.

Thickness The thickness of the struts was set to $4.8\,mm$. This was done because of the fact that the thickness of the composite needs to be changed with increments of $0.6\,mm$, as was described in section 10.6, while still obtaining a reasonable thickness to manufacture.

Centre Struts After a few iterations, it was found that the optimal diameter for this thickness is $75\,mm$. The length of the hub was set to $100\,mm$ to account for this.

Inner Triangle Struts After the centre struts, the part of the inner triangle struts close to the inner hub was most critical in terms of stress. With the thickness again set to $4.8\,mm$, the diameter to ensure sufficient strength of these struts is $40\,mm$.

Outer (Triangle) Struts The outer triangle and outer struts were found not to be critical in terms of stress at all. These struts were sized together. For both, a diameter of $20\,mm$ is sufficient. When only looking at stress, a lower diameter could suffice for these struts as well. However, increasing the diameter slightly, made the displacement of the structure stay within reasonable limits while increasing the mass of the structure by only a small amount.

Final Dimensions, Stress and Displacement In total, 28 simulations were run in the process of sizing the structure. The highest stress in, and displacement of the structure are found to be $339\,MPa$ and $425\,mm$, respectively. The Von Mises stress in, and displacement of the structure with its final dimensions can be seen in Figure 11.22 and Figure 11.23, respectively. Von Mises stress determines whether or not a material will yield or fracture, since it compares the stress in a structure to the yield stress of that material, and is mostly applied to ductile materials. Although the ductility of the carbon fibre/vitrimer composite is not yet determined, the Von Mises stress is assumed to be usable to perform

initial top structure sizing with, since no yield stress was defined for the material, but only the ultimate stress to which a safety factor was applied, as was described in subsection 11.5.2. [9]. The final mass of the top structure was determined to be 221 kg.

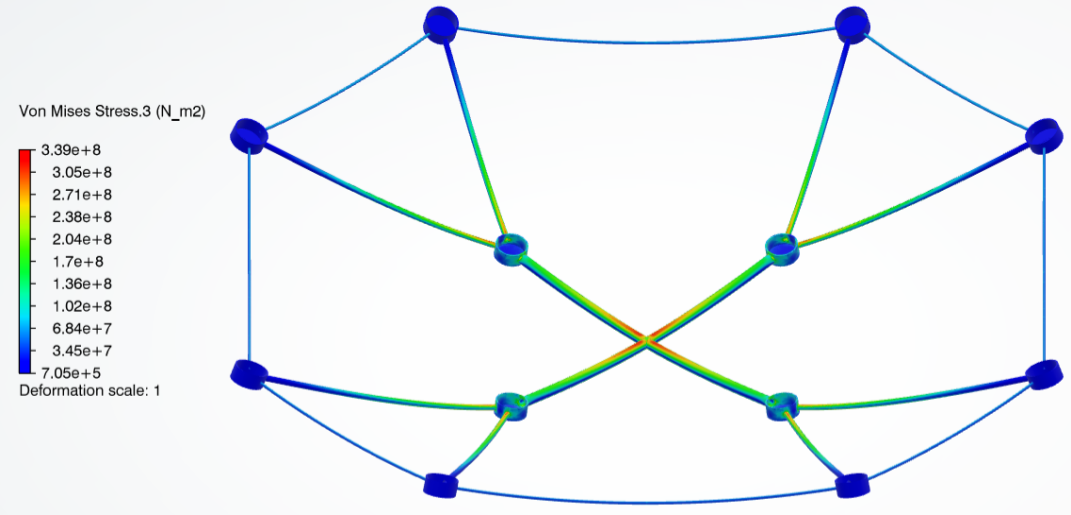

Figure 11.22: Von Mises Stress in the top structure

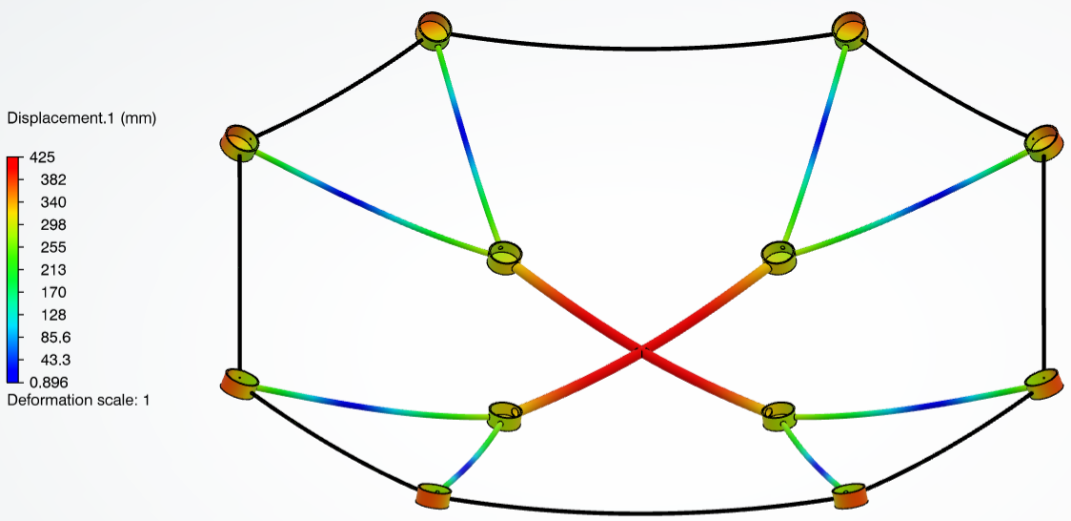

Figure 11.23: Displacement of the top structure

11.6. Results

This section represents an overview and summary of the main dimensions and weights of all subsystems in Table 11.12.

[9]From: `https://www.simscale.com/docs/simwiki/fea-finite-element-analysis/what-is-von-mises-stress/`. Visited on 20-06-2022

Table 11.12: Structure summary - dimensions and weight

Subsystem	Type	Dimensions	#	Total mass
Cabin	Interior	width: 1190 mm height: 2040 mm		25 kg
	Avionics	-		51.7 kg
Ribs	T-shape	thickness: 3.00 mm width: 47.0 mm height: 50.0 mm length: 26.3 m	4x	21.2 kg
Stringers	L-shape	thickness: 1.50 mm width: 7.00 mm height: 10.0 mm length: 3.57 mm	10x	4.46 kg
Skin		area: 16.8 m^2 thickness: 1.80 mm		45.2 kg
Skid	Leg hollow circular shaft	thickness: 1.80 mm diameter: 100.0 mm	4x	0.806 kg
	Ski rectangular beam	thickness: 30.0 mm width: 100 mm length: 2000 mm	2x	8.96 kg
Top	Struts	centre length: 1344 mm inner triangle: 1900 mm outer triangle: 1900 mm outer: 2664 mm		221 kg

11.7. Structure Verification & Validation

This section will elaborate on the verification & validation done for all parts of the structures design.

11.7.1. Fuselage: Verification

Determining the reaction forces in the ribs during the stress analysis is a crucial step for the whole rib design. It was thus, made sure that the free software *Easyciv* used for this purpose had been previously verified. This had been done by the authors of the software in their manual where a structure with theoretically predicted reaction forces was compared to the one put in the software[10]. The difference between the theoretical and software reaction forces was never higher than 0.68%. Additionally, it was concluded that this difference most probably is a result of neglecting the change in length of used structural members in the theoretical method.

Moreover, for the ribs' T-shaped cross-section a sensitivity analysis was performed to analyse how the critical stress changes when crucial dimensions H and B from Figure 11.7 are modified. In the graph it can be seen the relation between critical stress with H and B is not linear but rather quadratic. Also, it is visualised that the current dimensions, as specified in Table 11.3, let the critical stress stay below the allowable one of about $312\,MPa$.

[10]From: `https://www.easyciv.com/manual/EasycivStart.pdf`.Visited on 15-06-2022

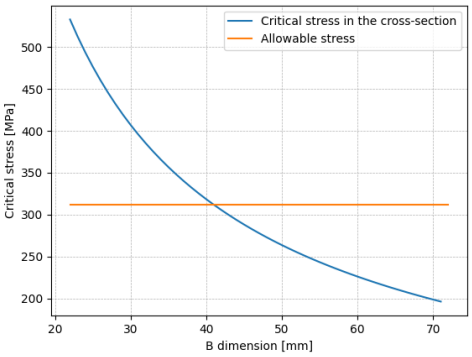

Figure 11.24: Sensitivity analysis of rib's critical stress and cross-sectional dimension B

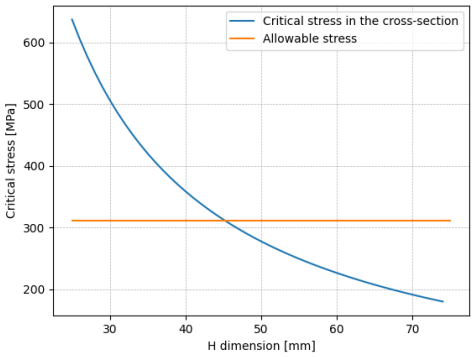

Figure 11.25: Sensitivity analysis of rib's critical stress and cross-sectional dimension H

11.7.2. Fuselage: Validation

The validation of the stresses in the fuselage is conducted by comparing the BonMobile's fuselage to the fuselage of an aircraft. As in terms of structural components they are similar. The idea is to find analytical solutions for particular load cases that can be comparable to the load cases found in the BonMobile. Figure 11.26 and Figure 11.27 [73] can be compared to Figure 11.13 and Figure 11.15 respectively. It is seen that the location and direction of stress along the cross section are similar to the results found.

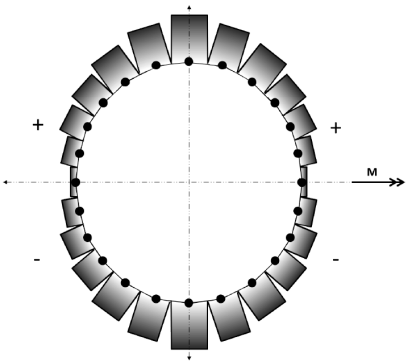

Figure 11.26: Aircraft fuselage analysis due to bending moments

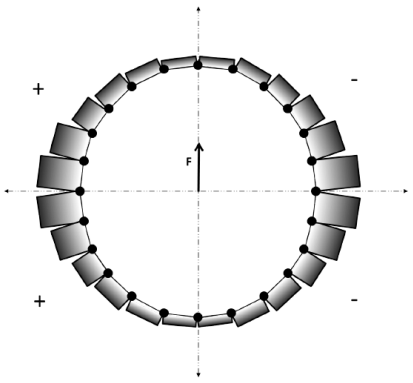

Figure 11.27: Aircraft fuselage analysis due to Shear

Furthermore, a comparison between magnitudes can be completed by creating a model in CAD and by perform finite element model on the frame of the fuselage in order to verify these results. Another validation method is by manufacturing smaller scaled models and running stress tests on them to see deflections that can be expected in the frame. Similar deflections can also be derived for the current stresses along the frame analytically and then validated by the actual test model.

11.7.3. Skid Landing Gear: Verification

Verification of the model built for undercarriage sizing has been performed with unit testing. Unit tests are put on multiple blocks in the code. Extra tests are performed on the stress calculations in the sections for all four stresses separately.

Friction coefficient and landing g-forces are adjusted to see if that influences the thicknesses for the skid components to expectations. Changing the friction coefficient influences the leg dimensions. Logically thinking, increasing the friction coefficient would have an influence on the skis and not affect the legs. However the contrary is true. Loads due to friction will not be the critical loads, as the loads will be spread out over the lengths of the skis. Higher g-forces cause higher stresses in the members that can be compensated by higher thicknesses. And indeed, for higher landing g-forces the thickness calculator

gives higher thicknesses as output.

11.7.4. Skid Landing Gear: Validation

The model and skid sizing can be validated by two methods. First a thesis by K. Shrotri was consulted, which stated that replacing conventional metals for skid landing gear designs by composites can save up to 49% of the total weight [74]. Filling in material properties for the conventional aluminium 7075 series result in a total mass of 46.41 kg. $46.41 \cdot 0.49 = 22.74kg$, whereas BonMobile's skid weights 21.16 kg, only being a difference of 6.9%.

Second validation method was performed with use of an investigation by D. Crist and H. Symes on helicopter landing gear designs[75]. The book states that the skid landing gear design accounts for 1.49% of the basic structural design gross weight, which is 20.04 kg. This is only a 5.4% difference with BonMobile's skid design. Both validation methods with literature show that the performed undercarriage structure design is once 6.9% below and once 5.4% above the estimated mass of the skid. This together confirms the validity of the written program.

11.7.5. Top Structure: Verification & Validation

Regarding verification, the 3DExperience programs are assumed to be verified software. Next to that, it is assumed that the mesh generation functionality and subsequent calculation sequence is validated by the developers for different structures. Also, as mentioned before, mesh quality was assessed before performing each simulation, which verifies proper mesh generation, as well as validates that a suitable mesh is used in the simulation. These criteria can be seen in Table 11.13 together with the values for which the mesh element will result in an error and a warning, and what the best value for the mesh element is. All mesh elements are divided into 'good', 'poor', and 'bad' categories based on the specified values for each criterion, from which it is determined whether or not the mesh passes all quality criteria sufficiently.

Table 11.13: Mesh quality criteria with associated values

Quality criterion	Error	Warning	Best
Aspect ratio	10	5	1
Maximal angle	179.9°	160°	70.529°
Minimal angle	0.1°	10°	70.529°
Skewness	0.0001	0.02	1
Stretch	0.1	0.3	1

To further validate the analysis done on the top structure, a physical (scale) model would need to be built and tested, from which the outcome can be compared to the yield stresses and deflections from the finite element model.

11.8. Recommendations on Structure Design

In all the sections in structures no buckling and stiffness analysis was looked at. This is critical for the fuselage frame but also undercarriage and support structure. For future recommendation, with current sizing an in-depth analysis of these can be looked at. Other structural property that needs to be looked into is fatigue. As this vehicle is designed for taxi, the number of loadings and the structure design needs to fill the requirement of minimum 15 years.

11.8.1. Fuselage Recommendation

In the rib design out of 6 forces only 3 the most influential once were considered. However, to design the ribs in detail all of the appearing reaction forces should be taken into account. This also means that interaction between the shear stress and the tensional stress should be analysed. Moreover, to avoid overdesigning the ribs, the structure put in the *Easyciv* should have a less simplified frame body structure meaning the 1 stringer assumption should be substituted with the real number of stringers and their real position.

11.8.2. Skid Landing Gear Recommendations

For the design of the landing gear a simple structure was chosen, consisting of four straight hollow shafts attached to the the vehicle on top, and two skis on the bottom. Three discussion points and recommendations are shortly discussed in this section.

First, so far, four legs for the skid are considered. However, when adding more legs, the thickness per leg decreases, finally resulting in a lower total weight for the undercarriage structure. However, for the current design, the legs are mounted to the fuselage where the ribs are positioned. The addition of more legs will require more supporting structures in the fuselage. Introducing more support by adding materials increases the weight of the vehicle, and is for this report not chosen to do. In further research a trade-off can be performed on the addition of legs and how that weights up to the additional weight required for extra support.

Second, only basic sizing has been performed, and vibrations are not considered. This skid design performs very poorly in damping, that also being the reason that in other VTOL vehicles, curved legs are often seen. This shape is able to resonant the frequency from the rotors more than the selected design[71], making touch down more comfortable and resulting in lower critical stresses on the legs. Current research investigates optimum energy absorption capacities for skid designs [76]. Future research can continue on this research and investigate sustainable materials optimising this property.

Third, for now a friction coefficient of 0.70 has been taken which does not cover composite materials for landing gear design. In K. Shrotri's investigation on using composite structures as undercarriage material, a friction coefficient of 0.35 was taken[74]. In the following iteration this coefficient will therefore be updated.

11.8.3. Top Structure Recommendations

During the sizing of the top structure, various assumptions were made and limitations to the use of the model were found. These will be split up in several categories and elaborated on in this subsection.

Loads First recommendation is related to the fact that the top structure is not designed for torque loads, which could occur in case one or more motors become inoperative. For example, if one of the outer motors fails, the centre strut on that side is put under a torque load, since the offset load of the other outer motor is not balanced out anymore. The effect of such a torque on the top structure needs to be investigated.

Next to that, the effect of the deflection of the top structure on the amount of thrust required needs to be investigated. That is, because if the thrust vector is tilted by deflecting the structure, essentially less upward lift is created. Since increasing the thrust to compensate for this is expected not to deliver the right solution, as this will cause even more deflection, the suggestion is to investigate shapes of the top structure that are more resistant to deflection under bending moments, while also taking into account the potential occurrence of torque loads as previously mentioned. However, the effect of increasing the thrust as (part of) the solution needs to be further investigated.

Also, the current top structure sizing relies on loading in hover flight, meaning the load from the weight of the fuselage is applied vertically downwards in the centre of the structure, as was mentioned in subsection 11.5.2. However, since the vehicle will be tilted during the climb phase and cruise flight, this load will be at an angle during these phases. This will cause a tensile and compressive load on the part of the top structure phasing up and down, respectively. The top structure needs to be designed for this as well. In terms of pure shear, so the force perpendicular to the top structure, the angled flight will decrease this force compared to the horizontal state. This is therefore not posing additional stress.

Regarding the torque that the electric motors generate: This torque was assumed to be fully reacted to within the electric motor, so no resulted torque is acting on the motor hubs. This will also briefly be touched upon in section 11.8.3.

Model First recommendation is to perform a mesh convergence study on the finite element model. This is done by assessing how much more accurate the result of running the model becomes from refining the mesh. This could also be checked for the use of quadratic elements instead of linear elements.

Next to that, the effect of sag of the mesh on the accuracy of the simulation outcome is recommended to be evaluated. The sag defines the maximum distance between curved geometry and straight mesh

elements[11]. Since the top structure mainly consists of curved elements, this is an important aspect to determine the effect from. As mentioned before, the sag was set at a constant value of $5\,mm$, as was advised by D. Atherstone. For the centre and inner triangle struts, this sag will still give accurate results, as the diameter of these struts is relatively high. For the outer and outer triangle struts, this value for sag might not work as well for the relatively small diameter of these struts. This has to be investigated.

Furthermore, as mentioned in section 11.8.3, the effect of a potential torque on the motor hub needs to be taken into account when designing the connection of electric motor to the hub. Even if there is no resulting force acting on the hub, the effect of the connection of the motor to the hub needs to be investigated in terms of stress concentrations.

Another recommendation would be to include the fact that two different materials are used in the top structure. As described in subsection 10.1.2 and subsection 12.2.2, respectively, carbon fibre/vitrimer composite will be used for the struts of the top structure, and aluminium for the motor hubs. However, as described in subsection 11.5.1, all separate bodies were combined into one body to not have to worry about all contact definitions. The downside of this is that only one material could be applied to the whole model. It was chosen to size the structure for carbon fibre/vitrimer material properties to the model, as the struts are the primary load-carrying parts in the top structure. Therefore, the Young's modulus and yield stress of the aluminium to be used will need to be taken into account for the hubs.

Finally, the top structure is currently only sized with static loads applied. However, it is recommended to also determine how the structure behaves under dynamic loads such as vibrations. Also, the eigenfrequency of the structure needs to be determined to prevent flutter.

Design As described in chapter 6, the cylindrical shape of the struts in the top structure is not the most suitable shape from an aerodynamics point of view. Next to that, this shape is not the most efficient shape in resisting bending. It is recommended to further look into how the shape of the struts can be optimised for both these issues. Since a cylindrical shape does work for a potentially applied torque as previously described, the cylindrical shape might need to remain. To make the struts more resistant to bending, one could look into the possibility of making the struts with a variable thickness, more specifically by applying a higher thickness on the top and bottom parts of the struts. It was discovered during the finite element analysis process that a higher stress occurs on the bottom of the inner triangle struts close to the inner hubs, than on the upper side. Variable strut thickness could also structurally optimise the struts in this regard. The manufacturability of this needs to be investigated, though. In terms of aerodynamics, a suggestion could be to look into applying aerodynamically shaped skins around the struts, which are not load carrying.

Furthermore, wiring running to the electric through the struts has not yet been considered, and it is recommended to do so. However, since the struts have been sized for diameter rather than thickness, as was described in subsection 11.5.2, it as likely that as least the centre and inner triangle struts can already accommodate wiring. For the outer and outer triangle struts, though, this needs more attention, as the low stress levels in those struts resulted in small strut diameters.

Material Behaviour It is recommended to further investigate the following material properties of the carbon fibre/vitrimer composite, and to see how these affect the model and include where possible, to get the most accurate results: buckling of the struts, behaviour under compression compared to tension, fatigue due to displacement of the structure, damage tolerance, yield stress, and ductility. Following from the last two aspects, the usability of Von Mises stress as output and evaluation parameter of the stress in the structure has to be reassessed.

Miscellaneous Finally, the cost of manufacturing different types of struts has to be assessed to see if it makes a difference compared to just manufacture one type of strut for the whole top structure.

[11]From: `https://help.3ds.com/2022x/english/dsdoc/mpmmeshingmap/mpm-t-3dmesh-octree3d.htm?contextscope=cloud` (login required). Visited on: 20-06-2022.

12 Manufacturing, Assembly & Integration Plan

In this chapter, the manufacturing, assembly and integration plan of the BonMobile will be laid out. This chapter, therefore, serves as starting point for processes that should be performed in the post-design phase. First, an overview will be given of the manufacturing, assembly and integration plan in section 12.1. Subsequently, the processes to manufacture the components from raw materials will be explained in section 12.2. After that in section 12.3 a plan for the assembly of these components will be laid out. Lastly, this chapter will explain the integration of all components in section 12.4.

12.1. Manufacturing, Assembly & Integration Plan Overview

Figure 12.1 gives an overview of the manufacturing, assembly and integration plan for the vehicle.

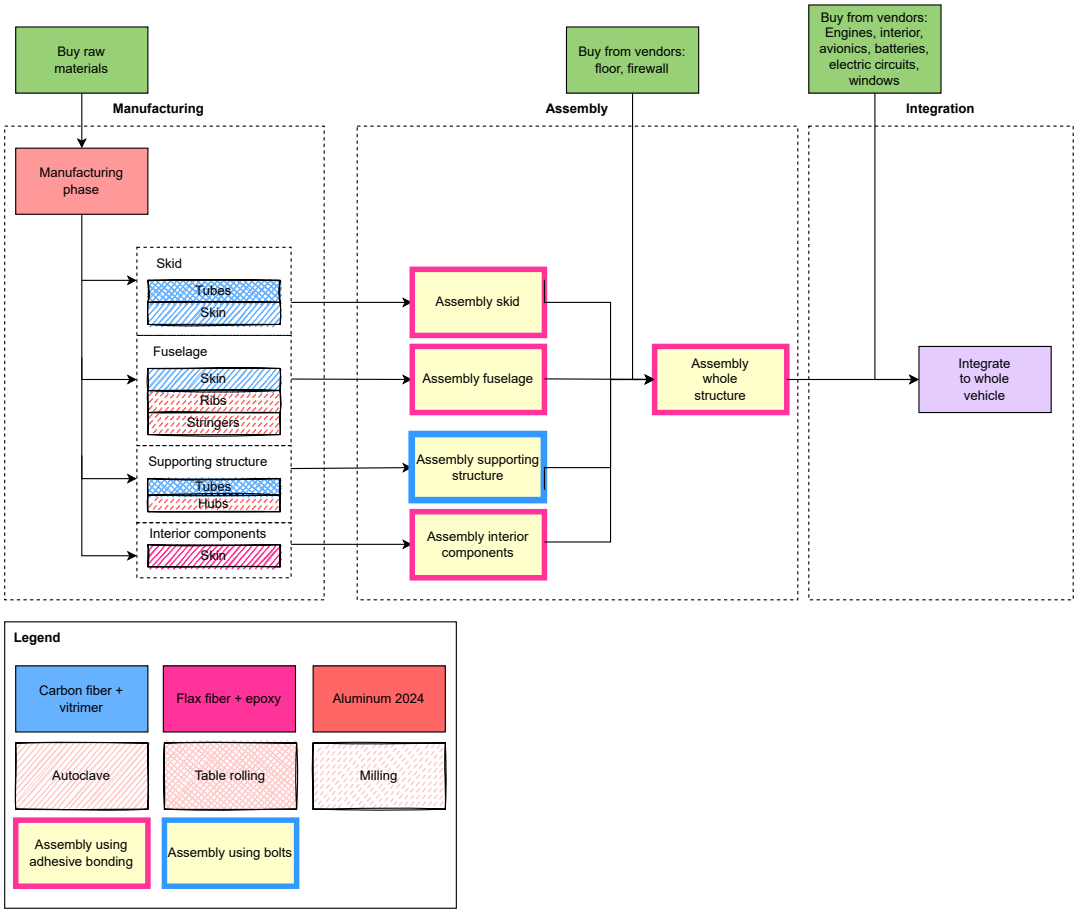

Figure 12.1: Overview showing the manufacturing, assembly and integration plan

As seen in Figure 12.1 the production of the vehicle starts with the manufacturing of components

from the raw materials, mostly recycled. In the assembly, these components are assembled into sub-assemblies which later will be combined in the assembly of the vehicle structure. Only at that moment, the floor and firewall are purchased from vendors. Important is to notice that these components are only purchased after the assembly of the skid, fuselage, supporting structure and interior components. This is done to reduce the storage space needed to store components that will be used in the assembly. Important to notice that this will be done after discussing delivering times and risks with the supplier. Such that the risk of not having a component in place when needed is minimized. Doing so reduces the amount of warehouse needed, hence producing fewer emissions. This is also one of the ways to reduce waste according to the Lean Methodology [77].

After the assembly of the structure of the vehicle the engines, interior, avionics, batteries, electric circuits and windows are integrated into the structure of the vehicle. The interior components earlier produced are used inside the fuselage structure for the finish of the walls. The interior delivered at the integration step is things like the lightning and seats inside the vehicle. Again, these systems are only delivered to the manufacturing facility at the time of finishing the assembly of the whole structure. Such that waste of resources is mitigated.

12.2. Manufacturing

For the manufacturing of components for the vehicle composites and metals are used as raw materials. Table 12.1 shows the various components and materials from which they are manufactured. This section starts off with the manufacturing processes for the composites, after that processes will be laid out for the alloys.

Table 12.1: Materials used for production of parts

Part	Material
Skin	Carbon fibres & Vitrimer
Tubes	Carbon fibres & Vitrimer
Hubs	Aluminum 2024
Ribs	Aluminum 2024
Stringers	Aluminum 2024
Interior components	Flax fibres & Epoxy
Windows	Polycarbonate

12.2.1. Composites

Carbon fibres combined with vitrimer are used for the production of the primary load-carrying structure of the vehicle. This composite is used for the skin and tubes of the vehicle. The windows of the vehicle are made from polycarbonate components. The interior components are made from epoxy and flax fiber composite.

For the manufacturing of the tubes table rolling is used. In table rolling prepregs are wrapped around a cylinder through rolling. By doing so a tube is produced. Multiple sheets of prepregs are used for the production of one tube. This is done to cope with the effect of decreased material properties at the end of a prepreg sheet. For example when rolling up only a single piece of fabric, at some parts along its diameter the tube will have a double layer of fabric. While at other parts only one layer is found. Due to the simple reason that the fabric is not exactly the size of 2 circumferences in length. As a result the thickness of the composites will vary along the radius of the tube. Hence, the tube will have varying material properties along its radius. Using multiple sheets this effect is distributed over the full circumference of the tube. Hence, not creating a local weak point for the tube. After rolling up the material the specimen should be cured. Therefore, the piece is placed in a curing oven. As a result the material is formed into a solid piece that can be used for further assembly of the vehicle [78].

Table rolling is chosen as a manufacturing process for the tubes for sustainability reasons. The sheets can be reused after dissolving the resin. Therefore, this process is chosen over filament winding. In filament winding a long chord of carbon fibres is pulled through resin and wrapped around a mould. As a result recycling of the carbon fibre will be difficult. Only by cutting the carbon fibres into smaller pieces, the fibre can be reused. This will result in significantly lower material properties and thus can be seen as downcycling. Furthermore, table rolling is seen as an option as the tubes have a nonvarying

simple circular cross section, as explained in section 11.4. Concluding, as a result of the advantages with regard to sustainability table rolling is used for the manufacturing of the tubes.

The main advantage of using prepregs is the recycling of the material. The prepregs use already formed pieces of fabric. These sheets of fabric easily can be retrieved by dissolving the vitrimer. By doing so the sheets of carbon fibres can be obtained which can be used in other components for other applications. The vitrimer can be subtracted from the solution and also reused. More information about this process can be found in subsection 15.1.2

The skin of the vehicle is produced using an autoclave process after layup. The skin is built up from prepregs such that the fibers in the prepregs are easily obtained after dissolving the resin. The prepregs are laid out on top of each other rather than next to each other. Positioning the prepregs next to each other likely will decrease the material properties of the component compared to building up of the prepregs. This is the result of only minor bonding between the fabrics when placing them next to each other. Thus altering the flow of the stresses in the fibres. After the vertical layup of the prepregs a vacuum is applied to the pack inside a bag. Furthermore, the external pressure and temperature are increased. By doing so the curing process of the polymers begins such that a solid component is produced. An example of an autoclave process used to produce a thin sheet is shown in Figure 12.2 [79].

It is decided to use this process and not Resin Transfer Moulding (RTM). In later iterations of the design of the vehicle, an option could be to produce the stringers and ribs out of composites. Therefore it is wise to already build the manufacturing facility for this purpose. As will be explained later in the recommendations these components shall be produced using the autoclave process. Therefore, it is more sustainable to purchase only one machine for both of these processes. Rather than having two setups both for the production using RTM and the autoclave process. Furthermore, autoclaving facilitates the option to use prepregs and thus facilitated the recycling of the fabrics.

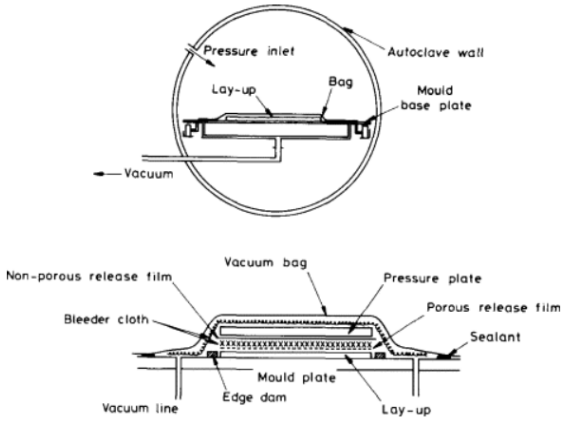

Figure 12.2: Autoclave process for thin sheet composite [79]

The windows of the vehicle are made of polycarbonate components. The windows are produced using injection moulding. As polycarbonate is a thermoplastic the material is heated before being injected into a mould. The polycarbonate granulates will be processed using a tapered screw. By doing so the thermoplastic will be uniformly heated and as a result become a liquid that is injected into the mould. The mould subsequently is cooled such that polycarbonate becomes hard after which the component can be used in further manufacturing of the vehicle. A visualisation of the injection moulding process can be seen in Figure 12.3. Notice that for the manufacturing of the windows a minor tint shade could be added by adding colorant to the process. This extra hopper for this application is shown in the figure [80]. For this manufacturing process this extra tool shall be purchased. This can be seen as waste as only for 100 vehicles this production tool is used, as specified in chapter 4. Therefore decided is the outsource the production of the windows.

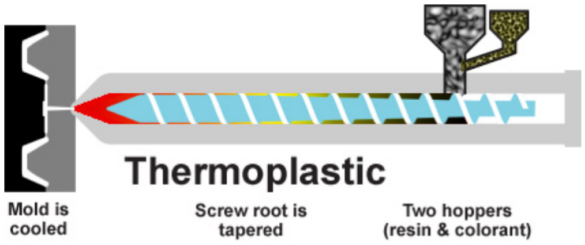

Figure 12.3: Injection moulding process for thermoplastic [80]

The interior components will consist mostly of thin sheets. Therefore manufacturing processes will be similar to the earlier described manufacturing processes for skins using carbon fibres and vitrimer. Therefore similar processes can be used for the production of the interior. The difference will be the use of different prepregs. The interior components will be made of flax fibres and epoxy composite. Therefore temperature and pressure of the autoclave machine shall differ. Outside of this manufacturing processes will be highly similar.

12.2.2. Alloys

In the design of the vehicle the Aluminium 2024 alloy is used. This material is used for the ribs and stringers which will carry most loads. Furthermore, it is used for the hubs of the vehicle which connect the tubes in the supporting structure for the engines. The floor also is made from Aluminium 2024. Lastly, the firewall is made out of steel with an aluminium coating.

The ribs and stringer are made in house through milling. In milling, material is removed to produce the final product. The material removed from the aluminium piece started with can be recycled to be used in other aluminium parts. As milling is an optimal tool to manufacture complex geometry, the machine also can be used to produce the hubs of the vehicle. The additional advantage of milling is that the machine can be used to manufacture various shapes without needing to replace a mould. Therefore, by producing the ribs, stringers and hubs using the same tool, fewer machines are needed compared to the use of a variety of tools. This is also in line with the sustainability philosophy of this project as the use of only one machine for the aluminium alloys means a lower emissions rate. As fewer machines are manufactured and transported and need to have space in the manufacturing facility. Hence, lowering the emissions.

The floor of the vehicle therefore also is purchased from vendors. The floor should be produced through forming. However, this means that such a machine should be purchased which means again extra emissions. Especially, considering that only 100 vehicles are produced only 100 times the forming machine is used. For this reason it would be a waste of resources to make the floor in house. Hence, the floor is purchased from vendors. Similar to this is the manufacturing of the firewall. Producing this part in house means that dedicated machines should be purchased which are only able to manufacture the steel parts. Buying these machines only for these 100 firewalls is seen as waste and therefore the firewalls also will be purchased from vendors.

12.2.3. Manufacturing Recommendations

In current design the stringer and ribs elements are made from aluminium. However, these parts could also be made from composites. The ribs and stringers can be produced by using advanced prepregs. With prepregs of carbon fibres and vitrimer ribs and stringer shapes could be potentially produced. Prepregs are materials in which the fibres and resins are already combined. Using these prepregs shapes can be formed. Doing so for I beams, a built up similar to Figure 12.4a can be made. To cure the materials together the temperature and pressure should be increased. This is done by using an autoclave. The component worked on is placed in the mould of the autoclave on which subsequently temperature and pressure are increased to cure the resin. The autoclave should have a mould to produce the stringers and ribs. In the case of an I-shaped beam, a mould similar to the one shown in Figure 12.4b can be used.

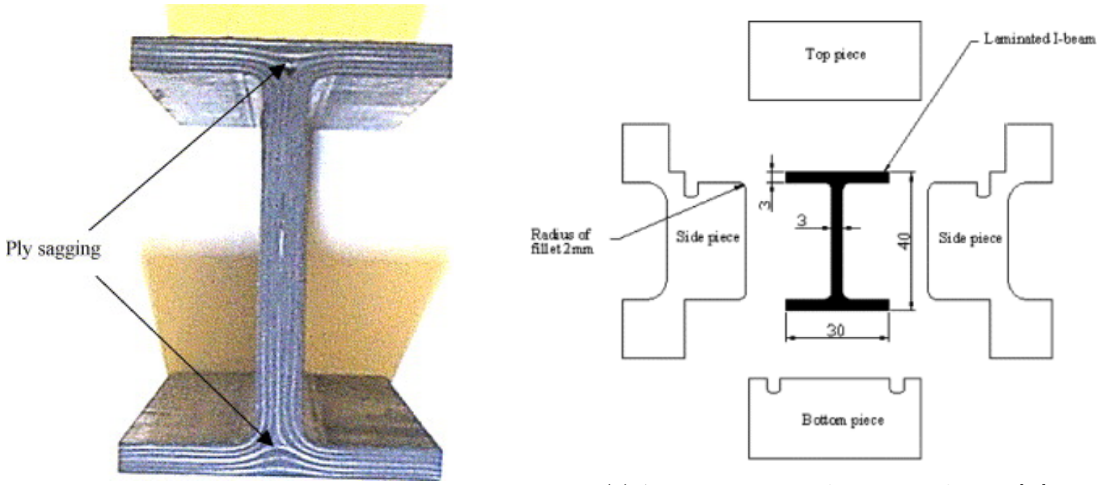

(a) Co-curing method lay up of prepregs for I beam [81]

(b) Autoclave mould used for co curing of I beam [81]

Figure 12.4: Co-curing using prepregs

If the stringers and ribs still would be made from aluminium, it could be an option to consider the extrusion manufacturing process. In this process aluminium is melted and squeezed through a dies. Resulting in less scrap metal compared to milling. Furthermore, it could be the case that less energy is used in extrusion compared to milling. Therefore, it is recommended to investigate the possibility and effects to outsource the production of the stringers and ribs. Under the assumption that production shall be done by extrusion.

12.3. Assembly

Now that all individual parts are either obtained by means of manufacturing or are purchased from vendors, these parts should be assembled. The assembly is split up into two phases. The sub-assemblies of the skid, fuselage and supporting structure and the assembly of the whole structure. In this section first, the type of bondings will be discussed. After that, the sub-assemblies and assembly of the structure will be laid out.

The joining methods being used in the UAM highly influence the sustainability of the vehicle. On the one hand, one wants to minimise the mass related to the type of joining for the vehicle to limit the energy used. However, on the other hand, one wishes to implement modularity to avoid waste in case of a subsystem of part failure. The type of joining methods used for the different structural parts shall be discussed in this section.

12.3.1. Type of Joining Methods

The information on joining methods presented in this section is based on the Production of Aerospace Systems reader by Jos Sinke [80]. Riveting, bolting and adhesive bonding will be discussed below. Welding however will not be discussed due to the limited use of metals in the UAM.

Riveting is a versatile permanent joining method that is commonly used in the aerospace industry. It transfers loads from two parts by shear, as depicted in Figure 12.5.

Figure 12.5: Rivet load transfer[80]

General advantages of rivets are:

- Rivet joints allow for easy inspection and repairs.
- Rivets are readily available in all geometries and sizes.
- Rivets require simple tools and limited skills to install.
- Rivets are generally made from well recyclable materials, namely metals.

General disadvantages of rivets are:

- Rivets may only be loaded in shear. They should not carry axial loads.
- Rivets have limited efficiency, because they require holes in the parts. This creates stress concentrations in the surrounding material and therefore also limits their fatigue life.
- Rivet joints are not air- or watertight and can therefore not be used in liquid-carrying or pressurised areas. This also makes the joints sensitive to corrosion.
- Rivets disrupt smooth aerodynamic surfaces because they are, even countersunk, difficult to smooth them with the surrounding part.
- Rivets are difficult to remove at End-of-Life, limiting or even removing recyclability of the material.

Bolts are a similar joining method to rivets in terms of them being pin-loaded joints. However they have some key differences to riveting:

General advantages of bolting are:

- Bolts may also be loaded in tension, where rivets can only be loaded in shear.
- Bolts are ideal for modularity. They allow for easy detaching and attaching.
- Bolts can be pre-loaded to increase their fatigue life.

General disadvantages of bolting are:

- Bolts and nuts are more expensive then rivets.
- Bolts are generally heavier than rivets.
- Bolted joints are more difficult to fit. They should be fitted with care to avoid unexpected stress concentrations.

Adhesive bonding uses a polymer to adhere two parts permanently. They transfer loads mainly in shear as depicted in Figure 12.6. Tension or ”peel” forces should be avoided since they create high stress concentrations that can disconnect the adhesive. Peel forces are forces applied to remove stickers and tape from surfaces.

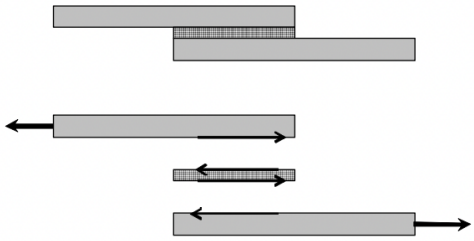

Figure 12.6: Adhesive bond load transfer [80]

General advantages of adhesives are:

- Adhesives are generally very corrosion resistant.
- Adhesive bonds have long lifetime (up to ten times that of rivet bonds) due to the absence of in-plane stress concentrations. They therefore also limit the increase of mass.
- Adhesive bonds can be well air- and liquid tight.
- Although manufacturing is complicated, the bonding process for adhesives is usually less labor intensive than riveting and bolting.
- Adhesive bonds allow for connecting a variety of different materials, like metal to composite, composite to polymer, etc.
- Adhesive bonds do not weaken surrounding material. They can therefore also be applied to more specific structures.
- Adhesive bonds can be applied to create smooth, aerodynamic surfaces.

General disadvantages of adhesives are:

- Adhesive bonding requires complicated manufacturing, like the use of high temperatures and pressures, or autoclaves.
- Adhesive bonding requires extensive pretreatment of the part.
- Adhesive bonded parts are difficult, or in some cases unsuitable, for disassembly.
- Adhesives bonds can only be loaded in shear.
- Adhesives are in general not recyclable and therefore compromising sustainability.

Adhesives are beneficial in terms of stress concentrations and therefore mass, but compromise sustainability. Hence sustainable adhesives are desired. Although few are available today, a possible sustainable adhesive named Plankton is found[1]. The material properties can be found in Table 12.2.

Table 12.2: Properties of the Plankton adhesive[1]

Property type	**Value**
Recyclable	Yes
Glass Transition Temperature	$65°C - 75°C$
Compressive strength	$87 - 112\,MPa$[2]

12.3.2. Adopted Joining Methods

As discussed, it is desired to chose a bonding method that will not compromise sustainability, either by having too high of a mass penalty or compromising the modularity of components. The above presented Plankton can meet these desires better than rivets, bolts and other adhesives. It will save weight since it is an adhesive, but it will not compromise modularity either. This is because the detachment can be performed by heating up the adhesive above its glass-transition temperature of about 70°, which will allow for easy detachment of parts and the adhesive. This high temperature is still considered safe for main materials like carbon fibre/vitrimer composite which glass-transition temperature can reach more than 130°. Once parts are detached the adhesive can be recycled. The parts can be then repurposed, reattached or also recycled due to them being cleaned from the adhesive.

However, few parts will still be joined by making use of bolts, mainly in the propulsion subsystem. The electromotors will be connected to the hubs using bolts, to avoid adhesive failure in case of temperature peaks.

The skid, fuselage and supporting structure are assembled separately. Most bonding's used will be made out of Plankton adhesives. When aluminium alloys are bonded using an adhesive the material first has to be prepared such that the adhesive can bond properly. This is done by activating the material's surface by cleaning, roughening or by similar surface treatment. Important is to notice that

[1]From: `https://livingrconcept.com/wp-content/uploads/sites/7/2022/06/TDS_Plankton.pdf`. Visited on 10-06-2022.

[2]The difference in compressive strength comes from the filling of the Plankton, see[1].

regarding the exact application of different bonding types further research should be done. Furthermore, residual stress which can occur during adhesive curing when bonding two different materials with different thermal expansion coefficients should be investigated. The same goes to a possible galvanic corrosion between carbon fibres and aluminium once these materials are in contact.

Furthermore, residual stress which can occur during adhesive curing when bonding two different materials with different thermal expansion coefficients should be investigated. The same goes to a possible galvanic corrosion between carbon fibres and aluminium once these materials are in contact.

After the sub-assembly of the skid, fuselage and supporting structure, the whole structure of the vehicle can be assembled. These sub-assemblies are combined with the components purchased from other companies. Most bonding's again will be adhesives because of the advantages given in subsection 12.3.2. However, further analysis should be done on the exact results of this decision.

12.4. Integration

The integration focuses on the placement of all the systems inside the structure. Important is to take into account the accessibility of components for maintenance and replacement.

First avionics will be placed inside the fuselage structure. The avionics are placed by moving them through the front window of the fuselage structure. Subsequently, the electric circuit can be placed in the vehicle and connected to the avionics. In the meantime the engines can be placed in the supporting structure. Lastly, the interior components are fitted through the windows and placed inside the fuselage. Other interior components like the Interior lights and carpets are also integrated into the design. After which the windows are placed in the vehicle. Finally, the batteries are placed in the vehicle. This is the final step as the design is made such that batteries can be replaced easily. As a result, reducing downtime and thus profit for the customer of the vehicle. In addition, the batteries will degrade in time, however as the vehicle shall be used for a longer duration the batteries should be easily replaceable.

13 Risk & RAMS Analysis

This chapter aims to give an overview of the technical risk management for this project. Section 13.1 aims to describe the technical risks, section 13.2 aims to give an overview of their probability and impact, while the section 13.3 talks about risk prevention/contingency plan to describe ways to prevent and mitigate their consequences. Section section 13.4 aims to give an overview of the safety, reliability, availability and maintainability of the vehicle.

13.1. Risk Identification

This section presents the potential risks that negatively affect the design of the vehicle. The identified risks can be found in Table 13.1.

Table 13.1: Identified risks

Code	Risk
TECH-RISK-01	Legislation on the certification of the fully autonomous system by EASA is not created in time for the launch of the product or is not created at all
TECH-RISK-02	The autonomous system reacts unexpectedly in critical/emergency situations
TECH-RISK-03	Control system of the vehicle is hacked/compromised by external agents
TECH-RISK-04	The performance of vitrimers in aircraft design is not yet fully researched
TECH-RISK-05	The material chosen for the interior of the cabin, flax fiber, may pose a flammability risk
TECH-RISK-06	The performance of natural adhesives (Plankton) in aircraft design is not yet fully researched
TECH-RISK-07	Drilling holes in composite materials used for the cabin/structure might lead to their delamination

13.2. Risk analysis

This section presents an analysis of each of the risks mentioned in the previous section, identifying the probability and impact of each risk. Table 13.2

Table 13.2: Analysis of identified risks

1. Legislation on the certification of the fully autonomous system by EASA is not created in time for the launch of the product or is not created at all	The probability of this risk event is high. Studies show that it is difficult to create reliable verification and validation tools for fully autonomous systems and it is not yet known how long it will take to do so [82]. The impact of this risk event is moderate. Although it might not be possible to fully certify the vehicle before the launch date, it might be possible to still thoroughly test the functionality of its systems together with experts from EASA and ensure it is up to safety standards.

2.The autonomous system reacts unexpectedly in critical/emergency situations	The probability of this risk event is high. Autonomous systems have not yet been fully tested yet. They might never be fully tested, since it is difficult to think of all the possible situations that might arise. Even if the algorithm used is a deep learning one, there is a possibility that it will learn undesirable behaviours, which could compromise the safety of the vehicle. The impact of this risk event is high, since in case the algorithm takes an incorrect decision, lives of passengers on board and potentially of people outside cannot be saved.
3.Control system of the vehicle is hacked/compromised by external agents	The probability of this risk event is moderate. Installation of firewalls and other cybersecurity systems ensure the software is not reachable by external people. Even so, there is no system that cannot be hacked. The impact of this risk event is high, since viruses/malware in the system could compromise its controllability and hence pose a safety concern.
4.The performance of vitrimers in aircraft design is not yet fully researched	The impact of this risk event is high, since it leads to a lot of uncertainty in the design, and it cannot be certain how well these materials perform.
5.The material chosen for the interior of the cabin, flax fiber, may pose a flammability risk	The impact of the risk event is high, since a flammable material in the interior of the cabin poses a big safety risk for the passengers.
6.The performance of natural adhesives (Plankton) in aircraft design is not yet fully researched	The impact of this risk event is high, since it leads to a lot of uncertainty in the design, and it cannot be certain how well these adhesives perform.
7.Drilling holes in composite materials used for the cabin/structure might lead to their delamination	The probability of this risk event is high, since the chosen bonding method (bolting) involves drilling holes in the material. The impact of the risk event is also high, since a delamination of the composite material will lead to the failure of the structure.

Figure 13.1 depicts the probability and impact of each risk before mitigation measures are implemented.

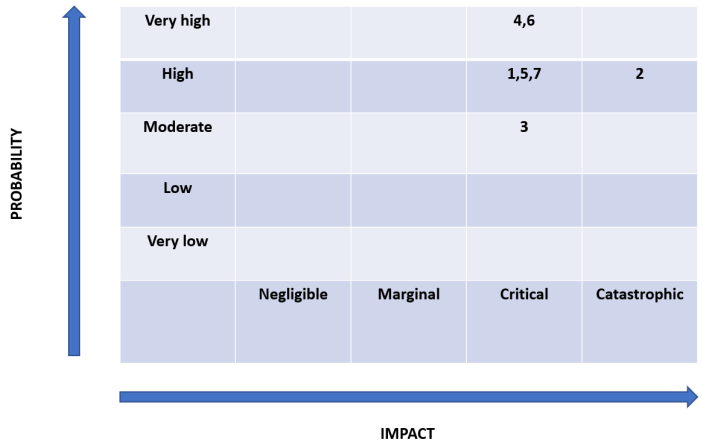

Figure 13.1: Technical Risk Map before mitigation measures are implemented

13.3. Risk prevention/ contingency plan

The following section describes ways in which technical risks can be prevented and their negative impact mitigated. Table 13.3 presents the prevention plans for each risk.

Table 13.3: Prevention plan of risks

1.Legislation on the certification of the fully autonomous system by EASA is not created in time for the launch of the product or is not created at all	The impact of this risk can be mitigated by collaborating closely with EASA and testing the vehicle separately, even when general regulations on autonomous vehicles are not available.
2.The autonomous system reacts unexpectedly in critical/emergency situations	The probability of this risk event can be reduced by putting the autonomous system software through rigorous testing without passengers until it is ensured that safety standards are met. Creating appropriate verification and validation tools for such systems will aid in reducing the impact of this risk event [82].
3.Control system of the vehicle is hacked/compromised by external agents	The probability of this risk event can be by installing appropriate software and firewalls that would make the vehicle less susceptible to cyber attacks.
4.The performance of vitrimers in aircraft design is not yet fully researched	The impact of the risk event can be mitigated collaborating with companies that work with this material and adjusting the design according to their advice/research.
5.The material chosen for the interior of the cabin, flax fiber, may pose a flammability risk	The probability of the risk event can be mitigated by using carbon fibres, which are not are not as flammable, next to critical spots, such as the battery. The impact of the risk event can be mitigated by applying a coating either to the fibers themselves or to the resin, in order to decrease the flammability.
6.The performance of natural adhesives (Plankton) in aircraft design is not yet fully researched	The impact of the risk event can be mitigated collaborating with companies that work with these adhesives and adjusting the design according to their advice/research.
7.Drilling holes in composite materials used for the cabin/structure might lead to their delamination	The probability of this risk event can be reduced by applying appropriate tools - drills with sharp cutting edges and hard substrate [1]. The impact of this risk event can be reduced by careful inspection of the composite material after the drilling. Techniques such as ultrasonic measurements and acoustic emission analysis can be used to check for delaminations [80].

Figure Figure 13.2 depicts the probability and impact of each risk after mitigation measures are implemented.

[1]From: `https://telconpcd.com/how-to-drill-right-to-avoid-delamination-in-composites/`. Visited on 10-06-2022.

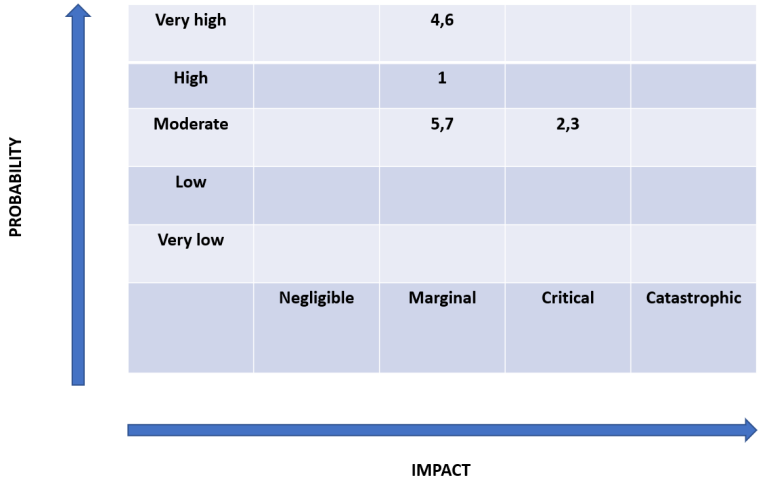

Figure 13.2: Technical Risk Map after mitigation measures are implemented

13.4. RAMS analysis

This section presents an analysis of safety, reliability, availability and maintainability characteristics of the UAM.

13.4.1. List of safety critical functions

- Damage to the automated landing system
- Damage to the automated control system
- Damage to the structure of the cabin
- Damage to one (or more) of the rotors
- Damage to the landing gear leg (the strut connecting the sky to the fuselage)
- Damage (leaking or catching fire) of the lithium sulphur battery

13.4.2. Redundancy philosophy applied

- Recommendation - include a capability of manual/remote control capability of the vehicle in case of emergency
- Recommendation - include a capability of manual/remote control capability of the vehicle in case of emergency
- Safety factor of 1.5 was applied when sizing the cabin structure, hence aiming for a more conservative design
- Multiple rotors (12) were included in the design. Therefore, in case one (or more) rotor(s) fail(s), the vehicle can still remain stable and controllable
- Recommendation - create a design with 6 landing gear legs, as opposed to 4
- The material surrounding the battery, the firewall, was chosen to be made out of steel with aluminium coating, which does not pose a flammability risk

13.4.3. Reliability

A reliable system is one that is able to perform its function as intended. The less complex a system is, the more reliable it is. As the vehicle was designed according to the philosophy that a simple, modular design is more sustainable, this also increases its reliability.

The following requirements on the UAM are determined in order to increase its reliability:

- UAM-SYS-03: The lifespan of the vehicle shall be more than 15 years
- UAM-SYS-04: The lifespan of the structure of the vehicle shall be more than 15 years
- UAM-SYS-05: All modules in the design shall be replaceable

13.4.4. Availability

Availability is the amount of time that the vehicle is available to the clients. For this case, it is the time when the vehicle is not in maintenance, it is fully charged, and it is ready to fly.

The following requirements on the UAM are determined in order to increase its availability:

- UAM-SYS-01: The charge time to 80% energy level shall be less than 45 minutes
- UAM-SYS-02: The turnaround time shall be less than 1 hour

13.4.5. Outline of scheduled and non-scheduled maintenance activities

- Battery change
- Inspection of the autonomous control system
- Inspection of the rotors
- Inspection of the landing gear
- Inspection of the structure for fatigue
- Inspection of the connection of the electromotors to hubs

14 Validation

This chapter will discuss the results of the design and validate these. As this project is still in the design phase, validating if the end product meets the customer requirements is not possible. The biggest part of product validation will be performed with a scaled version of the BonMobile. This chapter does however present two comparison methods that will be used to make a preliminary validation. The first method compares the results of this DSE to a model [83]. The second method compares the BonMobile with operational UAM-vehicles.

14.1. Comparison with a model

In Figure 14.1 a weight estimation with range and cruise speed is presented for multirotor eVTOLs with a payload of 360 kg. The payload of the BonMobile is approximately 30 % less, the BonMobile is therefore expected to have a much lower mass. With a range of 40 km and a cruise speed of 100 km/h the total mass becomes 1900 kg. The BonMobile weighs 31 % less. Because of the exponential behaviour of the total mass seen in both Figure 14.1 and Figure 14.2 this difference is expected to be bigger. This result can be accredited to the fact that the BonMobile is designed to take-off and land twice unlike the multirotor from Figure 14.1.

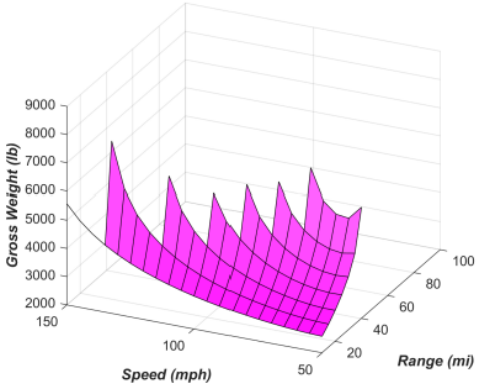

Figure 14.1: Multirotor weight estimation [83]

14.2. Comparison with other vehicles

Currently a lot of UAM-vehicles are in development or are operational. Some companies have published data on these vehicles that can be used for comparison. A big problem with comparing UAM-vehicles with each other is the difference in mass and mission profile. A vehicle with a similar range could still differ in MTOM because of a different payload. This fact should be taken into account when comparing the BonMobile with similar UAM-vehicles. For the comparison, data of 5 other UAM-vehicles is chosen. This data is plotted in Figure 14.2. In both plots the mass of the BonMobile lies a bit above the graph. This fact can again be accredited to the reasoning of the double take-off and landing maneuver of the BonMobile unlike the other vehicles on the plot. If the energy used for take-off and landing would be used for cruise, the BonMobile would move to the right in Figure 14.2a./ as the range increases and the point would thus get closer to the graph.

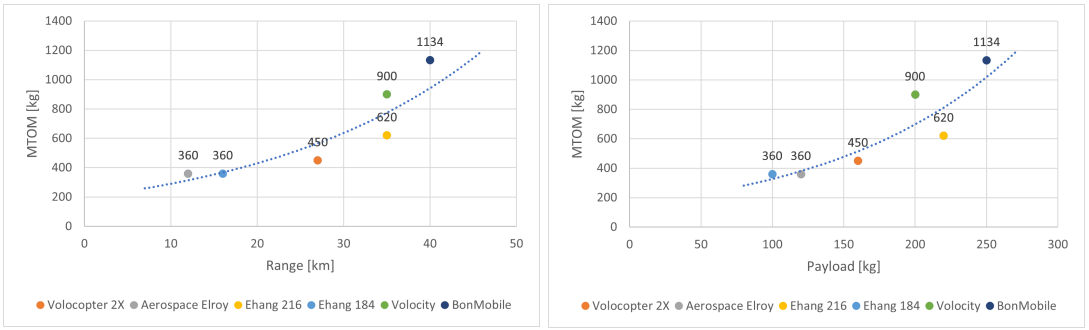

(a) Range against Maximum take-off mass

(b) Payload against Maximum take-off mass

Figure 14.2: Comparison of mass with other UAM vehicles

15 Sustainability

It is aimed that BonMobile will be the first 100% sustainable urban air mobility vehicle on the market. Built from sustainable materials and flying electrically, this vehicle will transport passengers through the urban environment. Achieving this high recycling rate however brings some challenges along. All these will be discussed in this chapter. First, the Life Cycle Analysis (LCA) will be performed in section 15.1 to quantitatively value the environmental impact of the design choices made. Next, the Cradle to Cradle approach for BonMobile is discussed in section 15.2. Finally, the conclusion on sustainability approach is presented in section 15.3.

Three Pillars of Sustainability In order for a product or service to be sustainable, the subject must be approached from three different viewpoints, namely economically, environmentally and socially. From an economic point of view the business should be profitable and have certain economic value. For the environmental approach the natural order is aimed to be maintained by minimising the environmental impact of the service. The social sustainability pillar covers the stability of social and maintenance of cultural systems, and relates to the interrelations between the BonMobile and the urban environment in this case. Regarding the sustainable development of BonMobile, the values of all three pillars are aimed to be maximised as much as possible throughout the whole design and manufacturing process.

15.1. Life Cycle Analysis

This section will present a life-cycle analysis of the UAM, starting with a break-down of the materials presented in Subsection 15.1.1. Next, in Subsection 15.1.2, manufacturing processes for each of the UAM parts are presented. Finally, in 15.1.3 and 15.1.4 end-of-life disposal solutions for the materials are presented. Initially, it was planned that the OpenLCA software would be used as a way to conduct a detailed analysis on the environmental impact. However, after exploring the software and its features more, it was discovered that the EcoInvent database would not be appropriate for an accurate life cycle analysis. This is because the data in the database did not include the new materials used in the UAM - vitrimers and flax fibres. Therefore, it was decided to do a life-cycle analysis based on literature.

15.1.1. Break-down of the vehicle materials

The raw materials used in the UAM are the following:

- Carbon fibres
- Vitrimer
- Aluminium 2024
- Flax fibres
- Epoxy
- Polycarbonate
- Steel
- Lithium Sulphur
- Aluminium 6082
- Hardened steel
- Copper

For each material a percentage value of the total vehicle weight was calculated. One example of such calculation is shown for carbon fibres and vitrimer. As seen in Table 10.6, the supporting structure, fuselage skin, skid and rotor blades are made of this material. The respective weights of these subsystems are calculated in chapter 11 to be 248.46 kilograms, 42 kilograms, 21.16 kilograms and 32.2 kilograms. This represents 26.2 % of the total vehicle weight. For the remainder of the materials, the percentages of the total vehicle weight can be seen in the table below.

Table 15.1: Materials' percentage value of the total vehicle weight

Material	Percentage of the total vehicle weight
Composite carbon fibres	15.72%
Vitrimer	10.48 %
Aluminium 2024	7.4%
Flax fibres	1.14%
Epoxy	0.76%
Polycarbonate	1.64 %
Lithium Sulphur	32%
(Aluminium 6082 & hardened steel & copper with epoxy coating)	8.6%
Steel	1.6%

Some of the raw materials are combined with each other in order to fullfil their purpose. They way in which this is done in the UAM is as follows:

- Carbon fibres and vitrimer
- Flax fibres and Epoxy
- Steel with aluminium coating
- Copper with epoxy coating

15.1.2. Manufacturing processes for UAM vehicle parts

For each of the vehicle parts/subsystems, the manufacturing/production processes used will be listed in Table 15.2.

Table 15.2: Subsystems and their manufacturing methods

Subsystem	Production process
Supporting structure	Table rolling
Fuselage skin	Autoclave
Interior design	Autoclave
Windows	Injection moulding
Battery	Purchased from vendor
Propulsion motors	Purchased from vendor
Rotor blades	Purchased from vendor
(Ribs & Stringers)	Milling
Hubs	Milling
Firewall	Purchased from vendor
Floor	Purchased from vendor

Purchasing the propulsion motors, rotor blades and batteries from the vendor is a recommendation. Further research has to be done on their sustainability.

15.1.3. Disposal/recyclability of the materials present in the UAM vehicle

Recyclability is a significant part of the sustainable approach in the design of the UAM vehicle. Thus, in the following subsections the recycling method is treated for the most important and the most used materials within the design.

Polycarbonate

The polycarbonate used for the windows in the vehicle should easily fulfill expectation regarding recyclability. This is because polycarbonate is a thermoplastic which can be melt once the vehicle reaches the end-of-life or windows get damaged. Such melted polycarbonate can be subsequently used to create new parts or products.

Carbon Fibre/Vitrimer

Finding an appropriate recycling method for carbon fibre/vitrimer composite is especially pivotal. Not only because this composite will account for a greater part of the vehicle structure but also because it consists of synthetic carbon fibres which can happen to be challenging in this matter.

Thus, the choice of vitrimer was well-thought-out with regards to the recycling process. The vitrimer presents special properties which make it a different family of polymers than just thermoplastics or thermosets. These properties make it very similar in terms of mechanical performance to thermosets but nevertheless, it is still possible to heat the material up for reshaping. This is already a great asset which can be used for making new products out of the same prepregs. However, probably the best way to recycle a vitrimer is to dissolve it in acid in a process called solvolysis. Such a dissolved vitrimer resin can be later on used for making new vitrimers in a new set of composites [84]. This enables closing the cycle of vitrimer use. But the solvolysis process is also very beneficial for the carbon fibres which do not have to be cut or damaged in this method. This means that carbon fibres fabrics could be easily retrieved from the prepregs and thus, they could reach 100% recyclability just like the resin. The process of retrieving carbon fibre fabric from a vitrimer is illustrated in Figure 15.1 by Mallinda company[1] producing this type of prepregs.

Figure 15.1: The steps in chemical processing of carbon fibre/vitrimer from Mallinda company[1]

Flax Fibre/Epoxy

Flax fibre/epoxy composite will not be as widely used as carbon fibre/vitrimer composite but its recyclability should also be touched upon. First of all, the main problem in recycling of this material would be epoxy. One of the common methods to deal with it, in order to recycle a composite, is to go through pyrolysis which is a thermal decomposition of the polymer leading to its evaporation. This lets to fully recover the fibres left however, the resin is not of any use anymore [85] thus, the pyrolysis is not really considered as a possible recycling process for flax fibre/epoxy design.

[1]From: `https://mallinda.com/responsibility/`.Visited on 14-06-2022

Nevertheless, it is also possible to approach recyclability of epoxy just like vitrimers through solvolysis by using for instance nitric acid in this case. However, this recycling process is not as efficient as for vitrimers[86]. This method should enable the recyclability of both the resin and the fibres although the natural background of flax fibres should be taken into account when choosing a potential solvent because some of fibre mechanical features could deteriorate during the process. [87].

Aluminium 2024
The process of recycling aluminium has been already quite well mastered nowadays and it should not cause any problems provided that the composition of the used aluminium is well known in advance. It means that Aluminium 2024 can be safely used in the vehicle structure without concerns about its recyclability. At the end of aircraft service Aluminium 2024 can be just cleaned and melted to create new aluminium parts once again. It should be noted here, that the cleaning process of aluminium is crucial. It helps in avoiding unwanted pollution in newly produced parts. It means that any paint or epoxy should be first removed from the aluminium surface by for example dissolving it. Bolts should be removed as well since they can belong to a different aluminium alloy and melting them with the rest of Aluminium 2024 can change the final composition of the recycled material.

It could be also possible to apply the recycled Aluminium 2024 for the vehicle structure from the very beginning, although special care should be taken to ensure the delivered aluminium parts have the element composition identical to clean Aluminium 2024. Nevertheless, it should be considered that parts' properties made of a recycled aluminium alloy may have declined.

15.1.4. Recommendations for recyclability of materials

Regarding the recyclability of the materials it should be examined in more detail how exactly the epoxy could be processed using solvolysis method without damaging the natural flax fibres. It is expected that natural fibres may be significantly affected by the type of the acid used in dissolving the epoxy resin. Thus, finding and proving a solvent not to be really detrimental to the fibres highly influences the composite's recyclability and usefulness. Additionally, it could be worth investigating how flax fibres would behave, especially during the recycling process with a vitrimer resin. So far such a composite has not been offered on the market and thus, the readiness level of such a composite combination is taken to be very low. However, it could be a very interesting domain for further investigation.

Also, a very interesting alternative to the resin in flax fibre/epoxy composite could be the polylactic acid (PLA) which as a biodegradable polymer should be more sustainable than epoxy. The only disadvantage it has is a quite low glass-transition temperature between 50 and 80 $°C$ [62] which may be risky to apply it for aircraft. If a solution is found to increase this glass-transition temperature in a sustainable way then it would be advised to use it with flax fibres instead of using a flax fibre/epoxy composite.

15.2. Cradle to Cradle

Reaching the goal of designing a 100% sustainable vehicle is not only achieved by maximising the value in the three pillars of sustainability. Especially for materials a certain approach must be found to achieve the set goal. This new framework is called Cradle to Cradle Certified® (C2C) [88], which does not try to minimise waste, but use waste as new resources. By keeping the value of the waste or by increasing it (also called upcycling) it mirrors the life cycle of all systems in nature, where the waste of one cycle is the food for the next. Designing for C2C constantly considers whether all design choices positively influence the life cycle of the product.

There are four different levels of cradle to cradle certifications that can be achieved when the product meets the specific requirements; bronze, silver, gold and platinum. A bronze certification shows the intention of a company to improve the way their product is made towards the C2C approach and the three pillars and is the base for all higher level certifications. The product must be eligible for certification and the required documentation must include i.a. a material health assessment and a review of environmental risks. Both deliverables will be discussed in this section.

15.2.1. Product Eligibility

The first step towards C2C certification is a check on eligibility of the product. But since this approach has been followed throughout the whole design process, this can already be checked off. Products

not eligible for the sustainability approach have been cancelled in the first design stages. Examples of products on the list that cannot be C2C certified are weapons, tobacco, products that consume non-renewable fuel, products intended for single use, products with non-optimisable chemicals or raw materials and products not in compliance with local laws and regulations. The last two product criteria are still debatable and will be discussed below.

Lithium as substance in the battery First, the battery chosen as BonMobile's power source is lithium-sulfur. Sulfur is already recycled but lithium currently still comes from raw materials, which negatively influences the environment branch in the three pillars approach. The economic pillar is positively influenced by this new type of batteries compared to Li-ion batteries that are widely used nowadays, due to lower raw material costs. Lithium sulfurs' higher energy density is also cost advantageous. The fact that the battery supplies energy to electric vehicles, replacing cars that emit greenhouse gasses on the roads, contributes to the social pillar of sustainability.

The battery, and thus the whole vehicle, can only be certified provided that it can be optimised. UK's companies InoBat and Green Lithium have started the mission to make lithium's supply chain sustainable [1]. Further development in upcoming coming years and collaboration with Oxis Energy could make the battery fit within the circular vision. An arising risk for this promising business is the dependence on the investment of new production capacity and supply chains, for which close managing is required.

The battery mentioned above is purchased from an external vendor. Special attention must be paid to products or materials from external parties. C2C requires the buyer keep close contact with the supplier. For outsourced services, control on manufacturing process or the origin of materials can be challenging. For any changes that might occur in the supply chain for C2C products, the suppliers are required to inform the buyer. The supplier must also provide the chemical composition and amount of recycled content of their product. Special focus should go to managing all material data and updates over time.

The standard requires that applicant companies identify the environmental risks associated with processes occurring at final manufacturing stage facilities, countries in which the final manufacturing stage facilities are located, the product's supply chain, product use, and product end of use.

Fully autonomous control Second, BonMobile would not be able to be certified yet due to the autonomous control level of the vehicle. Regulations and certifications around the complete autonomy have not been completed. Current infrastructure and air traffic management is not ready for urban air mobility yet, and full autonomy is still in full development. In Figure 2.1, section 2.2, BonMobile's development time line has been discussed, showing that at launch in 2030 fully autonomous vehicles will be certified and local laws and regulations will approve urban air mobility. Therefore, the the vehicle will be eligible for C2C certification.

15.2.2. Material Health

For C2C certification a Material Health Assessment (MHA) must be performed. Within this assessment, scenarios for the product's use, production and end of life must be defined. Below the three phases for the vehicle will be discussed.

BonMobile In Use The vehicle is primary used for passenger transportation. The block diagram in Figure 15.2 made for the Baseline Report [89] shows a functional flow diagram of BonMobile in use. The flow starts at preparing the vehicle for flight, and ends at either (un)scheduled maintenance or retirement of the vehicle.

Production The vehicle is an assembly of multiple subsystems, also called a *multi-component product*. Final assembly of these kinds of products occur at the last facility before shipment to the customer. MHA should include a lay out of the route of exposure at this final facility. And based on the proposed assembly and production processes the product or parts can be assessed for certification. Also special focus must be paid to environmental risks occurring at the final assembly and manufacturing stage

[1] From: `https://inobatauto.eu/newsroom/inobat-and-green-lithium-agree-strategic-partnership-to-advance-shared-sustainabl` Visited on 14-06-2022

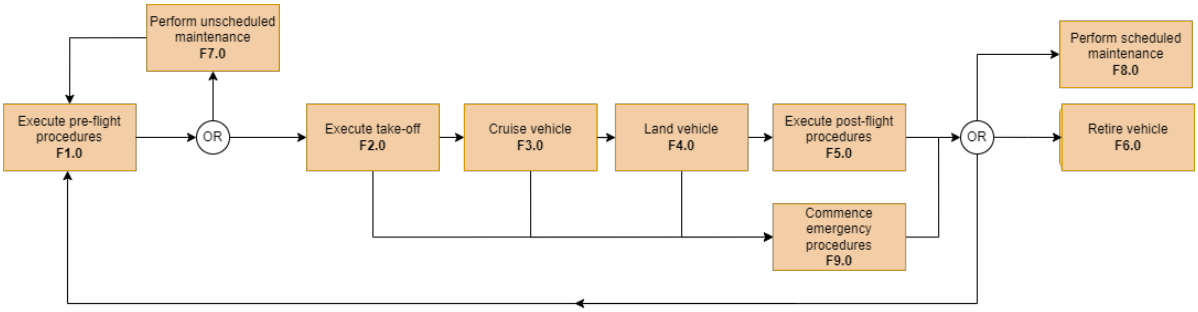

Figure 15.2: Functional flow BonMobile in use

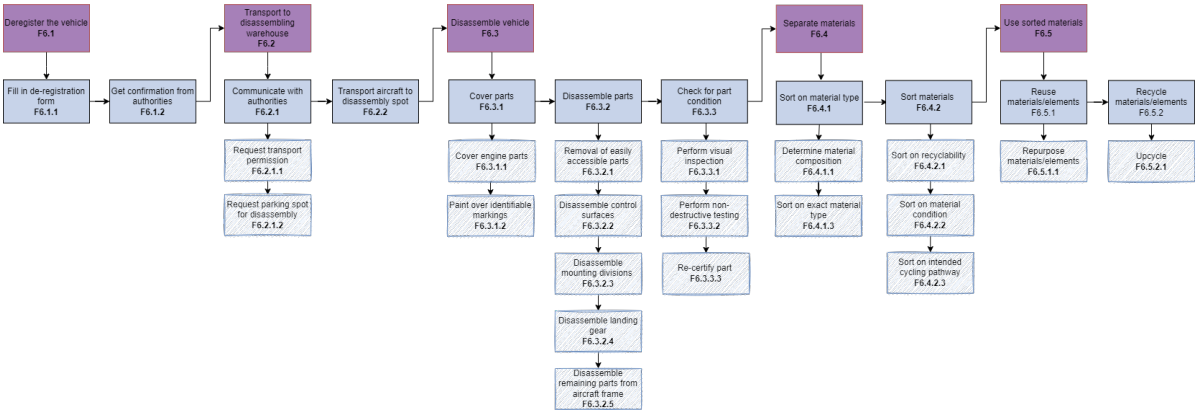

Figure 15.3: Functional flow BonMobile at end-of-life

facilities. Product assembly is covered in chapter 12, and an overview of final manufacturing processes for the different subsystems of the vehicle are given in Table 15.3.

Table 15.3

Category	Final manufacturing process	Subsystem
Carbon fibres & vitrimer	Table rolling, curing, autoclave	Skin, tubes
Aluminium	Milling, forming	Ribs, stringers, hubs, floor, firewall
Polycarbonate	Injection moulding	Windows

End-of-life scenario When the vehicle has reached its end of life, the structure will be disassembled and sorted such that the parts can be reused, upcycled or further processed. The retiring process is visualised in Figure 15.3.

15.3. Conclusion on Sustainability Approach

In order to design a complete environmentally friendly air mobility vehicle, special focus should go into each single design phase considering sustainability. A life cycle analysis was performed to give an insight on where products come from and what happens to them after use. By focusing on the use of all elements before and after use, gaps in sustainability become clear, and extra steps towards a circular economy can be taken. Next to the products being environmentally sustainable, they should also be socially and economically sustainable. Therefore the approach of Cradle to Cradle was used for the design where waste of one product is the for for the next, and ensuring that the product positively contributes to all three sustainability aspects. The performed analysis shows that the aim of BonMobile to get C2C certified was a realistic goal and is feasible for the year 2030.

16 Iterations

An engineering project almost never is a linear process. It involves highly complex collaboration between subsystem departments. As a result, the engineering process itself will become an integrated, iterative process. This chapter will give a general description of how iterations are adopted in this DSE and how they influenced the mass in chapter 16.

16.1. Iteration of Design

In the Midterm Report [5] a MTOM is estimated using class I mass estimation. This mass could then be used as an input to the design of subsystems. From this design phase, a new MTOM is generated, leading to the design of subsystems being iterated. This then again leads to a new MTOM, thus the iteration loop is initiated. Figure 16.1 graphically represents this loop and the influenced subsystems.

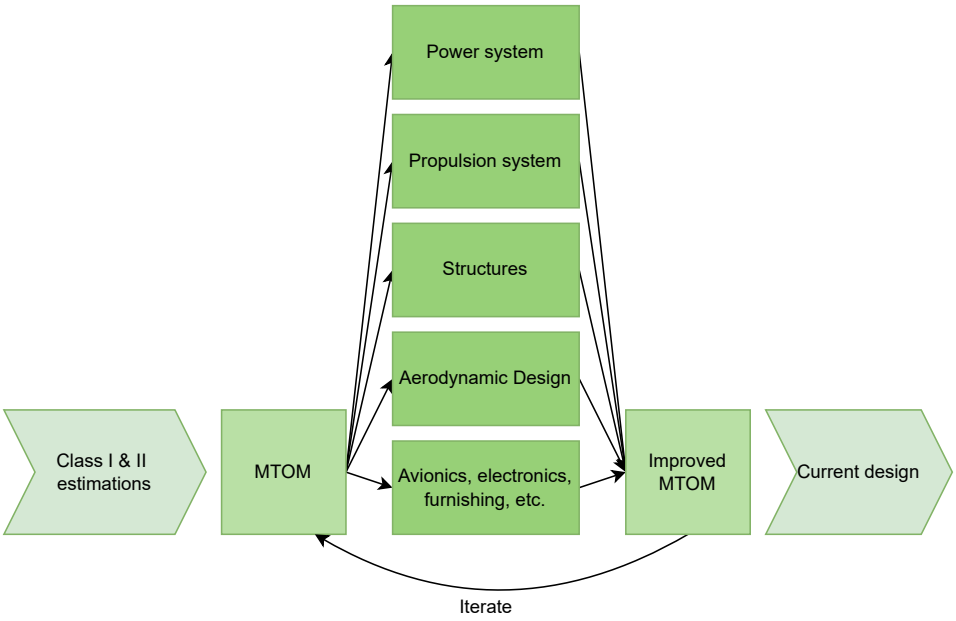

Figure 16.1: Iteration process

A classic phenomenon called the 'Snowball effect' arises from this: if the design of a certain system becomes lighter, and thus a lighter MTOM is calculated, it influences all the other subsystems. The propulsive system needs to provide less thrust, the battery can be smaller and the structure can be sized for lower loads. This in turn leads to an even lighter design, repeating this cycle. However, the snowball effect can also work the other way around: a higher subsystem mass can lead to an increased MTOM and therefore subsystems are sized up, leading to an even heavier design. This effect becomes especially critical for sustainability: a small increase in mass can lead to significant increases in materials and energy used.

16.1.1 Mass Iterations

The snowball described in chapter 16 effect can however not lead to an ever changing mass. At some point the design will converge to a set mass. To find this converged design, it is advised to keep close

track of the iteration process. Figure 16.2 shows the iteration process for the BonMobile's MTOM. From this figure it can clearly be seen that the design is converging in the last three iterations. The last iteration dropped a little over 2%, whilst iteration two and three drop between 7 and 14%. From the figure it is seen that the total MTOM has dropped from 1550 kg to 1134 kg in the five iterations.

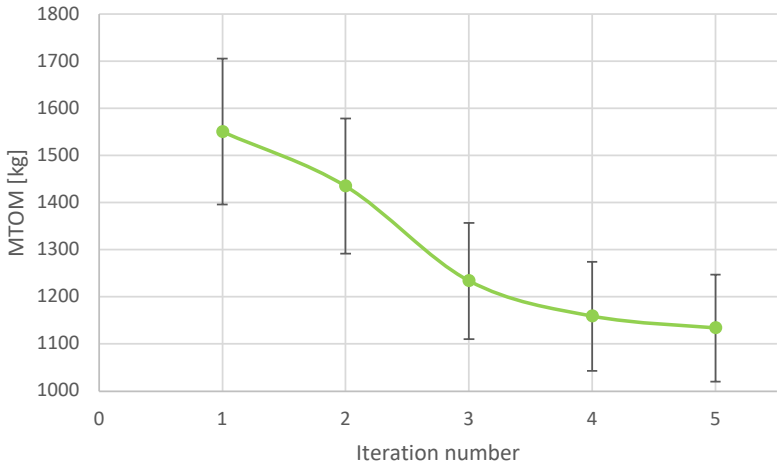

Figure 16.2: MTOM through four iterations

17 Conclusion

Urbanisation is causing traffic conjectures all around the globe. To solve this problem, a solution is sought in the third dimension: the air. However, more vehicles on the road and in the air cause CO2-emissions to be ever rising. This creates so-called flight shame, which makes the solution to urban traffic even more difficult.

This design synthesis exercise aims to solve both the traffic and greenhouse gas emissions problems simultaneously. This leads to the following mission needs statement:

"To provide 100% sustainable air mobility transport to meet growing demands of transport in urban areas"

Through extensive and thorough conceptual designing, the DSE has lead to a preliminary solution to the mission needs statement, called the BonMobile. The BonMobile makes use of 100% recyclable materials, minimises the energy required for flying and is designed according to the Cradle-to-Cradle design philosophy. Therefore, it will pose as one of the first truly sustainable Urban Air Mobility vehicles in the world. Furthermore, proper cooperation with users, stakeholders and infrastructure can give the BonMobile a big advantage on 2030's market, the launch date of the vehicle.

The current characteristics of the BonMobile are presented in Table 17.1. A render of the current design can be found in Figure 17.1.

Table 17.1: Current BonMobile parameters

OEW [kg]	**Payload [kg]**	**No. of passengers [-]**	**Range [kg]**	**Flight time [s]**	**Design speed [km/h]**	**Energy Used [MJ]**	**Turn-around time**
930	250	2	2x20	1921	114	445	<1

Figure 17.1: Render of the vehicle.

The design solution is however yet to be finished. Future design iterations and improvements are required to converge the design. It may lead to an even more sustainable design.

References

[1] Roser M. "Future Population Growth". In: *Our World in Data* (2013).

[2] Becken S. et al. "Climate crisis and flying: social media analysis traces the rise of "flightshame"". In: *Journal of Sustainable Tourism* (2020). DOI: 10.1080/09669582.2020.1851699.

[3] Roskam J. *Airplane Design - Part VIII - Cost estimation*. DARcorporation, 2002.

[4] Urdu M. "Aircraft maintenance cost modelling considering the influence of design parameters". Sept. 2015.

[5] van Alkemade I. et al. *Midterm Report DSE Spring 2022*. Tech. rep. Delft University of Technology, May 2022.

[6] Patterson M.D., Antcliff K.R., and Kohlman L.W. *A Proposed Approach to Studying Urban Air Mobility Missions Including an Initial Exploration of Mission Requirements*. Tech. rep. Phoenix, Arizona: NASA, May 2018.

[7] EASA. *Second Publication of Proposed Means of Compliance with the Special Condition VTOL*. Tech. rep. MOC-2 SC-VTOL. June 2021.

[8] Garrow L.A., German B.J., and Leonard C.E. "Urban air mobility: A comprehensive review and comparative analysis with autonomous and electric ground transportation for informing future research". In: *Transportation Research Part C: Emerging Technologies* 132 (2021), p. 103377. DOI: 10.1016/j.trc.2021.103377.

[9] Gunady N. et al. "Evaluating Demand of Emerging Urban Air Mobility Vehicles with Changing Cost". Dutch. In: *AIAA SCITECH 2022 Forum* (2022). DOI: 10.2514/6.2022-1517.

[10] Jyotika A. et al. "Chip-Level Considerations to Enable Dependability for eVTOL and Urban Air Mobility Systems". In: (Oct. 2020), pp. 1–6. DOI: 10.1109/DASC50938.2020.9256436.

[11] Watson D.P. and Scheidt D.H. "Autonomous vehicles". In: *Johns Hopkins APL Technical Digest* 26.4 (2005), pp. 368–376.

[12] Fu M., Rothfeld R., and Antoniou C. "Exploring Preferences for Transportation Modes in an Urban Air Mobility Environment: Munich Case Study". In: *Transportation Research Record: Journal of the Transportation Research Board* 2673.10 (2019), pp. 427–442. DOI: 10.1177/0361198119843858.

[13] Taylor M., Saldanli A., and Park A. "Design of a vertiport design tool". In: *Center for Air Transportation Systems Research at George Mason University* (2020).

[14] NASA Urban Air Mobility. *Urban Air Mobility (UAM) Market Study*. PowerPoint. Nov. 2018.

[15] Department of Transport. *Mode of transport to the airport [Data sheet]*. UK government. 2021.

[16] Ennis N., ed. *Working paper 35: Come fly with me - Airport choice in Greater London*. Glaeconomics. Greater London Authority, City Hall, London: Greater London Authority, Apr. 2009.

[17] Volocopter GmbH. *Pioneering the urban air taxi revolution*. Volocopter White Paper. June 2019.

[18] *Fast-Forwarding to a Future of On-Demand Urban Air Transportation*. UBER Elevate. Oct. 2016.

[19] Kissounko D.A., Taynton P., and Kaffer C. "New Material: vitrimers promise to impact composites". In: *Elsevier* 00 (2017).

[20] Finger D. F. et al. *Cost Estimation Method for Hybrid-Electric General Aviation Aircraft*. Tech. rep. RMIT University, FH Aachen, 2019.

[21] Hoerner S.F. *Fluid-dynamic drag : practical information on aerodynamic drag and hydrodynamic resistance*. 2nd ed. Hoerner Fluid Dynamics, 1965.

[22] Anderson J.D. *Introduction to Flight*. New York: McGraw-Hill Education, 1985.

[23] Anderson J.D. *Fundamentals of Aerodynamics*. 6th ed. New York: McGraw-Hill Education, 2017.

[24] Roshko A. "Experiments on the flow past a circular cylinder at very high Reynolds number". In: *Journal of Fluid Mechanics* 10.3 (1961), pp. 345–356. DOI: 10.1017/S0022112061000950.

[25] Brown A. and Harris W. L. *A Vehicle Design and Optimization Model for On-Demand Aviation*. Tech. rep. Cambridge, MA: Massachusetts Institute of Technology, Jan. 2018.

[26] Seddon J. *Basic helicopter aerodynamics*. Oxford, England: BSP Professional, 1990.

[27] Zhao Y., Shi Y., and Xu G. "Helicopter Blade-Vortex Interaction Airload and Noise Prediction Using Coupling CFD/VWM Method". In: *Applied Sciences* (Apr. 2017).

[28] Johnson W. *Rotorcraft aeromechanics*. Cambridge University Press, 2013.

[29] Vanderover J. S. and Visser K. D. *Analysis of a Contra-Rotating Propeller Driven Transport Aircraft*. Tech. rep. Clarkson University.

[30] Won Kim H. and Brown R. E. *A Comparison of Coaxial and Conventional Rotor Performance*. Tech. rep. Imperial College London, 2010.

[31] Bolam R.C. and . Vagapov Y. *Review of Electrically Powered Propulsion for Aircraft*. Tech. rep. Glyndwr University.

[32] Malpica C. and Withrow-Maser S. *Handling Qualities Analysis of Blade Pitch and Rotor Speed Controlled eVTOL Quadrotor Concepts for Urban Air Mobility*. Tech. rep. NASA Ames Research Center.

[33] Hepperle M. "JavaProp users guide". In: (June 2009).

[34] Adkins C. N. and Liebeck R. H. *Design of Optimum Propellers*. Tech. rep. Douglas Aircraft Company,

[35] Mourão Bento H. "Aerodynamic interaction effects of circular and square ducted propellers". In: (May 2019).

[36] Ugwueze O. et al. "Investigation of a mission-based sizing method forelectric VTOL aircraft preliminary design". In: *AIAA SciTech 2022 Forum* (2022), p. 13.

[37] Leishman J. G. *Principles of Helicopter Aerodynamics*. Cambridge University Press, 2016.

[38] Lee A. and Zhang F. "Gemini: A Compact yet Efficient Bi-copter UAV for Indoor Applications". In: (2020).

[39] Schulz M.J., Shanov V. N., and Yin Z. "Nanotube Superfiber Materials". In: 2014. Chap. Development of Lightweight Sustainable Electric Motors, pp. 595–626.

[40] Pranoto F.S., Wirawan A., and Purnamasari D.A. "Electrical Power Budgeting Analysis for LSA-02 UAV Technology Demonstrator". In: *IOP Conference Series: Materials Science and Engineering* 160.1 (2016). DOI: 10.1088/1757-899x/160/1/012088.

[41] Cervone A. and Zandbergen B.T.C. *Electrical Power Systems for Aerospace Vehicles*. AE2230-II: Propulsion & Power. Feb. 2017.

[42] Xu P., Tan D.H.S., and Chen Z. "Emerging trends in sustainable battery chemistries". In: *Trends in Chemistry* 3.8 (2021), pp. 620–630. DOI: 10.1016/j.trechm.2021.04.007.

[43] Bruce P.G. et al. "Li–O2 and Li–S batteries with high energy storage". In: *Nature Materials* 11.1 (2011), pp. 19–29. DOI: 10.1038/nmat3191.

[44] N. Chawla. "Recent advances in air-battery chemistries". In: *Materials Today Chemistry* 12 (2019), pp. 324–331. DOI: 10.1016/j.mtchem.2019.03.006.

[45] Li O.L. and Ishizaki T. "Development, Challenges, and Prospects of Carbon-Based Electrode for Lithium-Air Batteries". In: *Emerging Materials for Energy Conversion and Storage* (2018), pp. 115–152. DOI: 10.1016/b978-0-12-813794-9.00004-1.

[46] Martha S.K. et al. "A low-cost lead-acid battery with high specific-energy". In: *Journal of Chemical Sciences* 118 (2006), pp. 93–98. DOI: 10.1007/BF02708770.

[47] Salminen A. Väyrynenand J. "Lithium ion battery production". In: *The Journal of Chemical Thermodynamics* 46 (2012), pp. 80–85. DOI: 10.1016/j.jct.2011.09.005.

[48] Lee J. et al. "Metal-Air Batteries with High Energy Density: Li-Air versus Zn-Air". In: *Advanced Energy Materials* 1.1 (2010), pp. 34–50. DOI: 10.1002/aenm.201000010.

[49] "Gravimetric and volumetric energy densities of lithium-sulfur batteries". In: *Current Opinion in Electrochemistry* 6.1 (2017), pp. 92–99. ISSN: 2451-9103. DOI: https://doi.org/10.1016/j.coelec.2017.10.007.

[50] Christensen J. et al. "A Critical Review of Li/Air Batteries". In: *Journal of The Electrochemical Society* 159.2 (2011), R1–R30. DOI: 10.1149/2.086202jes.

[51] Girishkumar G. et al. "Lithium−Air Battery: Promise and Challenges". In: *The Journal of Physical Chemistry Letters* 1.14 (2010), pp. 2193–2203. DOI: 10.1021/jz1005384.

[52] Bruce P.G. "Energy storage beyond the horizon: Rechargeable lithium batteries". In: *Solid State Ionics* 179.21-26 (2008), pp. 752–760. DOI: 10.1016/j.ssi.2008.01.095.

[53] Yan J., Liu X., and Li B. "Capacity Fade Analysis of Sulfur Cathodes in Lithium–Sulfur Batteries". In: *Advanced Science* 3.12 (2016), p. 1600101. DOI: 10.1002/advs.201600101.

[54] Liu Y.-T. et al. "Strategy of Enhancing the Volumetric Energy Density for Lithium–Sulfur Batteries". In: *Advanced Materials* 33.8 (2020), p. 2003955. DOI: 10.1002/adma.202003955.

[55] Furse C. and Haupt R. "Down to the wire [aircraft wiring]". In: *IEEE Spectrum* 38.2 (2001), pp. 34–39. DOI: 10.1109/6.898797.

[56] Rambabu P. et al. "Aluminium Alloys for Aerospace Applications". In: ed. by Prasad N.E. and Wanhill R.J.H. Vol. 1. Singapore: Springer, 2017, pp. 29–52.

[57] Zhang X., Chen Y., and Hu J. "Recent advances in the development of aerospace materials". In: *Progress in Aerospace Sciences* 97 (2018), pp. 22–34. ISSN: 0376-0421. DOI: https://doi.org/10.1016/j.paerosci.2018.01.001.

[58] Peters M. et al. "Titanium Alloys for Aerospace Applications". In: *Advanced Engineering Materials* 5.6 (2003), pp. 419–427. DOI: 10.1002/adem.200310095.

[59] Mirdehghan S.A. *Engineered Polymeric Fibrous Materials*. Woodhead Publishing, 2021, pp. 1–58.

[60] Yan L., Chouw N., and Jayaraman K. "Flax fibre and its composites – A review". In: *Composites Part B: Engineering* 56 (2014), pp. 296–317. DOI: 10.1016/j.compositesb.2013.08.014.

[61] Yang Y. et al. "Functional epoxy vitrimers and composites". In: *Progress in Materials Science* (2021). DOI: 10.1016/j.pmatsci.2020.100710.

[62] Matyjaszewski K. and Möller M. *Polymer Science: A Comprehensive Reference*. 1st ed. Vol. 10. Elsevier, 2012.

[63] Arockiam N.J., Jawaid M., and Saba N. "Sustainable bio composites for aircraft components". In: *Sustainable Composites for Aerospace Applications* (2018), pp. 109–123. DOI: 10.1016/B978-0-08-102131-6.00006-2.

[64] Wang S. et al. "Taking advantages of intramolecular hydrogen bonding to prepare mechanically robust and catalyst-free vitrimer". In: *Polymer* 210 (2020). DOI: https://doi.org/10.1016/j.polymer.2020.123004..

[65] *Manual for EMRAX Motors / Generators*. 5.4. EMRAX. May 2020.

[66] Niu M.C.Y. *Composite airframe structures*. First edition. Conmilit Press LTD., 1992.

[67] Kassapoglou C. *Design and Analysis of Composite Structures*. First edition. John Wiley & Sons, Ltd, 2010.

[68] Babetto L. and Stumpf E. "Recent Development of a Conceptual Design Methodology for Unmanned Aerial Vehicles". In: *AIAA AVIATION 2021 FORUM* (2021). DOI: 10.2514/6.2021-3219.

[69] Megson T.H.G. *Aircraft Structures for engineering students*. Sixth edition. Elsevier Ltd, 2017.

[70] *Certification Specifications for Small Rotorcraft CS-27*. Amendment 3. European Aviation Safety Agency. Dec. 2012.

[71] Federal Aviation Administration. *Helicopter Flying Handbook*. U.S Department of Transportation, 2019.

[72] Hibbeler R.C. *Mechanics of Materials*. Pearson, 2018.

[73] Şen I. "Aircraft Fuselage Design Study". Master of Science Thesis. Delft: Delft University of Technology, Dec. 2010.

[74] Shrotri K. "Composite skid landing gear design investigation". Thesis. School of Aerospace Engineering Georgia Institute of Technology, Aug. 2008.

[75] Crist D. and Symes H. *Helicopter landing gear design and test criteria investigation*. Bell Helicopter Textron. Aug. 1981.

[76] Saleh M. "Analysis, Design Optimization, and Semi-Active Control of Skid Landing Gear Featuring Bi-Fold Magnetorheological Dampers". In: 2017.

[77] Sundar R., Balajib A.N., and SatheeshKumar R.M. "A Review on Lean Manufacturing Implementation Techniques". In: *Procedia Engineering* (Dec. 2014).

[78] Berg J.S. and Kanne J.T. "Composite Applications in Sports Equipment: table rolling of composite tubes". In: *Composites Applications and Design* (July 1997).

[79] Dhakal H.N. and Ismail S.O. "Sustainable Composites for Lightweight Applications". In: 2021. Chap. Design, manufacturing processes and their effects on bio-composite properties, pp. 121–177.

[80] Sinke J. *Production of Aerospace Systems Reader*. AE3211-II: Production of Aerospace Systems. Feb. 2022.

[81] Zhou G. and Hood J. "Design, manufacture and evaluation of laminated carbon/epoxy I-beams in bending". In: *Composites Part A: Applied Science and Manufacturing* 3.3 (2004), pp. 506–517. DOI: 10.1016/j.compositesa.2005.01.005.

[82] Fisher M. et al. "Towards a framework for certification of reliable autonomous systems". In: *Autonomous Agents and Multi-Agent Systems* 35 (2021).

[83] Kadhiresan A.R. and Duffy M.J. *Conceptual Design and Mission Analysis for eVTOL Urban Air Mobility Flight Vehicle Configurations*. Tech. rep. Cornell University, Ithaca, June 2019. DOI: 10.2514/6.2019-2873.

[84] Yu K. et al. "Carbon fiber reinforced thermoset composite with near 100% recyclability". In: *Advanced Functional Materials* 26.33 (2016), pp. 6098–6106. DOI: 10.1002/adfm.201602056.

[85] Liu Y. et al. "Recycling of Carbon/Epoxy composites". In: *Wiley InterScience* (Apr. 2004).

[86] Dang W. et al. "An approach to chemical recycling of epoxy resin cured with amine using nitric acid". In: *Polymer* 43.10 (2002), pp. 2953–2958. DOI: 10.1016/S0032-3861(02)00100-3..

[87] Dang W. et al. "An approach to chemical recycling of epoxy resin cured with amine using nitric acid". In: *Polymer* (May 2002).

[88] *Cradle to Cradle Certified® User Guidance*. Version 4. Cradle to Cradle Products Innovation Institute. 2021.

[89] van Alkemade I. et al. *Baseline Report DSE Spring 2022*. Tech. rep. Delft University of Technology, May 2022.